

THÈSE DE DOCTORAT DE L'ÉTABLISSEMENT  
UNIVERSITÉ BOURGOGNE FRANCHE-COMTÉ  
PRÉPARÉE À L'INSTITUT DE RECHERCHE  
**FEMTO-ST**

ÉCOLE DOCTORALE 37  
SCIENCES POUR L'INGÉNIEUR ET MICROMECHANIQUE

Doctorat d' Automatique

par  
Chibundo NWAFOR

**Contribution to the Miniaturization  
of Continuum Robots by Using Glass**

Soutenue à Besançon le 15 novembre 2023

Composition du Jury :

PRELLE Christine  
NAGEOTTE Florent  
LAMBERT Pierre  
BERGELES Christos  
LAURENT Guillaume  
RABENOROSOA Kanty

Professeure à l'Université Technologique de Compiègne  
Maître de conférences HDR à l'Université de Strasbourg  
Professeur à l'Université Libre de Bruxelles  
Professeur au King's College London  
Professeur à l'ENSMM-SUPMICROTECH  
Maître de conférences HDR à l'ENSMM-SUPMICROTECH

Présidente du jury  
Rapporteur  
Rapporteur  
Examinateur  
Co-directeur  
Directeur



## Acknowledgements

I would like to thank my lovely parent and my beautiful wife, for their support and encouragement throughout my PhD. Sincerely and most importantly, I am so grateful to my supervisors, who have been the backbone of my success story and pivot points to the breakthrough achievements during these years of my PhD research work. It is really an honor and blessing working with them. Finally, I feel very happy and thankful to God almighty for seeing me through ...

## Acknowledgements

---

# Contents

<b>Acknowledgements .....</b>	iii
<b>Contents .....</b>	v
<b>Abstract .....</b>	1
<b>General Introduction .....</b>	3
<b>1 State-of-the-art: CTR and PCR .....</b>	17
<b>1.1 Objective .....</b>	18
1.1.1 Glass material/properties .....	18
1.1.2 Continuum robots .....	20
<b>1.2 Concentric tube robots (CTR)s .....</b>	22
1.2.1 Tube design.....	24
1.2.2 Tube fabrication .....	26
1.2.3 Applications .....	32
<b>1.3 Parallel Continuum Robots (PCRs).....</b>	34
1.3.1 Concept .....	34
1.3.2 Classifications.....	38
<b>1.4 Continuum robot modeling.....</b>	41
1.4.1 Kinematic frameworks .....	43
1.4.2 Mechanics formulation .....	47
1.4.3 Numerical resolution solvers .....	49
1.4.4 Proxy models .....	52
<b>1.5 Conclusion.....</b>	53
1.5.1 For CTR .....	53
1.5.2 For PCR .....	54
1.5.3 For modeling.....	54
<b>2 Fabrication of pre-curved glass tubes .....</b>	57
<b>2.1 Glass fabrication method at small scale .....</b>	58
2.1.1 Additive method .....	58

2.1.2	Subtractive method.....	60
2.1.3	Shaping method.....	62
<b>2.2</b>	<b>3D Microfabrication using Femtosecond laser-assisted wet etching (FLWE).....</b>	<b>63</b>
2.2.1	Fabrication of standing microglass beams by FLWE..	64
2.2.2	Experiment plan for microscale glass tube fabrication by FLWE .....	65
2.2.3	Experimental results and discussion .....	67
<b>2.3</b>	<b>Fabrication of pre-curved glass tubes using heat treatment approach .....</b>	<b>69</b>
2.3.1	Heat treatment approach.....	69
2.3.2	Tube shape setting by heat treatment .....	70
2.3.3	Experimental result.....	72
<b>2.4</b>	<b>Tube shape setting using polymer heat-shrink jacket .</b>	<b>73</b>
2.4.1	Materials and methods.....	73
2.4.2	Characterization and validation.....	74
2.4.3	Bending stiffness analysis of microglass tubes.....	76
<b>2.5</b>	<b>Conclusion.....</b>	<b>78</b>
<b>3</b>	<b>CTR made of glass.....</b>	<b>81</b>
<b>3.1</b>	<b>Objectives .....</b>	<b>82</b>
<b>3.2</b>	<b>Introducing CATURO.....</b>	<b>82</b>
3.2.1	CATURO tubes .....	83
3.2.2	CATURO actuation unit .....	85
3.2.3	CATURO control system.....	86
<b>3.3</b>	<b>Model validation of the sub-millimeter glass CTRs ..</b>	<b>87</b>
3.3.1	Forward kinematic model (FKM) validation: .....	87
3.3.2	Path following based on IKM .....	90
3.3.3	Stability analysis and validation .....	93
<b>3.4</b>	<b>Glass CTR deployment.....</b>	<b>96</b>
3.4.1	3D conical-spiral free space deployment .....	97
3.4.2	Helical pre-curved CTR glass deployment .....	98
3.4.3	Constraint deployment of CTR through needles .....	99
<b>3.5</b>	<b>Applications .....</b>	<b>100</b>
3.5.1	Deployment of pre-curved optical fiber with laser transmission .....	100
3.5.2	Fluid suction and delivery.....	102
3.5.3	Vitreoretinal deployment under the OCT .....	103

---

3.6	Conclusion and Discussion .....	104
<b>4</b>	<b>Miniaturized PCR made of glass.....</b>	<b>109</b>
4.1	Objective .....	110
4.2	Robot architecture and modeling .....	110
4.2.1	Design concept and architecture .....	110
4.2.2	Modeling .....	112
4.3	The PCR design analysis.....	115
4.3.1	Workspace .....	116
4.3.2	End-Effector Orientation .....	117
4.3.3	Manipulability .....	118
4.3.4	Stiffness .....	120
4.4	Geometrical design parameter analysis.....	122
4.4.1	Actuation length .....	122
4.4.2	End-effector dimension.....	124
4.5	Model validation and experimental results .....	127
4.5.1	Prototype design and fabrication.....	127
4.5.2	Experimental demonstrations and validations .....	129
4.6	Conclusion.....	132
	<b>Conclusions and Perspectives.....</b>	<b>135</b>
<b>A</b>	<b>Tube design approaches.....</b>	<b>145</b>
A.1	Tube design approaches .....	147
A.1.1	Optimization of a Tube Set:.....	147
A.1.2	Modification of the Mechanical Properties of Tubes via material removal: .....	149
A.2	Tube Design: Perspectives .....	150
<b>B</b>	<b>CTR actuation units.....</b>	<b>153</b>
B.1	CTR actuation units .....	154
B.1.1	Actuation Unit Elements.....	155
B.1.2	Parallel Actuation Units .....	155
B.1.3	Hybrid Actuation Units.....	157
B.1.4	Serial Actuation Units .....	158
B.2	Actuation Units: Perspectives .....	159

---

<b>C CTR end-effectors</b>	161
<b>C.1 CTR end-effectors</b>	162
C.1.1 Manipulation	162
C.1.2 Inspection	163
C.1.3 Excision/Resection	163
C.1.4 Hybridized Architectures	164
<b>C.2 End Effectors: Perspectives</b>	164
<b>D Applications of CTRs in MIS</b>	167
<b>E Precurved Optical Fibre Join by Fusion and RealSense D405 stereo depth camera of precurved tube</b>	171
<b>Bibliography</b>	175
<b>List of Figures</b>	235
<b>List of Tables</b>	247

# Abstract

Continuum robots are gaining increasing interest in medical applications, due to their slender shape and compliant nature which makes them safer for human-to-robot interaction. In addition, they are able to follow a 3D complex path, thanks to their infinite degrees of freedom. The goal of this thesis is to take advantage of glass flexibility at the microscale to actualize novel and more miniature continuum robots when compared to those in the literature. The first contribution is a conceptual study, addressing the design and fabrication of different CTR prototypes and deriving a general classification approach while proposing to the research community a concise methodology for the evaluation of CTR in the future. Secondly, we proposed a new generation of a miniaturized sub-millimeter CTR that is made of glass, which has a tube with an external diameter down to  $90\mu\text{m}$  and a 5mm radius of curvature. Furthermore, we presented a novel, easy, and rapid patient-specific/customizable approach to obtaining a pre-curved tube using glass, which was characterized, followed by the robot model validation (forward kinematic, inverse kinematics, and stability analysis). Various demonstrations of proofs-of-concept for the different application capabilities e.g. vitreoretinal deployment in a fish eye, constraint deployment through 3-stationed needles ( $\sim 1\text{mm}$  orifice), pre-curved helical and fiber optics CTR deployment with laser transmission capability, and then, fluid suction and delivery. The third contribution was the investigation and demonstration of a miniaturized 3-Dof PCR using glass optical fiber. The robot design has a dimension of  $2.5 \times 2.5 \times 6\text{mm}$  and can reach  $+90$  to  $-80$  degrees in the tip and tilt angle. The robot's performance such as the workspace, manipulability, and stiffness was evaluated as a function of variations of different geometrical parameters of the robot. For the model validation, different path movements were presented such as vertical plane circumradius and workspace followed by the circular and square shapes in the horizontal plane, which shows the great prospect of the robot for increasing dexterity in confined space. Finally, for both cases, the robot design analysis was very important for investigating the robot stability, for CTR due to torsion, and for PCR, due to the actuation length.

## Abstract

---

# General Introduction

## MOTIVATION

The evolution in medical intervention from traditional open surgery to minimally invasive surgery (MIS) has resulted in improved surgical outcomes such as less patient trauma, less blood loss, and shorter recovery time. These improvements are due to miniature incisions compared to the large openings in the patient's body. However, this technique has significant challenges such as difficulty in accessing surgical targets through complex 3D paths and the ability to control the rigid instruments due to limited maneuverability, dexterity, and degrees of freedom [Vitiello 13]. The goal of robotic-assisted surgery was to improve surgical procedures while maintaining the advantages of open surgery in MIS [Satava 04]. These include facilitating easy access to complex or hard-to-reach surgical targets with greater dexterity and DoFs, enhanced visualization of the anatomy; improved tool deployment precision/accuracy; reduced surgeon hand tremors and fatigue during tool manipulation or teleoperation [Satava 11]. All these have paved the way for developing different MIS intervention tools and instruments categorized into three by Dupont et al. [Dupont 10b] as presented in Figure 1. With lots of

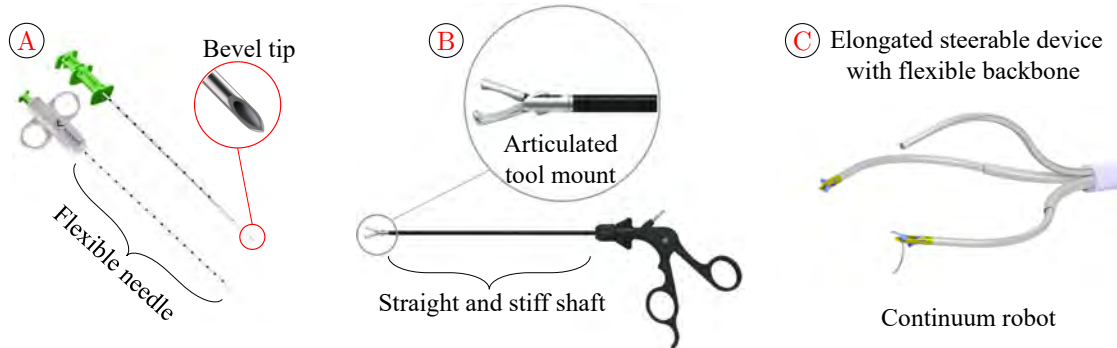


**Figure 1:** The three classes of MIS intervention instruments A) Flexible needle with a straight shaft having a bevel tip that steers and changes its direction upon application of lateral force at the base. Its drawback is high dependence on solid tissue penetration to produce lateral tip motion and secondly, it cannot maneuver through curved cavity/anatomy, B) Straight and stiff shaft with a tip-mounted articulated tool, which reaches the surgical site through a straight path. It is difficult to steer through complex anatomy and the tool manipulation can often cause tissue deformation e.g. forceps and da Vinci, Intuitive Surgical tools, C) Elongated steerable device with a flexible backbone. They consist of flexible catheters or multistage dexterous devices like continuum robots.

different progress today, there are still huge areas in medical intervention needing technological improvements. The majority of these demands have been in the area of developing smart devices with better properties and characteristics for targeted applications. These include achieving high overall robot miniaturization for possible handheld capability and single-port deployability. Among other features are high dexterity, high precision, high maneuverability, and safer robot-to-human interaction. To that effect, all these have resulted in the paradigm shift in medical robotics research, from the traditional rigid robot to the continuum (continuously deformable) and soft robots. This emerging field of research has drawn enormous focus today due to its overwhelming potential and benefits.

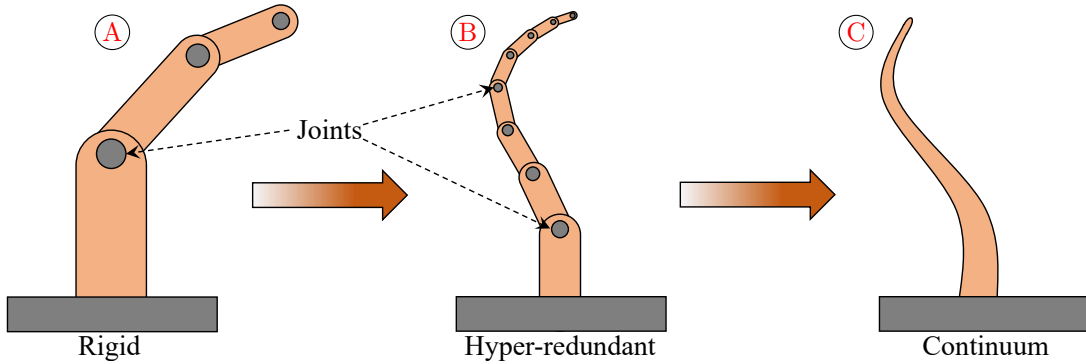


**Figure 2:** Transition from conventional rigid robot to continuum robot due to its benefits, A) a typical conventional serial robot with discrete links connected by joints B) a hyper-redundant type of rigid robot in order to increase its dexterity and maneuverability, C) continuum robot type with infinite DOFs and deformable link(s) which is safer for human-to-robot interaction.

One of the key challenges in MIS is navigating to the surgical site through complex 3D curves while avoiding sensitive organs or bony structures and most preferably passing through a natural body orifice e.g. nose, mouth, or ear. In fact, on reaching the surgical site, the next issue is the capability to control its distal tip, while the proximal end is held relatively immobile during tool manipulation. These have motivated the constant rise in the development of smart compact devices with the possibility of teleoperation, as seen in the high research throughput on continuum robots today. Comparing the three categories of MIS intervention instruments (see Figure 1), the continuum robots which includes the concentric tube robots (CTR), tendon-driven, and parallel continuum robot (PCR) possess the best properties of all the three types [Dupont 10b]. The reasons for the paradigm shift in the field of robotics from conventional robots that are composed of rigid links connected by discrete joints to continuum robots as shown in Figure 2 include:

1. Infinite degree of freedom thanks to its continuously deformable backbone meaning high dexterity and maneuverability,

2. Provides much more safe human-to-robot interaction due to its inherent compliant property,
3. With all the motors/actuators located externally at the proximal end, this makes the robot suitable for MIS.

These have given rise to the creation and upsurge of new research communities/clusters around the globe focusing on continuum robots. Today, there are vastly different design prototypes and publications on continuum robots as the majority of them are proposed for medical applications [Jones 05, Yang 18a]. Though, Chapter-1 discussed extensively the state of the art of the two continuum robots of interest. Notably, the benefits and advantages of MIS today are undeniable and these are the driving force for the several proposed use of continuum robots due to their scalability. Even with the current state-of-the-art of continuum robots, there are still demands for further invasiveness, which are aimed at accessing hard-to-reach surgical regions in clinical interventions. These have resulted in the need for miniaturization of clinical instruments/devices, which are detailed further below.

## NEED FOR MINIATURIZATION

To further enhance MIS capabilities, there is a growing demand for smaller and more precise devices. Considering the most popular commercial surgical robotic system, which is da Vinci, has more than 10 million MIS performed worldwide [Badani 07, D'Ettorre 21, Marcus 14, Intuitive 21]. This surgical robot uses instruments that are rigid and straight with articulating tips. In addition, they also have a large footprint in the operating room. Hence, the trend toward miniaturization of MIS tools is evident in order to maximize the benefits and advantages that come with it [Yang 18a]. Some of the key benefits or reasons for MIS device miniaturization include:

1. **Enable less invasive procedures:** With smaller devices, surgeons can perform interventions through smaller incisions or natural orifices, minimizing tissue damage and reducing patient trauma. This approach results in faster healing times, shorter hospital stays, and improved patient outcomes.
2. **Need for improved dexterity:** The availability of highly specialized instruments and devices allows surgeons to perform tasks swiftly with a high level of dexterity and reliability. Indeed, miniaturized devices can navigate intricate anatomical structures, enabling surgeons to access challenging areas that were previously difficult to reach. For example, transcatheter procedures like aortic valve replacement can now be performed entirely from a groin-area access site [Onan 20, Kalogeropoulos 22, Toggweiler 13], thanks to miniaturized devices.

3. **Easy patient-specific adaptability:** In all cases, due to the fact that at the same scale, one has to adapt to the anatomy, this benefits by having a smaller device that can easily be customized to adapt patient-specific need or anatomy structure. There is a higher benefit/possibility of organ collision avoidance using a miniaturized MIS device.
4. **Cost reduction and improvement of patient comfort:** Smaller devices require fewer resources and materials, resulting in cost savings in manufacturing and medical procedures. Additionally, the use of miniaturized devices can contribute to reduced pain, scarring, and discomfort for patients, enhancing their overall experience during and after surgery.

As technology advances, the convergence of various aspects is expected to drive development in terms of smaller, more dexterous, and less expensive devices for a wide range of procedures. The ongoing improvements in MIS device miniaturization are vital for pushing the boundaries of what is possible in surgical interventions, ultimately leading to enhanced patient care and outcomes. Therefore, having manipulators that are scalable to a small size, flexible yet strong, and capable of reaching difficult-to-access surgical sites via complex pathways and completing the surgical task with dexterity would be extremely beneficial. Continuum robots with small sizes are more suitable for MIS compared to using straight rigid instruments [Burgner 15a]. Although, among all the different types of medical robots, the continuum robot has witnessed a sporadic rise in research and the highest publication throughput currently. Yet, one major aspect of research and need in the field of medicine that was identified was the area of miniaturization [Yang 18a]. In as much the importance of robots in medicine is undoubtedly overemphasized, there are still large areas calling for a research breakthrough, especially in microsurgery and micromanipulation.

Miniaturized manipulators are designed to manipulate small objects with a high degree of accuracy and repeatability in confined spaces. These devices have a wide range of applications in different fields, such as the manipulation of samples inside scanning electron microscopes (SEM) or for endoscopic medical procedures. For endoscopic medical procedures, the manipulators are inserted into the body through small incisions and are used to perform delicate procedures, such as imaging, biopsy, suturing, or removing small tissue samples. Inside SEM, miniaturized manipulators are used for handling samples for imaging, performing various measurements, or assembling components. One of the current challenges of micromanipulation e.g in SEM or medical is to increase the dexterity of the manipulators by integrating rotations at the distal end, to actualize tool orientation with large angles. Indeed, the three translational movements of the end-effector in the  $x$ –,  $y$ –, and  $z$ –axis, can be generated by proximal joints, whereas only distal ones can produce the orientation of the tool. Having a distal orientation section is well known to improve manipulator dexterity [Wu 17b, Chikhaoui 16, Peyron 22, Li 17]. When considering parallel manipulators, which has many advantages such as

high precision, high speed, high payload/force capabilities, and extrinsic actuation, that enable locating the actuators outside of the confined space leading to a very high miniaturization potential but they are often limited in workspace volume [Jin 15]. Presently, the smallest parallel manipulators in the literature include Millidelta [McClintock 18] and Migribot [Leveziel 22]. Though each presents key benefits thanks to their parallel configurations, they are both restricted to translative motion. Conversely, this issue and limitation can be solved using a new type of parallel robot called parallel continuum robots (PCRs) [Bryson 14]. For this reason, added to the benefits and possibilities of using flexible glass at a small scale, this is one of the key research investigations and analyses in this dissertation.

Current MIS tools still have challenges to access some confined regions of surgical sites due to the size, location, or sensitivity/complexity nature of anatomical structure e.g. when considering the use of the conventional rigid straight instrument. Considering the trend in medicine for further miniaturization, which targets the possibility of accessing hard-to-reach zone of interest. In fact, the rising trend

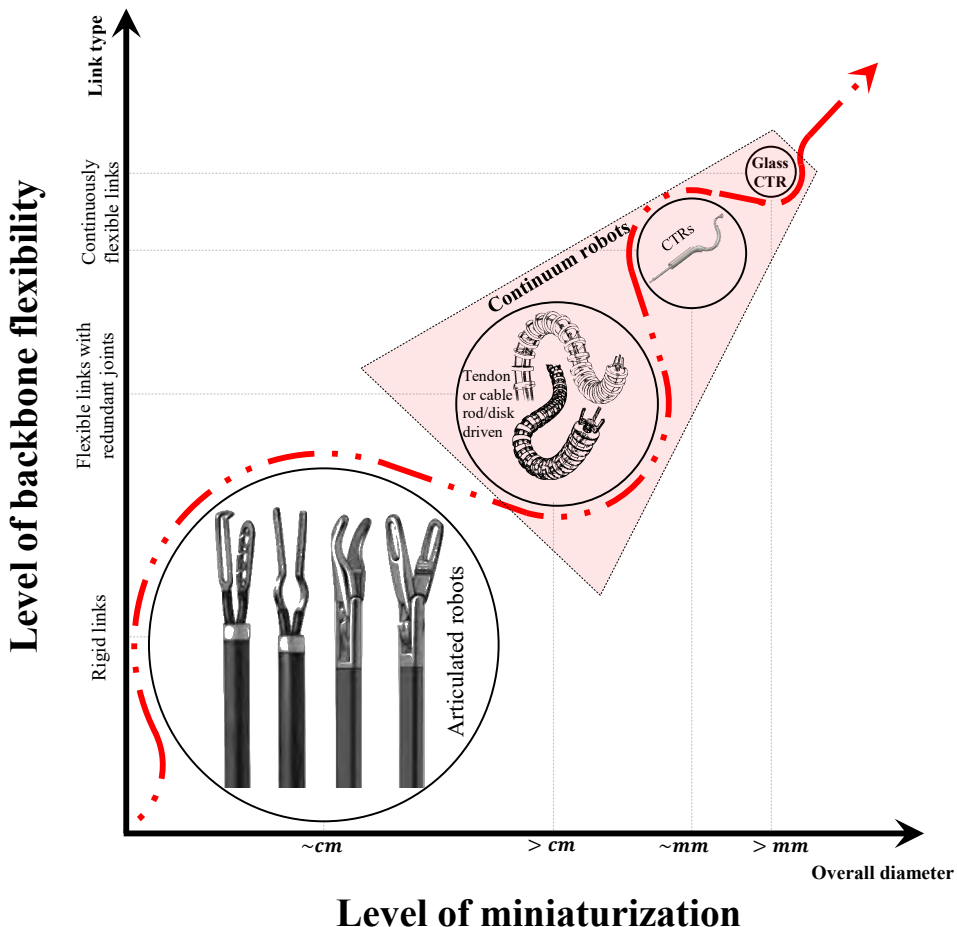


**Figure 3:** Trend in medical robotic devices with a paradigm shift from rigid link/articulated robots to continuum robots on the bases of backbone flexibility and level of miniaturization.

in medicine for micro-port multi-deployment strategy has given rise to the need for the development of devices that can meet the demand, especially in neurosurgery. The ongoing advancements in MIS device miniaturization contribute to the evolution of surgical techniques, offering numerous benefits to patients and healthcare providers alike. In general, the need for miniaturization has motivated the rise in small-scale smart devices, which are proposed for microsurgery or MIS, and has paved the way for the high research throughput in compact continuum robots. The trend for further miniaturization with its benefits, has put continuum robots on top of the ladder among clinical instruments and devices for MIS (refer to Figure 3).

In Figure 3, concentric tube robots (CTR) are at the top of the ladder when considering the level of backbone flexibility due to no redundant joint by disk. In the case of miniaturization, they are simply composed of nested pre-curved tubes that can be easily scaled down sub-millimeter level. Considering the conventional use of Nitinol for continuum robot fabrication, which is now the predominant material for prototyping different continuum robots in the literature. However, researchers had reached a stagnating point of constant use of Nitinol and then began to call for investigation of other viable materials [Gilbert 16b]. These paved the way for the use of 3D print materials but unfortunately, the process is highly dependent on the printer setting, and output or mechanical qualities were poor compared to the use of Nitinol. To that effect and in regard to the present demand for further miniaturization, we considered and explored the use of glass at a small scale for the fabrication of miniaturized continuum robots. Since thin glass at a small scale is flexible e.g. optical fiber, this presents great benefits considering the inherent properties of glass like the light carry capacity, and this will open entirely new doors in the domain of continuum robots along with the application potentials.

## USING GLASS MATERIAL FOR MINIATURIZED CONTINUUM ROBOTS

Glass has proved to be one of the most inevitable materials for the fast-emerging field of micromachining technology. It has a desirable optical and good isolation property [Tay 06, Takahashi 13], which in addition to their biocompatibility, chemical stability, hydrophilicity, and optical transparency, makes them suited for various applications ranging from Optical/Bio-MEMS, micro-actuators, micro-sensors, and the Lab-on-chip device. The development of microfabrication in glass techniques over the years enabled different microcomponents and applications ranging from microfluidic (microchannels) [Tang 21, Cheng 03a, Kikutani 02, Hnatovsky 06], optical (optical alignment, waveguide, and positioners) [Rosa 15, Karnaushkin 21, Kronig 18, Mittholiya 16], mechanical parts (nozzles, gears) [Niza 10, Montanero 10, Eklund 08, Wang 10], micro-actuators [Lenssen 12a, Hata 99, Wang 09,

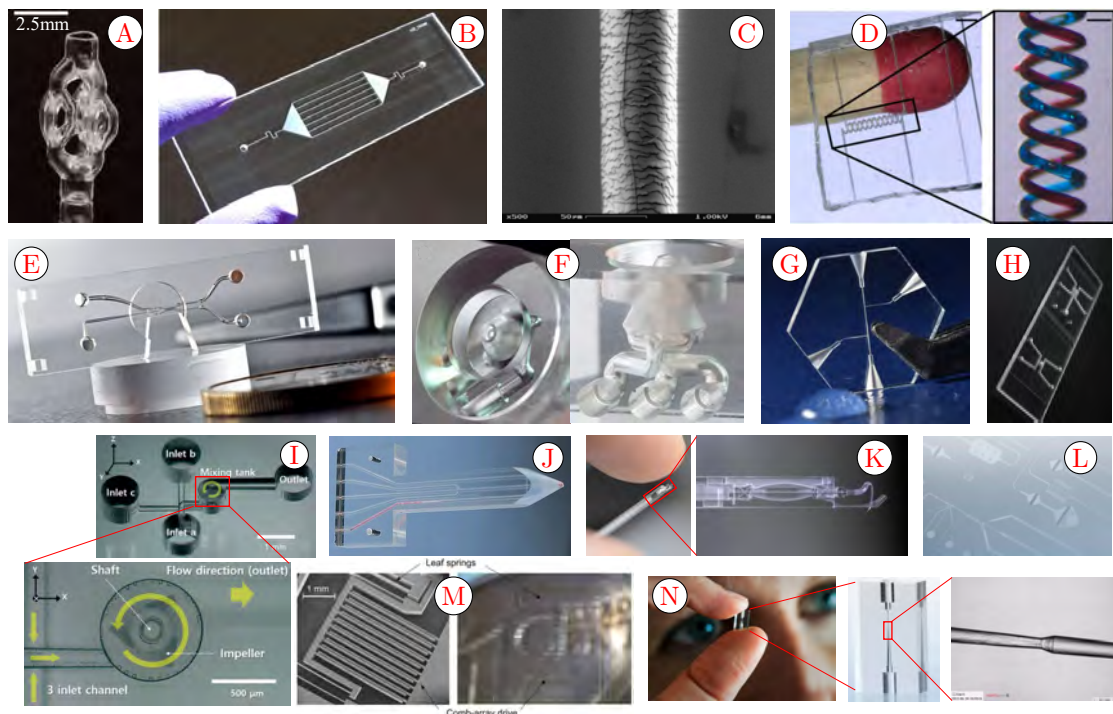


**Figure 4:** Different 3D miniature devices and monolithic microstructure fabricated in glass **A)** Volumetric 3D printing of silica glass with microscale computed axial lithography to fabricate a 3D transparent and complex microfluidic structure, having trusses and lattice with minimum feature sizes of  $50\mu\text{m}$ , [Toombs 22a], **B)** Microfluidic device using laser micro-welding process in which the two glass plates are permanently bonded together without using any adhesives nor intermediate layer [Wlodarczyk 19], **C)** SEM image of a  $500\text{nm}$  diameter silica micro/nanofibre (MNF) tied into a ring and placed on a  $60\mu\text{m}$  diameter human hair, with the MNF often used for optical sensors [Tong 18], **D)** Intertwined microfluidic spiral channels in fused silica glass with a channel width of  $74\mu\text{m}$ , which is filled with dyes (scale:  $140\mu\text{m}$ ) [Kotz 19], **E)** Quartz glass chip for cell sorting application with a dimension of  $34\text{mm} \times 12\text{ mm} \times 2\text{mm}$ , fabricated by selective laser-induced etching [Gottmann 17], **F)** Top and side view of a nested nozzle in quartz glass for biological application (diameter:  $10\text{mm}$ , height:  $7\text{mm}$ ), fabricated by selective laser-induced etching [Gottmann 17], **G)** Quartz glass connector for capillary electrophoresis, diameter  $15\text{mm}$ , thickness  $2\text{mm}$ , fabricated by selective laser-induced etching [Gottmann 17] **H)** Transparent suspended microchannel resonator (SMR) in fused silica with fluidic channels with a cross-section around  $10\mu\text{m} \times 5\mu\text{m}$  flowing underneath [FEMTOprint 18b], **I)** Monolithic 3D micromixer with an impeller for glass microfluidic systems using selective laser-induced etching [Kim 20d], **J)** Microfluidic mixer with 5 inlets and 1 outlet (channels diameter of  $100\mu\text{m}$ ) [FEMTOprint 17], **K)** Passive compliant tool for retinal vein cannulation (RVC) that relies on a buckling mechanical principle [FEMTOprint 18a], **L)** 3D complex lab-on-a-chip (smallest channel diameter of  $3\mu\text{m}$ ) [FEMTOprint 17], **M)** Optically transparent glass micro-actuator fabricated by femtosecond laser exposure and chemical etching [Lenssen 12a], **N)** 3D microfluidic channel fabricated by using selective laser-assisted etching [FEMTOprint 23].

Minami 93, Sakurai 15, Kometani 04, Wang 09, Füzesi 07] and sensors [Lin 97, Waltermann 15, Zusman 90, Rogers 95, Gao 10, He 14, Vlasov 94, Gharbi 23, Butt 22, Zhang 22a]. Figure 4 presents some of the 3D miniaturized and monolithic devices in the literature that are fabricated with glass using different approaches. Figure 4A show the possibility of 3D volumetric additive manufacturing of silica glass

with microscale computed axial lithography for microstructures with minimum feature sizes of  $50\mu\text{m}$ . It is also possible to use a maskless approach to fabricate in glass by laser micro-welding which usually involves non-adhesive bonding of two pre-printed surfaces (see 4B). The case of  $500\text{ nm}$  diameter silica micro/nanofibre for optical sensors, which is fabricated by taper-drawing glass fiber at high temperature is presented in 4C. It is also possible to fabricate arbitrary 3D suspended hollow microstructures in transparent fused silica glass using stereolithography as shown in 4D. Using selective laser-induced etching, this presents the most predominant approach which is used from Figure 4E to Figure 4N, for designing different complex 3D monolithic micro-structures in a glass.

While conventional glass at the macro scale is rigid and brittle, conversely, at the micro-scale level, thin glass is flexible with high tensile strength [Rafael 16, Garner 17]. These inherent properties of glass on a micro-scale are beneficial in the design of miniaturized 3D structures. Therefore, one can take advantage of glass at the micro-scale to design and fabricate miniaturized flexible microstructure [Tong 18]. Consequently, this solidifies the possibility of designing and fabricating a continuum robot using thin glass. Moreover, for CTRs, higher dexterity in a tightly confined region requires a small radius of curvature [Chikhaoui 16]. For this reason, we ask the question of whether tubes made of glass, with a sub-millimeter diameter can permit a small radius of curvature without breaking. The proposed glass for the robot design is fused silica. Its surface stress can significantly be reduced by using a protective polymer coating, which is common in optics fiber to increase its mechanical rigidity. In addition, its mechanical strength can be further improved by minimizing the flaws in glass and enabling a low surface area because a small size limits the risk of the presence of flaws [Tomozawa 96, Wondraczek 22, Bellouard 11]. All these factors guarantee the ability of capillary glass to withstand high bending stress (see Figure 5). It also allows the capillary glass to have flexibility similar to the spring steel. Fused

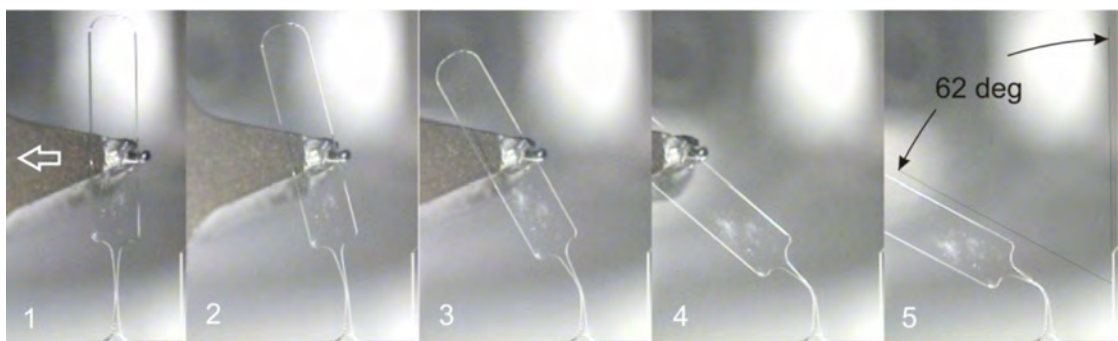


**Figure 5:** Illustration of glass beam bending experiments undergoing several stress deformation for loading and unloading without breaking ([see video](#)). The beam is characterized by a  $40\mu\text{m}$  thick flexure in its thinnest part, Image © 2011 Optical Society of America [Bellouard 11].

silica has a non-linear elastic property and the applied strain determines the elastic modulus [Scott 17, Matthewson 93], with the maximum bend radius of curvature, deduced by considering tensile strength in Equation 1.

$$\sigma = E_o \frac{r_c}{r} \left[ 1 + \alpha \frac{r_c}{r} + \beta \left( \frac{r_c}{r} \right)^2 \right] \quad (1)$$

$\sigma$  is the surface stress,  $E_o$  is Young's modulus at zero strain (70GPa),  $r_c$  is the capillary radius, and  $r$  is the bending radius of curvature.  $\alpha = 2.30$  and  $\beta = 8.48$  are the second-order and third-order nonlinear material coefficients, respectively.

For the proposed miniaturized CTR, when considering the glass tube diameters used, the relationship between their bending stress and the obtainable radius of curvature, as derived using Equation 1 is presented in Figure 6. The figure explains why it was possible to obtain a small bend radius of curvature in glass down to 5 mm with tube diameter below 440 $\mu\text{m}$  (full detail in Chapter 1), which is very flexible to sustain bending stress below nominal value without fracture. This is highlighted and considered as our target area in Figure 6. Considering its ultimate tensile strength, the figure indicates that it can withstand more stress in cases of path contact during deployment and manipulation. Figure 6 also demonstrated that it is theoretically possible for a 1 mm glass tube to sustain bending stress over a 10 mm radius of curvature like that of Nitinol, which has a minimum radius of curvature of 15 mm in literature [Sears 06]. The various approach explored to obtain a pre-curved tube using thin glass for the proposed miniaturized concentric tube robot (CTR) in Chapter 3 is discussed in detail in Chapter 2. Whereas for

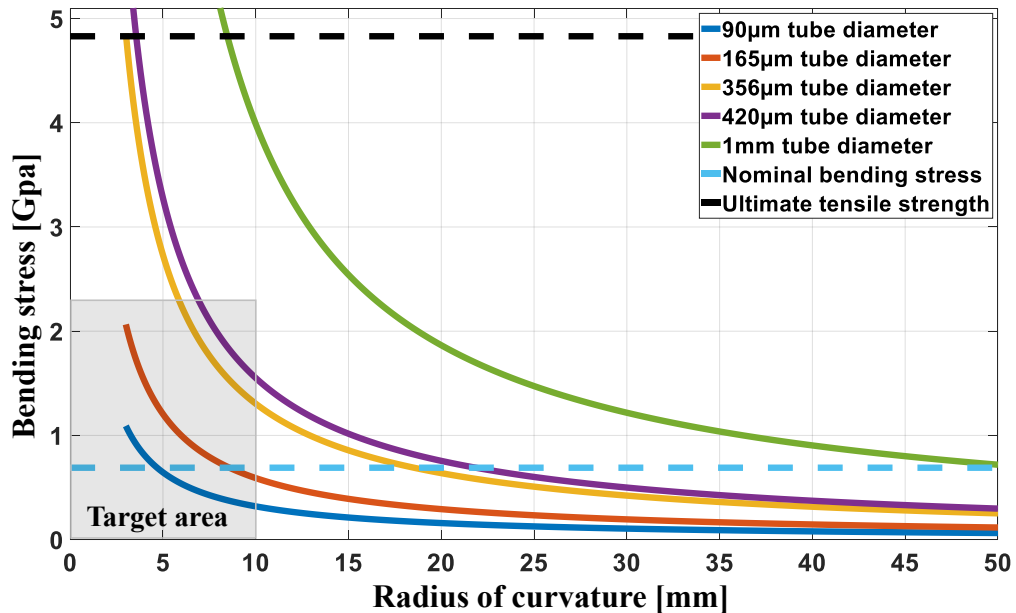


**Figure 6:** The relationship between the glass capillary bending stress and the obtainable bend radius of curvature for the glass diameters.

the parallel continuum robot (PCR), a standard optical fiber was used directly for the robot modeling, design, and experimental prototype, which is detailed in Chapter 4. Overall, we demonstrated the possibility to actualize the first of its type, a miniaturized continuum robot using glass material. This landmark achievement and scientific breakthrough has huge prospects in the robotics and material domain as regards microsurgery or micromanipulations.

## DISSERTATION CONTRIBUTIONS

The key focus of this research is on two different continuum robot kinematics of interest. These are concentric tube robots (CTR) and parallel continuum robots (PCR), which are analogous to the conventional serial and parallel robots respectively. Generally, the idea of the proposed robots involves, taking advantage of glass flexibility at the microscale to actualize a novel and the smallest continuum robot of each kind, when compared to those in the literature. The outcome of the research is targeted for possible endoscopic biomedical applications and other micromanipulations. The individual key contributions are detailed as follows:

### For concentric tube robot (CTR)

1. An IEEE Transactions on Robotics (T-RO) journal paper [Nwafor 23b], titled “Design and Fabrication of Concentric Tube Robots: A Survey”, the different contributions include:
  - (a) The paper fills the gap in the literature by providing a thorough review of the large variety of designs and fabrication methods for all aspects of a physical prototype, including tubes, actuation units, and end effectors.
  - (b) We proposed to the community, a set of specification details for future CTR prototype assessment and evaluation as regards paper publication and its new contribution.
  - (c) Next, we proposed and presented to the community a more general and unifying way of classifying CTRs, which is based on the kinematics of the actuation unit after studying the different concepts and approaches that have been developed and proposed by research groups.
  - (d) Finally, the creation of an online public resource for the research community which provides details on the existing and new CTR tube designs and actuation units reported in the literature ([online resource directory](#)). This is geared to help find an avenue for creating a more mature robotic platform, as the ultimate goal is for the researchers to channel major efforts towards other vital research challenges for rapid improvements without requiring the development of new prototypes each time.

2. Next is a research article on Advance Intelligent Systems (AIS) journal paper [Nwafor 22], titled “The Caturo: A Submillimeter Diameter Glass Concentric Tube Robot with High Curvature”. Its contributions include:
  - (a) An introduction of a new generation of CTRs called Caturo, which stands for capillary tube robot with all glass tubes  $< 500\mu\text{m}$  in diameter.
  - (b) Design and fabrication of smallest CTR, which possesses the tiniest external tube diameter ( $90\mu\text{m}$ ) and an unprecedented radius of curvature ( $5\text{mm}$ ) compared to those in the literature.
  - (c) Present a novel approach of fabricating pre-curved CTR tubes with glass capillaries and even standard optic fibers, by heat treatment using a thin heat-shrink polymer and a 3D printed mold. The fabrication process and results were characterized and moreover, the procedure is quick, versatile, and relatively low-cost when compared to conventional Nitinol. It can also permit patient-specific customization which is beneficial for MIS applications.
  - (d) Actualization of the first ever CTR prototype that is composed of glass tube material and used for different CTR demonstrations such as 3D helical pre-curved tube deployment, conical-spiral deployment, constrained 3D deployment through a  $<1\text{mm}$  orifice of three positioned needles, pre-curved optic fiber deployment with laser emission capability, fluid sample suction, and delivery operation, and finally, vitreoretinal deployment using fish eye under optical coherence tomography (OCT) visualization.
  - (e) Lastly, the proposed miniature CTR prototype was used for different applications after model validation (FKM and IKM) and stability analysis in order to highlight the robot’s capabilities and it has the benefit/possibility of end-effector functionalization by using fluid or light-driven actuators/sensors for distal tip micromanipulation.

## For parallel continuum robot (PCR)

The research article is currently published in IEEE/ASME Transactions on Mechatronics (TMECH) journal publication [Nwafor 23a], titled “Miniature Parallel Continuum Robot Made of Glass: Analysis, Design, and Proof-of-Concept”. Its contribution includes:

1. Here, we present the smallest PCR in terms of footprint (actuation unit and all links), capable of generating large rotations of the end effector from  $-80^\circ$  to  $+90^\circ$  in a tiny volume. This provides the solution to tackle the limitation and challenge of large workspace/rotation associated with miniaturized parallel manipulators in the literature.

2. We investigated in detail the effect of the variation of geometrical parameters of the robot in terms of the arc length or input actuation and the end effector dimension to the achievable stiffness, manipulability, and obtainable tip orientation within the entire robot workspace.
3. Numerical simulation using the Cosserat rod modeling approach was adopted for the FKM and IKM, which was used to demonstrate different path shape tracing such as vertical plane circumradius path following, the horizontal plane circular and square shape path tracing, and finally, to assess through experimental validation the robot boundary workspace.

## ORGANIZATION OF THE MANUSCRIPT

The organization of this dissertation is as follows:

- Chapter-1 deals with the state-of-the-art of continuum robot, particularly on the two different kinematics of interest (CTR and PCR). Starting with the CTR by presenting an in-depth review of the design and fabrication of all the CTRs in the literature, which covers generally the CTR tube design and fabrication, its different actuation units, end-effectors, and finally their applications. Next is PCR with a major focus on its design and fabrication, modeling, and its classifications.
- Chapter-2 focuses particularly on the different approaches to the fabrication of pre-curved glass tubes at a small scale. This start with the problem statement and then, the discussion on the different fabrication approaches exploited which include 1) subtractive manufacturing using the FEMTO-print machine, 2) heat treatment and annealing of a glass tube to the desired shape, and finally 3) curving of glass tubes using an ultra-thin polymer with heat shrink property.
- Chapter-3 presents the smallest CTR in the literature that is made of glass. It starts with a description of the sub-millimeter glass CTR, followed by the model validation; forward kinematics model (FKM), inverse kinematics model (IKM), and stability analysis. Next are the various demonstrations of the sub-millimeter glass CTR deployment and their proposed applications, which are 3D conical-spiral free space deployment, helical pre-curved glass tube deployment, constrained deployment through the orifice of three positioned needles, deployment of pre-curved optical fiber with laser transmission, fluid suction, and delivery demonstration and lastly, vitreoretinal deployment under the optical coherence tomography (OCT). The various limitation, challenges, and possibilities of end-effector functionalization were also discussed here.

- Chapter-4 is concerned with the miniature parallel continuum robot made of glass: analysis, design, and proof-of-concept. First is the presentation and discussion of the robot's novel prototype design and then the in-depth analysis and characterization of the robot based on its achievable workspace, stiffness, manipulability to variation of its geometrical parameters e.g. actuation length, and end-effector size. The last aspect involves various experimental demonstrations for different desired path shape movements (square and circle) and model validation.
- Finally, the last part is the conclusions and perspectives that summarize and covers proposed areas of further research and advancement. These are categorized as short-term (master thesis) and long-term (possible Ph.D. project/dissertation or commercialization).



---

# Chapter 1

## State-of-the-art: CTR and PCR

---

<b>1.1</b>	<b>Objective</b> .....	18
1.1.1	Glass material/properties .....	18
1.1.2	Continuum robots .....	20
<b>1.2</b>	<b>Concentric tube robots (CTR)s</b> .....	22
1.2.1	Tube design .....	24
1.2.2	Tube fabrication.....	26
1.2.3	Applications .....	32
<b>1.3</b>	<b>Parallel Continuum Robots (PCRs)</b> .....	34
1.3.1	Concept.....	34
1.3.2	Classifications.....	38
<b>1.4</b>	<b>Continuum robot modeling</b> .....	41
1.4.1	Kinematic frameworks.....	43
1.4.2	Mechanics formulation .....	47
1.4.3	Numerical resolution solvers.....	49
1.4.4	Proxy models .....	52
<b>1.5</b>	<b>Conclusion</b> .....	53
1.5.1	For CTR.....	53
1.5.2	For PCR .....	54
1.5.3	For modeling .....	54

## 1.1 OBJECTIVE

### 1.1.1 Glass material/properties

Glass, a versatile material, has been a part of human history for thousands of years. From ancient stained glass windows to modern high-tech applications, glass continues to evolve. The state of the art in glass properties reflects a dynamic field of research and innovation. Here, we explore the current understanding of glass properties.

1. Transparency and Clarity: The transparency property of glass refers to its ability to transmit light without significant distortion, allowing objects to be seen clearly through it [Liu 21]. Transparent glass allows light to pass through it with minimal scattering or absorption, resulting in a clear view of objects on the other side. When light encounters a material, it can interact with it in several different ways. These interactions depend on the wavelength of the light and the nature of the material. Photons interact with an object by some combination of reflection, absorption, and transmission. Glass remains unmatched in its transparency [KotzHelmer 17, Scholze 91]. Recent advancements have led to ultra-clear glasses used in displays, optical lenses, and architectural facades. It's important to note that some types of glass may have specific properties that alter their transparency. For example, tinted glass or glass with a low-emissivity (Low-E) coating may have reduced light transmission or a slight alteration in color [Jelle 15, Khaled 21, Mohelnikova 09]. However, they can still be considered transparent if they meet the criteria of allowing clear visibility through the material.
2. Strength and Durability: Several types of glass, depending on their specific composition, are known for having a high theoretical structural strength and being very durable [Jones 18, Minko 13]. However, certain practical factors can significantly diminish their actual strength. For example, various elements can result in less-than-ideal strength for a given glass type [PHILLIPS 65, Haldimann 06]. These include 1) Imperfections or blemishes on the glass surface, 2) Thermal stresses induced during rapid cooling processes, and 3) The introduction of tiny crystals into the surface through the annealing process. Imperfections on the surface of glass can serve as focal points for stress. When a load exerts pressure exceeding the glass's theoretical strength, concentrated stress can often lead to fractures or breakage. Therefore, surface flaws and imperfections play a significant role in reducing a product's fracture strength. Nonetheless, manufacturers can mitigate or prevent the occurrence of these surface flaws and cracks by employing precision and careful procedures during the manufacturing process. The strength of glasses can differ significantly based on their composition and purpose [swiferglass 23]. For instance, "Tempered soda-lime" glass, often referred to as Type-III glass, is notable for its robust mechanical strength. On the other hand, "Aluminosilicate

"glass" excels in terms of compressive strength, making it a preferred choice for applications like solar cells, cover glass, and touch displays. Lastly, "Borosilicate glass" stands out for its exceptional structural strength and is commonly utilized in applications such as glass tubing, medical devices, and equipment designed for space exploration. Innovations in glass tempering and laminating techniques have produced incredibly strong and shatter-resistant glass. This is crucial in construction, automotive, and consumer electronics.

3. Thermal Properties: Rapid and significant temperature changes can lead to the fragility and breakage of glass. Temperature plays a vital role in the glass manufacturing process, where thermal properties are harnessed to enhance its strength. One method to fortify glass is through heat tempering. Uneven temperature distribution within the glass can generate varying internal pressures, rendering it susceptible to fractures and breakages [Mirrors 21]. This phenomenon is referred to as thermal shock resistance and serves as an indicator of how prone the glass is to breaking in response to temperature fluctuations. Today, smart glass with controllable transparency and self-healing glass, which can repair minor cracks are becoming prominent.
4. Electrical property: Electrical characteristics of glass are frequently explored in the context of applications such as lasers, solar energy conversion, semiconductors, and electronic devices [Mirrors 21]. Several factors must be considered when examining the electrical properties of glass. Glass types exhibit varying resistivity, influenced by factors like changes in composition. The electrical properties encompass aspects like AC and DC conductivity, dielectric constant, electrical modulus, and dielectric loss. Temperature plays a crucial role in conductivity, affecting activation energy in relation to glass composition [Shirai 21, Hrma 12]. It's worth noting that temperature is positively correlated with the resistivity of metals and inversely correlated with the resistivity of semiconductors. Given the diverse conductive behaviors in different materials, various glass variants are engineered. To determine the electrical energy storage capacity of glass, assessing the dielectric constant of the glass is essential.
5. Chemical Resistance: Glass exhibits varying degrees of chemical resistance depending on its composition and type [Company 23]. Glass is chemically inert and corrosion resistant due to its unique composition. Some specific types of glass, such as borosilicate glass, are known for their exceptional resistance to chemical corrosion [Yazawa 93] and are often used in laboratory glassware and industrial applications where contact with aggressive chemicals is expected. The speed at which chemical reactions lead to the corrosion of glass, including ion exchange, hydration, and dissolution, is influenced by variables like the type of glass, temperature, and the level of acidity or alkalinity (pH) [Zanini 23]. These reactions can take place concurrently when glass is exposed to liquid water and can act as limiting factors in relation to the specific conditions of an experiment. It's important to note that

while glass is generally resistant to many chemicals, it may not withstand prolonged exposure to strong acids or alkalis, which can lead to surface etching or weakening.

6. Bioactive Glass Property as Emerging Field: Bioactive glasses react chemically with the body fluids and the reaction product is an apatite, which, with the intervention of biological drivers, assists the generation of bone matrix and bone growth [ValletRegí 03]. Numerous variations of bioactive silicate glass, each with diverse compositions that include specific metallic ions known to affect cells, have undergone extensive examination for their potential application in the field of bone tissue regeneration [Hoppe 11]. The initial bioactive glass (BG), specifically identified as 45S5 Bioglass (comprising 45% SiO<sub>2</sub>, 24.5% Na<sub>2</sub>O, 24.5% CaO, and 6% P<sub>2</sub>O<sub>5</sub> by weight), was pioneered by Hench and colleagues. This particular formulation has garnered extensive attention in the realm of biomedical research, being extensively studied for its potential applications in various medical contexts [Hench 91]. The typical feature of BGs is their high surface reactivity (or bioactivity [Hoppe 11]), which enables the effective interaction of the material with host tissue, leading to strong bone (and in some cases soft) tissue attachment. The bonding to bone has been traditionally explained by considering the formation of a carbonated hydroxyapatite surface layer on BGs when they are in a biological environment [Erol-Taygun 13].

The state of the art in glass properties showcases an ever-evolving field where scientists and engineers are pushing the boundaries of what glass can achieve while opening up new possibilities in research, such as robotic design and fabrication which is the main focus of this manuscript.

### 1.1.2 Continuum robots

Continuum robots are designed to have a continuously curving backbone, which can be actuated to produce elastic deformation and achieve complex movements and tasks. The family of continuum robots is quite vast with different architectural designs, material components, and kinematics (see Figure 1.1). The ones of Figure 1.1A, B, and C, which are typically single backbones have great potential in biomedical applications, particularly relating to MIS and NOTES (Natural orifice transluminal endoscopic surgery). Generally, there are an increasing number of research groups emanating each year around the globe. In fact, hardly will one see medical seminars, conferences, or journals without finding a continuum robot. This research domain has seen rapid research outcomes and developments in design, modeling, control, and fabrication. The drive for continuum robots is to overcome the limitations of traditional rigid-link robots and provide enhanced flexibility, maneuverability, and adaptability in various environments. The unique structure of continuum robots enables them to navigate through tortuous paths to



**Figure 1.1:** Examples of different types of continuum robots in the literature **A)** Concentric tube robot (CTR) actuated by axial rotation and translation of pre-curved tubes (image from [Chikhaoui 18a], (online)), **B)** Hybrid continuum robot with a combination of tendon-driven segments in a concentric assembly manner [Chikhaoui 18a], **C)** Tendon-driven continuum robot with extensible segments, using self-repelling magnetic spacer disks, (image from [Chikhaoui 18a]), **D)** Planar tendon actuated parallel continuum robot [Sven 21], **E)** Stewart type compliant legs parallel continuum robots [Bryson 14]

reach confined spaces and interact with delicate or complex objects with precision and dexterity. They tend to mimic the natural movements of biological organisms, such as the motion of an elephant trunk, octopus, or snake. With their ability to navigate through narrow and tortuous environments, they are characterized by reduced patient trauma and fast healing/recovery time. For industrial applications, their flexibility, and adaptability make them suitable for tasks such as inspection, maintenance, and repair in confined space. They are particularly advantageous in sectors such as aerospace, where they can navigate within aircraft fuel tanks or inspect aero engines. Their ability to navigate through cluttered and unpredictable environments makes them suitable for scenarios where human-like dexterity and adaptability are required.

The design and development of continuum robots are driven by several key objectives. Firstly, researchers aim to improve the robots' mechanical design to enhance their range of motion, payload capacity, and manipulation capabilities. Various design approaches which include the use of tubes, rods, tendon/wire, and disks are all explored to achieve different desired characteristics and goals. Secondly, modeling techniques, such as the link kinematic representation, mechanical model framework, and/or data-driven model approach. These are employed to accurately represent the deformations and behavior of continuum robots. Lastly, control algorithms and actuation methods are developed to enable precise and coordinated movements of the robot's segments, allowing for efficient navigation and

manipulation in complex environments. Herein, this manuscript focuses mainly on two types of continuum robots of interest with different kinematics: the concentric tube robot (CTR) and the parallel continuum robot (PCR). The focus on CTR kinematics is because it better suits most MIS applications and due to its design benefits when compared to other continuum robots e.g. simple structure and highly scalable as they are made of merely elastic tubes. Also, we extended the research to PCR, so as to investigate and benefit from both the advantages of conventional parallel robots and continuum robots for micromanipulation. Therefore, this chapter presents a general literature review of the existing works regarding the two continuum robots of interest. The first section is focused on the state-of-the-art of CTRs, which we published in IEEE Transactions on Robotics [Nwafor 23b], but due to brevity, we only included selected areas that are majorly within the scope of our research context and the rest at the Appendix Section. Whereas the second section is focused on PCRs and to the best of our knowledge, there is no literature review or survey on it. So its state-of-the-art is detailed and arranged to incorporate the concepts, classifications, and modeling.

## 1.2 CONCENTRIC TUBE ROBOTS (CTRs)

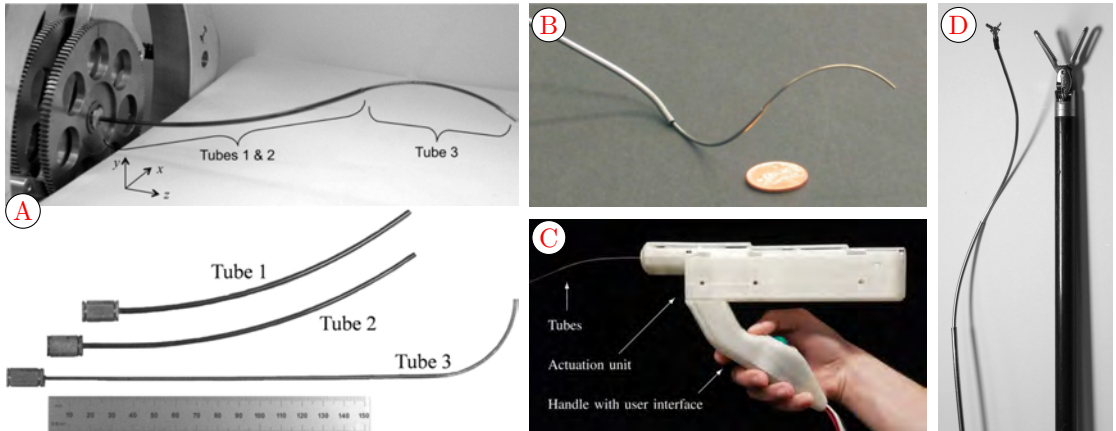


**Figure 1.2:** Examples of CTR prototypes in the literature **A)** Three-tube CTR as Tubes 1 and 2 forms a variable curvature balanced pair that dominate tube 3 [Dupont 10a], **B)** Active cannula prototype made of pre-curved superelastic nitinol tubes [Webster 06a], **C)** A hand-held CTR prototype with deployed tubes and actuation unit [Girerd 20d], **D)** A CTR next to a standard da Vinci laparoscopic tool [Gilbert 16b].

CTRs are composed of a set of pre-curved, thin, telescoping tubes/rods, nested concentrically [Webster 06b, Sears 06]. Translation and rotation at the proximal end, causes the tubes to interact elastically with each other, leading to changes in the backbone configuration and distal tip pose. Due to the simplicity of their structure and their extrinsic actuation, they can be easily miniaturized [Burgner 15b] and are among the smallest type of continuum robots. In

addition, their shape during deployment can be controlled along 3-D curves, without relying on or causing damage to body tissue [Dupont 10c]. They can also be easily deployed through fluid-filled channels or open cavities (e.g. blood vessels, air tracts, etc) [Alfalahi 20, Dupont 10c]. Figure 1.2 presents a few selected examples of CTR prototypes in the literature.

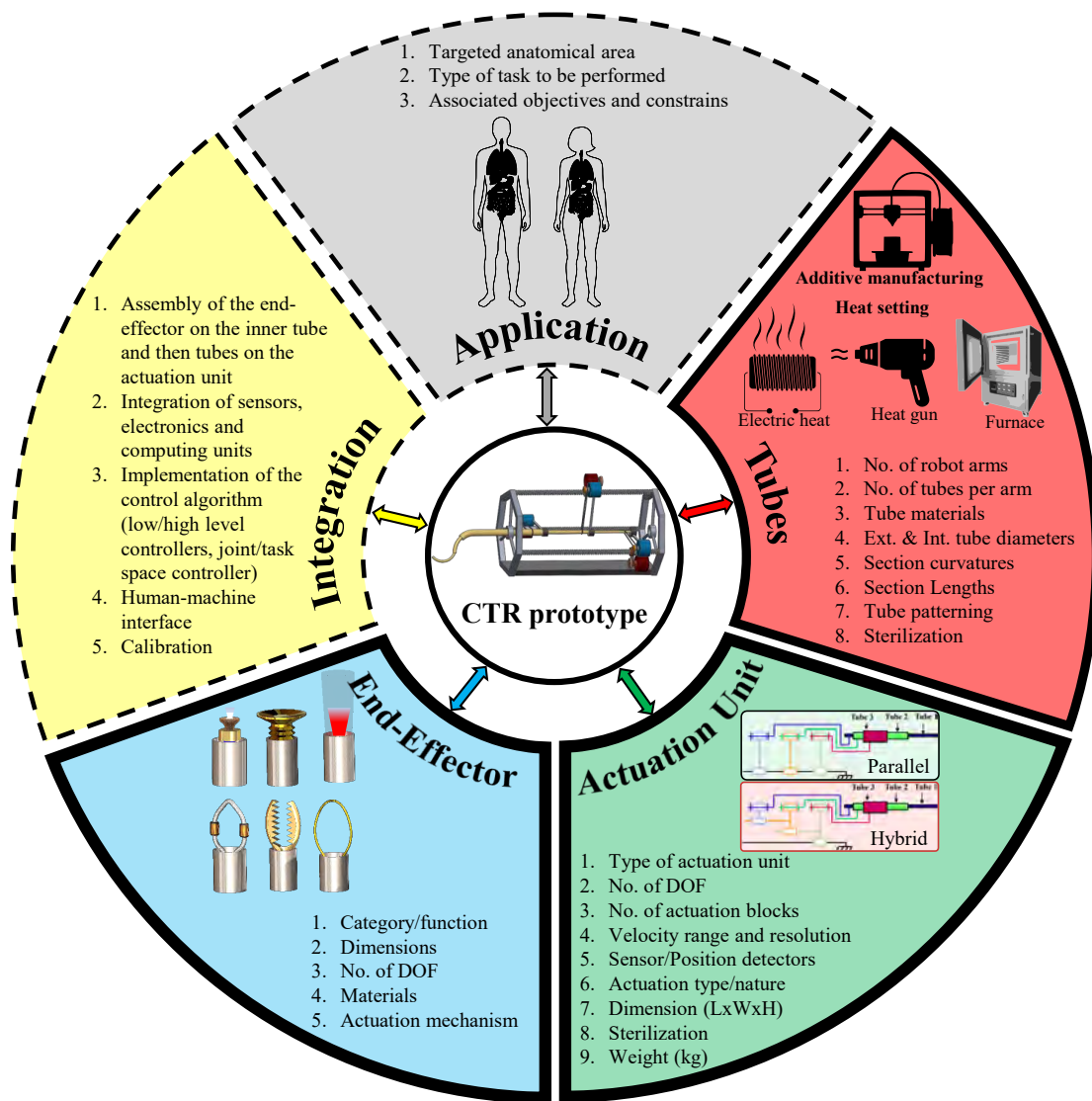


**Figure 1.3:** The various components of a CTR prototyping, along with their respective specifications. The targeted application influences and determines the CTR design and its validation criteria. The CTR tubes are designed based on the geometry of the anatomical area and fabricated with processes that depend on the material selected. The actuation unit is also designed and fabricated using application and tube requirements. End effectors are selected and integrated into the innermost tube. An integration step consists in assembling all of these elements together, along with the implementation of a control system and validation of the CTR performance.

Over the years, CTRs have attracted a lot of scientific interest, notably because of their use in minimally invasive surgery (MIS). They do really provide various potential advantages for MIS due to their tiny size, flexibility, and great dexterity. In the fields of CTR design, fabrication, control, and applications, research has led to a rising number of discoveries and scientific achievements. From several research groups around the globe, an extensive number of prototypes with various designs and specifications have been created. The methods for designing and fabricating the tubes, actuation unit, and end effector are all covered in this Section, along with the state-of-the-art in mechatronics for CTRs. In addition to the different hardware and related manufacturing techniques, a unified scheme for CTRs classification is proposed to the research community, which is based on their actuation unit architecture. Last but not least, a set of specification information for assessing upcoming CTR prototypes is presented. Since CTR structural design is divided into three main parts: the tubes, the actuation unit, and the end effector, as shown in Figure 1.3, this is the basis for Section organization and discussion. Although the part of actuation unit and end effector are shifted to Appendix-B and Appendix-C respectively since they are not the main focus of this Ph.D. dissertation.

### 1.2.1 Tube design

In general, the CTR tube section is the most discussed in the literature. Figure 1.4 illustrates the overall shape of each developed CTR prototype that has been described with sufficient detail in the literature (refer to our online [CTR Prototyping Resources](#) for full details). The shape was obtained considering a torsionally rigid, constant curvature model with the tube curvatures aligned in a plane. The tube design process involves finding the desired/optimal tube properties/specifications for the given application, which may involve the use of pre-operative medical images. These tube specifications are presented in the red section in Figure 1.3.

While the individual segments of a CTR cannot be independently controlled, that of serial or hyper-redundant robots may because of the actuated joints that are put between them. Indeed, translating or rotating a distal segment of a CTR requires the innermost, longest tubes to be actuated. This changes the bending and torsional equilibrium of the preceding robot segments, leading to a change in the entire robot's shape. Therefore, designing a tube set to perform a given task in a constrained environment is not intuitive to designers, and necessitates the use of simulations that rely on the kinematic models of these robots. The synthesis of CTR tubes has mostly been aided by three kinematic models from the literature. These models are the constant curvature model [Webster 10], a torsionally-rigid model, and a torsionally-compliant model [Dupont 10b], which are arranged according to their computational time and complexity.

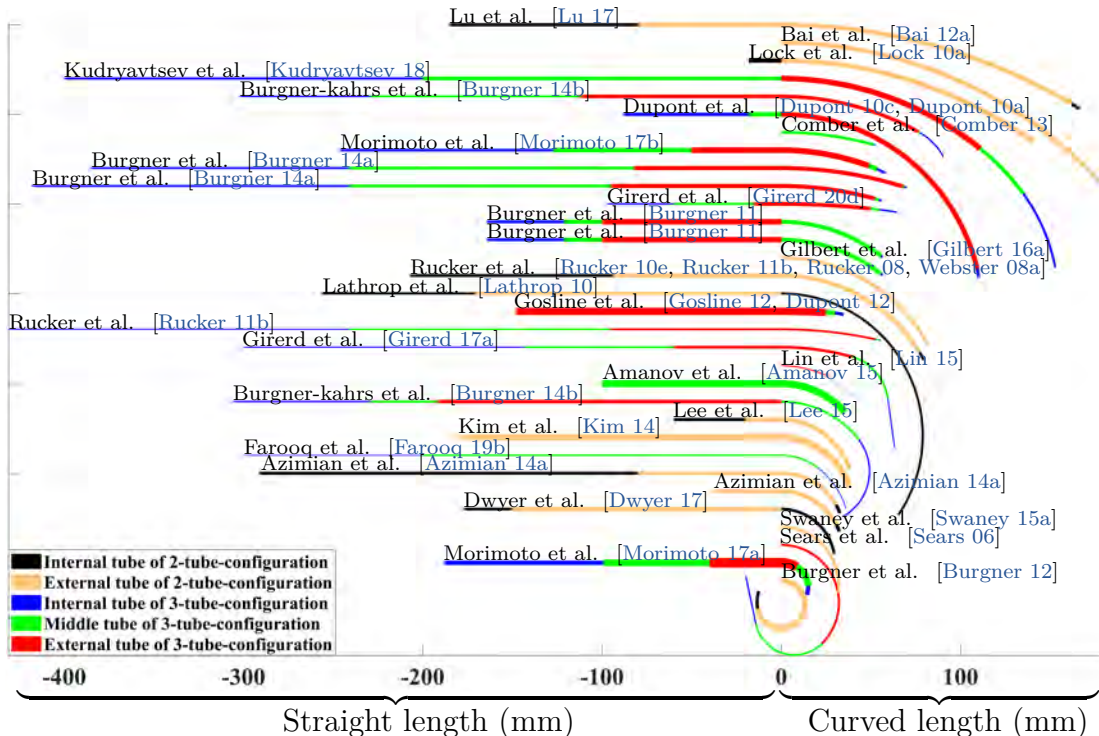


**Figure 1.4:** Representation of the CTR prototypes in the literature (extracted from our online [CTR Prototyping Resources](#) with the necessary parameters) aligned in a single curvature plane for clear presentation. One can observe the number of tubes for each prototype and the considered curvatures.

The simplest CTR model created to date is the constant curvature or dominant stiffness model [Furusho 05]. The robot's shape is determined by the shape of the stiffest tube in each connection, according to the assumption that each tube is infinitely stiff relative to the tubes inside it. This model was used in some early work for the robot model synthesis, as well as special situations like the piece-wise constant assumption [Webster 10]. As the ratio of relative bending stiffness between the tubes approaches one, the assumptions, however, often do not hold, prompting the creation of a second model that takes into account the bending interactions between the tubes [Dupont 10b]. Since it is more accurate, this model has often been utilized often for the robot model synthesis (see Table A.1 in Appendix-A). The torsionally rigid model, although adding some complexity over the prevailing dominant stiffness model, is still an algebraic closed-form model. Due to its computational tractability, it has continued to be utilized in recent years as a preliminary step in the synthesis before being further improved using a torsionally-compliant model [Dupont 10b, Bergeles 15]. It is still useful today for the synthesis of CTRs in which tubes are not subject to torsional interactions and for which the torsionally-rigid and compliant models give identical results for stable robots, which is the case for CTRs that deploy in a follow-the-leader (FTL) manner [Gilbert 13, Gilbert 15b, Garriga 18, Girerd 20a].

The limitations of this model for tubes that interact torsionally were demonstrated, and this sparked the creation of torsionally-compliant models [Dupont 09a], which take into consideration both the bending and torsional equilibriums between the tubes. Torsion was first exclusively modeled in the straight tubes portions [Webster 08a, Webster 09a], but it was later generalized to include both the straight and curved sections [Dupont 09a, Dupont 10c, Webster 10, Rucker 09, Rucker 10e]. These models are considered in the literature as the sweet spot in terms of modeling complexity and accuracy [Gilbert 16b], compared to the simpler dominant-stiffness [Furusho 05] or torsionally-rigid models discussed [Dupont 10c, Webster 10], and more complex models recently developed, that take tube clearance and friction into account [Lock 11a, Ha 19]. It is important to note that CTR design optimization has not yet utilized these more complex kinematic models that take into account friction and tube clearance effects. In addition to the three main models presented, a torsionally-compliant kinematic model that takes external loads into account [Rucker 10a] has been used in one tube design approach [Granna 19].

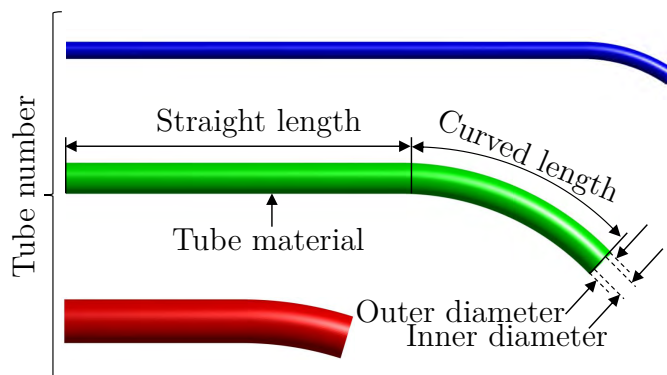


**Figure 1.5:** Illustration of a set of CTR tubes, with their design variables represented.

The variables that can be considered for the synthesis of CTRs are the ones that appear in the kinematic models used and are reported in Figure 1.5. The parameters for the dominant stiffness model are the number, lengths, and curvatures of the tubes. The torsionally-rigid model adds the bending stiffnesses of the tubes, which depends on their inner and outer diameters, and on Young's modulus of the material used. Finally, the torsionally-compliant model adds the torsional stiffness, which depends on the inner and outer diameters of the tubes, as well as on the shear modulus of the material used. See Appendix-A for further detail concerning CTR tube design, model, and its perspectives.

### 1.2.2 Tube fabrication

One critical aspect of CTR prototyping is tube fabrication, which often depends on the material to be used. CTR tubes are primarily made using Nitinol, which is a superelastic alloy of nickel and titanium, and more recently, polymer

materials have also been used [Morimoto 16b, Amanov 15, Picho 22]. A comparison of the mechanical properties of materials used to date is given in Table 1.1, which can serve as a reference for choosing a tube material. This section presents the main CTR tube fabrication methods to date: heat-setting of Nitinol and heat-shrink plastic tubes, additive manufacturing for plastic tubes, and the fabrication of patterned tubes. Collections of the various tube prototypes in the literature are provided in our CTR Prototyping Resources ([CTR Tube Repository](#)) for both single and multi-arm robots.

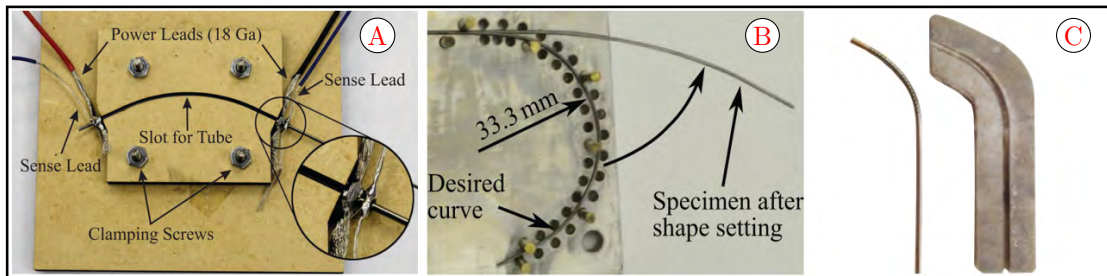


**Figure 1.6:** A) Joule heating effect by high current flow through the tube [Gilbert 16c], B) Air furnace heat treatment using a metal fixture with brass pins [Gilbert 16c], C) Air furnace annealing process using engraved aluminum mold [Kim 14].

### 1.2.2.a Heat setting

**Heat setting of Nitinol tubes:** Nitinol tubes are typically sold as straight tubes by manufacturers (see [Thomasnet 21, SMST 21, in China 22] for lists of various manufacturers/suppliers). It is the predominantly used material for CTR tubes thanks to its large superelastic range, which enables large workspaces compared to CTRs made of other materials [Gilbert 16c, Amanov 15]. There are several patents related to the shape setting of Nitinol, including patents for shape alloy treatment [Pelton 99], drawing heated Nitinol followed by forming and rapid quenching [Johnson 11], and treatment for cold worked Nitinol under non-stress induced shape setting [Boylan 11]. Although some companies (e.g. Minitubes [[Minitube 22](#)], Memry [[corporation 22a](#)], Nimesis [[Nimesis 21](#)]) have mastered the shape setting of Nitinol using proprietary processes, obtaining these pre-curved tubes is typically expensive. The research community has therefore developed processes for bending commercially available straight tubes, typically using heat treatment approaches.

Heat treating depends on the state of the Nitinol acquired from the provider and requires considerable technical knowledge and specialized equipment in order to obtain an optimized, consistent, and accurate result without any unwanted spring-back or material aging [Gilbert 16c]. There are two main heat treatment methods for shape-setting Nitinol tubes: (1) heat diffusion using a furnace and (2) joule heating by passing current through the tubes. For both methods, a patterned fixture or mold with the desired shape engraved, is used to fix the shape of the initially straight tubes, as shown in Figure 1.6. These processes require accurate

**Table 1.1:** Mechanical comparison of the different tube materials.

Property	Material	Rating	Remarks
Elasticity and recoverable strain	Nitinol	*****	Yield strength: 195 - 690 MPa and Young modulus: ~83 GPa [Matthey 0], recoverable strain up to 11% [Duerig 99]
	PLA	***	Yield strength: 60 - 70 MPa and Young modulus: 2.5 - 7.8 GPa [Amanov 15]
	PCL	**	Yield strength: 16.1 MPa and Young modulus: 0.34 - 0.36 GPa [Amanov 15]
	NYL	***	Yield strength: 60 - 70 MPa and Young modulus: 1.5 - 4 GPa [Picho 22, Amanov 15]
	Heat-shrink tube	**	Tensile strength: 23 - 39.6 MPa and Young modulus: 0.44 - 0.64 GPa [Noh 16, Corporation 22b]
Tip repeatability error and Fatigue resistance	Nitinol	*****	1.49 mm [Amanov 15]
	PLA	***	0.3 - 3.1 mm (the mean error = 1.7 mm) [Amanov 15]
	PCL	**	0.2 - 9.8 mm (the mean error = 5 mm) [Amanov 15]
	NYL	***	0.4 - 7.6 mm (the mean error = 4 mm) [Amanov 15]
	Heat-shrink tube	**	1.0 - 2.1 mm (the mean error = 1.55 mm) [Makarets 14]
Miniaturization and minimum resolution	Nitinol	*****	Min. internal/external diameter: 0.258/0.33 mm; min wall thickness 0.036mm [GoodFellow 21]
	PLA	***	Min. int./ext. diam: 0/1.2 mm, 0.6 wall thickness and resolution 100 microns [Amanov 15]
	PCL	***	Min. int./ext. diam: 0/1.2 mm, 0.6 wall thickness and resolution 100 microns [Amanov 15]
	NYL	***	Min. int./ext. diam: 0/1.2 mm, 0.6 wall thickness and resolution 100 microns [Amanov 15]
	Heat-shrink tube	****	Min. int./ext. diam: 1.17/1.67 mm, 0.5mm wall thickness [Noh 16]
Thermal effect/shock (Expan. coeff.)	Nitinol	*****	11e-6/°C [Matthey 0]
	PLA	****	8.5e-5/°C [Omnexus 21]
	PCL	***	16e-5/°C [Omnexus 21] this can even reshape by heating in hot water [Amanov 15]
	NYL	****	5e-5/°C [Omnexus 21]
	Heat-shrink tube	**	(8.3-10.5)e-5/°C [Corporation 22b]
Surface friction/ smoothness	Nitinol	*****	High surface smoothness (best)
	PLA	**	Low surface smoothness (worst) [Amanov 15]
	PCL	***	Medium surface smoothness (good) [Amanov 15]
	NYL	****	Medium surface smoothness (best among 3-D printed polymers) [Amanov 15]
	Heat-shrink tube	***	Medium surface smoothness [Noh 16]
Fabrication complexity/ customization	Nitinol	***	More complex and challenging fabrication process [Morimoto 16b, Amanov 15]
	PLA	****	Not rigorous and direct process [Morimoto 16b, Amanov 15]
	PCL	****	Not rigorous and direct process [Morimoto 16b, Amanov 15]
	NYL	****	Not rigorous and direct process [Morimoto 16b, Amanov 15]
	Heat-shrink tube	*****	Simple and direct process [Noh 16, Makarets 14]

\*: Symbol used for the ranking/grading, PLA: Polylactic, PCL: Polycaprolactone, NYL: Polyamide/Nylon

timing and temperature in order to achieve the desired goal, and deviations can lead to the relaxation of the tubes from the desired shape (although not quantified in the literature) or a loss of their superelastic properties [Burgner 13b].

For the furnace heat treatment approach, the use of a box/small furnace has been widely adopted due to cost, versatility, precise temperature profile, uniform heat distribution, and the ability to rapidly prototype without much risk [Shrivastava 04, Gilbert 16c, Wang 20b], since most are equipped with advanced features, such as temperature control. Using this approach, the bending process involves constraining the straight commercial Nitinol tubes in a variety of fixtures designed to have the desired pre-curved shape (see Figure 1.6b. and Figure 1.6c). Once constrained, the tubes will be heated in the furnace for 10 minutes

at 500°C [Shrivastava 04, Russell 01, Pelton 04, Kapoor 17] and finally quenched in water at room temperature to suppress the aging effect. The resulting tubes, however, were said to have a high spring-back which was not quantified and the quality of the results seemed difficult to predict. In addition, this process is said to be highly inefficient and requires several trials, significant time, energy, and material, especially the cost of mold machining and the use of thick steel to minimize buckling and thermal expansion bulge, which conversely absorb more heat than the tube itself. All these prompted the development of electric heat-setting techniques.

Electric heating on the other hand relies on joule heating, where electric current passing through the Nitinol tube (which acts as a resistance) generates the heat needed to shape the tube with the desired curvature [Shrivastava 04, Gilbert 16c, Sun 18]. The proposed setup includes temperature control and monitoring using real-time resistance measurements of the tube. This method was observed to have several advantages, including (i) the use of high current enables the shape setting temperature to be reached very quickly, and (ii) there is minimal equipment required to control the heating while supplying the required current. It should be noted that the fixture with an engraved pattern must be an electrical insulator with low thermal conductivity, which excludes the use of metals. A medium-density fiberboard, ceramic, or 3D printed mold has been used by researchers [Gilbert 16c, Wang 20b] (see Fig. 1.6a) for this purpose. The cooling was done through natural convection, and it was observed that the system operates correctly even when considering the non-uniformity of the heat sinking effect. Finally, a comparison between the two heat setting methods showed that the electric heating technique results are more energy efficient with less spring-back for the tubes compared to the furnace heating method, as well as faster shape-setting processes [Gilbert 16c, Wang 20b, Sabetian 19]. However, the drawbacks of electric heating are: (1) the requirement for a specific setup, which has some hardware limitations (2) tuning and calibrating the system to match the tube-specific transition temperature is challenging, and (3) the uneven thermal gradient/expansion along the tube can result in undesirable distorted shapes near the clamped ends [Wang 20b]. Despite the high cost and inefficiency, the most commonly used approach is still the furnace heating technique, as recorded in 24 papers [Kudryavtsev 18, Mitros 22, Kim 20c, Rox 20c, Xu 16a, Ayvali 12, Yan 22, Kim 20b, Nguyen 22, Baran 17a, Gao 16, Dwyer 20, Kim 14, Xin 18, Lee 15, Mitros 20, Qi 21, Luo 21, Comber 17, Farooq 19b, Farooq 18, Farooq 19a, Gilbert 15b, Ha 17], as compared to the electric heating with only 6 papers [Wang 20b, Morimoto 17b, Alfalahi 21, EHRAT 17, Pitt 16, Remirez 16], while both approaches are recorded in [Gilbert 16c, Gilbert 16e, Sabetian 19].

**Heat setting of plastic tubes** Although heat treatment has mostly been used for Nitinol tubes, recent work has investigated the use of heat-shrink tubes. This approach provides an alternative, rapid, and cost-effective fabrication method. Indeed, medical-grade heat-shrink tube HS-S14 (Insultab, Inc., Woburn, MA, USA) has been used in [Noh 16, Makarets 14] for the innermost tube of a three-tube

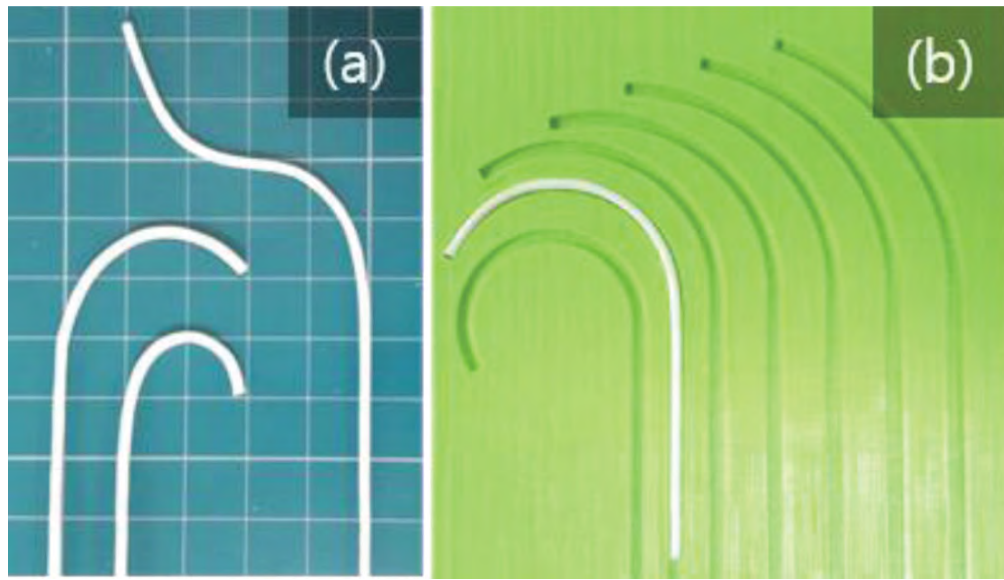


**Figure 1.7:** (a) Fabricated heat-shrink plastic tubes and (b) the jig for fabrication of tubes, extracted from [Noh 16].

CTR. The bending process consisted of placing the heat-shrink tube in a jig with a metallic guide wire inside its lumen to preserve its shape. The assembly was heated with a heat gun and quenched in water after shrinkage of the material with results as shown in Figure 1.7. The benefits of using heat-shrink tubes include the low cost and simple process that does not require any expensive and specialized equipment, such as a furnace or electrical heat setting setup. In addition, heat-shrink tubes can be bent in a timely manner, allowing for the fast fabrication of patient- and task-specific tube sets. Nevertheless, some limitations remain with this type of material. Indeed, the fabricated bent tubes had their radius of curvature permanently increased when translated inside a straight metal tube. More precisely, rapid changes in their radius of curvature occurred below a few dozen cycles, most likely due to fatigue [Noh 16, Makarets 14] and tended to stabilize afterward. Presently, this approach seems to be discontinued, as it is limited to the fabrication of only the innermost CTR tube. However, there are many potential benefits of the approach, which could be worthwhile to explore.

#### 1.2.2.b Additive manufacturing for plastic tubes

Additive manufacturing has made it possible to transform a digital model into a physical 3-D object and is now often used to create rapid prototypes in a number of industries. It has enabled personalized prototyping, where a given patient scan can be used to generate a personalized digital model, as can be seen, in [Amanov 15, Morimoto 17a]. Additive manufacturing is a layer-by-layer controlled process of creating physical objects using a digital model. There are many different technologies and materials available for additive manufacturing, and several were studied in the context of CTRs [Morimoto 16b], each with its pros and

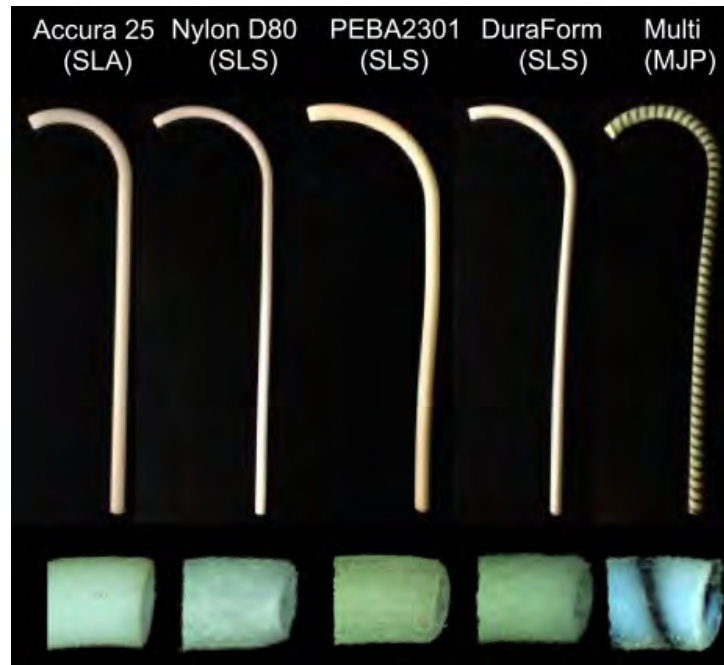


**Figure 1.8:** CTR tube prototypes fabricated with additive manufacturing using different materials and processes. The stereolithography-SLA (for Accura 25). The selective laser sintering-SLS (for Nylon D80, PEBA 2301, and DuraForm). multijet printing-MJP (with different material) by Morimoto et al. [Morimoto 17a].

cons. The first step for prototyping using additive manufacturing is to create a mesh file of the part to be printed. It was observed that the key to obtaining optimal results, depends heavily on the printer settings [Amanov 15]. Once the print is complete, there may be additional post-processing steps to clean unwanted material, depending on the additive manufacturing process used.

The different materials that were investigated by Amanov et al. [Amanov 15] lead to varying results. Sixteen tubes for each material were evaluated, and it was observed that Nylon and Polycaprolactone (PLC) had a comparable accuracy/tip position error range to that of Nitinol tubes and possess better properties (e.g. surface friction and stiffness/elasticity, etc.) than Polylactic (PLA), with Nylon having the smoothest surface. Amanov et al. demonstrated that prototypes created using additive manufacturing can be fabricated quickly and can easily be patient-specific and made on-site even in a hospital. Another extensive investigation of prototypes created using additive manufacturing was carried out by Morimoto et al. with a focus on personalized designs for pediatric patients using ultrasound images. In [Morimoto 18], a PCL material was used and follow-the-leader deployment was implemented. In another paper [Morimoto 16b], Morimoto et al. used several additive manufacturing processes and materials, as shown in Figure 1.8, to investigate their different performances. It was observed that the combination of both SLS (using a polyether block amide) for the outer tube and stereolithography (polypropylene-like material) for the inner tube, gave the required maximum strain combination although biocompatibility was not considered. The use of multijet

additive manufacturing (MJT) was later explored for printing Nylon-12 [Picho 22] and was found to have higher accuracy, finer resolution, and a smaller minimum wall thickness compared to SLS, which improved the result of the printed CTR tubes.

#### 1.2.2.c Fabrication of patterned tubes

Patterning tubes involves removing material from annular cross-section tubes. Although patterned tubes can be implemented with any of the materials cited previously for CTRs, they have mainly been explored for Nitinol, and fabrication techniques adapted to this material were explored. Various manufacturing techniques have been considered, including milling [York 15], laser cutting [Lee 15], electro discharge machining [Devreker 15] and femtosecond laser machining [Chitalia 18]. Milling can lead to unintentional heat treatment of the material due to high temperatures during the process, and the diameters of the milling bits limit the dimensions of the notches that can be made on the tubes. Laser cutting with long pulse widths can also generate significant heat but allows for smaller patterns to be made. Electro-discharge machining and femtosecond laser machining both enable small patterns to be made, with femtosecond laser machining being able to produce the smallest ones. Femtosecond laser machining also minimizes the heat-affected zones at the edges of the pattern, limiting the undesired heat treatment of the material [Chitalia 18].

#### 1.2.2.d Tube fabrication: perspectives

Although both Nitinol and polymers have been used to create CTRs, but Nitinol continues to be the most commonly used material. Plastic tubes gained some popularity due to their potential for being low-cost and enabling fast fabrication. The apparent decline and lack of adoption of additive manufacturing for CTR tubes can likely be attributed to the present state of additive manufacturing technologies (printer resolution and obtainable material properties) and some of the comparable factors identified in Table 1.1. However, Nitinol is an expensive material and involves complex processes for shape-setting. Currently, the research community has almost reached a stagnating point, with the challenge of the constant use of Nitinol for CTR tube design and prototyping. To enable more efficient customization, improvements in miniaturization, lower-cost tubes, and rapid onsite fabrication, there is a need for complementary, alternative materials with viable properties.

### 1.2.3 Applications

There are different prominent research that proposes the use of CTR in surgical applications. Though, the various CTR application and survey discussions are already detailed extensively in [Alfalahi 20, Mitros 21]. They can actually be organized by MIS surgical disciplines which include: neurosurgery, ocular surgery,

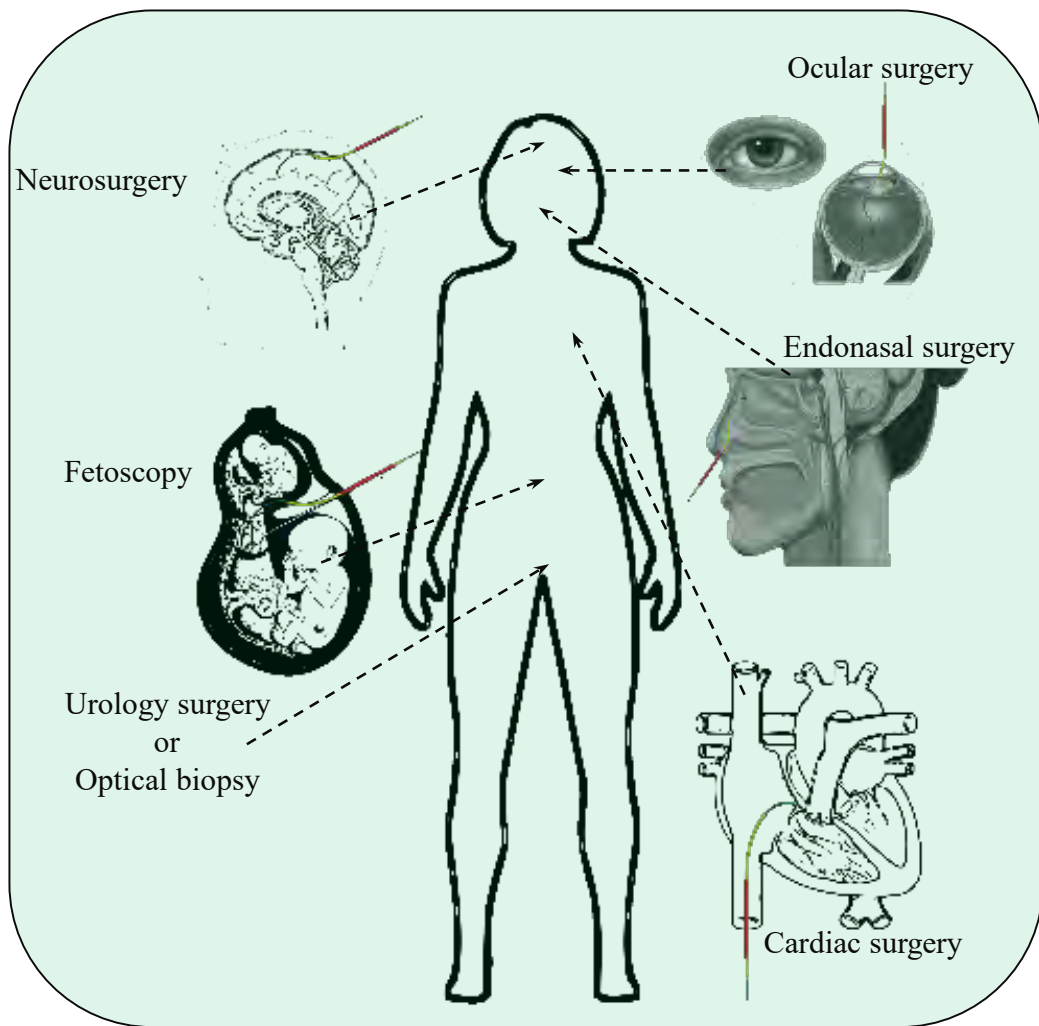


**Figure 1.9:** Applications of CTR for MIS illustrating the different areas of human anatomy for the proposed interventions in literature

endonasal surgery, cardiac surgery, fetoscopy, urology surgery, or biopsy (see Figure 1.9). The Figure illustrates the various ways through which the CTR is deployed through the anatomy to the surgical site for each scenario. Generally, in the interest of brevity, the applications of CTRs for medical interventions are detailed in Appendix-D (Table D.1 & D.2).

Particularly, as regards application, current CTRs are still limited in terms of their size dimensions for some hard-to-reach clinical interventions e.g. neurosurgery, vitreoretinal surgery. These kinds of anatomical structures pose challenges for robots due to their size, complexity, and often delicate nature. A case study is the retinal vein cannulation, which is a theoretical remedy for retinal vein occlusion (RVO), that involves the injection of an anticoagulant into the retinal veins to dissolve the occlusion; however, practical implementation is im-

peded by inherent physiological limitations like hand tremor and limited depth perception [Yu-Ting 22]. To that effect, Lin et al. [Lin 15] proposed a vitreoretinal surgery using CTR through sclera incision which has the advantage of non-post operation suturing and no risk of lens contact. The external Nitinol tube has a diameter of  $635\mu\text{m}$ , which follows the 23G vitreoretinal surgery protocol constraint, that specified a maximum diameter of  $650\mu\text{m}$ . This has a difference of  $15\mu\text{m}$  without even considering tube size tolerance due to manufacturing errors. Moreover, in 2019, Farooq et al. [Farooq 19b] proposed a CTR-based puncturing needle for vitreoretinal surgery but the external tube has a diameter of  $812\mu\text{m}$ . To that effect, the current state-of-the-art of CTRs in the literature for viteroretinal surgery is limited and has a daunting challenge towards further invasiveness in terms of Nitinol tube size.

## 1.3 PARALLEL CONTINUUM ROBOTS (PCRs)

### 1.3.1 Concept

In discussions about robotics, we often come across parallel robots, also known as parallel manipulators or parallel kinematic machines. These robots are unique in that they utilize a closed-loop kinematic chain, where the end effector is connected to the base through several independent kinematic chains or legs that operate in parallel. When comparing parallel robots to their serial counterparts, one notable difference is that each leg of a parallel robot tends to have a simpler and shorter design [Jin 15]. This characteristic contributes to increased rigidity, making the robot more stable and resistant to external forces. Additionally, the motors in parallel robots are intentionally positioned near the base, which serves the purpose of reducing the overall moving mass. By minimizing the mass that needs to be moved, parallel robots can achieve higher speeds and accelerations. Parallel robots offer several advantages stemming from their unique design features which are listed below as follows:

1. High stiffness or force capabilities: The load on a parallel robot is distributed among multiple legs, which results in higher stiffness compared to serial robots. At the same time, they leverage the contribution of multiple actuators working in parallel to generate output forces. Each leg tends to be simpler and shorter, leading to increased rigidity or load-carrying capability. This distributed load sharing helps reduce deflection and enhances the overall stiffness of the system. Consequently, parallel robots can provide higher accuracy and stability during operation, particularly in applications requiring precise positioning.
2. High acceleration and speed: Parallel robots typically exhibit lower moments of inertia due to their compact and lightweight design. The shorter and simpler limb structures contribute to reduced moving masses. As a result,

parallel robots can achieve higher accelerations and velocities, enabling them to perform rapid and dynamic motions. These characteristics make them well-suited for tasks that require quick and agile movements, such as pick-and-place operations or high-speed machining.

3. Improved accuracy: In parallel robots, joint manufacturing and assembly errors are distributed and evened out across the multiple kinematic chains. Unlike serial robots, where errors can accumulate along the entire chain and affect the end effector accuracy, parallel robots can minimize such error propagation. This leads to higher overall accuracy, making them suitable for applications demanding precise positioning and repeatability.

However, it is important to note that parallel robots do come with certain limitations. One notable disadvantage is their limited workspace volume resulting from the parallel architecture. The arrangement of multiple legs in parallel restricts the range of motion and operational space available to the robot. This limitation can pose challenges in applications that require a large workspace or the ability to reach various positions. Additionally, another drawback of parallel robots is the presence of singularities within their workspace. Singularities refer to specific configurations where the robot's kinematic chain becomes over-constrained or degenerate, resulting in reduced mobility or loss of certain degrees of freedom. These singular configurations can affect the robot's performance and motion capabilities, potentially leading to issues such as reduced accuracy, increased stress on the structure, or undesired behavior. Understanding and mitigating the limitations associated with workspace volume are essential considerations in the design and implementation of parallel robots. In fact, recently, there is a further push and demand for miniaturized smart devices for different applications. Considering the research development over the years, the smallest parallel manipulators in the literature include Millidelta [McClintock 18] and Migribot [Leveziel 22]. Though

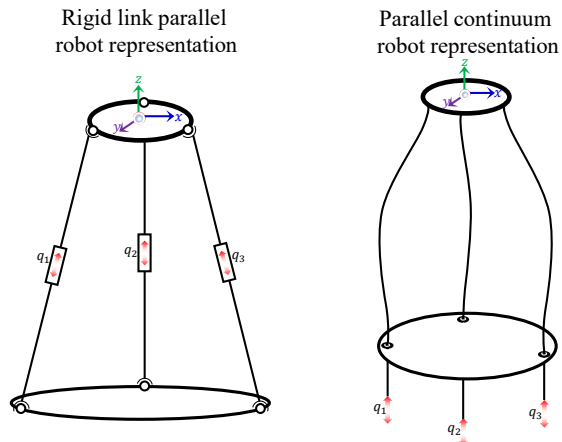


**Figure 1.10:** Schematic representation of rigid link parallel manipulators and parallel continuum robot.

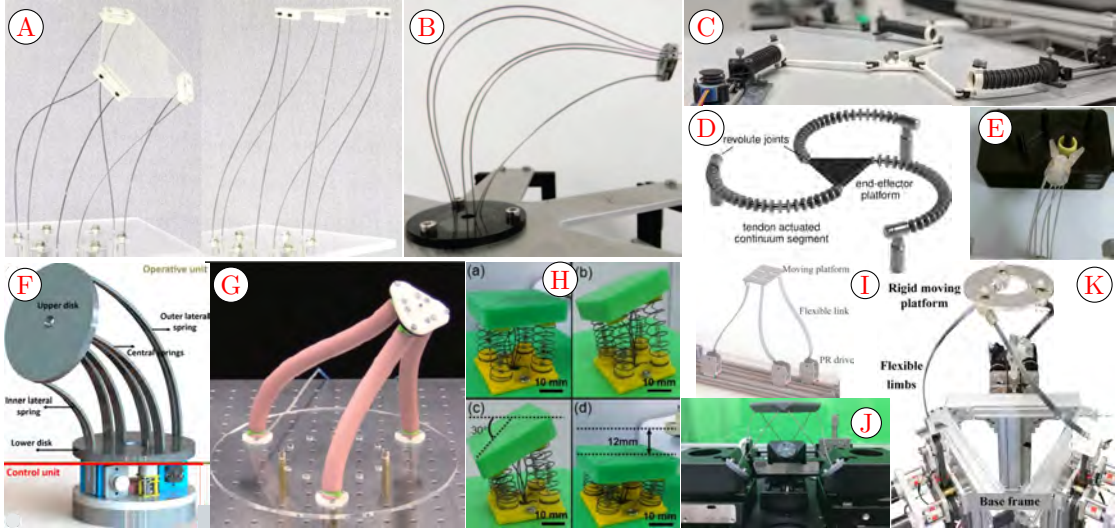


**Figure 1.11:** Different PCR prototype design in the literature **A)** 6-DoFs Stewart-Gough type of continuum robot [Till 19a], **B)** A 6-DOF articulation PCR design prototype with possible intermediate constraints for large deflection [Orehkov 17], **C)** & **D)** Tendon actuated planar PCRs [Sven 20, Nuelle 20], **E)** miniaturized 6-DoFs Stewart-Gough type of continuum robot with gripper [Till 19b], **F)** A modular type of PCR consisting of operative and control units [Mishra 18], **G)** Delta type pneumatically actuated silicon rubber PCR [Huang 22], **H)** An SMA actuated miniature PCR prototype [AbuZaiter 15], **I)** A slender flexible link PCR design type [Wei 21], **J)** 6-DOF articulated PCR design [Gallardo 21], **K)** Three-limb 6-DOF PCR prototype design [Chen 21a].

each presents key benefits thanks to their parallel configurations, they are both restricted to translative motion, which often results in a small workspace. Conversely, this issue and limitation can be solved using a new type of parallel robot called parallel continuum robots (PCRs) [Bryson 14]. Figure 1.10 presents the schematic representation and difference between the traditional parallel rigid link manipulator and the PCR.

PCRs are members of the continuum robots family which are composed of parallel flexible legs or links and actuated at their proximal end. The flexible link part is often made of rods, tendons, wires, and disks. Figure 1.11 presents some of the different types of PCR prototype designs in the literature. Notably, aside from the benefits of parallel kinematic, PCRs have several added advantages which are as follows:

1. They are characterized by high miniaturization potential and scalability because no joints are required as they utilize flexible, continuum structures that allow for continuous bending and deformation, enabling them to achieve various shapes and motions. In fact, the absence of traditional joints in PCRs offers several advantages. First, it allows for a higher level of dexterity and maneuverability. The continuous and smooth bending of the flexible structure enables PCRs to navigate through tight spaces, reach challenging po-

sitions, and adapt to complex environments more effectively. Moreover, the absence of rigid joints eliminates the need for complex mechanical linkages and constraints, simplifying the design and reducing the number of moving parts. This can lead to advantages such as improved reliability, reduced maintenance requirements, and potentially lower manufacturing/prototyping and assembly costs.

2. Unlike conventional robots with rigid joints that require space for articulation and motion, PCRs rely on the inherent flexibility of their links to achieve a wide range of motions. Moreover, one of the notable features of PCRs is that they are often extrinsically actuated, which offers benefits for miniaturization and is ideal for MIS. This extrinsic actuation setup contributes to the miniaturization potential of PCRs active part in several ways and is beneficial for MIS. Firstly, by locating the actuation components at the base, the overall size and weight of the PCR active part can be reduced. The flexible links and segments can be designed to be thin and lightweight, without the need to accommodate bulky internal actuators or power sources. Also, the absence of rigid joints eliminates the need for bulky mechanical components, allowing for a more compact and streamlined overall structure. Furthermore, the compact design of PCRs enhances their portability and adaptability. Therefore, they easily be transported and deployed in various environments due to their reduced size and weight. This makes them suitable for applications in fields such as healthcare, where portability and accessibility are crucial.
3. They possess better stress distributions and large deformations than compliant structures while maintaining their high scalability and large workspace [Black 18a]. Compliant structures, which rely solely on the flexibility of their materials, may experience localized stress concentrations or uneven load distribution. In contrast, PCRs with their parallel kinematic chains distribute external loads across multiple legs, resulting in a more balanced and uniform stress distribution. This characteristic contributes to enhanced structural integrity, reduced risk of material failure, and improved overall performance. Furthermore, PCRs possess the capability to undergo large deformations while maintaining their functionality. This enables them to achieve significant changes in their shape, curvature, and configuration, allowing for versatile manipulation and interaction with the environment.
4. In addition, they offer the possibility of tracking the interaction forces if the deformations of the legs can be measured [Black 18a, Aloi 18a]. The flexible links of a PCR exhibit deformation when subjected to external forces or interactions with the environment. These deformations can be measured using various sensing techniques such as strain sensors, optical sensors, or even by analyzing the kinematics and dynamics of the robot. By monitoring the deformations of the legs, it becomes possible to estimate the interaction forces between the robot and its surroundings. Tracking the interaction forces in PCRs has several benefits. Firstly, it allows for the implementation

of force feedback control, enabling the robot to have a sense of touch and the ability to exert the appropriate forces during interaction tasks. This is particularly valuable in applications such as manipulation, haptic feedback, or tasks that require delicate force control.

Currently, there is a huge paradigm shift from the conventional rigid link robots to the continuum (continuously deformable) ones in medical applications. This is due to their compliant nature and safer robot-human interactions. All these advantages and benefits open up opportunities for the design of many PCR manipulators of all sizes and kinds, which are explained in detail below.

### 1.3.2 Classifications

Classification of PCRs					
	Spatial PCR		Planar PCR		
Schematic diagram	Actuation type	References	Actuation type	References	
Link type	Boundary actuation PCRs	Motorized <a href="#">[Till 17a, Orekhov 16a, Black 18a]</a> <a href="#">[Till 17b, Till 19a, Alois 18b, Wu 22]</a> <a href="#">[Young 19, Wu 19, Vanneste 21]</a> <a href="#">[Alois 18a, Orekhov 17, Li 20, Wei 21]</a> <a href="#">[Bryson 14, Till 15, Black 18b]</a> <a href="#">[Gallardo 21, Chen 21b, Orekhov 16b]</a> <a href="#">[Jiang 15, Zheng 20, Orekhov 15]</a>	Motorized <a href="#">[Koehler 19, Campa 19, Mauze 20]</a> <a href="#">[Mauze 21a, Shahabi 19, Kuo 17]</a> <a href="#">[Altuzarra 19c, Wang 23]</a>		
	Distributed actuation PCRs	Motorized <a href="#">[Lilge 23, Wen 22, Yang 18b]</a> Pneumatic <a href="#">[Hopkins 15, Rivera 14, Huang 22]</a> <a href="#">[Yuan 18, Singh 17, Amanov 21]</a> <a href="#">[Falkenhahn 15, Zhang 20]</a> SMA <a href="#">[AbuZaiter 15]</a>	Motorized <a href="#">[Lilge 21, Kathrin 20, Lilge 20]</a> EAP <a href="#">[Moghadam 15]</a>		

**Figure 1.12:** General classification of PCRs based on their structural design configuration or architecture, which is either non-planar that is characterized by out-of-plane motion or planar, which is restricted to in-plane motion when actuated.

The family of PCR is quite vast and they have different nomenclature in the literature such as their mode of actuation e.g. pneumatic, motorized, semiconductor memory alloy (SMA), and electro-active polymer (EAP) actuated or even by their number of links e.g 3 links (delta), 6 links (stewart Gough). Generally, PCR can be classified based on its structural architecture, which is either planar configuration or non-planar configuration (See Figure 1.12). Although we have

two different PCR link types, which are 1) boundary actuated: here, the deformation/configuration of the PCR goes with the variation of boundary actuation length, and 2) distributed actuation: link deformation is a result of a change of stiffness distributed along it upon actuation. The boundary actuated link PCRs are simple to design and their links can be easily scaled down unlike the distributed actuated counterpart, whose mechanics are even more complex. The different PCR classifications are discussed in detail below in the following.

### 1.3.2.a Planar parallel robots with continuum legs

This is a type of PCR whose structural configuration and kinematic mechanism only allow in-plane motion or displacement of the flexible continuum link when actuated. Figure 1.11C & D, present some planar robot prototype designs in literature, while the schematic diagram representation of this kind of PCR with 3-links is shown in Figure 1.12. Moreover, two straight-link PCR can be regarded as planar because its motion upon actuation is restricted in-plane. This category of PCR is often limited in workspace area due to their in-plane motion but conversely, they are characterized by good precision and accuracy [Mauze 20, Mauzé 21a]. This feature is very beneficial in micromanipulation applications. Although, the majority of this category of PCRs are mostly actuated by a set of motors rather than a pneumatic approach (see Figure 1.12). Planar PCRs are not limited to motorized types as Moghadam et al. [Moghadam 15] demonstrated the ability to use electro-active polymer (EAP), which is an active deformable link to design a planar PCR for micromanipulation.

### 1.3.2.b Spatial PCRs

These are types of PCRs whose architecture and mechanics are characterized by out-of-plane motion or displacement upon actuation. We have so many different kinds of spatial PCRs in the literature, such as 1) tendon-driven PCRs [Peiyi 21, Orekhov 17, He 18, Wu 19, Till 17a, Black 18a, Gallardo 21], 2) wire & disk or cable-driven PCRs [Jiang 15, Azamat 18, Rone 14, Boettcher 21, Sven 22], 3) pneumatically driven soft PCRs [Hopkins 15, Rivera 14, Huang 22, Sun 20, Singh 17, Lakhal 16], and 4) Electric driven or shape memory alloys (SMA) link PCR [AbuZaiter 15]. A detailed summary of sub-classifications of the spatial PCRs in the literature, which is based on their continuum link type is presented in Table 1.12.

The spatial or non-planar type of PCRs with their different schematic diagrams presented in Figure 1.13, are more pronounced in the literature (see Figure 1.11 and Figure 1.12). This is due to the benefit of higher DOFs by increasing the number of links and large workspace considering its large out-of-plane bending/rotation. Moreover, it is suitable for lots of PCR designs such as pneumatically driven soft PCRs unlike the planar counterpart (see Figure 1.12). Figure 1.13 illustrates through a schematic diagram, the different spatial PCR designs and concepts in the literature. The majority of this category of PCRs are designed with a motorized actuated type followed by pneumatic actuation. In fact, there are hybrid types of non-planar PCRs that are been actuated by both motor and pneumatic

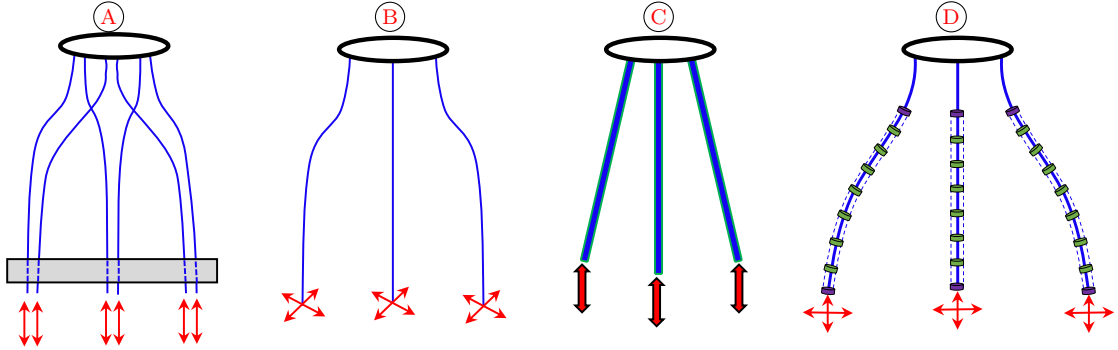


**Figure 1.13:** Schematic diagram for the different types of spatial PCRs in the literature  
**A)** vertical linear actuator rod or slender tendon PCR type, **B)** horizontal linear actuator rod or slender tendon PCR type, **C)** Electric/pneumatic driven PCR type, **D)** wire/cable and disk actuated PCR type.

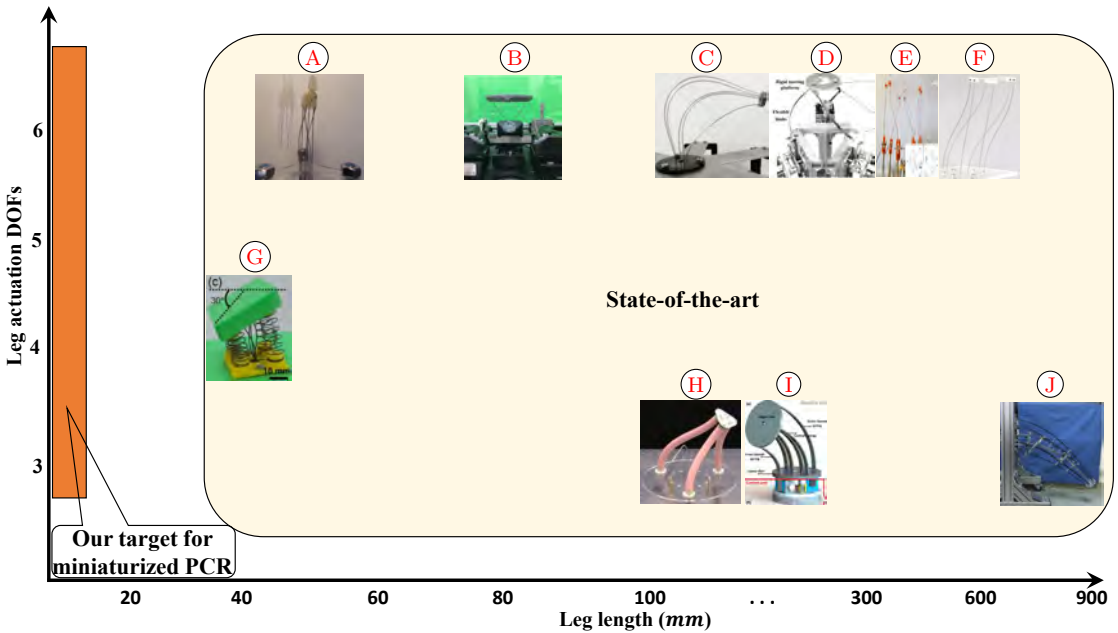


**Figure 1.14:** A state-of-the-art of spatial PCRs in the literature considering their actuation DOFs versus the leg length, so as to compare their individual sizes. **A)** Miniature 6-DOF PCR with a cable-driven grasper [Orekhov 15], **B)** A design that turns an articulated 3-PPSR Manipulator into a PCR [Gallardo 21], **C)** A 6-DOF articulation PCR design with possible intermediate constrained with disk integration for large displacement [Orekhov 17], **D)** Three-limb 6-DOF PCR prototype design [Chen 21a], **E)** Stewart-Gough configuration PCR which allows for full six degrees of freedom end effector control [Aloi 22], **F)** A similar 6-DoF Stewart-Gough type of continuum robot [Bryson 14], **G)** An SMA actuated miniature PCR prototype [AbuZaiter 15], **H)** Delta type pneumatically actuated silicon rubber PCR [Huang 22], **I)** A modular type of PCR consisting of operative and control units [Mishra 18], **J)** Three DOF multi-constrain PCR [Wu 19].

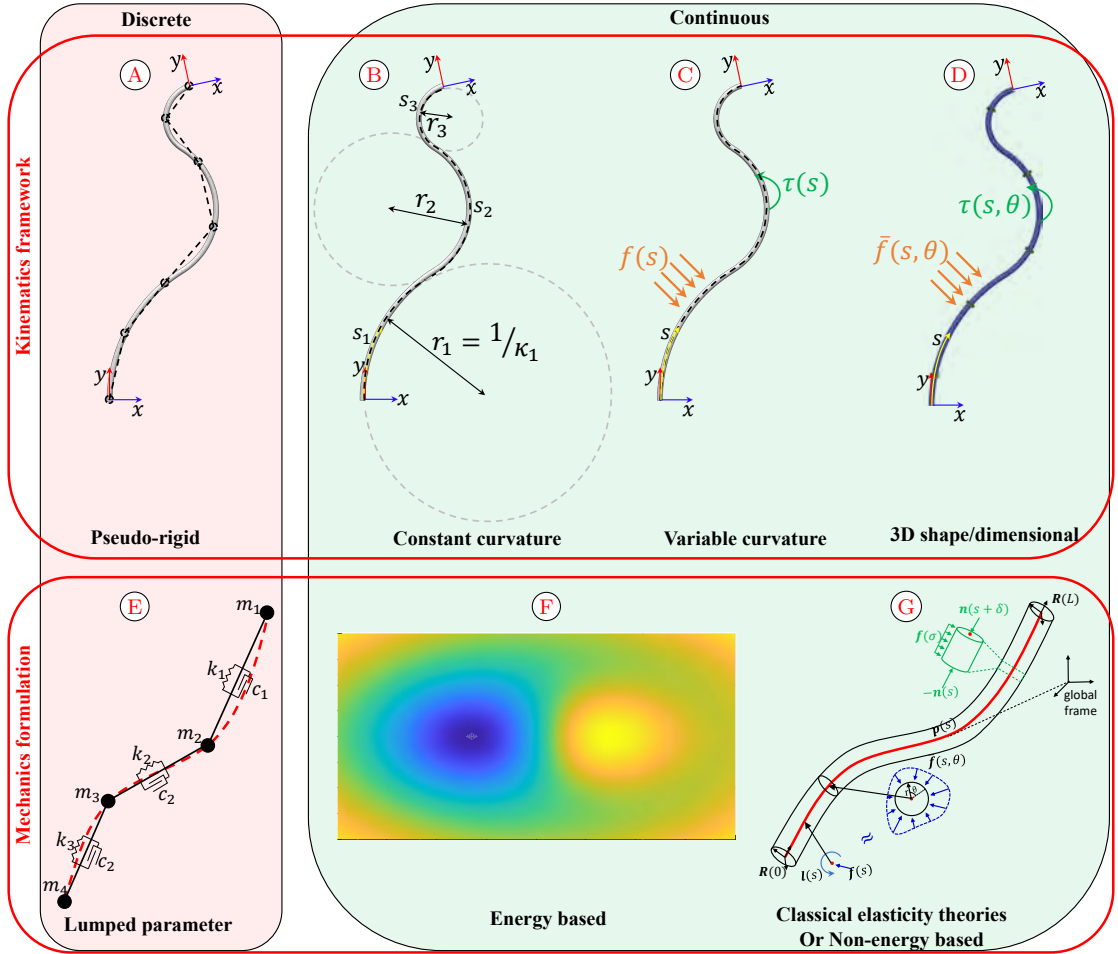
as proposed in [Sun 20, Yaxi 21]. In addition, there is a reconfigurable non-planar PCR design proposed by Mahoney et al. in [Mahoney 16b].

Figure 1.14 presents the state-of-the-art of spatial PCRs from publication papers under our reach, that gave clear details of the robot design specification. The figure shows the position of each PCR when considering its leg actuation DOF and the leg length at nominal configuration. One can notice that irrespective of the DOF, the leg lengths of all the robots are above 30mm. This shows a level of limitation in terms of the miniaturization of the robot for micromanipulation, in order to benefit the advantages of parallel configuration and continuum robot design. From Figure 1.14, most of the proposed PCRs are characterized by 6-DOF actuation, which requires extra motors and makes the system bulky. Moreover, considering that most of the PCR design uses Nitinol rods/tubes, this presents a literature gap in obtaining a miniaturized PCR. Potentially, the use of sub-millimeter rods like glass optical fiber could serve as a possible solution to bridge the gap. At the micro-scale, materials become flexible and in fact, the possibility of using optical fiber comes with the benefits of light carrying capability of glass for possible end-effector actuation or manipulation. In the subsequent Chapter, the research interest will be focused on the actualization of a miniaturized PCR made of glass, which falls within the target boundary as shown in Figure 1.14.

## 1.4 CONTINUUM ROBOT MODELING

The standard rigid-link manipulators are well-understood and discussed extensively in the literature, whereas in contrast, for continuum manipulators there is still debate within the robotics community especially in terms of its modeling and control [Robert 10, Rucker 11a, Chikhaoui 18a]. The flexible link characteristic of continuum robots serves as their main advantage for practical applications but poses challenges in understanding and describing their physical behavior. The complex relationships between actuators and end effector dynamics further complicate the modeling of continuum robots, resulting in significant attention and the emergence of various concepts within the robotics community [Russo 23].

In continuum robotics, robot configuration refers to the shape and arrangement of its flexible structure, where the pose of the system elements is compatible with the internal (joints) and the external (geometric boundary conditions) kinematic constraints [Armanini 23]. The motion of a continuum body is defined by a continuous sequence of configurations along time, whereas, a change of its configuration results in a displacement, which usually has two components: a rigid-body displacement and a deformation. To design and control such complex robots effectively, accurate modeling techniques are crucial. Modeling on the other hand is often a mathematical or analytical framework, that links the behaviour and kinematics of a robot to the applied load/stress or upon actuation. The formulation



**Figure 1.15:** Different approaches of modeling continuum robots in the literature based. This is arranged in terms of the kinematic framework and the mechanical formulation used while considering either the discrete or continuous approach. **A)** Approximation of continuous shape by series of discretized rigid links connected by spherical or revolute joints, **B)** Constant curvature with geometrical arc segment representation of continuum shape, **C)** Variable curvature which involves a continuously evolving reference frame achieved by integrating along the continuum rod, **D)** representation of the robot kinematics in a 3D shape dimension, **E)** Lumped parameter mechanics which approximate the response of a continuum robot upon actuation or load by using discrete spring( $k$ ) mass( $m$ ), damper( $c$ ) system, **F)** Energy-based mechanics formulation to describe the continuum robot shape while using any of the kinematic frameworks, **G)** Non-energy-based approaches using the classical elasticity theorems that consider the conservation/equilibrium relationship of forces and moment acting on the continuum link/robot.

of continuum robot modeling is more complex when compared to conventional robots [Trivedi 08b] and their level of complexity depends on the number of constraints considered or the approach used. Each one is subject to a different level of complexity, accuracy, and computational requirement along with the robot's architectural design or composition. An overview of the different continuum mod-

eling approaches in the literature is discussed below. Apparently, the different approaches to modeling continuum robots are discussed in detail as presented in Figure 1.15.

### 1.4.1 Kinematic frameworks

This is used to represent the shape/geometry of a continuum body as shown in Figure 1.15. Among the kinematic framework for continuum modeling, we have; 1) pseudo rigid, 2) constant curvature 3) variable curvature, and 4) 3D dimensional shape representation framework approach.

#### 1.4.1.a Pseudo rigid kinematic framework

The pseudo-rigid body model is a familiar discrete approach employed for modeling compliant mechanisms. The development of this model for continuum robots stemmed from the desire to leverage the existing theories and principles of rigid robotics. These models represent the continuum bodies as a sequence of interconnected rigid links joined by revolute, universal, or spherical joints [Armanini 23, Burgner 15a]. In this approach, a series of homogeneous transformations generated from standard Denavit–Hartenberg (D–H) parameter tables are used to describe a continuum curve by discrete approximation (see Figure 1.15A). When it comes to modeling continuous elastic structures, the effectiveness of this approach varies depending on the type of robot being modeled. Certainly, these models are perfectly suitable for discrete structure manipulators. However, it is important to note that discrete models can also offer accurate approximations for continuous elastic structures. As such, they can produce satisfactory results for hyper-redundant or snake-like robots, but they exhibit a lower order of spatial approximation accuracy when dealing with continuous elastic structures. Additionally, the identification procedure required for these models remains expensive. In a specific study presented in [Kutzer 11], a dexterous catheter manipulator is represented using a series of pin joints that are interconnected by rigid links. Another approach, described in [Khoshnam 13], uses a pseudo-rigid 3D model to capture the behavior of a steerable ablation catheter. The catheter itself is considered a cantilever beam, represented by four rigid links connected through three revolute joints and three torsional springs. This kinematic framework was also used for the medical continuum robot modeling of a catheter for intracardiac navigation [Ganji 09].

#### 1.4.1.b Constant curvature models

Unlike rigid-link models, constant-curvature kinematic frameworks portray continuum robot geometry through a finite set of curved segments, all of which are mutually tangent and maintain a consistent curvature along their length (refer Figure 1.15B). This approach is widely regarded as a favorable attribute in continuum robots, primarily due to the inherent simplifications it offers in the domains of kinematic modeling, real-time control, and other pertinent computa-

tions [Armanini 23, Burgner 15a]. Noteworthy to mention that in this context, “constant” refers to being unchanged in regards to arc length, not in relation to time. In this kinematic framework, the position and orientation at any point on the robot can be written as a function of the arc parameters, which are the curvature, length, and angle. Moreover, this approach provides an alternative and is regarded as the most common form of lumped parameterization [Robert 10], where the entire link segment is assumed to have a constant bending curvature. While the variable curvature is described by functions that are integrated over the arc length, the constant curvature consists of a finite number of curved links which are described by a finite set of arc parameters that can be converted into analytical frame transformation [Robert 10]. The formulation involves constant curvature assumption, which minimizes the number of model parameters, thereby making it simple and can be used for efficient kinematics and static models [Camarillo 08]. However, they suffer from low accuracy and can only account for pure bending with no external force [Rao 22]. This huge limitation paved the way for a new approach called piece-wise constant curvature assumption that accounts for both twist and bending curvature with the link centerline modeled as a series of mutually tangent circular arc [Rone 14, Yuan 19]. Here, the tip coordinate frame can be computed by analytic integration of each constant-curvature segment followed by the concatenation of the resultant set of relative transformations [Dupont 10b, Sears 06]. The arc parameter that defines the configuration space of the link centerline is composed of three variables; 1) curvature  $\kappa$ , 2) plane rotation angle  $\phi$  and 3) arc-length  $s \in [0 \quad l]$ , with arc bend/rotation  $\theta = \kappa s$  (see Figure 1.16).

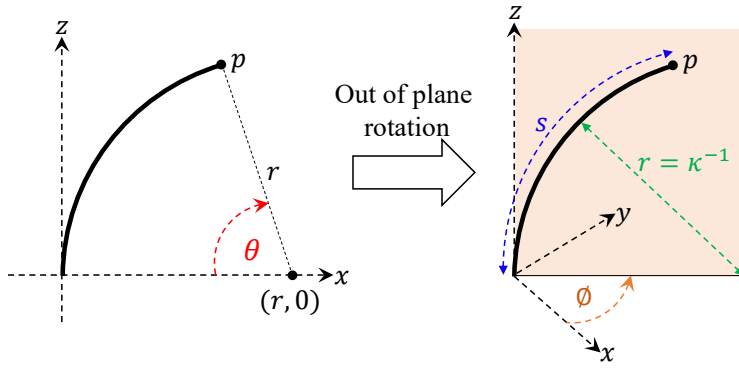


**Figure 1.16:** The geometry of a continuum robot provides a means of determining the pose of points along it [Neppalli 07, Webster III 07]. Using arc geometry approach with  $\mathbf{p} = [r(1 - \cos\theta) \quad 0 \quad rs\sin\theta]^T$ , and then  $\mathbf{R}_y(\theta) \& \mathbf{R}_z(\phi) \in \text{SO}(3)$ . Left figure, consider  $\phi = 0$  then the arc segment lies in  $x - z$  plane whereas, the right figure is a case where the arc rotates  $\phi$  out of  $x - z$  plane.

There are different approaches that gave identical results e.g arc geometry, D-H parameter, Frenet-Serret frames, integral representation, and exponential coordinates that can be used to obtain the pose of the link centerline in terms of homogeneous transformation matrix  $\mathbf{T}$  parameterized by  $(\kappa, \phi, l)$  as reviewed

in [Robert 10]. This matrix is used to derive the task space coordinates or pose. Where  $\mathbf{T}$  is the transformation from base to tip given in Equation 1.1 & 1.2. To orient the tip frame to align with the base frame when no rotation about the local  $z$ -axis e.g adding a gripper, then  $\mathbf{T}(\kappa, \phi, l) = {}^b\mathbf{T}_p(\phi) {}^b\mathbf{T}_p(\theta) {}^b\mathbf{T}_p(-\phi)$ .

$$\mathbf{T}(\kappa, \phi, l) = {}^b\mathbf{T}_p(\phi) {}^b\mathbf{T}_p(\theta) = \underbrace{\begin{bmatrix} \mathbf{R}_z(\phi) & 0 \\ 0 & 1 \end{bmatrix}}_{\text{Rotation}} \underbrace{\begin{bmatrix} \mathbf{R}_y(\theta) & \mathbf{p}(s) \\ 0 & 1 \end{bmatrix}}_{\text{Inplane transformation}} \quad (1.1)$$

$$\mathbf{T}(\kappa, \phi, l) = \begin{bmatrix} \cos \phi & \cos \kappa s & -\sin \kappa s & \cos \phi & \sin \kappa s & \frac{1}{\kappa} \cos \phi (1 - \cos \kappa s) \\ \sin \phi & \cos \kappa s & \cos \kappa s & \sin \phi & \sin \kappa s & \frac{1}{\kappa} \sin \phi (1 - \cos \kappa s) \\ -\sin \kappa s & 0 & 0 & \cos \kappa s & 0 & \frac{1}{\kappa} \sin \kappa s \\ 0 & 0 & 0 & 0 & 0 & 1 \end{bmatrix} \quad (1.2)$$

For piece-wise constant curvature, the pose is computed as the concatenation of the different arc segments that makes up the centerline shape, composing a series of arc-to-arc transformation matrices, with the resultant pose as  $\mathbf{P} = \mathbf{T}_1 \dots \mathbf{T}_n$ . Where  $n$  is the number of arc segments. By precurving each tube such that its curvature is piecewise constant, the combined telescoping curvature is also approximately piecewise constant and this is true even when torsion is considered [Dupont 10b]. One of the main restrictions of these PCC models is that the use of parametrization and kinematic maps can implicitly provide a numerical singularity that occurs when the curvature tends to vanish ( $\kappa \rightarrow 0$ ), resulting in an infinite or undefined radius of curvature. To address this constraint, several solutions have been proposed in the literature. One approach, presented in [Godage 11c, Godage 15a], involves representing the rotational and positional components of the homogeneous transformation (Equation 1.2) in modal form. Additionally, a Lagrangian-based method was presented in [Godage 11a, Godage 11b] to analyze the spatial dynamics of a single-section continuum arm. This approach was subsequently extended to encompass multi-section continuum arms in [Godage 16]. The PCC approach has been used in PCRAs as presented in [Lilge 20, Yang 18b, Moghadam 15, Grace 22, Nuelle 20]. One could see that the number of papers using this approach is quite few due to the drawbacks associated with it, although it is the reverse for CTRs because the robot shape with the nested pre-curved tubes conforms well to arc geometry. For CTR, it has been used in [Robert 10, Neppalli 07, Webster III 07, Dupont 10b, Sears 06, Webster 06b, Sears 07, Webster 08a, Webster 09c, Rucker 10b, Gilbert 13, Bergeles 15, Anor 11b, Webster 10]. In fact, this is the approach we adopted for the forward kinematic and inverse kinematic modeling of the sub-millimeter robot made of glass in Chapter 3.

Clearly, the lumped parameter approach is an extension of the discrete-link or pseudo-rigid kinematic framework, although this mechanics has been used along with constant curvature kinematic framework in [Zheng 12]. To approximate the mechanical behavior of a continuous elastic and/or viscous medium, the approach involves attaching discrete mechanical elements such as point masses, springs, and

dampers to the kinematic framework (refer to Figure 1.15E). Representing a continuum body as a collection of discrete masses, dampers, and springs is one of the simple methods for modeling continuum robots. This approach enables the derivation of governing equations by using energy methods or applying classical Newton equations [Armanini 23, Burgner 15a]. These equations accurately describe the transmission of forces between particles within the configuration space. In [Habibi 18, Habibi 19], the mass-spring-damper arrays were used to accurately model the extensive deformations of a continuum surface (LDCS) actuated by a continuum arm that undergoes large deformation. Lumped-parameter mechanics models offer a significant benefit due to their simple structure, which allows for the easy incorporation of complex phenomena like nonlinear friction, material hysteresis, and inertial dynamics. However, to achieve the same level of accuracy as continuum mechanics models or the FEM, they necessitate a large number of DOFs and an extensive system identification process that requires a substantial amount of data.

#### 1.4.1.c Variable curvature kinematic framework

This was used in the early days of continuum robots to resolve redundancies and control the shape of hyper-redundant serial manipulators [Burgner 15a]. The backbone pose of a robot in variable-curvature frameworks is represented by a material-attached homogeneous reference frame. This frame includes a position vector  $\mathbf{p}(s) \in \mathbb{R}^3$  and a rotation matrix  $\mathbf{R}(s) \in \text{SO}(3)$ , which express the pose as a function of the robot's arc length, denoted as ' $s$ ' (see Figure 1.15C). The rotation matrix undergoes progressive changes along the arc length and the evolution of the pose from the base to the tip along the arc length is given by the differential kinematic relationships below:

$$\begin{aligned}\mathbf{p}' &= \mathbf{R}\mathbf{v} \\ \mathbf{R}' &= \mathbf{R}\hat{\mathbf{u}}\end{aligned}\tag{1.3}$$

Where ' $'$ ' denote derivative with respect to arc length,  $\mathbf{v} \in \mathbb{R}^3$  denote the linear velocity vector of a rigid body expressed in body-frame coordinate, while  $\mathbf{u} \in \mathbb{R}^3$  denotes the curvature vector which expresses the angular rate of change about the current axis of  $\mathbf{R}(s)$  and finally, ' $\hat{\cdot}$ ' represents a mapping from  $\mathbb{R}^3$  to  $\mathfrak{so}(3)$ . By knowing the functions  $\mathbf{u}(s)$  and  $\mathbf{v}(s)$ , it becomes possible to calculate the shape of the continuum robot's backbone. This calculation involves solving the differential kinematic equations 1.3 as an initial value problem, starting from the base and proceeding towards the tip of the robot. Equations 1.3 can be integrated using standard explicit numerical integration methods such as the widely used fourth- to fifth-order Runge–Kutta scheme. Moreover, most continuum robot designs have short integration arc lengths and relatively low curvatures. Therefore, utilizing the explicit integration approach can yield highly precise approximations for both  $\mathbf{R}(s)$  and  $\mathbf{p}(s)$  [Rucker 10b, Lock 10b, Burgner 15a]. Due to the simplicity and

faster computation, quasi-static modeling is often used in the literature, which was what we used in Chapter 4 for the miniaturized PCR made of glass that adopted this approach.

#### 1.4.1.d 3D shape dimension kinematic framework

Here, the continuum structure of the robot is discretized into finite volumetric or beam elements. Each element represents a small segment or mesh of the continuum robot, and the deformations within each element are described using interpolation functions. This approach often goes with the finite element modeling approach which is detailed in 1.4.3.a.

### 1.4.2 Mechanics formulation

This involves the use of constitutive equations of forces and moments balance or equilibrium relationship to relate continuum body shape and motion to actuation/external loads. Each of the mechanics' formulations as presented in Figure 1.15 can be combined with the different kinematic frameworks to actualize a mechanics-based representation of the robot shape via governing equations and so, they are not mutually exclusive. The various mechanics' formulation approaches are detailed as follows:

#### 1.4.2.a Energy-based approach

This robust method has found extensive application in continuum robot research, serving diverse objectives but most importantly as related to analyzing instability or bifurcation. It is a special approach using an energy minimization or Lagrangian approach that relates the continuum link deformation elastic energy. This permit obtaining the robot dynamic potential and kinematic energy which provide an easier and more efficient method for continuum robot stability analysis or even singularity configuration while considering the bending and torsional energy [Rucker 10e, Gilbert 16a, Briot 22b, Xu 10a, Zaccaria 20]. The energy minimization approach was used alongside the constant and variable curvature kinematic framework for modeling/analyzing the torsional instability behavior of concentric tube robot [Rucker 10e, Webster 09b].

Although, this approach is challenging to formulate depending on the complexity of the continuum design and it is less intuitive. From the literature and as regards the PCR modeling, this approach has been used in [Zaccaria 20, Briot 22b, Goldman 14], though they are quite a few in number. For CTR, this approach has been used in [Bai 12b, Webster 08a, Hendrick 15a, Webster 09b, Rucker 10d, Xu 14, Dupont 09a, Gilbert 16a, Gilbert 16a]. In fact, we used this method for the bifurcation and stability analysis of our sub-millimeter CTR made of glass in Chapter 3.

Considering CTR, this approach of using minimization of energy and that of Newtonian equilibrium of forces and moments have been shown to be equivalent [Gilbert 16b, Rucker 10b].

#### 1.4.2.b Classical elasticity theories or Non-energy-based approach

In the absence of specific assumptions, these formulations rely on classical three-dimensional continuum mechanics theory. Although, alternative approaches involve conceptualizing the robot as slender structures such as beams and rods, which utilize Cosserat, Kirchhoff, and non-linear Euler-Bernoulli beam theories. For the past decades, classical elasticity theories have served as a reliable tool in accurately describing the mechanics of continuum robots, while presenting a well-established and comprehensive framework accessible to the continuum robotics community. Actually, it has become one of the most used approaches for continuum robot formulation. Starting with the widely used classical Bernoulli–Euler beam theory which states that internal moment is proportional to change in curvature, given as  $M = EI\kappa$ . It is most effective when considering large deflection. The next one which is very popular is the Cosserat rod theory, which is used for both dynamic and static continuum robot modeling. In fact, an extension of it when shear and axial strain are neglected is known as Kirchhoff's theory. The Cosserat rod formulation is a simplified approach that involves directly modeling the slender rod as a material line, where a sequence of rigid cross-sections is continuously arranged as shown in Figure 1.15. This particular modeling approach has become recently and popular tool for obtaining a general model of continuum robots [Burgner 15a]. The model was developed in the early 20th century [Antman 05] and has been used by different research communities, the popular being in computer graphics [Pai 02], whereas it was first applied for a continuum robot in 2008 [Trivedi 08a].

In the static scenario, the classical Cosserat rod model comprises a set of nonlinear ordinary differential equations that describe the internal force and moment vectors supported by a rod-like object in a state of static equilibrium as a function of  $s$ , given as:

$$\begin{aligned}\mathbf{n}' &= -\mathbf{f} \\ \mathbf{m}' &= -\mathbf{p}' \times \mathbf{n} - \mathbf{l}\end{aligned}\tag{1.4}$$

where  $\mathbf{n}$  and  $\mathbf{m}$  are the internal force and moment vectors carried by the rod at  $s$ , and  $\mathbf{f}$  and  $\mathbf{l}$  are the external distributed force and moment vectors. The static equilibrium Equations 1.4 are coupled to the kinematic Equations 1.3 through some material constitutive law (linear elastic relation of stress-strain) to fully constrain the ODE system, given as:

$$\begin{aligned}\mathbf{v} &= \mathbf{v}^* + \mathbf{K}_{se}^{-1} \mathbf{R}^T \mathbf{n} \\ \mathbf{u} &= \mathbf{u}^* + \mathbf{K}_{bt}^{-1} \mathbf{R}^T \mathbf{m}\end{aligned}\tag{1.5}$$


---

The variables  $\mathbf{v}^*$  and  $\mathbf{u}^*$  indicate the shape of the rod in a stress-free situation, while the homogeneous stiffness matrices given as  $\mathbf{K}_{se} = \text{diag}([GA, GA, EA])$  and  $\mathbf{K}_{se} = \text{diag}([EI_{xx}, EI_{yy}, GI_{zz}])$ . The set of Equations 1.3, 1.4, and 1.5) can then be solved subject to any appropriate boundary conditions on  $\mathbf{p}$ ,  $\mathbf{R}$ ,  $\mathbf{n}$ , and  $\mathbf{m}$ . This formulation is generally applicable for different varieties of robots whose shapes are governed primarily by elasticity [Burgner 15a] e.g. CTRs and PCRs, which are going to be discussed in the subsequent Chapters. To compute the general continuum robot mechanics, one needs to solve for the closed formulation obtained by the set of nonlinear PDEs/ODEs along with the boundary conditions (BCs) imposed by the robot couplings at the proximal point, distal point, and including intermediary constraints if any. Most times, the close-form solutions to the derivatives are unknown, therefore, numerical integration along the continuum link arc length from base to tip is employed. From the literature, the numerical resolution solvers include a 3D finite element model (FEM), finite difference, and shooting method. These are detailed below as follows:

### 1.4.3 Numerical resolution solvers

#### 1.4.3.a FEM method

This approach uses the finite element method (FEM) as presented in 1.15D. Moreover, FEM is a well-known and widely-spread numerical technique for finding approximate solutions to PDEs. FEM provides accurate representations of the flexible structures as it permits to incorporate or build the 3D robot shape but conversely, it is computationally demanding. Instead of describing continuum robots as a set of discretized centerlines/backbones, the FEM uses mesh (triangular, tetrahedral e.t.c) or nodal coordinates for element-by-element discretized volumetric computation, which captures the full features of the robot under analysis. By solving the governing equations for the finite elements, the overall deformation and configuration of the continuum robot can be determined. According to [Armanini 23], once the space discretization is performed, the continuous field is approximated within each element using polynomial interpolation based on values at the element edges, also known as nodes. This discretization process transforms the original continuous formulation into a system of ODEs for transient problems or algebraic equations for steady-state problems, resulting in a static equilibrium given as:

$$\mathbf{Q}_{int}(\mathbf{q}) = \mathbf{Q}_{ext}(\mathbf{q}) \quad (1.6)$$

where  $\mathbf{Q}_{int}(\mathbf{q})$  and  $\mathbf{Q}_{ext}(\mathbf{q})$  represent the internal and external generalized forces, respectively, while  $\mathbf{q}$  are the generalized coordinates, i.e. the nodal positions. On the other hand, the dynamic equilibrium is given by a system of ODEs:

$$\begin{aligned} \dot{\mathbf{q}} &= \mathbf{v} \\ M\ddot{\mathbf{v}} + \mathbf{Q}_{int}(\mathbf{q}, \mathbf{v}) &= \mathbf{Q}_{ext}(\mathbf{q}, \mathbf{v}) \end{aligned} \quad (1.7)$$

where  $\mathbf{M}$  is the (constant) generalized mass matrix. Note, Equation 1.6 and 1.7 are evaluated by integrating the distributed variables element-wise using shape functions as a kinematic map, while the assembly process guarantees the correct positioning of each mesh element. This approach requires FEM software as the method is often used for most soft continuum robots that need to incorporate some material inelastic features/behavior or directional deformation which are hard to model in one dimension. Moreover, the FEM represents a standard for many popular simulation software, such as Abaqus, ANSYS, SOFA, and Comsol. This software offers a significant benefit in its versatility, as it can be utilized for various physical problems including structural dynamics, fluid-structure interactions, contact, and thermodynamics. However, this broad applicability comes at the expense of higher computational requirements, resulting in longer convergence times for simulations, particularly in dynamic scenarios.

There are some FEM software that has been used in the literature for modeling and simulation of CTRs and PCRs. For PCRs, this include include 1) “SOFA” [Duriez 13, Gallardo 21, Vanneste 20, Cangan 22, Vanneste 21], 2) “MATLAB (ANCF-based)” [Huang 22], 3) “Abaqus” [Zhang 20, Huang 22, Zheng 20], 4) “ANSYS” [Yaxi 21]. One would notice that with this approach, researchers tend to use SOFA mostly because it is dedicated to soft robotics simulation and control based on real-time modeling for the robot deformation [Schegg 23]. For CTRs, this includes: 1) “ADINA” [Baek 16, Lee 15], 2) “Abaqus” [Kim 19a, Wang 19b], 3) “Altair/Solidworks” [Xin Jue Luo 18, Azimian 14b], 4) “Creo” [Xu 20], 5) “COMSOL” [Song 23]. In general, this method has it benefits of higher accuracy and taking into account the entire robot shape, for cases of non-slender part/section or soft robots but the drawback includes the challenge in model formulation and higher computational time/resources required since it’s 3D composition. These are the more reason researchers tend to use the slender rod approach.

#### 1.4.3.b Finite difference method

The finite difference method is a well-established and straightforward technique for solving PDEs and it is commonly employed for tackling various computational challenges. Considering the deformation energy of a planar slender rod, this approach was used in [Zaccaria 20] to approximate the derivative of the rotation  $\theta$  of a slender rod. The expression for the derivative of the rotation  $\theta_i$  of the element  $i$  is given as:

$$\theta'_i = \frac{\theta_i - \theta_{i-1}}{d_e} \quad (1.8)$$

where the rod length  $L$  is discretized into  $N$  elements given as  $d_e = L/N$ . In the field of continuum robotics, researchers have successfully utilized the finite difference method for both cases of statics [Peyron 18, Briot 22b, Peyron 19, Zaccaria 20], and dynamics [Lang 11, Renda 14]. Some of the drawbacks include grid dependence, limited geometrical flexibility, and difficulty to handle BC for complex sys-

tems properly [KREISS 74, Mantzaris 01, Perrone 75]. For the continuum robot community, the most often used approach is the shooting method, which is discussed in detail below.

#### 1.4.3.c Shooting Method

The shooting method is a widely used numerical technique for solving boundary value problems (BVPs) in one-dimensional space or time. It is also applicable to solving BVPs for continuum robots. The shooting algorithm involves integrating a series of initial value problems, where the unknown proximal conditions are initially estimated and then iteratively adjusted using a Newton-type algorithm. This process continues until a solution to the BVP is obtained, satisfying the given distal boundary conditions. By employing the shooting method, BVPs for continuum robots can be effectively solved through the step-by-step refinement of initial conditions. Figure 1.17 summarizes the process of using the shooting method for solving problem formulation of continuum robot as presented in [Black 18a, Till 19b, Black 17, Aloi 22]. To update the guesses, MATLAB's `fsolve()` function is often used, which is configured to implement several algorithms e.g. trust-region dogleg algorithm, Levenberg-Marquardt Method.

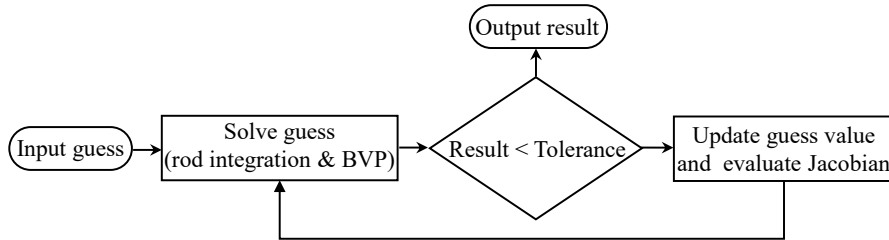


**Figure 1.17:** Flowchart for shooting method for numerical solver. The input variables are specified, and the unknown and output variables are guessed.

For example, considering the inverse kinematics problem of a PCR, which involves finding the unknown arc lengths  $\mathbf{L}_i$  that satisfy the known desired pose  $\mathbf{p}_e$  and  $\mathbf{R}_e$ . This problem is considered a boundary value problem due to the geometric and equilibrium constraints imposed on the system [Till 19b]. The boundary conditions are divided into distal boundary couplings, proximal boundary couplings, and optional intermediary boundary couplings. However, the end effector is subjected to static equilibrium conditions, which are enforced by summing forces and moments around the global origin. These conditions apply regardless of the specific joint type/coupling used to connect the flexible links to the end-effector platform. This is given as:

$$\begin{aligned} \sum_{i=1}^n [\mathbf{n}_i(L_i)] - \mathbf{F} &= 0 \\ \sum_{i=1}^n [\mathbf{p}_i(L_i) \times \mathbf{n}_i(L_i) + \mathbf{m}_i(L_i)] - \mathbf{p}_e \times \mathbf{F} - \mathbf{M} &= \mathbf{0} \end{aligned} \quad (1.9)$$

where  $\mathbf{F}$  and  $\mathbf{M}$  are external force and moment vectors, expressed in global coordinates and applied at the centroid of the end effector,  $\mathbf{p}_e$ . The remaining distal or proximal boundary conditions are based on the joint types which connect the rods to the actuators at one end and the rods to the mobile platform at the other end respectively, (see [Black 18a] for full detail on geometrical constraints and BCs formulation). The shooting method formulation in solving BVP involves a unique choice of guessed variables and residual equations. The guess vector  $\mathbf{G}$ , considering the number of parallel links  $i$  is given as:

$$\mathbf{G} = [\mathbf{n}_i^T(0), \mathbf{m}_i^T(0), L_i]^T \quad (1.10)$$

The objective function error  $\mathbf{E}$  is expressed as:

$$\mathbf{E}(\mathbf{G}) = [(\mathbf{E}_i^p)^T, (\mathbf{E}_i^R)^T, (\mathbf{E}^F)^T, (\mathbf{E}^M)^T]^T \quad (1.11)$$

These are evaluated via the shooting method following the algorithm in Figure 1.17. This is the most used method for the PCR and in fact, this is the approach we adopted for that of the miniaturized PCR made of glass in Chapter 4 due to its computational efficiency, accuracy, and simplicity. Nevertheless, there are other approaches for continuum robot modeling and control which are not within the classical kinematic and mechanics framework approach. This involves the use of a proxy or surrogate model approach as discussed in detail below.

#### 1.4.4 Proxy models

In contrast to the previously discussed models, an alternative approach to modeling a continuum robot involves using extensive datasets. These approaches are commonly known as proxy or surrogate approaches and [Kim 21, Wang 21] provide a survey on some of them. While one advantage of these solutions is their independence from a physical model, they heavily depend on collecting substantial amounts of representative data, which can be challenging. Though, this approach presents a computationally fast estimation of the kinematics without requiring the knowledge and the uncertainties in the physics-based model [Grassmann 18, Xu 16b, Pourafzal 21]. The majority of this approach for continuum robot modeling primarily employs the neural network method and data-driven approach.

In various application domains including robotics, neural networks (NN) or data-driven approach have demonstrated their efficacy in interpolating nonlinear functions. Drawing inspiration from biological neural networks found in animal brains, NN consists of artificial neurons functioning as elementary units. These artificial neurons transmit signals to other neurons, forming a high-dimensional set of nested functions that constitute each layer. The approach has extreme flexibility, a simplified structure, and the capability of mapping nonlinearity within complex datasets [Makwana 21, Shahabi 19]. However, it will require retraining if a new sample is introduced and their answers are often approximated. After

training, the neural network learns from the model, which allows the use of a model-free/data-driven approach to achieve efficient control [Zhang 22b].

It has been used for PCR as demonstrated in [Wu 17a, Shahabi 19, Singh 17]. For the CTR aspect, it has been used extensively in the literature such as in [Kuntz 20, Grassmann 18, Grassmann 22, Liang 21, Iyengar 21, Abdel-Nasser 21, Xu 16b, Iyengar 20, Donat 23, Thamo 23, Donat 23, Wang 18, Sefati 19]. Moreover, in [Thamo 21], they proposed an algorithm that combines both model-based and data-driven algorithms to provide real-time motion control of CTRs interacting with an unknown external environment.

## 1.5 CONCLUSION

### 1.5.1 For CTR

The design and fabrication of CTR tubes over the years have depended on Nitinol. A patterned engraved steel mold is used to constrain the tube in the desired shape, which may not permit patient-specific, fast, and on-site fabrication. Although the spring back effect was not characterized in the literature. The advances made in 3D additive manufacturing paved the way for the use of polymers and plastics in CTR tube prototyping. For medical applications, the possibility for an on-site and direct fabrication approach constitutes a major advantage in patient-specific and procedure-specific scenarios when compared to Nitinol [Amanov 15, Morimoto 16c]. However, the tube properties depend highly on the 3D printing technology and its setting (e.g., the resolution, obtainable surface smoothness, thickness, and available materials) [Amanov 15]. The continuum robotics community is highly dependent on the use of Nitinol due to its more desirable mechanical properties (e.g., obtainable strain, miniaturization, and surface smoothness), which partially explains why it is the predominantly used material for the fabrication of the pre-curved CTR tube. Consequently, there are challenges posed by the fabrication of miniaturized, high curvature, and on-site fast customizable complex 3D CTR tube shapes. For that reason, it seems researchers have reached a stagnating point for constant use of Nitinol for CTR design. In that regard, we are proposing a novel approach with the use of a thin heat shrink on glass capillary to obtain pre-curved tubes which permit to obtain CTR made of glass material. In this regard, we propose a new generation of CTR made of glass, introduce novel fabrication approach with the benefit of miniaturization to an unprecedented scale, rapid, inexpensive, easy patient customization, and possible on-site fabrication. These and many many more are discussed in detail in Chapter 2—“Fabrication of pre-curved glass tubes at small scale” and Chapter 3—“CTR made of glass”.

### 1.5.2 For PCR

Considering the fact, that PCR is a multi-backbone continuum robot with huge benefits because of its parallel mechanism or configuration, however, they are not as pronounced in the literature as CTRs. Moreover, its proposed applications in the literature are very few when compared to that of CTRs, which are vast and currently at the stage of a clinical trial by Virtuoso Surgical, that will soon advance for possible commercialization and public usage [Mitros 21, surgical 22]. Whereas for PCR, the story is not the same, and moreover, based on our knowledge, there is no single PCR survey/review paper published yet, unlike the CTR which has a number of literature survey/review papers e.g. [Gilbert 16b, Mahoney 16a, Alfallahi 20, Mitros 21, Nwafor 23b], each focusing on a specific aspect of the CTR state-of-the-art. For PCR also, the vast majority of its prototypes use beams and rods of metal or its alloy with Nitinol being the predominant used material, due to their flexibility and availability. However, we propose the use of optical glass fibers, which have the benefits of high elasticity, small diameter, and the possibility of using them to transmit energy to an active end effector. In addition, one of the key challenges for the PCR community is as regards the overall robot miniaturization. To that effect, the proposed design has a small footprint and in fact, it is currently the smallest PCR which opens the opportunity for possible endoscopic integration for medical applications or for micromanipulation needing a large workspace while benefiting from both conventional parallel and continuum robot mechanics. For more detail see Chapter 4—“Miniaturized PCR made of glass”.

### 1.5.3 For modeling

In summary, shooting method using Cosserat rod approach is the most commonly used approach for continuum robot modeling, since it benefits from the use of variable curvature kinematics and provides a more intuitive framework approach. This is the approach we adopted for the modeling of the proposed miniaturized PCR made of glass in Chapter 4. In fact, from the literature, this has been used in [Mauzé 20, Till 19b, Black 17, Aloi 22, Till 17a, Orekhov 16a, Black 18a, Till 17b, Till 19a, Aloi 18b, Orekhov 15, Bryson 14, Till 15, Mauzé 21b, Black 18b, Wu 19, Janabi-Sharifi 21a, Wu 17a, Altuzarra 19b, Altuzarra 19a]. This approach has been pushed further to dynamic modeling and analysis for PCR as presented by Till et al. in [Till 19a, Janabi-Sharifi 21b]. However, modeling the dynamics of PCRs is challenging due to the complex interactions between the flexible continuum structures, actuators, and the environment, in addition to the high computational requirement.

Though, the FEM approach captures the entire geometry of the robot shape and treats the shapes in volumetric segmentations making it possible to address non-slender shapes, and soft material and not limited by one-dimensional representation but the drawbacks are the kinematic formulation challenge and high computational expenses. However, the variable curvature is the most used approach because it provides a much better slender rod representation with high accuracy

but with no analytical solution as it requires numerical integration, which is a bit computationally tasking. Alternatively, a geometrical model approach using the piece-wise constant curvature provides an efficient kinematic computation and analytical approach to describing a continuum link but it lacks better accuracy due to the parameter lump for the constant curvature assumption. Though, some researcher in the literature has also used the discrete model approach, which was used for PCR kinematic modeling in [Briot 22a, Chen 19, Chen 21a]. The issue with this last approach is its poor accuracy as it tends to approximate continuum links as discrete finite rigid links connected by joints and its accuracy depends on the number of discretizations evaluated. Finally, the choice of kinematic modeling depends on the computational time, resources, and desired accuracy for the continuum link representation. Finally, in [Nwafor 23b], we presented an overview of the synthesis approach proposed in the literature for CTRs, classified by objective (Table A.1), which is in Appendix A.



---

# Chapter 2

## Fabrication of pre-curved glass tubes

---

<b>2.1</b>	<b>Glass fabrication method at small scale . . . . .</b>	58
2.1.1	Additive method . . . . .	58
2.1.2	Subtractive method . . . . .	60
2.1.3	Shaping method . . . . .	62
<b>2.2</b>	<b>3D Microfabrication using Femtosecond laser-assisted wet etching (FLWE) . . . . .</b>	63
2.2.1	Fabrication of standing microglass beams by FLWE . . . . .	64
2.2.2	Experiment plan for microscale glass tube fabrication by FLWE . . . . .	65
2.2.3	Experimental results and discussion . . . . .	67
<b>2.3</b>	<b>Fabrication of pre-curved glass tubes using heat treatment approach . . . . .</b>	69
2.3.1	Heat treatment approach . . . . .	69
2.3.2	Tube shape setting by heat treatment . . . . .	70
2.3.3	Experimental result . . . . .	72
<b>2.4</b>	<b>Tube shape setting using polymer heat-shrink jacket . . . . .</b>	73
2.4.1	Materials and methods . . . . .	73
2.4.2	Characterization and validation . . . . .	74
2.4.3	Bending stiffness analysis of microglass tubes . . . . .	76
<b>2.5</b>	<b>Conclusion . . . . .</b>	78

## 2.1 GLASS FABRICATION METHOD AT SMALL SCALE

For microscale, glass benefits from a high strength-to-weight ratio, flexibility, and low coefficient of thermal expansion [Yuan 20, Hahn 72, McCann 15]. Generally, it has many other desirable properties, such as transparency, biocompatibility, high tensile strength, low friction, and durability. These can be beneficial for medical applications such as endoscopy and microsurgery, but their brittleness and fragility may render them unsuitable for most applications in clinical intervention. Moreover, the handling and processing of glass require specialized equipment and expertise, adding to the complexity and cost of the fabrication process. In general, glass is a mixture of oxides whose properties depend on its concentration and composition which give rise to a different variety. Whereas fused silica is a form of pure glass ( $\text{SiO}_2$ ), and using conventional machining at room temperature, it was observed that fused silica is difficult to machine, mainly due to high brittleness, low fracture toughness, high strength, and poor plastic deformation [Song 18]. Therefore, the challenge lies in designing and constructing a robot using glass that can perform specific medical functions while ensuring its safety and reliability. For example, a robot designed for minimally invasive surgery must be highly precise and dexterous, with minimal risk of breakage or fracture during operation. In fact, the robot must be able to withstand the stresses and strains associated with the harsh medical environment, including exposure to body fluids, and chemicals. While the benefits of such technology are undeniable, the potential risks and unintended consequences must also be carefully evaluated. Thus, the problem statement can be spread to different aspects, which include how to design, fabricate, and operate a robot made of glass that is safe, functional, and cost-effective. Researchers have proposed various approaches and solutions to overcome the challenges associated with using thin glass with high mechanical strength. The design and fabrication of structures or devices using glass can be classified into three, which are: 1) the additive method, 2) the subtractive method, and 3) the shaping method. Each approach will be detailed in the following

### 2.1.1 Additive method

Additive manufacturing (AM) presents a valuable solution in this context, as it enables the production of intricate shapes without the need for preexisting molds, offering a cost-effective approach when customization holds significance [Atzeni 10, Atzeni 12]. The AM of glass has received limited research attention due to the difficulties in glass processing. Such as the high melting temperature of glass which necessitates high energy-intensive manufacturing methods, resulting in substantial temperature gradients within the built parts. These temperature variations induce residual stresses, which increase the risk of thermal cracking. Furthermore, the high transparency of glass in the visible and near-infrared range hinders the processing of glass using lasers operating in this spectral region. Additionally, the presence of microcracks or porosity in the fabricated

glass structures compromises their optical quality and leads to the formation of opaque surfaces. As a result, the combination of these challenges has impeded the progress and exploration of AM techniques for glass manufacturing. The current leading additive manufacturing (AM) techniques for glass involve using a composite mixture containing silica particles to fabricate a preliminary structure referred to as the "green" part [Datsiou 19]. This green part undergoes thermal post-processing to eliminate non-glass constituents, resulting in the formation of transparent and amorphous glass components. Successful applications of these methods have been observed in stereolithography [Kotz-Helmer 17a] and direct ink-writing [Nguyen 17] processes. However, it is important to consider that post-processing introduces a challenge in the form of volumetric shrinkage, which causes discrepancies between the intended design dimensions and the actual dimensions achieved in the final product.

There are two main categories for 3D printing of transparent glasses: direct printing methods and indirect printing methods. In direct printing approaches, glasses are printed in a molten state. One method that has been demonstrated is the Fused Deposition Modeling (FDM) of glasses. This technique involves extruding molten glass at high temperatures through a specialized high-temperature printer [Klein 15c]. The molten glass is deposited as strands onto a movable print platform, enabling the 3D printing of large glass components. However, this process is currently limited to low-melting soda-lime glasses. It also requires a printer capable of reaching temperatures up to 1165 °C and offers limited resolution, typically with strand diameters in the range of 4.5 mm [Klein 15c]. The high melting temperature of fused silica glass has prevented its use in FDM so far, with nozzle sizes <0.4 mm and layer heights of 100-300 µm. While the Fused Feedstock Deposition (FFD) approach is for large-scale applications. As an alternative approach, laser-based methods have been used to shape fused silica glass. In this technique, fibers of the glass are locally melted using a laser to achieve the desired shape. However, this method has limitations in terms of accuracy and resolution [Luo 18a].

Generally, each AM processing of pure glass yields varying degrees of success (see Table 2.1). In fact, one approach involved depositing molten glass through a motor-controlled nozzle, resulting in transparent and visually appealing parts primarily suitable for decorative purposes [Klein 15b, Klein 15a]. However, the use of thicker layers in this method presents resolution limitations, restricting its applicability in other functional applications. Filament-based approaches have been utilized to produce walls of different types of glass, including soda lime silica, borosilicate glass, and fused quartz [Luo 16b, Luo 17, Luo 16a, von Witzendorff 18]. Nevertheless, the manual feeding of the filament under the laser beam imposed constraints on the process, limiting the fabrication to basic shapes with limited design flexibility. Powder bed fusion techniques have also been explored for glass materials such as borosilicate [Klocke 04], quartz [Khmyrov 16, Khmyrov 14], and soda lime silica [Fateri 14b, Fateri 14a] glass. However, most of the investigations have

focused on the formation of single-layer scan tracks or basic multilayer structures, rather than complex three-dimensional geometries. In fact, complex multilayer glass structures have been investigated using a laser powder bed fusion approach for soda lime silica glass [Datsiou 19]. Even also the use of a stereolithography 3D printer involving photocurable silica nanocomposite, which converts it to a high-quality fused silica glass via heat treatment [Kotz Helmer 17b] and also by using Nanoscribe [Kotz 18a].

Overall, while research has been conducted on various AM methods, significant challenges remain in achieving high-resolution and complex structures with satisfactory design freedom. This is a great hindrance to achieving structures with high resolution on a microscale making subtractive manufacturing a better option.

**Table 2.1:** Different glass 3D printing techniques/technology

3D printing method	Final glass compositions	Resolution	References
Composite*	DIW $\text{SiO}_2$	250 $\mu\text{m}$	[Nguyen 17]
	DIW $\text{SiO}_2-\text{GeO}_2$	—	[Sasan 20]
	DIW $\text{SiO}_2-\text{TiO}_2$	—	[Destino 18, Dylla-Spears 20]
	SLA $\text{SiO}_2$	10 $\mu\text{m}$	[Kotz 17, Liu 18b, Liu 18a, Cooperstein 18]
	SLA $\text{SiO}_2-\text{B}_2\text{O}_3-\text{P}_2\text{O}_5$	100 $\mu\text{m}$	[Moore 20]
	FDM $\text{SiO}_2$	250 $\mu\text{m}$	[Mader 21a]
	2PP $\text{SiO}_2$	200 $\mu\text{m}$	[Wen 21, Kotz 21]
	micro-C $\text{SiO}_2$	20 $\mu\text{m}$	[Toombs 22b]
Direct	FDM chalcogenide glasses	—	[Baudet 19]
	FDM Phosphate/sodalime glass	100 $\mu\text{m}$	[Zaki 20, Klein 15c]
	SLS/SLM silica/sodalime glass	0.5mm	[Luo 18b, Luo 14]

**Composite\***: the 3D printing is used to pre-shape a polymer composite to form green parts, which are then sintered to form the final glass items, **Direct**: using 3D printer for everything.

**DIW**: direct ink writing, **FDM**: fused deposition modeling **SLA**: stereolithography **2PP**: two-photon polymerization **micro-C**: microscale computed axial lithography **SLS/SLM**: selective laser melting/sintering.

## 2.1.2 Subtractive method

Subtractive fabrication is a type of manufacturing process where a material is removed from a solid block substrate to create a desired shape. This method involves cutting, drilling, milling, or etching the material away from the sample block until the desired form is achieved. Some examples of subtractive fabrication techniques include ultrasonic machining [Lv 13, Fernando 17, Choi 07], laser ablation [Zhang 98, Xiong 12, Campbell 05, Ashkenasi 12, Řiháková 15, Queste 10], and subtractive etching [Lima 15, Takahashi 05, Fascio 99, Yang 01, Hof 17]. While subtractive manufacturing may be more wasteful than additive manufacturing, it can be used to create high-quality devices on a microscale. In fact, the micro-machining process is often referred to as **subtractive process** including MEMS fabrication [Prakash 17]. Subtractive fabrication is commonly used in microfluidic applications, which always involves using glass material due to its transparency

and biocompatibility. Glass is particularly useful in subtractive etchings to fabricate empty cavities, such as reservoirs and chambers [Lima 15].

The use of thin glass as a material for flexible continuum robots in biomedical applications and micromanipulation presents several challenges and opportunities that require careful consideration and evaluation. One of the primary challenges in using thin glass for flexible continuum robots is the fabrication process. Moreover, shaping and forming a thin glass sample into the desired structure by subtractive manufacturing can be complex and time-consuming. When considering the limitations surrounding the field of glass micromachining, such as the use of thermal processing which involves the use of laser technology, it is fast and flexible but lacks high surface quality. Whereas, the use of chemical processes which involves wet etching, gives smooth surfaces but masks are needed to make the process, moreover, it is complex. Finally, mechanical processing which includes drilling, milling, or jet sputtering often has rough surfaces and is slow. Most of these individual processing challenges can be overcome using various improvement strategies by the hybrid technique such as the femtosecond laser (thermal machining) and wet etching (chemical machining). This emerging 3D subtractive micromachining which combines the use of femtosecond laser exposure and chemical etching (mostly with hydrogen fluoride (HF) or potassium hydroxide (KOH)), makes it possible for a flexible fabrication of all-in-one 3D multifunctional device on a single glass substrate for various applications ranging from fluidic, optics and mechanical system (see Figure 4). The procedure involves at least two basic steps, first is the use of ultrashort laser pulses to modify the material properties of an exposed region, and then secondly, selective etching of the exposed modified region using either HF or KOH, finally other functionality can be integrated into it depending on the targeted application. In fact, any defects that may arise through the intense femtosecond laser beam are completely removed by slight over-etching [He 10]. This is in contrast to other subtractive manufacturing methods such as for example reactive ion etching (RIE) or focused ion beam (FIB) milling, where ion implementation can cause significant structural alterations [Mačković 17]. Moreover, the femtosecond gives the possibility of noncontact [Magee 06, Römer 15] and maskless 3D micromachining on optically transparent material with nanometer resolution and monolithic structure capability.

The various cleanroom room subtractive fabrication on a glass are often limited to 2D design but the femtosecond assisted by wet etching (FLWE) permits direct 3D fabrication on one substrate. This is key for the possible fabrication of pre-curved tubes in a glass as the technology is highly beneficial in applications where all the parts are fabricated inside a single glass, eliminating all the possible errors associated with product assembling i.e positioning tool error, individual parts fabrication tolerance, and the attachment method like soldering or gluing [Nazir 19]. With FLWE, a single substrate can be used to create any desired shape anywhere inside it and this was used to demonstrate the first direct 3D microfabrication in fused silica in 2001 [Andrius 01]. Recently, there are lots of investigations on

the use of FLWE for microstructuring in fused silica as a prospective micromachining approach to obtaining high performance whose applications include active and passive waveguide [Davis 96, Physics 03, Osellame 03], diffractive optical devices [Watanabe 02], flexures [Tielen 14], couplers [Minoshima 01, Streltsov 01], actuators [Lenssen 12b, Bellouard 05, Mishuk 19], sensors [Meng 15], polarizing optics [Beresna 11], optical circuit [Cheng 03b], microcoil [Shan 15], in fact see Figure 4. Finally, we applied this method for the possible fabrication of a pre-curved glass tube (detailed in Section 2.2), which is targeted toward miniaturized glass continuum robot prototyping.

### 2.1.3 Shaping method

Shaping glass involves transforming it from its initial form into a desired shape or design. There are various methods used for shaping glass, depending on the desired outcome and the properties of the glass being worked on. Some common techniques include glassblowing, kiln-forming, and molding/pressing. Conventional glass shaping methods involve harsh conditions like high temperature or annealing, although, some which involve the use of sol-gel chemistry, offer a milder approach, but its molding technique limits geometric complexity [Xu 21]. Another strategy involves using silica-polymer composites as glass precursors, allowing low-temperature molding [Kotz 18b]. Alternatively, precursor composites can be 3D printed, providing an attractive method for complex glass shapes. However, 3D glass printing faces issues such as printing speed, resolution, and surface roughness due to its layer-by-layer nature [Xu 21]. Support structures are often necessary for printing complex geometries, adding difficulty during their removal. Localized laser processing enables glass shaping but is limited to simple geometric manipulation like bending [Wu 10].

Generally, other shaping methods include the use of pyrolysis and sintering to produce transparent origami glass in three dimensions, which involves several steps as presented in [Xu 21]. Initially, a liquid precursor containing silica nanoparticles is cured to form a polymer composite sheet. This sheet is then cut into the desired shape and folded using an origami technique, similar to folding paper origami, but at room temperature. Subsequently, the folded composite sheet undergoes pyrolysis and sintering processes to eliminate the polymer binder and transform the object into glass. Despite its apparent simplicity, two essential conditions must be satisfied for this process to work. Firstly, the origami-shaped sheet must retain its form during the high-temperature pyrolysis stage. This poses a challenge because polymers typically possess entropic elasticity, meaning they tend to return to their original shape when heated beyond their thermal transition, such as the glass or melting point. Secondly, the composite material must be foldable like a regular sheet of paper, requiring suitable mechanical properties such as modulus and stretchability.

## 2.2. 3D Microfabrication using Femtosecond laser-assisted wet etching (FLWE)

Another approach of glass shaping is the use of sacrificial polymer wires. To shape complex geometries with inorganic glass powders, organic binders are often used for easier molding [Liu 22]. In this process, sacrificial polymer wires of pre-determined sizes and shapes are inserted into a nanocomposite material consisting of silica nanoparticles and a polymer binder. Heating the material in the presence of air removes the organic components, creating channels within a porous silica framework. Through densification, a solid silica structure is formed, containing embedded conductive hollow channels. The width of these channels can be smaller than  $100\mu m$ , depending on the initial diameter of the polymer wires. This capability to create microscale channel structures with specific designs in single-piece silica glass could have immediate applications in the field of microfluidics.

Finally, Mader et al. [Mader 21b] utilized injection molding as a preliminary shaping process for creating silica glass. They prepared granules of a nanocomposite material by combining polyethylene glycol (PEG), polyvinyl butyral (PVB), and  $\text{SiO}_2$  nanoparticles using a twin-screw extruder. To ensure successful injection molding, it was crucial to carefully control the viscosity of the material, keeping it below 1000 Pa.s at a shear rate of approximately  $10^3 s^{-1}$ . The authors opted for injection molding at a temperature of approximately  $130^\circ\text{C}$  and a pressure ranging from 700 to 1000 bar, utilizing a piece of commercial molding equipment and a two-step molding process along with a sintering process to achieve densification. Using this approach, they successfully produced various pure silica glass parts, including tubes, beakers, and microfluidic channels. The production rate achieved was up to 5 seconds per part. All these approaches are complex with a poor resolution to guarantee flexible miniature pre-curved tubes at a small scale.

Therefore, in our investigation, the first approach was subtractive manufacturing, which involves femtosecond laser-assisted wet etching. Next, we evaluated the shaping of thin glass capillaries by annealing in a furnace using steel mold. For the third method, we developed a novel approach that involves hybrid material composition, where a glass capillary is combined with other material(s) for shape setting. The use of a hybrid material/coating like the case of optical fiber, provides additional rigidity and mechanical strength. The two glass shaping approaches to achieving a pre-curved glass tube in fabricating miniaturized continuum robots are detailed in Sections 2.3.2 and 2.4 below.

## **2.2 3D MICROFABRICATION USING FEMTOSECOND LASER-ASSISTED WET ETCHING (FLWE)**

The fabrication of glass tubes using FLWE is a promising technique that offers several advantages in terms of precision and accuracy. FLWE is a subtractive manufacturing that uses ultrashort laser pulses e.g. picosecond or femtosecond laser, to create three-dimensional structures with submicron resolution, which is

followed by wet etching in a chemical solution. This technique can be used to fabricate complex geometries, including microchannels, microfluidic devices, and MEMS, in a glass.

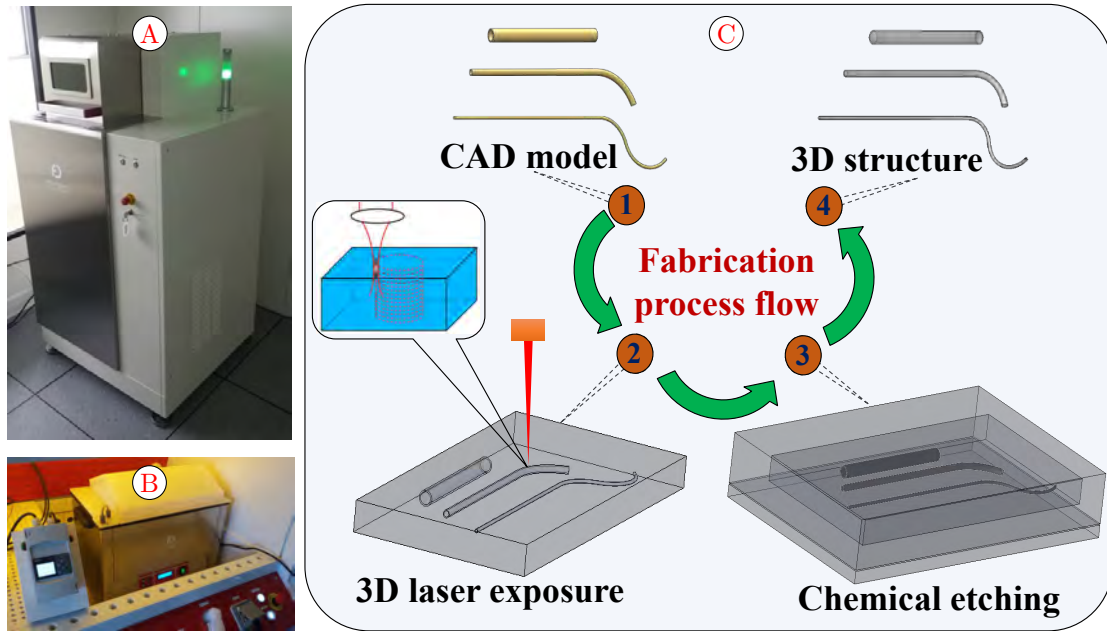


**Figure 2.1:** FLWE fabrication process. **A)** FEMTOprint machine, **B)** automatic ultrasonic wet etching station **C)** FLWE step-by-step fabrication process: **1)** the design of the laser-machining process utilizing specialized software, such as ALPHACAM, **2)** the direct laser writing of the pattern onto the substrate with a zoomed part showing the trenching/grooving pattern of the laser exposure within the substrate, **3)** the release of the desired structure through wet etching in a KOH or HF etchant, **4)** the 3D shape structure

### 2.2.1 Fabrication of standing microglass beams by FLWE

We used FLWE, which is a cutting-edge technique and a mask-free subtractive method for the precise fabrication of complex three-dimensional microstructures. This process combines the advantages of femtosecond laser technology and wet chemical etching to create high-precision structures with accuracy and control. A femtosecond laser is a powerful tool in microfabrication, as it emits pulses of light lasting only femtoseconds ( $10^{-15}$  seconds), providing the ability to precisely manipulate the material property with a high spatial resolution in the micrometer range. These ultrashort laser pulses can generate high-intensity energy that leads to a nonlinear interaction with the material while changing its refractive index without heating or damaging the surrounding areas. The FLWE process begins with the femtosecond laser exposure by scanning the material sample in a specific pattern and creating line grooves/trenches (see Figure 2.1). These grooves or trenches serve as the penetration path for the wet etching process, which provides the conditions for the etchant to penetrate the material and allows for a controlled, high-precision etching process. The etchant solution used in FLWE can

vary depending on the material being etched. Hydrofluoric acid (HF) and potassium hydroxide base (KOH) are the common etchant solution used in micro- and nano-fabrication processes, which typically reacts with the laser exposed region of the material, dissolving it and leaving behind the 3D desired microstructure. The use of a femtosecond laser allows for the creation of highly precise and complex 3D structures with feature sizes down to the nanoscale. This technique provides an attractive alternative to traditional manufacturing methods, as it enables the creation of complex geometries with high precision, low cost, mass production, and a high degree of reproducibility. Generally, the FLWE fabrication process comprises three primary stages, namely: 1) the design of the laser-machining process utilizing specialized software, such as ALPHACAM, 2) the direct laser writing of the pattern onto the substrate, and 3) the release of the desired structure through wet etching in a KOH or HF etchant. See Figure 2.1 for the detailed pictorial illustration of the entire process.

### 2.2.2 Experiment plan for microscale glass tube fabrication by FLWE

The feasibility study we embarked upon before proceeding to obtain a pre-curved micro tube in glass was the fabrication and characterization of a standing beam using the FLWE approach. The theoretical framework for the characterization analysis is given as follows:

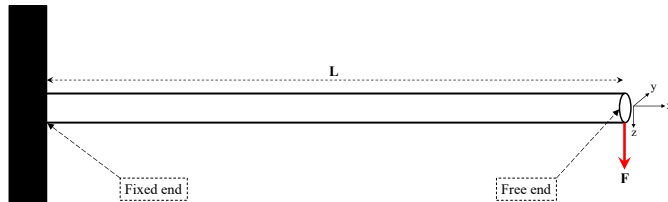


**Figure 2.2:** Circular cantilever tube fixed at one end

From Figure 2.2, using Euler-Bernoulli beam theory, the microglass tube bending stiffness can be derived as:

$$\begin{aligned}
 F &= \frac{d^2}{dx^2} \left( EI \frac{d^2 w}{dx^2} \right) \\
 w(x) &= \frac{Fx^2(3L - x)}{6EI} \quad \xrightarrow{x=L} \quad w(L) = \frac{FL^3}{3IE} \\
 K &= \frac{F}{w(L)} = \frac{3EI}{L^3}, \quad \text{where } I = \frac{\pi(R^4 - r^4)}{4}
 \end{aligned} \tag{2.1}$$

Bending stiffness sensitivity is a concept that plays a crucial role in the design and engineering of various structures. It refers to the change in the bending behavior of a structure in response to changes in its stiffness, which is a function of

the structural components or variables. This phenomenon is particularly relevant for structures that undergo dynamic or cyclic loading conditions. It can be calculated using analytical or numerical methods. The analytical method involves the rate of change of stiffness with respect to the design parameters of the structure. Therefore its role is very essential in investigating the effects of the mechanical design parameters on the overall stiffness of the structure. The non-normalized stiffness sensitivity for a circular beam of Figure 2.2 is given as:

$$\nabla K = \begin{bmatrix} \frac{\partial K}{\partial d} \\ \frac{\partial K}{\partial D} \\ \frac{\partial K}{\partial L} \end{bmatrix} = \begin{bmatrix} -\frac{3\pi d^3 E}{16L^3} \\ \frac{3\pi D^3 E}{16L^3} \\ -\frac{9\pi E(D^4 - d^4)}{16L^4} \end{bmatrix} \quad (2.2)$$

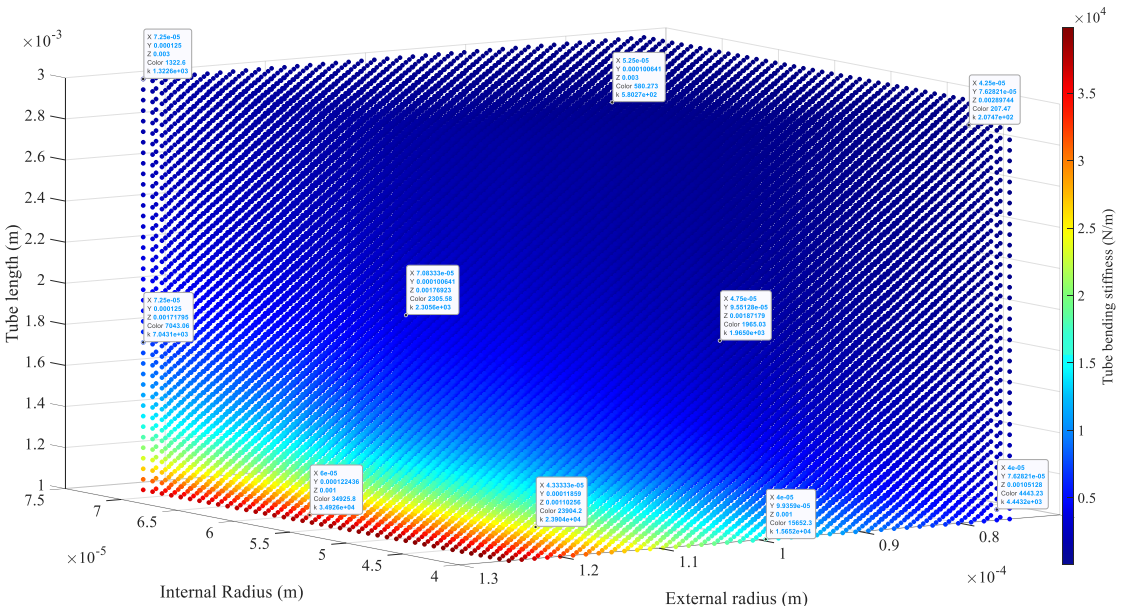


**Figure 2.3:** Sensitivity analysis plot of a microbeam structure, which helps one to easily visualize the combination of internal diameter, external diameter, and tube length for a given/required stiffness value or range.

Figure 2.3, presents the variation of stiffness with respect to the beam geometrical parameters. The plot could be used to identify the possible combination of internal diameter, external diameter, and tube length that is required for a range of stiffness when considering a particular design task or application. It is also used to investigate Equ. 2.2, which helps to highlight the region with high sensitivity as shown by the stiffness colormap as a function of variation of the geometrical parameters under consideration  $K(D, d, L)$ .

Figure 2.4 below, presents the table for the different tube specifications to be fabricated by the FLWE and their expected bending stiffness for the characterization of each sample. For each case of the tube specification, the expected bending stiffness is computed in order to analyze the effect of glass stress at the microscale.

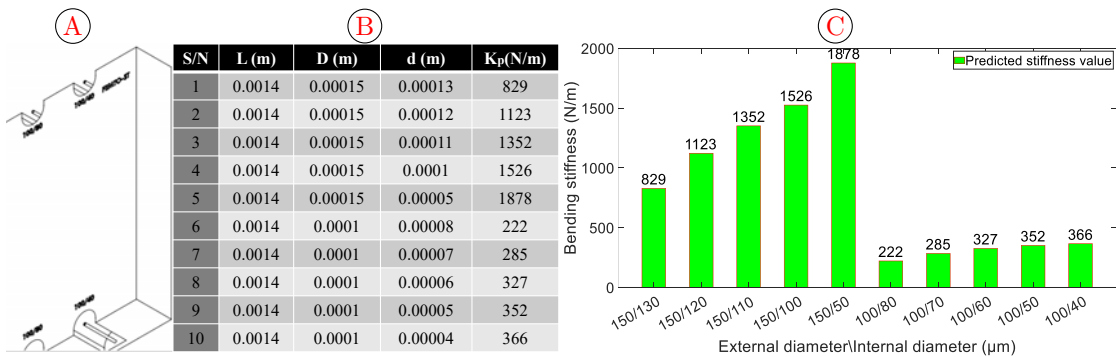


**Figure 2.4:** Analysis of the expected results of the microglass fabricated by FLWE, **A)** The CAD drawing of the different standing tubes with the inscribed specifications on a 1.7mm thick glass sample. **B)** and **C)** the different tube dimensions/specifications to be fabricated by the FLWE with their corresponding expected stiffness value using Equ 2.1

### 2.2.3 Experimental results and discussion

The experimental results for the microglass beam fabricated by FLWE are shown in Figure 2.5. The outcome of the result is presented in the table of Figure 2.5C in which: i)  $L$  is the rod length from the base to the position where the hook is placed during the characterization ii)  $D$  is the rod external diameter shown by the red circles as captured under the microscope iii)  $K_t$  is the theoretical bending stiffness computed for each rod considering only external diameter iv)  $K_e$  is the experimental result gotten from the slope of each plotting v)  $E_e$  is the computed Young modulus for each rod sample which gave a mean of 72.8 GPa. Unfortunately, due to logistics related to the fabrication process, time, and since it was the initial design, only 6 samples were fabricated (see Figure 2.5). The output result obtained was more of a rod instead of a tube because the chemical solution could not penetrate effectively through the tube's internal laser-exposed glass walls. Even after multiple etching processes that lasted for over 11 hours in an ultrasonic bath, where the sample was immersed inside the KOH solution. The external diameters of each sample were evaluated using a specialized microscope in the cleanroom. The majority of deviations are  $< 5\mu\text{m}$  as shown in Figure 2.5, which is very impressive. Though one could see the engraved pattern of the internal diameter which did not etch out, therefore in the analysis of the result, we treated each sample as a rod instead of a tube. The result of the characterization is presented in Figure 2.5, the mean value for the experimental Young modulus was obtained as 72.8GPa, whereas the standard value for fused silica is 70GPa. Overall, the result shows how the theoretical and experimental values for the bending stiffness are closely matched for each case and in addition, this shows that the Young modulus of fused silica remains fairly the same even on a microscale dimension.

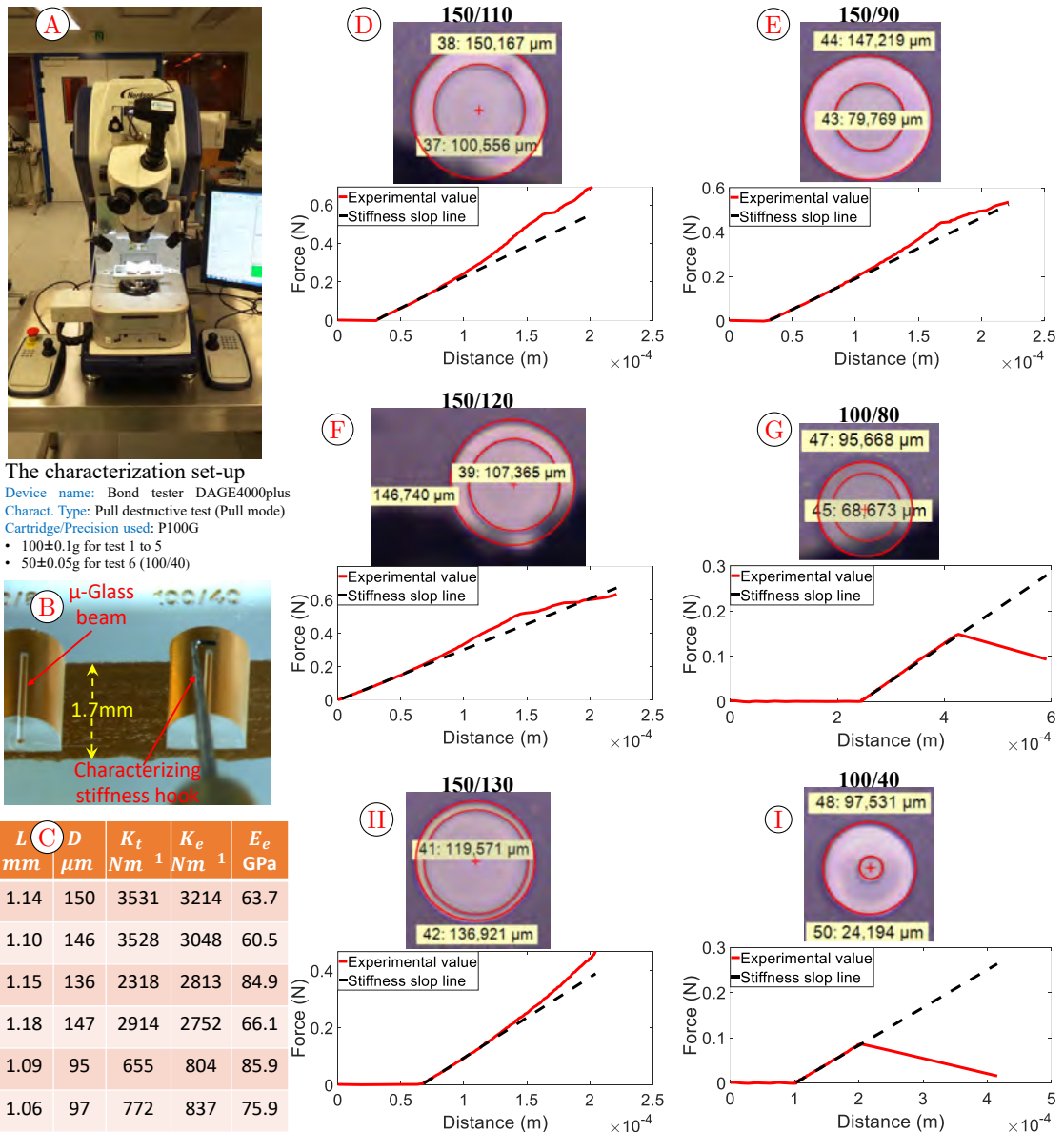


**Figure 2.5:** The experimental result for the microglass rods fabricated by FLWE which was characterized A) characterization set-up for measuring the bending stiffness of each rod B) sample during characterization C) table of the results, D) - I) show the results of the designed external/internal diameters versus the realized ones along with the measured bending stiffness for each one.

Although the fabrication process was optimized to obtain better results, however, despite the potential benefits of using the FLWE process, there were still several challenges. These include:

1. issues relating to defects in glass due to uncontrolled/uncalibrated high energy density of the laser beam
2. high precision requirement of laser beam's parameters such as pulse energy, repetition rate, and focus position to guarantee successful fabrication

3. time-consuming and expensive process e.g long hours of machine calibration, the laser exposure time per sample volume, and then etching which in some cases all night. In fact, all the fabrication process takes place in the cleanroom
4. extensive Alphacam design time and post-processing related to the difficulty of controlling the etching process, which generally requires some level of an expatriate or experience.

In general, irrespective of the drawbacks regarding the main challenge in using this technology, obtaining a pre-curved tube will be extremely difficult. We already saw that obtaining a standing tube was not easy, though the machine even broke down along the line. Notwithstanding, the major challenge is even how to extract the internal substrate from the curved cavity that will be exposed by laser. In fact, it is not guaranteed that adopting a patterned tube cut approach for the wet etchant penetration can be successful, because the etching time will not be uniform and smooth extraction of the internal substrate is not assured. This inevitable challenge is a major hindrance to the actualization of a microscale pre-curved tube in glass for CTR design using the FLWE. Alternatively, another option is the thermal treatment of a straight capillary glass tube to obtain a pre-curved/complex shape for the robot design, which is discussed in the following.

## 2.3 FABRICATION OF PRE-CURVED GLASS TUBES USING HEAT TREATMENT APPROACH

### 2.3.1 Heat treatment approach

Heat treatment of glass tubes is a process by which the glass is transformed from its original straight shape into a predetermined curved shape under a high temperature. This process is typically accomplished through a combination of heating and cooling, which allows the glass to be manipulated into the desired form. The process begins with a straight glass tube that is heated to a temperature above its glass transition temperature, typically around 600-700°C [Proctor 67] or even more depending on the type/nature of the glass. The tube is then allowed to cool, during which time the glass undergoes a phase transition and becomes rigid in the new shape. This approach of heat setting is the most used for the precurving of Nitinol used for the continuum robot design as presented in [Shrivastava 04, Gilbert 16c, Sun 18, Nwafor 23b]. The ability to precisely control the shape of a glass tube allows for the creation of complex and customized components with specific functionality. For glass shape setting, this process involves heating the straight capillary tube to a specific temperature range, allowing it to undergo a gradual transition in its molecular structure, and cooling it back to room temperature while holding it in a curved desired shape using constrained

fixtures or engrave mold. The thermal treatment process is typically carried out in a high-temperature furnace, where the tube is exposed to controlled heating and cooling cycles. The furnace control setting is carefully selected to induce the desired molecular transformation and shape the tube into the desired pre-curved form. For the investigation analysis, the sub-millimeter tubes consist of fused silica, which is coated with a thin standard polyimide to prevent direct glass surface exposure and provide mechanical rigidity ([Polymicro](#)).

### 2.3.2 Tube shape setting by heat treatment

Fused silica, also known as quartz glass, is a high-purity material that exhibits excellent optical, mechanical, and thermal properties. However, due to its high melting point and low thermal conductivity, it is challenging to manipulate and shape. For this analysis, the thermal treatment approach to obtain pre-curved microglass tubes involves the use of a furnace and patterned engraved steel mold. This process is achieved by subjecting a straight glass capillary tube to high temperatures in a furnace, which bends into a predetermined shape of the pattern mold shape. In the literature, different molds have been developed for this purpose, including graphite, stainless steel, and tungsten carbide. Graphite molds are commonly used for low-temperature heat treatments, as they have excellent thermal stability and low thermal expansion coefficients. However, they are unsuitable for high-temperature treatments due to their susceptibility to oxidation [[Kim 19b](#), [Kim 20a](#)]. Stainless steel molds are more resistant to oxidation and can be used for high-temperature treatments [[Okada 08](#), [Al-Mangour 15](#), [Bressan 08](#)]. They are also more durable than graphite molds and can be reused several times. However, stainless steel molds have a higher thermal expansion coefficient than graphite, which can lead to a higher degree of distortion in the fused silica preform. Tungsten carbide molds have superior thermal stability and mechanical strength compared to graphite and stainless steel molds. They can withstand high-temperature heat treatments without deformation or oxidation. However, tungsten carbide molds are expensive and may require specialized manufacturing processes [[Liang 09](#), [Fischbach 10](#), [Kim 12](#)]. In our case, we adopted the stainless steel mold. Research has shown that forging can be an effective method for improving the performance of steel molds used for the heat treatment of fused silica tubes [[Chang 08](#), [Kuang 11](#)].

During the heating process, the glass tube undergoes a softening transition due to the relaxation of internal stresses. The polyimide coating carbonizes and flakes off in the furnace at  $> 600^{\circ}\text{C}$  leaving behind only a glass tube ([Polyimide in oven](#)). For the test analysis, we used the Polymicro tubing with internal and external diameters of  $100\mu\text{m}$  and  $165\mu\text{m}$  respectively. The cooling rate of the glass tube after bending is also critical, as it determines the degree of residual stresses in the tube, which can affect its mechanical properties and performance. These were observed in Figure 2.6 as natural cooling in air produced the best result. The use

### 2.3. Fabrication of pre-curved glass tubes using heat treatment approach

of a steel mold in precurving microglass tubes offers several advantages. For example, steel molds can be precisely machined to obtain different 2D and 3D shapes with high accuracy and repeatability. Additionally, steel molds provide a uniform distribution of pressure during the bending process, resulting in a consistent and reproducible pre-curved shape.

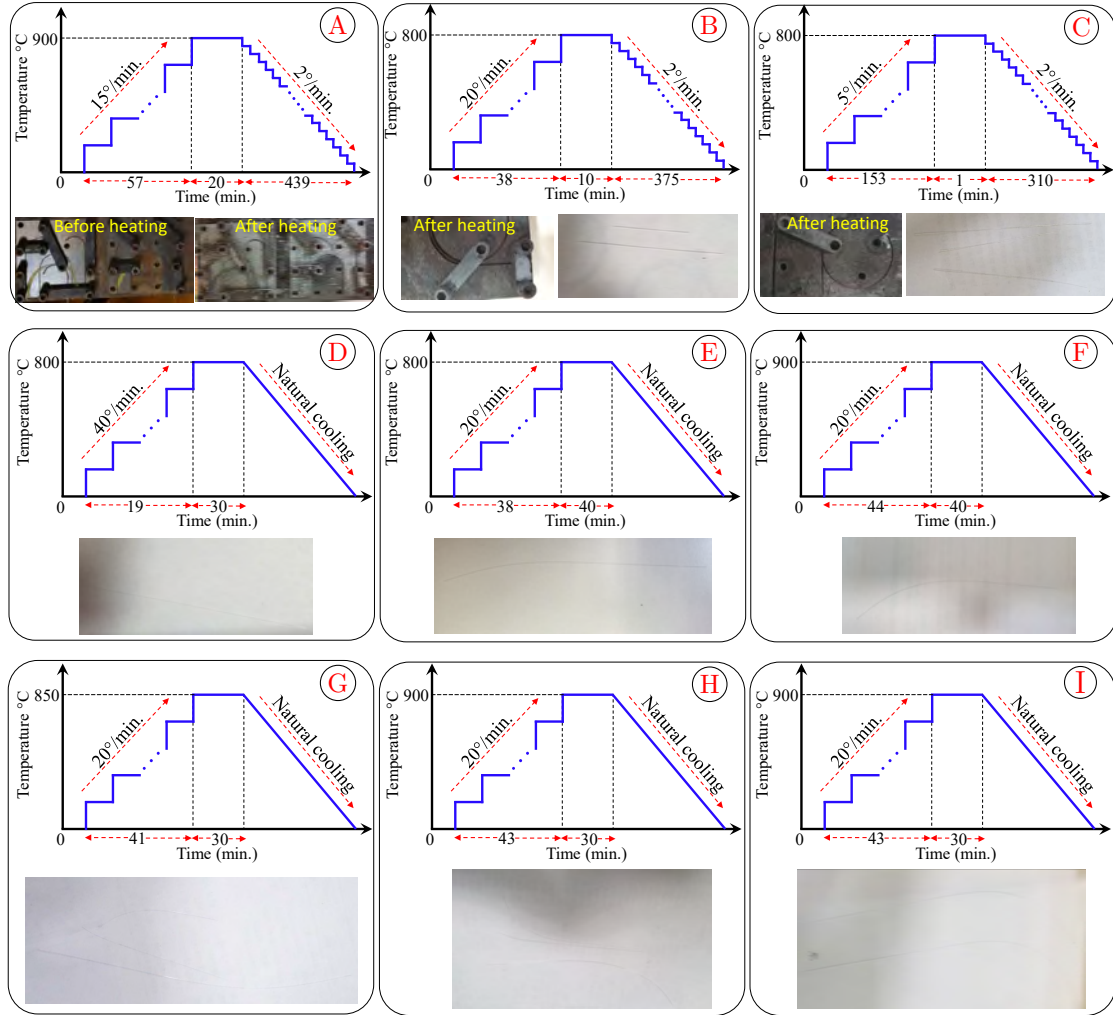


**Figure 2.6:** Pre-curved glass tube shaping by only thermal treatment approach, **(A)** plot of temperature and time duration for the heat treatment and the molds used, though the capillaries shattered in the furnace, **(B)** & **(C)** reduced temperature and time duration with different step ramp for both cases while using a solid steel mold. The outcome result shows straight glass capillaries without a pre-curved part, **(D)** & **(E)** maintained the same maximum temperature but with a longer duration of constant 800°C followed by natural cooling in the air. The result shows a high spring-back and no pre-curved shape, **(F)** only the maximum temperature was increased to 900°C and the result shows a lesser spring-back, **(G)** to observe the elastic property of the glass, the temperature was reduced to 850°C and lasted 30 minutes duration. The resultant output had little spring back but fragile for robot integration, **(H)** & **(I)** the maximum temperature was increased to 900°C under the same conditions as the previous for both cases. The result shows no spring back which was an interesting result but will be extremely difficult to be used for the robot design due to its fragility.

### 2.3.3 Experimental result

Finding the optimal shape-setting characteristic is very important in thermal treatment. The best shape setting temperature depends on the properties of the specific glass material being used. One approach to determine this setting is to perform a series of tests at varying temperatures and observe the resulting shape and mechanical properties of the microglass tube. Although, impurities in the glass can also affect the optimal shape setting temperature. Therefore, one needs to investigate and carefully set experimental procedures to determine the optimal temperature for pre-curving microglass tubes. For this reason, we carried out many experimental tests to ascertain the optimal temperature and time duration to obtain a flexible pre-curved glass tube for the robot design.

The first test as presented in Figure 2.6A, was carried out under high temperature ( $900^{\circ}$ ) and long time duration (8.6 hours) as to ensure correct glass annealing and to minimize residual stress but the outcome was shattered microglass capillaries due to peeling breakages of the steel sheet surface used. For the next test in Figure 2.6B & C, the molds was changed to a solid steel rather than sheet steel and then, both the temperature and heating duration were both reduced though with a different step ramp for the heating and cooling. Under this condition, part of the glass capillaries was recovered but without any pre-curved shape and there was only a minimal steel surface peeling compared to the first test. Same temperature of  $800^{\circ}$  was maintained in the next two test (see Figure 2.6D & E) but with longer duration at  $800^{\circ}$  for 30mins and 40mins respectively and then imposing natural cooling. Here, the capillary glass did not break but the result is characterized with a high spring-back, leaving only a small pre-curved part. Afterwards, only the maximum temperature was increased to  $900^{\circ}\text{C}$  (Figure 2.6F) and the result shows a lesser spring-back with appreciable curvature shape which was flexible to pass through a straight glass tube. To observe the elastic property of the glass, the temperature was reduced to  $850^{\circ}\text{C}$  for 30 minutes duration as presented in Figure 2.6G. The resultant output had little spring back but it was not flexible enough to be integrated and used for the robot design. Finally, for the last test as presented in Figure 2.6H & I, only the maximum temperature for the two cases was increased to  $900^{\circ}\text{C}$  while maintaining same conditions as the previous one. The result showed no spring back, which was very interesting but due to its level of fragility, it will be difficult to be mounted/integrated on the robot actuation unit.

In conclusion, the success of the precurving process relies on several parameters, such as the temperature of the furnace (the maximum temperature), the heating rate, the duration of the heating, the cooling rate, and the type of steel mold. For the experiment, we used a box furnace VULCAN 3-550 capable of maintaining temperature up to  $1100^{\circ}\text{C}$  and it is a three-stage programmable for the temperature to time ramp up or down control. Figure 2.6H & D show the best shape setting in obtaining a pre-curved glass tube, while temperatures  $\leq 800^{\circ}\text{C}$  give an undesirable spring back effect. The use of steel sheets mold is not advisable

as it results in peeling/cracks under high temperatures which can possibly shatter the microglass instead a forged steel block is recommended. The flexibility of the result obtained was tested by manually passing it through a straight tube. It was flexible enough to move through the tube but in general, it was still fragile and will be difficult to integrate into an actuator for the CTR design. Even at that, without a thin coating that provides mechanical rigidity and protects the surface, it will still be difficult for it use in a continuum robot with link deformation. Unless additional tests could be conducted to find the tube shaping parameters to guarantee high glass flexibility after heating, which may take a longer time for the investigation. For that, we had to devise another novel approach which involves the use of two composites (an ultra-thin heat shrink polymer on a microglass tube), to obtain complex pre-curved shapes.

## 2.4 TUBE SHAPE SETTING USING POLYMER HEAT-SHRINK JACKET

### 2.4.1 Materials and methods

The use of heat-shrink plastic tubing to obtain a pre-curved CTR tube is demonstrated in [Noh 16, Makarets 14]. The process involved using a pre-curved wire as a mold and a heat gun for thermal treatment. The resultant tube had a diameter range on the millimeter scale after shrinkage and a large radius change deformation. Thus, it was only used for the inner CTR tube. To overcome these challenges, we adopted an approach that involves the use of two materials: 1) a thin heat-shrink polymer known as Polyethylene terephthalate (PET) to enforce shape setting, and 2) flexible glass capillaries as the robot's active backbone. The step-by-step heat treatment fabrication procedure to obtain pre-curved glass tubes for CTR, using a thin heat-shrink polymer (from [Nordson Medical](#)) is described in Figure 2.7. The glass tubes are commercially sold in a straight form with multiple inner and external diameters; the diameters can be customized on request. The fabrication procedure for obtaining a pre-curved glass tube has four steps that include: 1) inserting the glass capillary into the thin heat-shrink polymer tubing; 2) constraining it to the desired 3D printed mold shape fabricated by Formlabs stereolithography printer using [FLHTAM02](#), which is a high temperature resistance material; 3) applying thermal treatment in the furnace for a short period; and 4) obtaining the pre-curved microglass tube. The design of every pre-curved tube begins by understanding the correct tube specifications (e.g., the inner and outer tube diameters, the tube length, and the material used, which affects the fabrication approach to be adopted). In this novel approach, commercially available straight microglass tubes (Molex glass capillary) and commercially available thin heat-shrink polymer tubing were used to obtain pre-curved tubes (Figure 2.7), using a heat treatment at about 300°C in a furnace for  $\leq 10$  minutes.

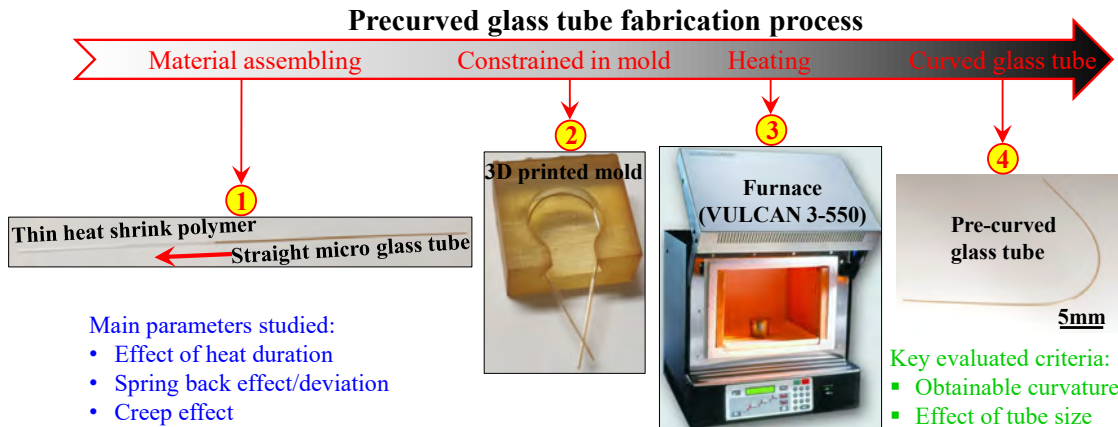


**Figure 2.7:** The pre-curved tube fabrication process: 1) inserting the glass capillary into the thin heat-shrink polymer tubing; 2) constraining it to the desired 3D printed mold shape; 3) applying thermal treatment in the furnace for a short period; and 4) obtaining the pre-curved microglass tube.

#### 2.4.2 Characterization and validation

Using the thermal treatment of a thin heat-shrink polymer tubing on the microglass capillary; pre-curved tube shapes were obtained and the radius of the curvature can be as small as 5mm (see Figure 2.8A). These fabricated samples were used for the characterization process. The specification of the heat-shrink polymer tubing used has a thickness of 6 $\mu\text{m}$  with an external diameter of 254 $\mu\text{m}$ . The glass capillary has an inner diameter of 20 $\mu\text{m}$  and an external diameter of 90 $\mu\text{m}$ . In order to ascertain the spring-back effect (which denotes the measure of deviation from the desired curvature), the outcome of the characterization test as a result of heat treatment duration for the different mold radii of curvature was obtained. This outcome is presented in Figure 2.8B, while the mold with the five different curvatures is shown in Figure 2.8C). The result obtained shows a level of linearity that was evaluated using the least square algorithm. The analyses of the results gave a straight line plot with the equation displayed in Figure 2.8B, which relates the realized radius of curvature in  $y - axis$  to the mold radius of curvature in  $x - axis$ . A 10-minute heat duration (represented in red) with almost a unit slope means that the realized radius of curvature due to the spring-back effect will fall within 1.28 mm of the mold radius of curvature and likewise for the 8-minute heat duration. The curvature of each pre-curved glass sample was obtained by post-processing using curve fitting as presented in Figure 2.8D. The process was further validated using two heat treatment durations (eight and ten minutes), with the obtained result shown in Figure 2.8E. This is represented by the star points in Figure 2.8B for the two temperature durations.

In the experimental validation, a new 3D-printed mold with a 4mm radius of curvature was fabricated, and the realized tube radius of curvature was evaluated for the two temperature heating durations. The result of the validation (indicated

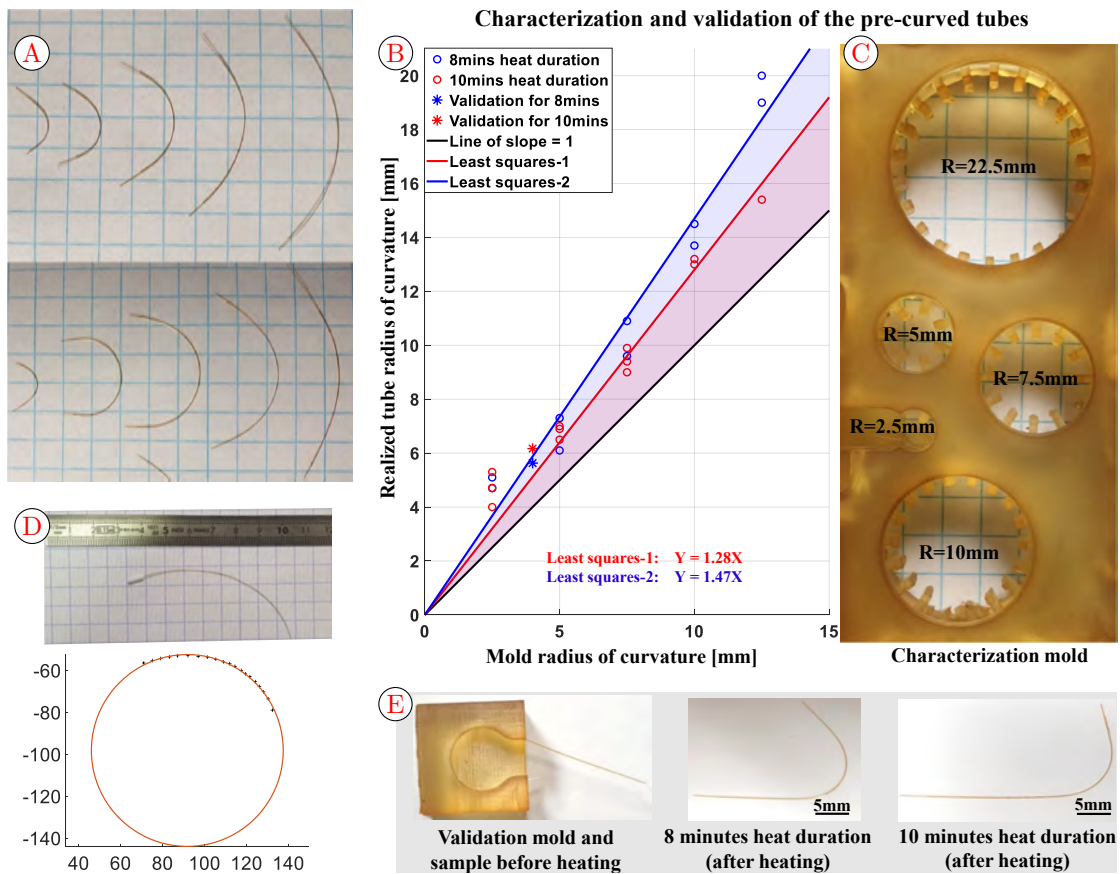


**Figure 2.8:** The characterization and validation of the novel shaping approach, **A)** Sample of the pre-curved glass tubes to be analyzed, **B)** Plot of the characterization and validation which were conducted for two different heat durations. The circle points are the various results while the lines are the least square algorithm. The radius of curvature in Y versus the mold radius of curvature in X was validated, as demonstrated by the star points on the plot, **C)** The 3D printed mold with five different radii of curvature that was used to constrain the glass in shape during the heat treatment, **D)** Obtaining the radius of curvature of each sample using curve fitting, **E)** Fabrication results that were used for the validation of the process.

by the star points on the characterization plot) shows the linearity, which was obtained while accounting for the two heat durations and how close they are to the least square line. The black line with a slope of 1 in Figure 2.8B represents the ideal scenario, where the realized tube radius of curvature equals the mold radius of curvature. This is not obtainable due to the spring-back effect, which can be represented as the colored boundary using the least square line plots. Furthermore, the effect of creep was investigated in order to analyze the relaxation of the pre-curved tube over several days. This effect was noticeable between the first and the second day after fabrication, with an acceptable relaxation of around 10%. The relaxation became very minimal later in the day. Generally, the results obtained with the specified heat shrink and the glass tube were satisfactory. Although, the detailed characterization results presented in Figure 2.8 are for one particular heat shrink and glass tube size but considering different mold constrained radius

of curvatures. This can be extended further to investigate the effect of different heat shrink thickness and for various glass capillary dimensions. However, we noticed that, the bigger the glass capillary the stiffer it becomes, which resulted in higher spring back effect depending on the heat shrink size used and it became less effective when glass tube diameter  $> 500\mu\text{m}$ .

### 2.4.3 Bending stiffness analysis of microglass tubes

To analyze the effect of the heat shrink on the microglass tube, bending stiffness was tested using three points method (see Figure 2.9 & 2.10). The bending stiffness was analyzed and plotted using Equ 2.3, for three different dimensions of capillary glass tubes.

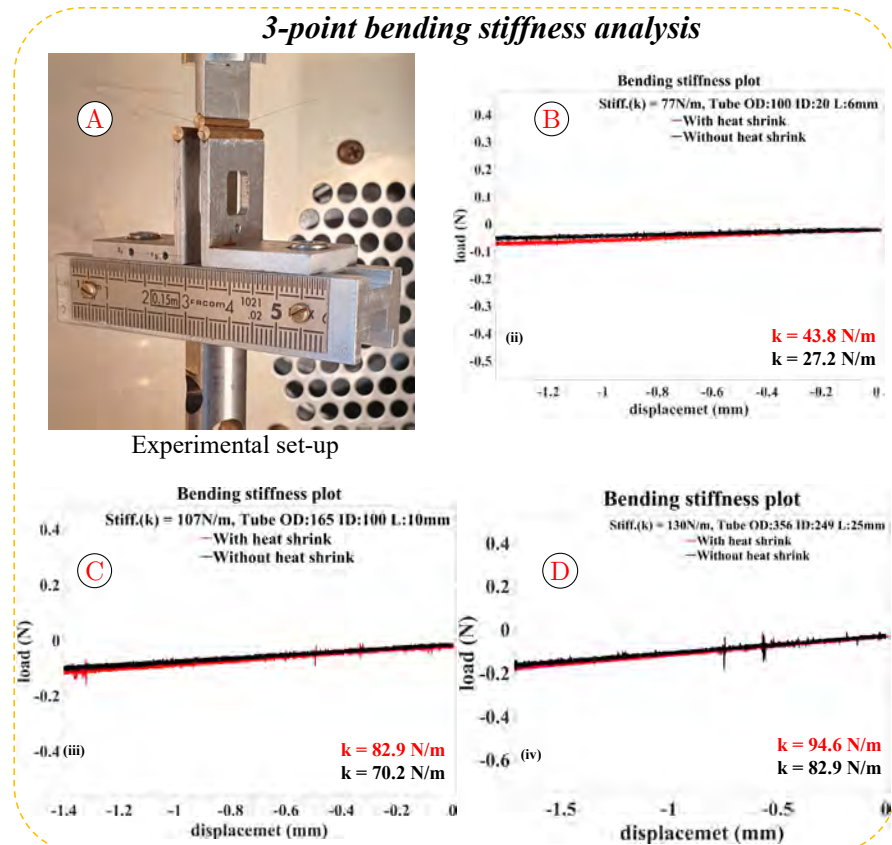


**Figure 2.9:** The three-point bending stiffness test result and analysis, **A)** the experimental set-up **B)** bending stiffness plot for for tube with 100mm external tube diameter and 20mm internal diameter for the case of with (red line) and without heat shrink (black line), **C)** bending stiffness but with 165mm external tube diameter and 100mm internal diameter, while **D)** bending stiffness with 356mm external tube diameter and 249mm internal diameter.

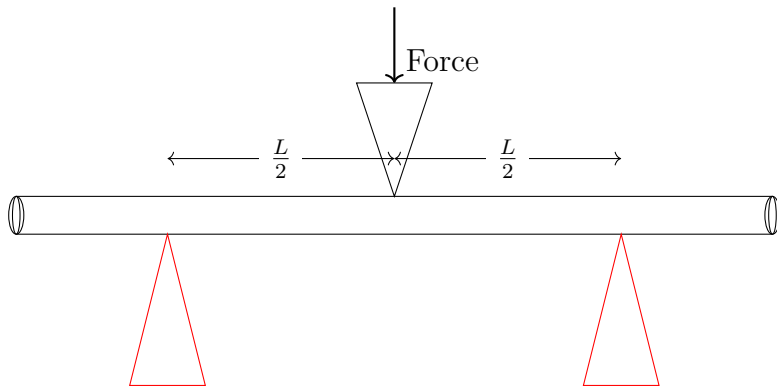


**Figure 2.10:** Three-point bending stiffness test

$$K = \frac{\Delta f}{\Delta \delta} = \frac{48 \cdot E \cdot I}{L^3} = \frac{48 \cdot E \pi (D^4 - d^4)}{L^3 \cdot 64} \quad (2.3)$$

Where:  $K$  is bending stiffness,  $\Delta f$  is applied force while  $\Delta \delta$  is the resultant deformation/displacement. Other parameters include  $E$  as Young modulus,  $L$  as the sample tube length, and  $I$  as the moment area of inertia which is a function of external diameter ( $D$ ) and internal diameter ( $d$ ).

Tube type	Tube length (m)	External diameters (m)	Inner diameter (m)	Bending stiffness (N/m)	Equivalent Young modulus (Pa)
tube-1 with heat-shrink	0.006	0.0001	2e-05	43.8	4.0153e+10
tube-1 without heat-shrink	0.006	0.0001	2e-05	27.2	2.4935e+10
tube-2 with heat-shrink	0.01	0.000165	0.0001	82.9	4.7511e+10
tube-2 without heat-shrink	0.01	0.000165	0.0001	70.2	4.0233e+10
tube-3 with heat-shrink	0.025	0.000356	0.000249	94.6	3.9119e+10
tube-3 without heat-shrink	0.025	0.000356	0.000249	82.9	3.4281e+10

**Table 2.2:** 3-point bending stiffness analysis for comparing the effect of thin heat shrink polymer on capillary glass

The experimental setup and plotting considering cases of with and without the heat-shrink polymer is shown in Figure 2.9. Table 2.2 presents the experimental result and when comparing the bending stiffness ratio between the tubes without heat shrink and those with heat shrink. This gives 1:1.61, 1:1.18, and 1:1.14 for three different glass tubes with the dimensions of  $T_1 = 90/20$ ,  $T_2 = 165/100$ , and  $T_3 = 356/249$  respectively. This result means that the effect of bending stiffness with regard to heat shrink is more significant with the smallest diameter tube and decreases as the tube diameter increases. This indicates that the approach best fits small glass diameters ( $< 500\mu\text{m}$ ). Additionally, when considering the same tube material, the bending stiffness is proportional to the moment area of inertia. The moment area of inertia is a function of the internal and external tube diameters, and its ratio between  $T_2$  and  $T_1$  is 1:6. The ratio for  $T_3$  and  $T_1$  is 1:122; this corresponds to the experimental result that shows an increment in bending stiffness as the tube dimension increases. It also explains why we

assume the dominant stiffness pair for the robot kinematic modeling (detail in the next Chapter). The resultant Young modulus of the polyimide-coated glass tube material was also derived from experimentation (see Table 2.2). However, the Young modulus (25-48GPa) obtained tends to differ from the standard values of fused silica, which have a value of 72.9 GPa [Comte 02]. Although in the theoretical analysis, we used only fused silica material properties while neglecting the thin polyimide-coating.

## 2.5 CONCLUSION

Considering the three possible approaches for the fabrication of pre-curved glass tubes, each one has its own drawbacks and challenges. Starting with the use of FEMTOprint machine for the FLWE approach, we saw through investigation that it is difficult to obtain a pre-curved tube in glass. Not only is the method the most expensive, the technology is still new and most suitable for structures that easy/fast chemical penetration during etching. In general, the current state of the technology has not advanced to obtain pre-curved glass tubes for the design of the robot of our interest. Next, which involved the heat treatment of a straight glass tube in a constrained steel mold under high temperatures. After several experimental trials, we were able to obtain a good heating parameter to achieve a flexible pre-curved glass tube. The advantage of this approach was that there was no spring-back effect after cooling but the sample is quite brittle/fragile which will be hard to integrate and too delicate for the robot design requirement. Finally, the use of a composite structure consisting of ultra-thin heat shrink polymer on a microglass tube gave an outstanding result. Although, with the level of spring-back effect which was characterized, in general, the pre-curved tube was flexible and suitable for a continuum robot design that is susceptible to high deformation. Moreover, the merit of the composite structure considering the heat shrink-on-glass approach is that glass capillaries are sufficiently stiff. The stiffness can enable the fabrication of CTR pre-curved tubes with an unprecedented diameter, unlike using polymers alone. For the design of the robot of interest, which is a concentric tube robot (CTR), the approach is less costly than Nitinol, which is a well-known conventional material. In addition, there is a benefit of reduced friction due to the lower friction coefficient between glass and PET (0.23),[Luethi 98] compared to the Nitinol-on-Nitinol friction coefficient (0.3) [Kim 08, Xu 10b]. Asides from obtaining a planar pre-curve tube in glass, complex shapes like 3D helical shapes were also possible, which are discussed and used for CTR demonstration in the subsequent Chapter. In fact, the utility of this approach can be broadened to other composite design structures, which can be used beyond the practice of heat shrink on microglass capillaries. For example, composite design of heat-shrink on materials other than glass for complex shape fabrication or patient-specific design.

The result of heat shrink on glass tube shape setting can also be extended to other different dimensions or specifications of interest. The advantage of this method compared to the Nitinol-based approach is that it does not require high temperatures and a long heat duration. These two factors permit the use of the 3D printed mold and also, allow the convenient fabrication of complex shapes such as 3D helical configuration or even the pre-curving of optical fiber (These are used for demonstration in the next chapter). In fact, a patient-specific pattern can be imposed simply by knowing the anatomy path and creating a suitable 3D-printed mold. Overall, the result obtained is very satisfactory with an interesting outcome of process characterization/validation, which can serve as a fabrication chart for design requirements.



---

# Chapter 3

## CTR made of glass

---

<b>3.1</b>	<b>Objectives</b>	82
<b>3.2</b>	<b>Introducing CATURO</b>	82
3.2.1	CATURO tubes	83
3.2.2	CATURO actuation unit	85
3.2.3	CATURO control system	86
<b>3.3</b>	<b>Model validation of the sub-millimeter glass CTRs</b>	87
3.3.1	Forward kinematic model (FKM) validation:	87
3.3.2	Path following based on IKM	90
3.3.3	Stability analysis and validation	93
<b>3.4</b>	<b>Glass CTR deployment</b>	96
3.4.1	3D conical-spiral free space deployment	97
3.4.2	Helical pre-curved CTR glass deployment	98
3.4.3	Constraint deployment of CTR through needles	99
<b>3.5</b>	<b>Applications</b>	100
3.5.1	Deployment of pre-curved optical fiber with laser transmission	100
3.5.2	Fluid suction and delivery	102
3.5.3	Vitreoretinal deployment under the OCT	103
<b>3.6</b>	<b>Conclusion and Discussion</b>	104

### 3.1 OBJECTIVES

Concentric tube robots (CTR)s are the smallest member of the continuum robot family. Considering the state-of-the-art of continuum robots, there is a need towards finding a better alternative or complement to the existing use of predominant Nitinol material. To that effect, we propose the use of pre-curved glass capillary tubes to design and fabricate the smallest CTR. Glass at the macro scale is brittle and fragile but at the small scale, they become flexible. This property at a small scale was the bedrock for achieving a functional sub-millimeter CTR prototype, with unprecedented tube specifications such as a radius of curvature down to 5mm with a glass tube having 20 $\mu\text{m}$  internal diameter. In fact, the backbone's flexibility is a crucial aspect of the robot for medical applications, as it allows it to access and maneuver through complex environments without relying on body contact for their deployment. This small-scale dimension is very beneficial in accessing difficult-to-reach areas of the anatomy with greater precision. In addition, the footprint (actuation unit and all pre-curved tubes) of most CTR prototypes in the literature are large due to the dimension and rigidity of the Nitinol tube. Considering the sub-millimeter dimension of the glass capillary tubes, therefore, the focus is on achieving a miniaturized compact overall robot design. Moreover, since the modeling aspect of CTRs has been established in the literature, our goal here is to investigate/validate them using glass material at a miniaturized scale for the forward kinematic model (FKM), inverse kinematic model (IKM), and stability analysis. After which full demonstration of the robot to ascertain its capabilities and potential through different experimental tests e.g. path following and maneuvering through 1mm orifice of three stationed needles, and deployment of a pre-curved optical fiber or 3D helical-shaped glass tube. In the application aspect, the objective is to use the robot for a proposed vitreoretinal surgery with the possibility of optical coherence tomography (OCT) 3D visualization.

### 3.2 INTRODUCING CATURO

We introduce a new generation of CTRs that is made of glass and used a novel approach for obtaining pre-curved CTR tubes in sub-millimeter diameters and a high curvature. As discussed in Chapter-2, this is achieved by using thin heat-shrink polymers on micro-glass capillaries to actualize the first ever sub-millimeter CTR prototype composed of glass material shown in Figure 3.1. This robot is called “CATURO”, which stands for a capillary tube robot with typical external tube diameters from 434 $\mu\text{m}$  to 90 $\mu\text{m}$  and an unprecedented radius of curvature as low as 5mm. While Figure 3.1A presents the robot’s mechanism of operation and working principle, Figure 3.1B displays the compact, miniaturized, and handheld robot prototype with a backbone comprising of pre-curved glass tubes. Figure 3.1C highlights the scaling difference with a side-by-side comparison of a

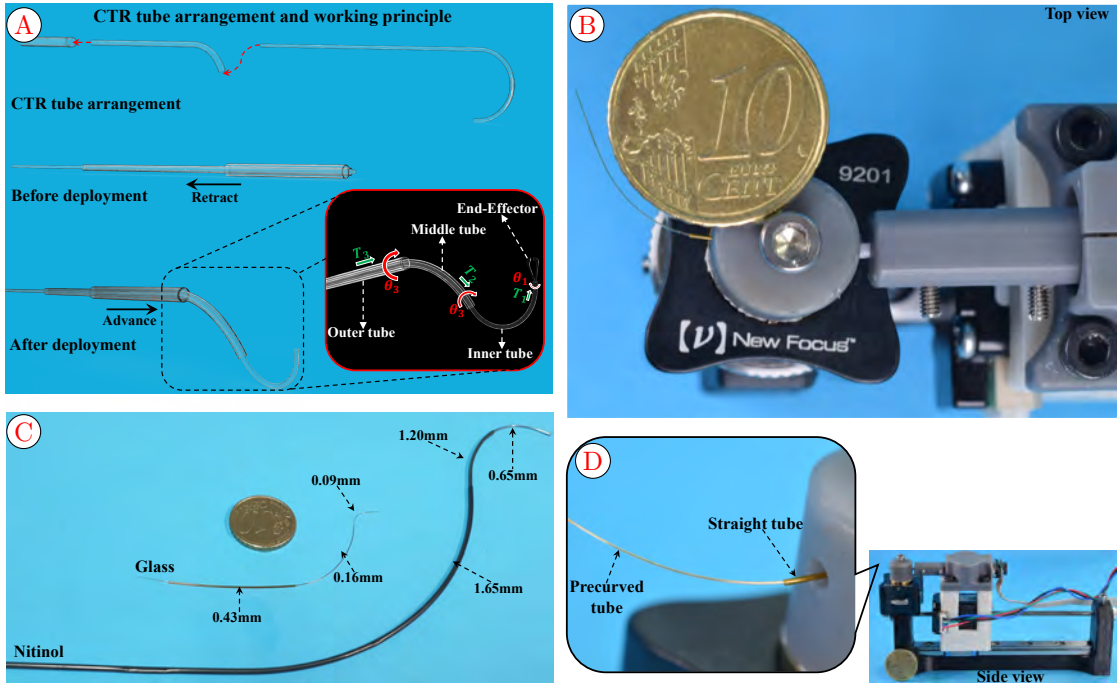


**Figure 3.1:** The Caturo: a capillary flexible CTR made of glass, with a high curvature and a sub-millimetric diameter. **A)** Arrangement of CTR tubes considering the case of dominance stiffness pair, where the inner tube that is characterized by a smaller diameter and less stiffness is inserted and conforms to the shape of the larger and thicker outer tubes, represented as “Before deployment”. During the deployment operation, each individual tube morphs into its original pre-curved shape as the robot takes its final configuration, represented as “After deployment”. **B)** A robotized two-tube Caturo, with sub-millimeter diameters (0.16mm & 0.35mm) and a very low radius of curvature (11.5mm), during a deployment. **C)** A comparison of three tube CTR configurations between the conventional Nitinol material and that of the sub-millimeter glass (diameter of each tube is displayed). **D)** The actuation unit is characterized by two DoF; the outer tube is fixed to the robot base while the inner tube is attached to the linear and rotary actuation for the demonstrations in this paper.

nested pre-curved tube configuration by the conventional Nitinol and a miniaturized sub-millimeter glass material. This captured the scale range of the Caturo. In fact, most of its actuation unit frame support was fabricated by a lightweight 3D-printed polymer as can be seen in Figure 3.1D. In addition to operating on such a miniaturized scale, the advantages of our approach are similar to those of 3D-printed CTR. These include low-cost, patient-specific capability, and lower temperature in short duration requirement, which permits the use of a 3D printed mold to obtain various complex glass tube shapes.

### 3.2.1 CATURO tubes

The arrangement and assembly of the sub-millimeter CTR glass tubes are the same as those of conventional CTRs (Figure 3.1A). The outer tube is usually straight with less curvature and is stiffer. Tube-1, tube-2, and tube-3 used for

the design of the Caturo have external to inner diameters of 90:20, 165:100, and 356:249, respectively. Therefore, there is a bending stiffness ratio between the possible combinations of tube-1 and tube-3 of 122:1. The ratio between tube-2 and tube-3 is 19:1. Considering the high stiffness ratios, the dominance stiffness approach illustrated in Figure 3.1A was used which was also adopted in the kinematic modeling. In this approach, each successive inner tube conforms to the shape of the stiffer outer tube before deployment and then takes its original shape as it extends out during deployment. The schematic diagram and CAD design of the actuation unit for each demonstration are presented in Figure 3.3. For Caturo, the outer tube is always fixed in position, while the inner tube is characterized by two DoF.

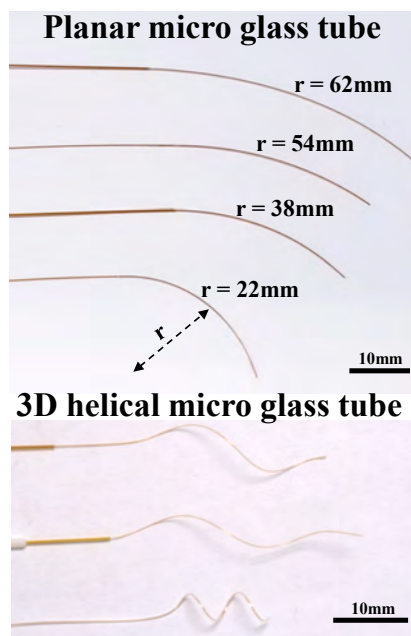


**Figure 3.2:** Sub-millimetre pre-curved glass tube samples with obtainable shapes and curvatures, such as the simple planar to complex helical curvatures, for various demonstrations of sub-millimeter glass tube flexibility and ability to slide into each other for possible CTR configurations or deployment.

Though full details regarding the fabrication procedure, curvature accuracy, validation, and characterization for a set of pre-curved glass tubes are detailed in Chapter 3 above. With this novel approach involving the thermal treatment of a thin heat-shrink polymer on the micro-glass capillary; pre-curved tube shapes were obtained, as shown in Figure 3.2B. A selection of the nested sub-millimeter planar pre-curved CTR glass tube samples is displayed in Figure 3.2B. The 3D helical pre-curved tubes in Figure 3.2B demonstrate that complex glass tube shapes can be obtained by merely changing the 3D printed mold design. The approach is less costly than Nitinol. Moreover, there is a benefit of reduced friction due to the

lower friction coefficient between glass and PET (0.23) [Luethi 98], compared to the Nitinol-on-Nitinol friction coefficient (0.3) [Kim 08, Xu 10b].

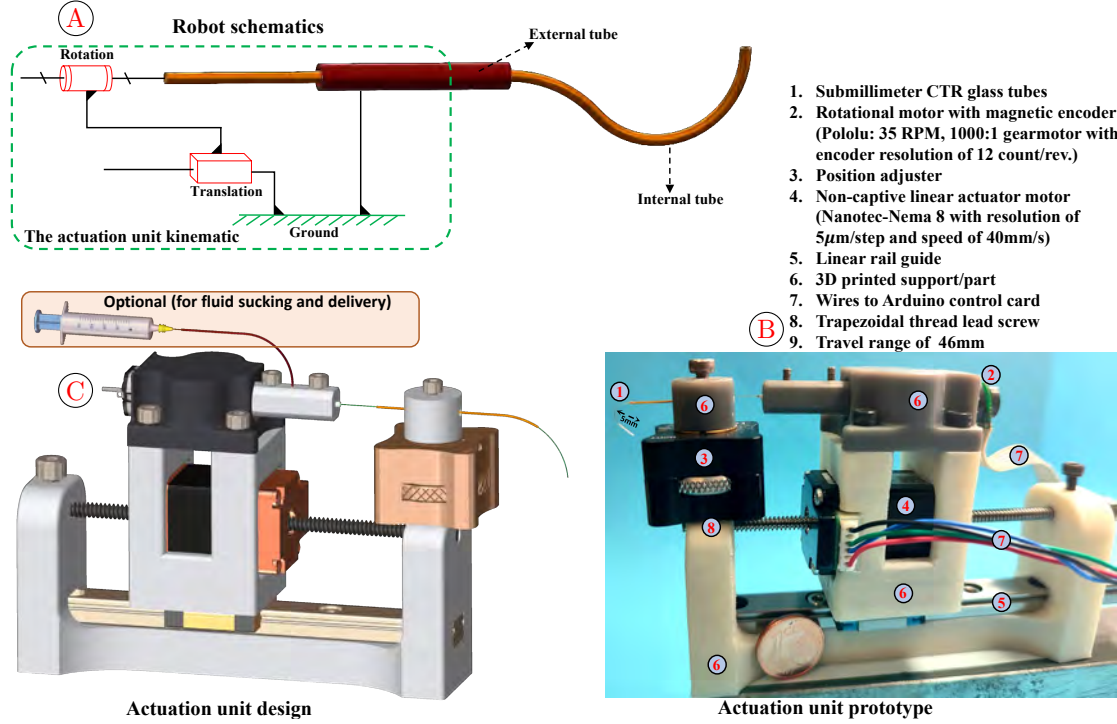


**Figure 3.3:** The Caturo CTR actuation unit design, showing the description of the CTR tube arrangement procedure and its deployment principle, **(A)** The design of the robot consisting of the schematic and **(B)** the CAD and **(C)** the realized prototype with the vital parts identified. The robot has two sections: the tube and the actuation unit.

### 3.2.2 CATURO actuation unit

The schematic of the Caturo actuation unit architecture is presented in Figure 3.3A. The schematic includes two DoF (translation and rotation) that actuate the inner tube while the outer tube is fixed to the ground. The majority of the actuation unit design parts are 3D printed (Figure 3.3B) for fast prototyping and to benefit from lightweight material. The actuation unit design has optional features for inner tube connectivity for either light or hydraulic integration for end-effector manipulation. One example is the fluid suction and delivery operation using a syringe (Figure 3.3C). The designed prototype is compact and small (10 cm × 2.5 cm × 5.4 cm) compared to many conventional CTR actuation unit prototypes in the literature. The components of the actuation unit design are identified in Figure 3.3B. The non-captive linear motor, which is mounted on the rail guide for smoother movement is used for the transitional actuation. The miniature dual-shift gear motor with an encoder is used to actuate the rotation of the inner tube.

### 3.2.3 CATURO control system

The control of the Caturo is divided into two which include: 1) model-based control and 2) teleoperation control using a miniaturized joystick. For each case, the control was programmed and executed on an Uno Arduino board, which has a motor shield connected to the motor power supply. The two methods for the deployment control of the robot used for various demonstrations as presented in the subsequent sections are as follows.

The first aspect is the teleoperation control, which involves the use of a miniaturized joystick ([SKU:BTN-026](#)) to control the rotation or translation deployment of the robot. For simplicity, the miniaturized joystick is connected through a wire to the Arduino for the robot demonstration, which was used for the 3D conical-spiral deployment. The configuration of the joystick is such that the diagonal ends are for the clockwise and anti-clockwise tube rotation control, whereas the central joystick pad axis controls the forward and reverse tube translation. All the program code was written in C++ on the script and uploaded to the Arduino board. The miniaturized joystick was often used for tube pose initialization adjustment in the absence of an automatic or self-robot calibration system.

The second part is the model-based or path-planning control. In this category, either the kinematic model or desired path tracing was programmed into the Arduino for the execution of the robot deployment, with respect to the chosen program/function. The open-loop control without the use of an external sensor approach is particularly useful if sensor integration is not available or possible. For feedback control, a 3D shape reconstruction and evaluation of the sub-millimeter glass diameter tubes is quite challenging. Following the survey for various 3D shape sensing techniques for continuum robots in minimally invasive surgery [[Shi 17](#), [Manakov 21](#)], three possible options were given which include: fiber optic sensors based using Fiber Bragg Gratings (FBG), electromagnetic-based tracking (EM), and intraoperative imaging modalities based shape reconstruction methods. The FBG sensing technique offers significant advantages due to its miniature size but suffers large errors with low stiffness, making it not ideal for Caturo. Moreover, for FBG techniques, multiple fibers are needed, and the same for EM-based technique that requires the attachment of multiples EM sensors or generators on the robot, whereas intraoperative imaging alternatives suffer from low resolution and diverse artifact. Although we tried to use visual servoing by non-contact 3D shape sensing involving the use of depth and stereo cameras. This approach suffers from the issues of low-resolution and diverse artifacts as shown in Figure [E.2](#) of Appendix [E](#). In the absence of a functional external sensor for feedback control, we have to rely on the internal feedback control of the motors and the accuracy of the model.

s/n	Demonstration type	Inner tube				Outer tube			
		$d_i$ [μm]	$D_i$ [μm]	$CT$ [μm]	$R_i$ [mm]	$d_e$ [μm]	$D_e$ [μm]	$CT$ [μm]	$R_e$ [mm]
1	The Caturo (3.3)	100	164	12	11.5	249	353	18	$\infty$
2	3D conical-spiral (3.10)	100	164	12	58.8	249	353	18	$\infty$
3	Fluid suck & delivery (3.14)	100	164	12	26.5	249	353	18	$\infty$
4	Vitreoretinal deployment (3.15)	20	90	12	8.9	249	353	18	$\infty$
5	FKM (3.6A & 3.6B)	100	164	12	63	249	353	18	120
6	IKM (3.8)	100	164	12	58.8	249	353	18	$2 \times 10^8$
7	Instability analysis (3.9)	100	164	12	42	249	353	18	92
		100	164	12	25	321	434	18	105
8	Needle constraint (3.12)	100	164	12	54.4	321	434	18	$\infty$
9	Helical precurved (3.11)	100	164	12	H	321	434	18	$\infty$
10	fibre optics precurved (3.13)	0	125 F	61	40	321	434	18	$\infty$

$D_i$ : External diameter of inner tube including CT  
 $D_e$ : External diameter of outer tube including CT  
 $FKM$ : Forward kinematic model  
 $d_i$ : Internal diameter of inner tube  
 $d_e$ : Internal diameter of outer tube  
 $IKM$ : Inverse kinematic model  
 $R_i$ : Inner tube radius of curvature  
 $R_e$ : Outer tube radius of curvature  
 $F$ : Optical fibre  
 $CT$ : Coating thickness  
 $H$ : Helical shape

**Table 3.1:** The different demonstrations and their respective Caturo tube specifications

### 3.3 MODEL VALIDATION OF THE SUB-MILLIMETER GLASS CTRs

CTR design is essential because it could prevent permanent tube deformation and robot instability. When modeling CTR, there are inevitable trade-offs to be considered among accuracy, computational cost, and model complexity [Burgner 15c]. For the Caturo validation, the piecewise constant curvature model was used for the FKM and IKM due to its simplicity [Robert 10, Rucker 10d, Neppalli 09]. The three aspects of continuum robots with the model kinematic flow from the actuation space to task space for constant curvature is presented in Figure 3.4. The robot kinematics can be decomposed into two mapping as shown in Fig.2a, thanks to the piecewise constant-curvature assumption. The mapping from arc parameters to the pose (position and orientation) along the backbone is called **robot independent** because this can be applied to all systems that can be approximated as piecewise constant curvature. The **robot-specific** maps the joint space ( $q$ ) to the configurations space ( $(l(s), \phi(s), \kappa(s))$ ). The joint variables are tube translation ( $L$ ) and rotation ( $\alpha$ ) (see full detail in [Robert 10]). The stability analysis, which considers the additional effect of torsion, involved the use of Cosserat rod formulation [Gilbert 15a]. In all the cases in which the classical elasticity theories were used, considering the robot's tube size, the effect of friction, extension, and shear were all neglected. For all the numerical modeling and data processing simulation analysis, MATLAB software was used. The model validation and evaluation are detailed in the following.

#### 3.3.1 Forward kinematic model (FKM) validation:

Inserting a curved tube into another, causes their common axis to form a mutual resultant curvature at equilibrium. Due to the inherent compliance of continuum robots, elasticity is one essential factor for their kinematics. The spec-

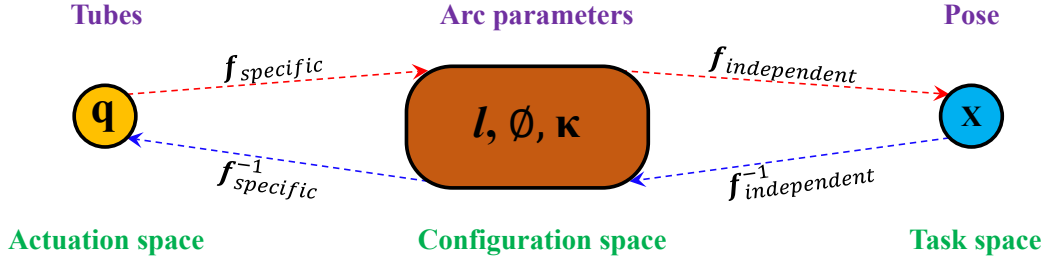


**Figure 3.4:** The FKM (red arrow) and IKM (blue arrow) model flow

Demonstration type	Inner tube				Outer tube			
	$d_i$ [ $\mu\text{m}$ ]	$D_i$ [ $\mu\text{m}$ ]	$CT$ [ $\mu\text{m}$ ]	$R_i$ [mm]	$d_e$ [ $\mu\text{m}$ ]	$D_e$ [ $\mu\text{m}$ ]	$CT$ [ $\mu\text{m}$ ]	$R_e$ [mm]
FKM (3.6A & 3.6B)	100	164	12	63	249	353	18	120

**Table 3.2:** Prototype tube specifications for the forward kinematic model.

ifications of the Caturo used for this demonstration are provided in Table 3.2, and the actuation unit prototype is presented in Figure 3.1D. The torsionally rigid CTR model which involves a simple arc geometry approach to the piecewise constant-curvature model was adopted here. The robot kinematics can be decomposed into two mapping as shown in Figure 3.4, thanks to the piecewise constant-curvature assumption. The arc parameter consists of triplet variables which are arc length  $l(\mathbf{q})$ , angle of the plane containing the arc  $\phi(\mathbf{q})$ , and curvature  $\kappa(\mathbf{q})$ . Note that transformation from arc base to tip involves two rotations which include:

- The backbone bending rotation  $\mathbf{R}_y(\theta) \in SO(3)$  about  $y$ -axis
- The backbone rotation  $\mathbf{R}_z(\phi)$  about the  $z$ -axis.

$$\mathbf{T}_{ctr} = {}^b\mathbf{T}_e(\phi) {}^b\mathbf{T}_e(\theta) = \underbrace{\begin{bmatrix} \mathbf{R}_z(\phi) & 0 \\ 0 & 1 \end{bmatrix}}_{\text{Rotation}} \underbrace{\begin{bmatrix} \mathbf{R}_y(\theta) & \mathbf{P} \\ 0 & 1 \end{bmatrix}}_{\text{Inplane transformation}} \quad (3.1)$$

$${}^b\mathbf{T}_e = \begin{bmatrix} \cos \phi & \cos \kappa s & -\sin \kappa s & \cos \phi & \sin \kappa s & \frac{1}{\kappa} \cos \phi (1 - \cos \kappa s) \\ \sin \phi & \cos \kappa s & \cos \kappa s & \sin \phi & \sin \kappa s & \frac{1}{\kappa} \sin \phi (1 - \cos \kappa s) \\ -\sin \kappa s & 0 & 0 & \cos \kappa s & 0 & \frac{1}{\kappa} \sin \kappa s \\ 0 & 0 & 0 & 0 & 0 & 1 \end{bmatrix} \quad (3.2)$$

$\mathbf{P} = [r(1 - \cos \theta), 0, r \sin \theta]^T$ , which is the coordinates of a point on the circular arc of radius  $r$  in the  $x-z$  plane centered at  $[r, 0, 0]^T$ , where  $r = 1/\kappa$ . Considering the case of two tube sections as shown below, it becomes

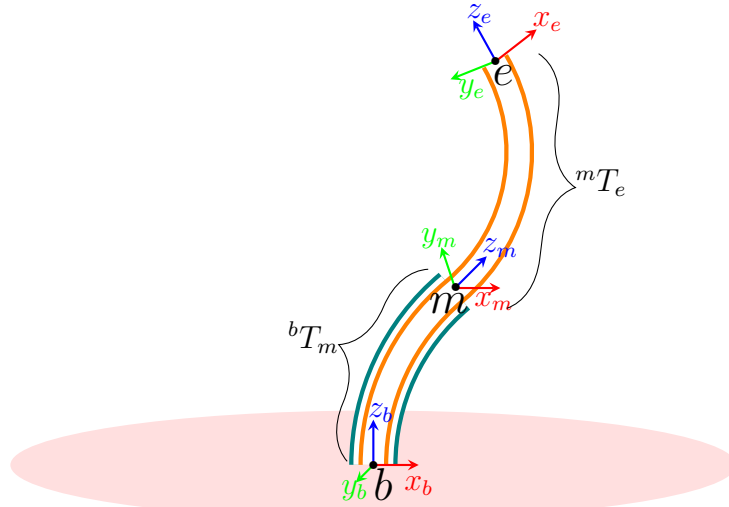


**Figure 3.5:** Two tube configuration with two sections for the Caturo FKM

$${}^bT_e = {}^bT_m \cdot {}^mT_e \quad (3.3)$$

#### Forward kinematic model configurations and validation

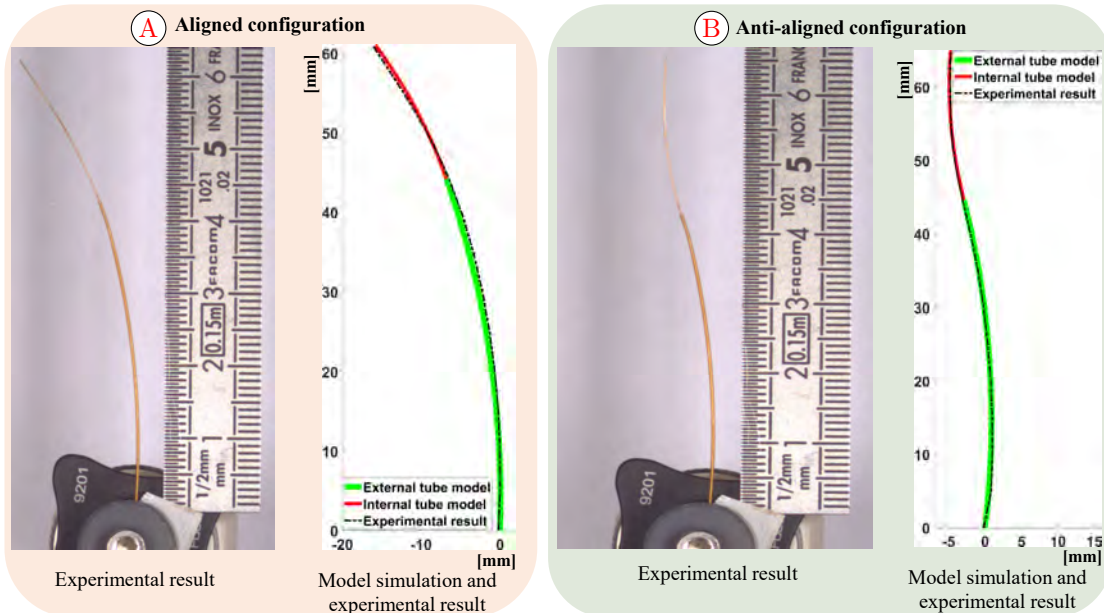


**Figure 3.6:** Sub-millimetre glass CTR FKM validation and comparison for two different cases. (A) aligned configuration where the two tubes are in the same direction, and (B) anti-aligned configuration in which the tubes are in the opposite direction.

This was simulated and experimentally validated using the sub-millimeter glass CTR. The tube curvatures are positioned in the same plane in the aligned robot configuration shown in Figure 3.6A. The configuration was chosen because the planar robot shape is perpendicular to the camera view. To compare the robot's experimental backbone to that of the constant-curvature CTR model, MATLAB

software was used to run the simulation and post-processing analysis. Comparing the experimental results to the model revealed a similarity along the robot's backbone, as presented in Figure 3.6A. This gave a mean deviation of  $\mu_x = 0.30\text{mm}$ , a standard deviation of  $\sigma_x = 0.17\text{mm}$ , and a percentage error of 0.83%. The same process was used for the case of anti-aligned robot configuration (where the two tube curvatures are aligned in opposite directions), as displayed in Figure 3.6B. The experimental robot's backbone closely matches the backbone of the model (see Figure 3.6B); comparing the two gave a mean deviation of  $\mu_x = 0.12\text{mm}$ , a standard deviation of  $\sigma_x = 0.07\text{mm}$ , and a percentage error of 0.47%. The results for both the aligned and anti-aligned cases indicate that the constant curvature CTR model can be adapted for the Caturo as well regardless of its sub-millimeter size and material.

### 3.3.2 Path following based on IKM

The simple and fast closed-form geometric approach to IKM was used to control the end-effector pose in an open-loop control scheme (see Figure 3.8C). The idea for the IKM was gotten from [Neppalli 09], where the tube arc parameters ( $l$ ,  $\phi$ ,  $\kappa$ ) for a single continuum section can be determined, given the endpoint location  $p = [x \ y \ z]^T$  in a closed-form expression. Analyzing the Figure 3.7 below for a single section of the continuum robot, the arc parameters can be derived as follows:

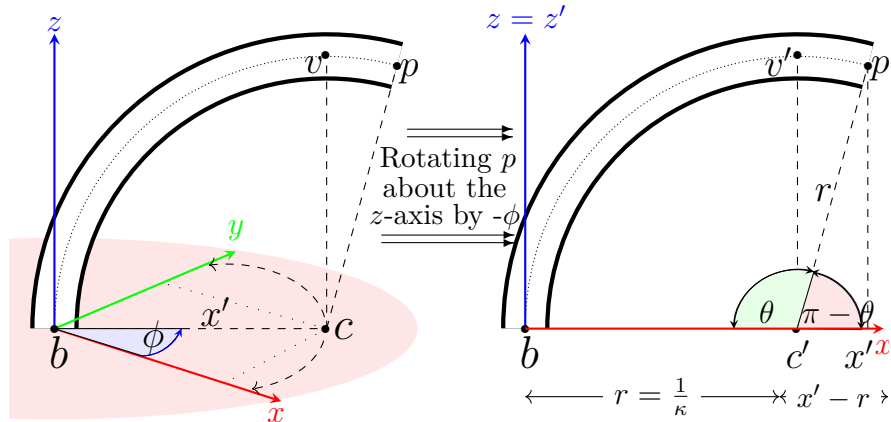


**Figure 3.7:** The inverse kinematic modeling of a single segment continuum robot using a closed-form analytic approach

From Figure 3.7, the rotation about the  $z$ -axis ( $\phi_z$ ) is given as:

$$\phi = \text{atan2}(y, x) \quad (3.4)$$

Rotating about the  $z$ -axis by  $-\phi$  produces an arc of the same curvature which lies entirely in the  $xy$  plane, with a new point  $p'$  such that:

$$x' = \sqrt{x^2 + y^2}, \quad y' = 0, \quad z' = z \quad (3.5)$$

by Pythagoras' theorem, we have

$$\begin{aligned} (x' - r)^2 + z'^2 &= r^2 \\ \kappa = \frac{1}{r} &= \frac{2x'}{z'^2 + x'^2} = \frac{2(\sqrt{x^2 + y^2})}{x^2 + y^2 + z^2} \end{aligned} \quad (3.6)$$

The angle of bending about  $y$ , given as  $\theta$  is derive as follows:

$$\theta = \begin{cases} \cos^{-1}(1 - \kappa\sqrt{x^2 + y^2}) & \text{for } z' > 0 \\ 2\pi - \cos^{-1}(1 - \kappa\sqrt{x^2 + y^2}) & \text{for } z' \leq 0 \end{cases} \quad (3.7)$$

we know that  $\theta = s\kappa$  and  $s \in (0, l)$ , therefore

$$s = \frac{\theta}{\kappa} \quad (3.8)$$

This gives us the deployment length to the desired position  $[x, y, z]$ , and the homogeneous in-plane transformation matrix such as in Equation 3.1, can be denoted as:

$$(\kappa, s, {}^bT_p(\theta)) = h(\mathbf{b}, \vec{z}, \mathbf{p})$$

Considering two tubes as shown in Figure 3.5 above

$$(\kappa_1, l_1 {}^bT_m(\theta_1)) = g(\mathbf{b}, \vec{z}_1, \mathbf{m}) \dots \dots \dots \text{Tube 1}$$

$$(\kappa_2, l_2 {}^mT_e(\theta_2)) = g(\mathbf{m}, \vec{z}_2, \mathbf{e}) \dots \dots \dots \text{Tube 2}$$

This can be expressed by global closed-form function  $f$  as:

$$(\kappa_1, l_1 {}^bT_m(\theta_1), \kappa_2, l_2 {}^bT_m(\theta_2)) = f(\mathbf{b}, \vec{z}_1, \mathbf{m}, \mathbf{e})$$

**Point of singularity:** singularity occurs in the inverse kinematic calculations for  $\phi$  and  $\kappa$  when the robot tip coordinate is places purely along  $z$ -axis with no  $x$  nor  $y$  components. The solution is gotten as follows:

- For  $x = 0, y = 0$ , then any arbitrary value of  $\phi$  is chosen
- To choose an appropriate value of  $\kappa$ , the solution can be grouped into two cases:
  - When  $z \neq 0$ , choose  $\kappa = 0$  and  $s = z$ . However,  $z < 0$ , implies a negative and not realizable
  - At  $z = 0$ , this implies end-tip at origin

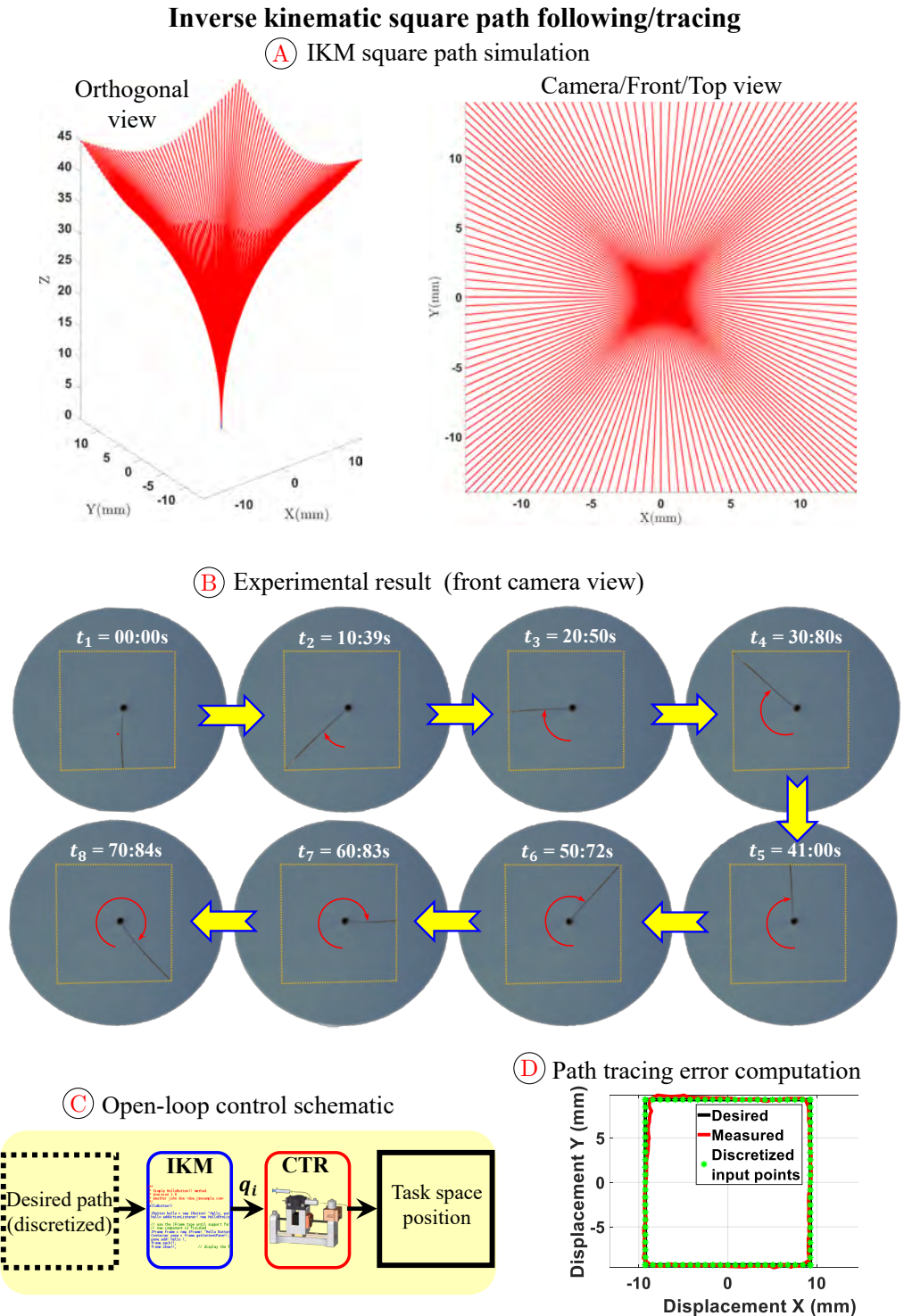


**Figure 3.8:** Sub-millimetre glass CTR path following based on IKM (A) Simulation results of the path tracing using the closed-form geometric approach to the IKM (B) Experimental result for a square path following which is achieved using a two DoF Caturo, (C) Open loop control block scheme using the IKM for square path, (D) The positioning accuracy of the Caturo with overall root mean square error of 0.201mm, for the open loop control based using the IKM.

Demonstration type	Inner tube				Outer tube			
	$d_i$ [μm]	$D_i$ [μm]	$CT$ [μm]	$R_i$ [mm]	$d_e$ [μm]	$D_e$ [μm]	$CT$ [μm]	$R_e$ [mm]
IKM (Figure 3.8)	100	164	12	58.8	249	353	18	$2 \times 10^8$

**Table 3.3:** Prototype tube specifications for path tracing using the IKM.

The IKM was used to generate the joint variables ( $q_i$ ) for the discretized square path, as displayed in Figure 3.8A. For the experimental demonstration, IKM control was implemented using a 2-DoF actuation unit, characterized by one translation and one rotation (refer to Figure 3.1D). The Caturo specification is provided in Table 3.3. The experiment was conducted by placing a camera fixed in the front defined as the camera view in the simulation in Figure 3.8B, while the robot translates and rotates out of the plane (for video see [experiment & simulation](#)). The square path tracing is a 2D projection on the front  $x, y$  plane when viewing the distal end of the inner tube, for the IKM simulation and deployment. The experimental result for the square path presented in Figure 3.8B, validates the possibility of actualizing path tracing. This validation is in line with the model simulation. The result obtained included the robot position accuracy with a root mean square error (RMSE) of 0.201mm ( $RMSE = \sqrt{\frac{1}{n} \sum_i^n \|\hat{p}_i - p_i\|^2} = \sqrt{\frac{1}{n} \sum_i^n (\hat{x}_i - x_i)^2 + (\hat{y}_i - y_i)^2}$ , refer to Figure 3.8D). The linearity in the x-axis are  $X_{down} = 4.9\%$ ,  $X_{up} = 7.7\%$ . The linearity in the y-axis are  $Y_{right} = 3.7\%$ ,  $Y_{left} = 10.1\%$ . This demonstration proves that the IKM of CTR can be applied to the sub-millimeter glass CTR with a satisfactory result. It is especially noteworthy considering the fact that the robot was used in an open loop control without any visual servoing or closed loop feedback for intermediary error correction.

### 3.3.3 Stability analysis and validation

It is often desirable to use curvatures that are as high as possible when designing CTR to achieve high dexterity. However, high curvatures could result in elastic instabilities [Hendrick 15b, Gilbert 15a, Peyron 19]. The final objective is to obtain robots that are guaranteed to remain elastically stable throughout the workspace. Instability has been one of the key challenges with CTRs as regards being used in medical intervention. CTR instability due to torsion (known as snapping) is a sudden leap from one equilibrium configuration to another. This leap is accompanied by the release of accumulated torsional (twist) energy. Eventually, it could lead to the damage of nearby fragile tissues or vital organs but controlling it can be used for dynamic tissue cutting [Rojas 18]. This particular phenomenon has been linked to the robot's transmission length, the tube curvatures, the length of the active overlaying tubes, friction, clearance between the tubes, and the ratio of tube torsion to bending stiffness [Webster 09b, Webster 08a, Dupont 10b, Girerd 17b]. There has been a greater focus on the first two aforementioned criteria in the literature and these are the focus here as regards Caturo. To analyze and evaluate the instability issues associated with the Caturo, two different experiments were

carried out. Both experiments used different tube specifications, as displayed in Figure 3.9. The tube specification is provided in Table 3.4 and the actuation unit is displayed in Figure 3.1D.

Demonstration type	Inner tube				Outer tube			
	$d_i$ [ $\mu\text{m}$ ]	$D_i$ [ $\mu\text{m}$ ]	$CT$ [ $\mu\text{m}$ ]	$R_i$ [mm]	$d_e$ [ $\mu\text{m}$ ]	$D_e$ [ $\mu\text{m}$ ]	$CT$ [ $\mu\text{m}$ ]	$R_e$ [mm]
Instability analysis (3.9)	100	164	12	42	249	353	18	92
	100	164	12	25	321	434	18	105

**Table 3.4:** Prototype tube specifications for the stability analysis/investigation

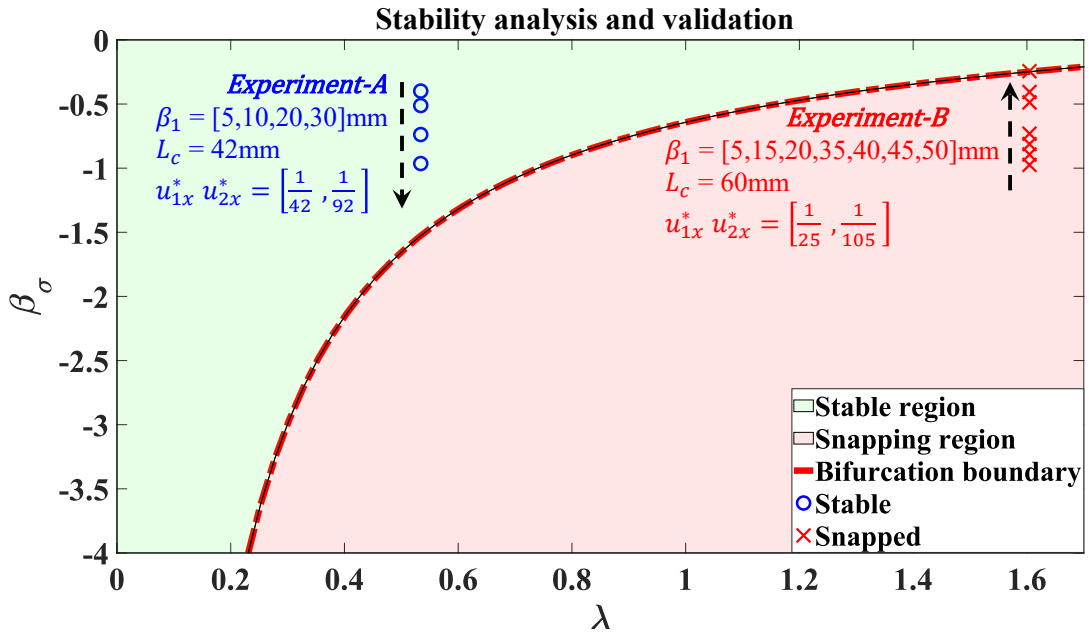


**Figure 3.9:** Stability analysis of micro-glass CTR under torsion, which is used to validate the effect of change in transmission length for two different cases, as displayed in *Experiment-A* and *Experiment-B* with a change in the curvature and active curve length of the tubes.

The stability investigation and evaluation were aimed at a snap prediction so as to guarantee a snap-free robot. The stability analysis adopted for the bifurcation investigation of Caturo was derived and detailed in [Gilbert 15a]. Therefore, we know that when the bifurcation parameter ( $\lambda$ ) becomes so large and exceeds the critical value ( $\lambda_0$ ), buckling will occur. Since we can control  $\lambda$ , one may seek to know the value of  $\lambda$  at which a CTR will snap. Applying bifurcation and elastic stability theory, along with the torsionally compliant model of CTR which considers the effect of twisting gives:

$$\lambda = L_c^2 \kappa_1 \kappa_2 \frac{k_{1b}}{k_{1t}} \frac{k_{2b}}{k_{2t}} \frac{k_{1t} + k_{2t}}{k_{1b} + k_{2b}}$$

If the tubes are of same material, then we can re-write it as

$$\lambda = L_c^2 u_{1x}^* u_{2x}^* (1 + \nu)$$

A bifurcation exists at point  $(\lambda, \pi)$  where  $\lambda$  obeys

$$\beta_\sigma = \frac{-\cot(\sqrt{\lambda})}{\sqrt{\lambda}} \quad (3.9)$$

When  $\beta_\sigma = 0$ , this gives  $\lambda = \pi^2/4$ , which is a well-known result for two tubes considering no transmission length [Rucker 10c, Dupont 10b]. However, when considering the fact that each tube must be exposed to be held at the actuation unit, the straight transmission lengths will not be equal physically. Therefore, this is resolved by determining an equivalent transmission length ( $\beta_{eq,\sigma}$ ), and for the case of two-tube CTR, it is given as:

$$\beta_{eq,\sigma} = \frac{\beta_{1,\sigma}k_{2t} + \beta_{2,\sigma}k_{1t}}{k_{1t} + k_{2t}} \quad (3.10)$$

Therefore, the snap prediction was facilitated using Equations 3.9 & 3.10, which is based on the bifurcation and elastic stability theory using the torsionally compliant model of CTR, which considers the effect of twisting [Gilbert 15a, Hendrick 15b, Ha 14a, Peyron 19]. The experimental validation was then carried out to justify possible snapping due to torsion in regard to the model prediction (For a video demonstration, see [stability](#)).

For *Experiment-A*, we used two pre-curved glass tubes whose specifications such as their respective curvatures and diameters are presented on the first row in Table 3.4.  $L_c$  is the active curve section length where the two assembled tubes are pre-curved with the given curvatures  $u_{1x}^*$  for the inner tube and  $u_{2x}^*$  for the external tube. Moreover,  $\beta_1$  is the transmission length which is the straight length of the inner tube that will be varied at 5mm, 10mm, 20mm, and 30mm while investigating instability due to twist. For this test, the external tube is fixed in position to the actuation unit, while the inner tube is actuated to rotate in clockwise and anti-clockwise directions two times for each transmission length considered (see [stability](#)). The purpose of this study is to investigate the Caturo instability due to the transmission length with the given curvature and curved active length of the two tubes. The theoretical result of Equ. 3.9 & 3.10 as presented in Figure 3.9, indicates that for all the given values of transmission length, the robot operates within the stable region, which is represented by the blue circles above the bifurcation black line. This was validated experimentally as demonstrated by the non-snapping effect of twist in the resulting video as shown [here](#).

In *Experiment-B*, we decided to reduce the radius of curvature of the newly fabricated internal tube from 42mm to 25mm, as well as increase the active curved length  $L_c$  of the two tubes from 42mm to 60mm. Likewise, the transmission length  $\beta_1$  starts from 5mm to 50mm at the interval of 5mm, so as to analyze in detail and validate the instability prediction due to twist. As presented in Figure 3.9, irrespective of the high number of iteration points for the transmission length under investigation, theoretically, all these points marked in red appeared below the

bifurcation line (the red region). This means that with this given robot specifications, there is instability and snapping effect irrespective of the tube's transmission length (for video validation, see [here](#)). This was the reverse case of what was obtained in *Experiment-A*.

In summary, with *Experiment-A*, the robot operates within the stable region, whereas this was the opposite in the case of *Experiment-B* as predicted. Generally, for the validation each test was observed twice for clockwise and anti-clockwise rotations of the inner tube. Based on the stability analysis result in Figure 3.9, one will notice that the higher the transmission length, the closer to the bifurcation boundary and vice versa as shown by the black arrow. Secondly, irrespective of the transmission length, the tube curvature and the aligned active curve length of the tubes under torsion also influence the robot instability, as seen by the comparison of *Experiment A and B*. Finally, according to this demonstration, it is noteworthy to mention that the usual criteria and factors that work for Nitinol CTR are also applicable to the Caturo. Knowing that when the bifurcation parameter  $\lambda$  exceeds the critical value  $\lambda_0$ , buckling will occur [[Gilbert 15a](#)]. Therefore, comparing the glass and Nitinol tube material while considering the same geometrical parameters (e.g., tube curvatures and active curved length) gave  $\lambda \propto 1 + \nu$ , where  $\nu$  is the material Poisson ratio. Using this relationship to compare both materials gives:

$$\frac{\lambda_g}{\lambda_N} = \frac{(1 + \nu_g)}{(1 + \nu_N)} = \frac{(1 + 0.17)}{(1 + 0.33)} = 0.87$$

Theoretically, this demonstrates that the relationship between the bifurcation parameter of glass  $\lambda_g$  and that of Nitinol  $\lambda_N$  tube is represented by  $\lambda_g = 0.87\lambda_N$ . This expression means that the glass tube material will have slightly less stability than the conventional Nitinol material under the same geometrical conditions. Noteworthy to mention, that for all the studies and demonstrations, two tubes were used based on the commercially available dimensions and our constraint (max. tube diameter  $< 500\mu m$ ).

## 3.4 GLASS CTR DEPLOYMENT

The use of sub-millimeter pre-curved glass capillaries for CTR prototyping and their respective demonstrations of the deployment capabilities of the robot are discussed in this Section. The proposed rapid fabrication approach enabled Caturo to be adaptable to various applications; this adaptability was made possible by imposing different tube specifications as presented in Table 3.1. The actuation unit for the Caturo is described in Figure 3.3, which uses open-loop control for the demonstrations.

### 3.4.1 3D conical-spiral free space deployment

Demonstration type	Inner tube				Outer tube			
	$d_i$ [ $\mu\text{m}$ ]	$D_i$ [ $\mu\text{m}$ ]	$CT$ [ $\mu\text{m}$ ]	$R_i$ [mm]	$d_e$ [ $\mu\text{m}$ ]	$D_e$ [ $\mu\text{m}$ ]	$CT$ [ $\mu\text{m}$ ]	$R_e$ [mm]
3D conical-spiral (3.10)	100	164	12	58.8	249	353	18	$\infty$

**Table 3.5:** Prototype tube specifications for the 3D conical-spiral free space deployment

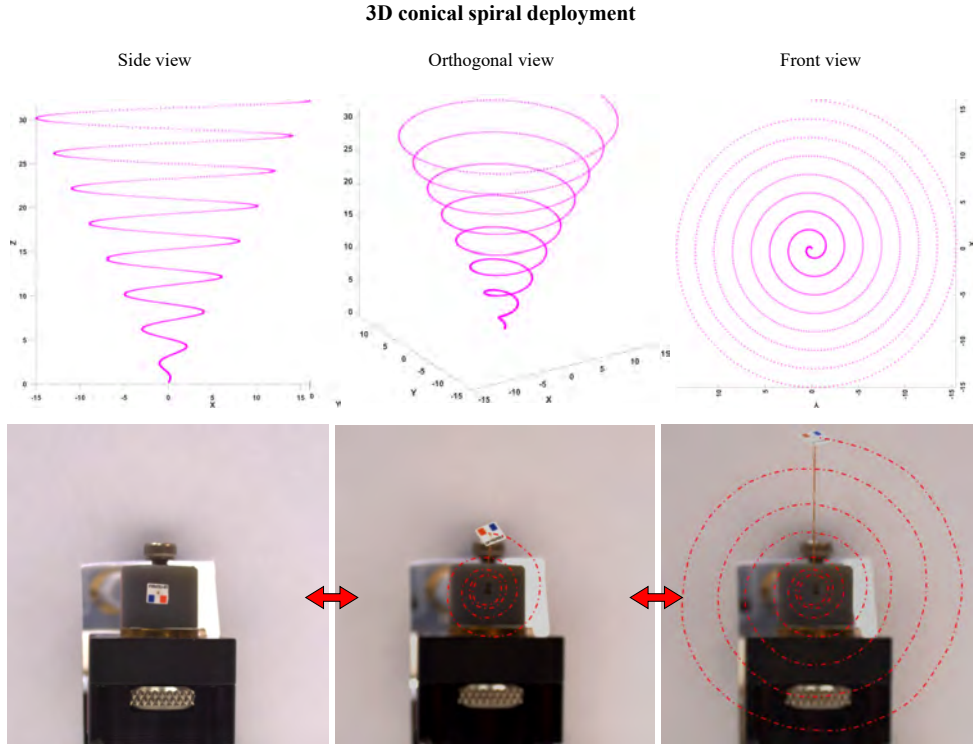


**Figure 3.10:** A 3D conical-spiral trajectory free space deployment strategy; which has a 4 x 4 mm tip attachment for better visualization during the navigation.

Table 3.5 presents the tube specifications used to demonstrate this free space deployment, as presented in Figure 3.10, (online video [here](#)). The navigation path begins in the central region and extends in a conical-spiral pattern. The distinct nature of the 3D conical-spiral deployment is described by the simulation in Figure 3.10, in which the side view shows a helical trajectory path; the orthogonal view shows a conical shape; and the front view shows a planar spiral navigation path. The experimental demonstration is presented in Figure 3.10; for better visualization, a 4x4mm paper sheet with distinct colors was attached at the tip of the inner pre-curved tube during the deployment. The conical-spiral path trajectory was achieved using the simultaneous rotation and translation of the inner pre-curved tube, which progressively expands in the workspace as it slides forward through a fixed outer straight tube and vice versa. This trajectory demonstrates the absence of stick-slip/friction of the glass CTR under translational and rotational actuation.

### 3.4.2 Helical pre-curved CTR glass deployment

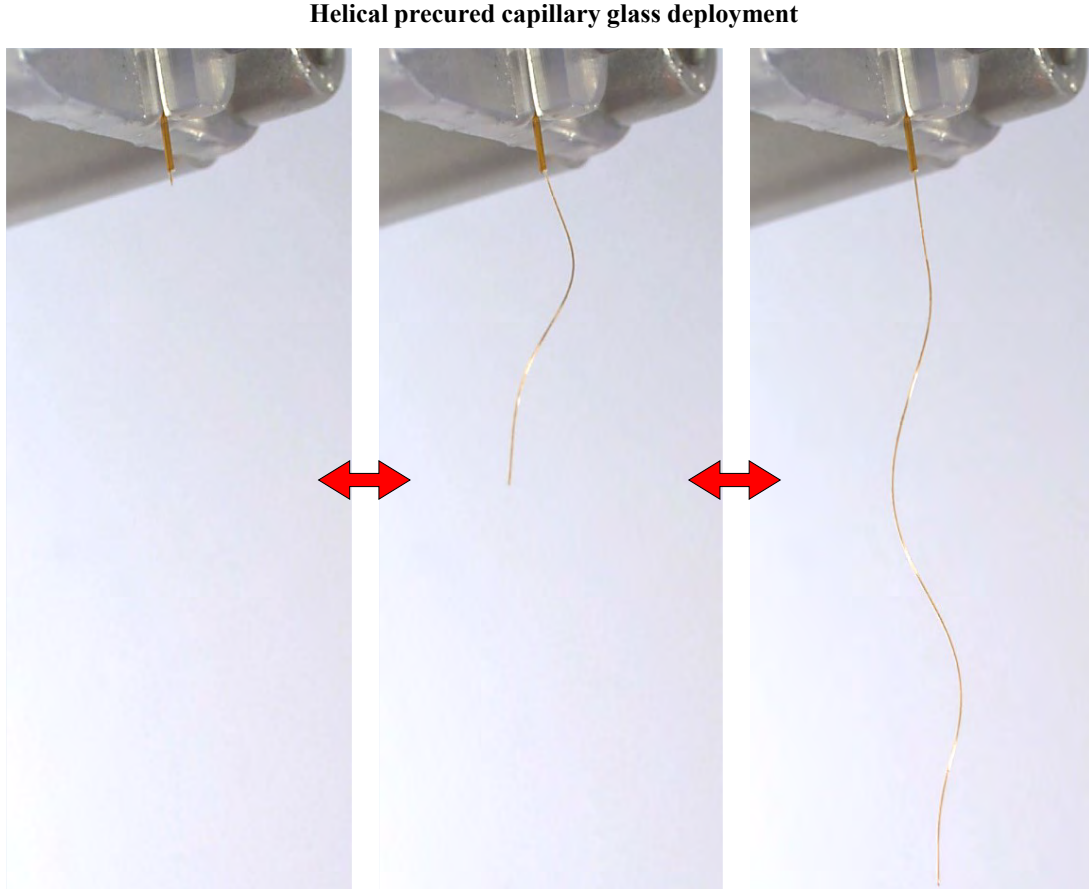


**Figure 3.11:** Demonstration of a complex helical pre-curved glass tube free space deployment, showing the flexibility of the glass tube in forward and reverse movement.

Demonstration type	Inner tube				Outer tube			
	$d_i$ [ $\mu\text{m}$ ]	$D_i$ [ $\mu\text{m}$ ]	$CT$ [ $\mu\text{m}$ ]	$R_i$ [mm]	$d_e$ [ $\mu\text{m}$ ]	$D_e$ [ $\mu\text{m}$ ]	$CT$ [ $\mu\text{m}$ ]	$R_e$ [mm]
Helical precurved (3.11)	100	164	12	H	321	434	18	$\infty$

**Table 3.6:** Prototype tube specifications for helical pre-curved CTR glass deployment

The novel fabrication approach of obtaining a pre-curved CTR glass tube was not limited to only the planar pre-curved shape. The approach was also applicable to other non-planar complex 3D shapes, such as a helix (Figure 3.2). A circular helix mold design was used and parameterized as a function of the arc-length ( $s$ ), which is obtained by:  $[x(s), y(s), z(s)]^T = [r\cos(s), r\sin(s), bs]^T$ . The radius ( $r$ ) = 1mm, pitch = 2mm,  $b = \frac{\text{pitch}}{2\pi}$  and the total arc-length = 32mm. The possibility of the free space deployment of a helical pre-curved glass CTR was demonstrated, as presented in Figure 3.10. For this demonstration, the tube specification used is given in Table 3.6, where a helical pre-curved inner tube slides through the straight outer tube. This presents a flexible helical Caturo and demonstrates its ability to

straighten its 3D backbone shape during deployment without the glass fracturing (for video demonstration see [here](#)). Similar to its planar pre-curved counterpart, irrespective of the complex shape of the pre-curved tube, the inherent flexible property is preserved. This best describes the concept of path-specific pre-curved tube prototype, obtained by adapting the complex desired path to the 3D printed mold.

### 3.4.3 Constraint deployment of CTR through needles

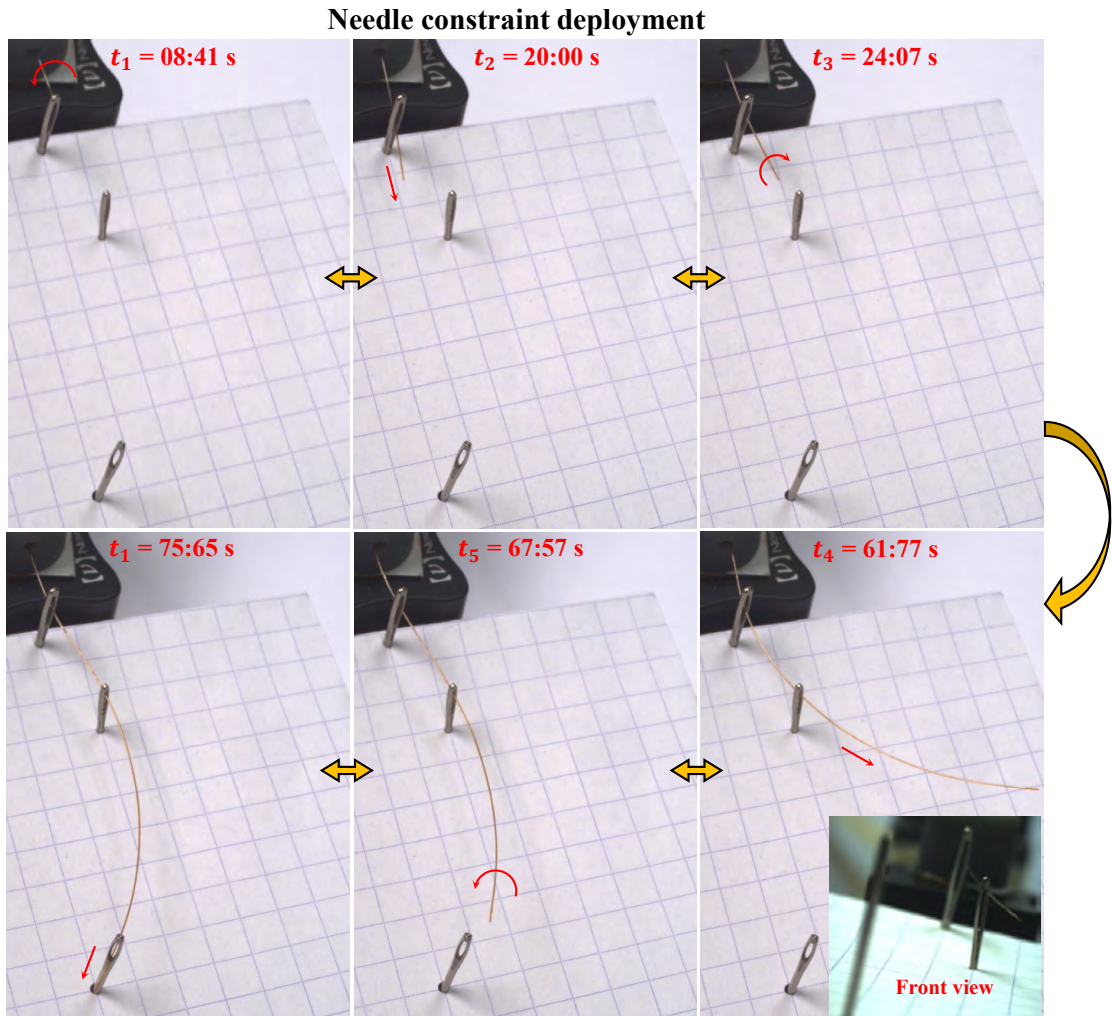


**Figure 3.12:** The robot's small scale size and its flexibility for a constraint path deployment maneuvering through a less than 1 mm orifice of three needles, using only one pre-curved tube with a 54.4mm radius of curvature.

Caturo was also used to demonstrate a constrained path deployment through the orifice of three stationed needles (each  $\sim$ 1mm in width), as displayed in Figure 3.12. It also involves a contact-aided deployment on the path with a higher radius of curvature than the robot. The flexibility of glass pre-curved tubes here

was exploited to allow us to maneuver the Caturo so that it could pass through three needle orifices to the distal point and safely navigate back again without the glass tube breaking during the navigation (online video [here](#)). For this demonstration, off-the-shelf metallic needles were used. The needles were positioned at different cross-points on the paper (see Figure 3.12). The specifications of the Caturo used for this demonstration are provided in Table 3.7; the actuation unit prototype is presented in Figure 3.3. The robot was then programmed to automatically pass through each needle opening, which involved several translations and rotation maneuvering, to ensure the constrained path was maintained throughout the path deployment. This demonstration demonstrates the flexibility and capability of the Caturo in miniaturized task-specific applications that involve complex 3D navigation through a miniature-constrained path.

Demonstration type	Inner tube				Outer tube			
	$d_i$ [μm]	$D_i$ [μm]	$CT$ [μm]	$R_i$ [mm]	$d_e$ [μm]	$D_e$ [μm]	$CT$ [μm]	$R_e$ [mm]
Needle constraint (3.12)	100	164	12	54.4	321	434	18	$\infty$

**Table 3.7:** Prototype tube specifications for constraint deployment through 3-needles

To the best of our knowledge, this is the first robot made of glass to maneuver through a small orifice of this size. This broadens the potential of applications that involve accessing areas through a small-scale aperture, such as microsurgery.

## 3.5 APPLICATIONS

The proposed application of CTRs in the literature is quite vast and mostly related to medical intervention [[Alfalahi 20](#), [Mitros 21](#)]. Although it could still be used for other applications aside from clinical intervention, which are yet to be exploited. In this section, the benefits of the miniature robot were discussed as related to how the intrinsic properties of glass for various demonstrations could lead to breakthroughs in medical applications.

### 3.5.1 Deployment of pre-curved optical fiber with laser transmission

Lasers are an important aspect of contemporary surgery. This is especially true for microsurgery, which often concerns procedures on small and fragile organs such as the eyes and vocal folds [[Fichera 21](#), [Mattos 11](#), [Mattos 21](#), [Nguyen 22](#)]. During medical interventions, lasers can cut tissue with precision due to their micron-spot-focusing capability and thermal sealing of blood vessel possibility. In fact, thermal sealing enables procedures with less blood loss [[Fichera 21](#)]. The two robotic approaches for laser aiming are the free space (this uses mirror deflection, which depends on the direct line of sight and is difficult to miniaturize for in vivo application). The other is the fiber-based approach (this uses optical fiber



**Figure 3.13:** The possibility of emitting laser through a pre-curved optical glass fiber to the end-effector tip, where the proximal end is connected to a laser source.

to remotely focus light on the surgical site). CTR dexterity could be improved by using a pre-curved optical fiber as part of the robot backbone. This is very beneficial as this approach of bringing light to the surgical site is not limited by the direct line of sight and there is room for high laser focus precision/accuracy. To actualize this, we use a fusion splicing and joining of the pre-curved optical fiber with another long part that has the right connector at its end ([Single Mode Fiber, Thorlabs](#)) (see Appendix E). The fusion ensured an effective connection to the laser source ([Thorlabs-S1FC635](#)). The obtained radius of curvature is 40mm (see Table 3.8) and Figure 3.13 presents the outcome of the laser emission at the CTR tip (video demonstration [here](#)). This demonstration of a pre-curved optical fiber Caturo, opens a new prospect for light or thermal-controlled end-effectors or manipulators, as it would be beneficial for safe/precise robot-assisted laser ablation.

Demonstration type	Inner tube				Outer tube			
	$d_i$ [μm]	$D_i$ [μm]	$CT$ [μm]	$R_i$ [mm]	$d_e$ [μm]	$D_e$ [μm]	$CT$ [μm]	$R_e$ [mm]
fibre optics precurved (3.13)	0	125 F	61	40	321	434	18	$\infty$

**Table 3.8:** Prototype tube specifications for the deployment of pre-curved optical fiber with laser transmission

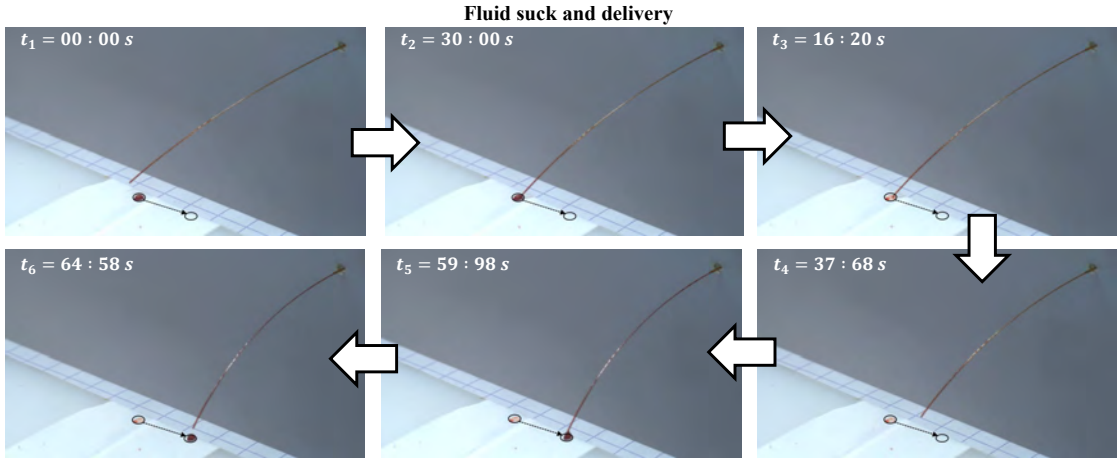


**Figure 3.14:** A two-in-one demonstration of the capability of the robot for either transferring a liquid sample or specimen from one point to another and its ability for drug delivery or sample collection.

### 3.5.2 Fluid suction and delivery

Compared to other members of the continuum robots family, the internal hollow cavity or lumen of a CTR is very beneficial. The internal hollow cavity can allow the passage of pressurized fluid (e.g., air and liquid) to the end-effector position for tip control or manipulation. The Caturo has the potential for drug delivery, as demonstrated in Figure 3.14, in addition to its 3D path deployment capability. In the context of medical intervention, Figure 3.14 features a 2-in-1 demonstration of the **ability for sample collection** and **a drug delivery capability** using the sub-millimeter glass CTR prototype. For this particular demonstration, a red ink sample (to mimic blood) was used. The distal end of the glass tube was connected to a manually operated pressurizing syringe (Figure 3.3). The robot was controlled to move to the sample collection location, which was followed by fluid suction operation and fluid delivery at the destination point, as displayed in Figure 3.14 (see video demonstration [here](#)).

Demonstration type	Inner tube				Outer tube			
	$d_i$ [μm]	$D_i$ [μm]	$CT$ [μm]	$R_i$ [mm]	$d_e$ [μm]	$D_e$ [μm]	$CT$ [μm]	$R_e$ [mm]
Fluid suck & delivery (3.14)	100	164	12	26.5	249	353	18	$\infty$

**Table 3.9:** Prototype tube specifications for fluid suction and delivery

According to this demonstration, there is a possibility for pressurized fluid flow from the proximal point to the distal end through the inner tube cavity. The demonstration also revealed the ability to hold the fluid sample at the distal tip region with a controlled pressurized air of the syringe, during sample transportation from the collection point to the delivery point. The Caturo tube specifications used for this demonstration are provided in Table 3.9. It had its internal tube glued to a long thin rubber pipe in order to connect to the syringe at the proximal end (Figure 3.3). Considering the miniature size of the robot and its ability to maneu-

ver through 3D curves, this opens up the prospect for multiple minimally invasive interventions (e.g., quick biopsy and drug delivery) through a natural body orifice or through small incision access to the surgical site, such as vitreoretinal surgery.

### 3.5.3 Vitreoretinal deployment under the OCT

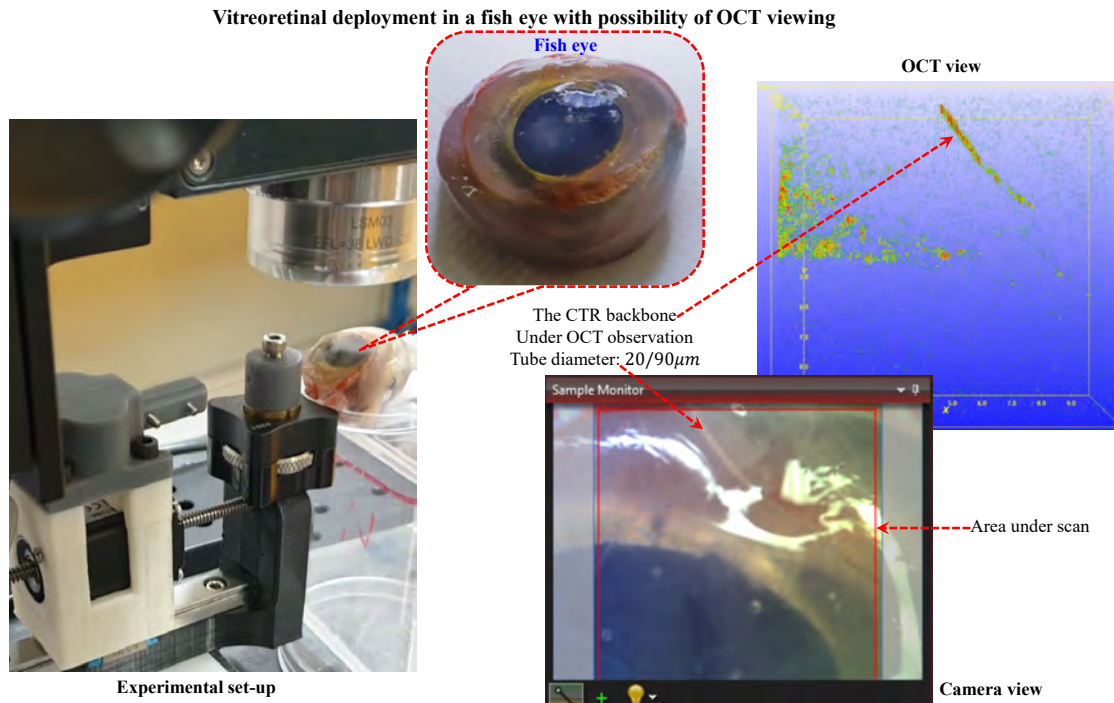


**Figure 3.15:** Vitreoretinal deployment through an eye of a fish with an OCT viewing capability.

Retinal microsurgery presents unique problems that are beyond the scope of current manual surgical technologies [Dupont 21]. The use of robotic technologies in vitreoretinal surgery has been investigated to overcome the barriers of perception, tremor, and dexterity [Ahranovich 21, Zhou 20]. Moreover, the use of CTR for this application has been proposed in [Lin 15, Wu 15, Zhou 19, Wei 09]. The benefits of robotics in vitreoretinal surgery include the use of tremor filtration that can help overcome natural human limitations, improve dexterity, enable in vivo navigation without direct visibility, enable high precision/safety, and finally facilitate possible long-distance teleoperation procedures by a specialist. Although there is a challenge posed by this procedure: the eye is delicate and small with complex nerve interconnections. The characteristics of the eye make it challenging for MIS. Considering these factors, we operate in the sub-millimeter range as presented in Figure 3.1 and Table 3.10.

Demonstration type	Inner tube				Outer tube			
	$d_i$ [μm]	$D_i$ [μm]	$CT$ [μm]	$R_i$ [mm]	$d_e$ [μm]	$D_e$ [μm]	$CT$ [μm]	$R_e$ [mm]
Vitreoretinal deployment (3.15)	20	90	12	8.9	249	353	18	$\infty$

**Table 3.10:** Prototype tube specifications for vitreoretinal deployment under the OCT

Vitreoretinal deployment operation is one of the target applications of this robot. With the internal composition of an eye (vitreous humor), CTR navigation as well as OCT visualization can be enabled. That is why we propose a vitreoretinal robot deployment, as presented in Figure 3.15 in a fish eye. The benefit of this robot (aside from its miniaturized size) is its high dexterity in small confined spaces, while simultaneously avoiding sensitive areas during its 3D path movement inside the eye. The idea is to simply use the straight external tube, which is stiffer ( $353\mu\text{m}$  of external diameter) to puncture at the entrance point, while the large workspace inside the eye is explored with the combined use of the two tubes. So there is a trade-off between flexibility and generated force to puncture the eye, which was why we used the external straight stiffer tube for puncturing. In addition to their potential biomedical applications, the CTR tube materials are bio-compatible, which makes them potentially important assets in medicine and vitreoretinal surgery. In fact, preliminary results of OCT-based position control of a CTR for an optical biopsy have already been proposed in our lab [Baran 17b] but with the use of Nitinol tubes and glass capillary at the distal end.

### 3.6 CONCLUSION AND DISCUSSION

Overall, one will notice that there has been a gradual shift from traditional open surgery to MIS due to its benefits. In addition, there is demand for further miniaturization, to benefit from deployment through sub-millimeter incision access to the surgical site or natural body orifice. This technology is particularly relevant in neurosurgery and microsurgery. In fact, all these advancements have led to the development of more innovative medical MIS tools and smarter devices. For this reason, we have proposed a sub-millimeter glass CTR called Caturo. Caturo is flexible, dexterous, and miniaturized, with the ability to pass through a 3D path to the site of interest. The novel approach of obtaining various pre-curved tube shapes in glass was achieved through thermal treatment with a thin heat-shrink polymer. The sub-millimeter diameter range (all tubes  $< 500\mu\text{m}$ ) is what made it possible to obtain a stringent and unprecedented tube radius of curvature as low as 5 mm.

Compared to Nitinol which is the dominant used material, ours has the potential for on-site fabrication and patient-specific procedures. In addition, it is low-cost, fast, and does not demand a very high temperature or time-consuming heating process, unlike Nitinol. Moreover, PET/glass has the benefit of reduced friction compared to conventional Nitinol/Nitinol, which is another very important aspect. The spring-back effect associated with this approach was also character-

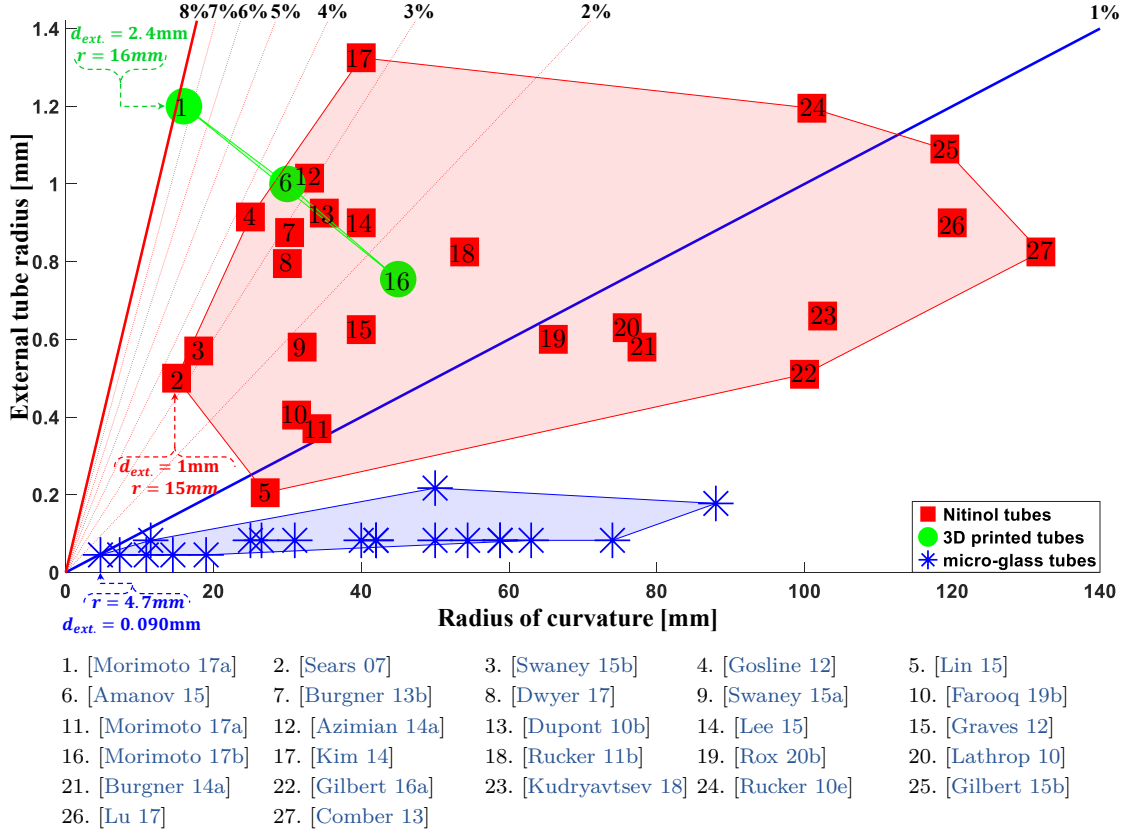


**Figure 3.16:** Sub-millimetre pre-curved glass tubes and the unprecedented region of interest we operate when comparing all the inner smallest CTR pre-curved tubes for the prototypes in the literature. It involves the conventional Nitinol (in red marker) and 3D printed technology (in green marker) and that of the sub-millimeter glass tubes (in blue marker). The external radius and radius of curvature of the innermost tube prototypes in literature were considered. The percentage lines are the recoverable maximum strain below permanent deformation or fracture for different tubes with an average of 8% for Nitinol [Webster 06a] (solid red line) and around 1% for glass [Cuellar 87] (solid blue line).

ized. By adapting the existing CTR model to the validation of the Caturo, we were able to validate the forward kinematics model, square path tracing using the inverse kinematic model, and the stability prediction/analysis of the robot. Finally, various demonstrations were carried out to present the micromanipulation capability of the robot. Due to the high demand for robots in MIS/NOTES, the valued specifications include smart capability, dexterity, and level of miniaturization [Yang 18a]. It is important to consider the ability of CTR to reach its destination without relying on any external support or influence, but rather by tube actuation at its proximal end. In addition, not only is the end-effector pose known, but the ability to estimate the entire robot backbone (Figure 3.6A), makes it ideal for in vivo anatomy deployment. The conformation of Caturo through validations (FKM, IKM, instability analysis) with the already existing model of

CTR in the literature, has shown how well the models can be adapted with glass material and on a miniaturized scale too.

As regards the state-of-the-art, the result of the fabrication of pre-curved CTR glass tubes is presented in blue in Figure 3.16. This figure highlights the region of interest for the Caturo by displaying the obtainable CTR tube radius of curvatures and the smallest diameter range with respect to the existing ones in the literature. For CTR, the recoverable strain under deformation is one of the key factors for the flexible material. Considering a single tube, the relationship between the strain limit  $\epsilon$  and radius of curvature  $R$  (without plastic deformation) in straightening a pre-curved tube is  $R = r/\epsilon + r$ , where  $r$  is the external tube radius. Note, since  $\epsilon$  is small,  $r \ll r/\epsilon$  and therefore,  $\epsilon \approx R/r$ . This relationship indicates that a miniaturized tube radius could enhance dexterity and enable mobility in tighter curves. Figure 3.16 displays the plot of strain as a function of the external tube radius and the radius of curvature for all inner tubes of the CTR prototypes in the literature. Most of the recoverable bending strain of Nitinol is considered as 8% [Webster 06a], which is represented by the straight red line in Figure 3.16; this demonstrates that all the Nitinol tubes operated below the recoverable boundary. The maximum strain of glass optical fiber before fracture is near 1% [Cuellar 87], which is represented as the straight blue line in Figure 3.16; it shows how the pre-curved sub-millimeter glass respected this boundary too. When comparing the pre-curved sub-millimeter glass tubes, to the smallest CTR prototype tubes in the literature (made of either Nitinol or 3D printed polymers), there were three key observations in Figure 3.16. First, using glass tubes to fabricate pre-curved CTR tubes with the smallest possible external diameter ( $\sim 90\mu\text{m}$ ), can permit manipulation at the sub-millimeter scale. Secondly, this fabrication method can allow deployment or manipulation within a very confined space, which is not as feasible for conventional CTRs (15 mm minimum radius of curvature in Figure 3.16 [Sears 06]). Finally, it is also possible to obtain pre-curved glass tubes with different radii of curvature and diameters, which could allow the use of micro pre-curved glass tubes along with or in place of Nitinol. Using these micro pre-curved glass tubes could either improve existing robot performance or address new applications that require a more miniaturized robot backbone.

CTR transmitting laser uses an optical fiber, which is merely passed through the cavity of the CTR inner tube [Nguyen 22]. Instead, our novel approach demonstrates that it is possible to obtain and use a pre-curved optic fiber as part of the robot's backbone (Figure 3.13). The constrained 3D path deployment, through the orifice (approximately 1 mm) of three positioned needles, highlights the maneuverability and flexibility of the robot by demonstrating its capability to follow the complex path in its entirety. This could be ideal for teleoperated operation or exploration of human non-accessible regions for maintenance checks or biopsies. Based on the demonstration of fluid suction and delivery operation of the robot in Figure 3.14, there is a possibility of fluid or light-driven actuators/sensors for functionalized end-effector integration. The demonstration presented in Figure 3.14

presents three functional capabilities associated with the Caturo: sample extraction ability (**biopsy**), sample delivery capability (**drug delivery**), and its ability to transport samples between points within an area of interest (**manipulation**). The small size of a glass capillary can be used to mimic a butterfly proboscis. Such mimicking could potentially enable other CTR applications in the future outside of medicine, such as robot-assisted indoor pollination. Furthermore, the kinematic model analysis conducted did not take into account the effect of contact friction existing between the thin external polymer and the inner glass surface. Although friction, unlike stiffness, does not determine the shape of the robot, there is still space for further investigation in this area. There are currently a few models for this phenomenon (see [Lock 11b, Ha 19]), however, they are much more complex and challenging to experimentally evaluate on a sub-millimeter scale.

On the areas of challenges, the spring-back effect is still one of the key issues in the fabrication of CTR tubes using thermal treatment approaches. This effect was also observed in the case of conventional Nitinol CTR tubes (for both the traditional air furnace-based shape setting and the electric joule heating technique) [Gilbert 16d]. For a bigger glass tube diameter, we observed that the micro-glass capillary became stiffer to bend and less effective. Therefore, this approach is quite suitable for sub-millimeter diameter glass tubes in the range of  $< 500\mu\text{m}$ . As a result, it can be complementary with an approach involving Nitinol or hybrid design in order to take advantage of both materials. Another issue is that, since the pre-curved glass tube is fixed in bending by the heat-shrink polymer, any defect in the polymer will affect the resultant tube shape. This influence on the tube shape leads to the possibility of pre-curved edges degrading over time as they slide against the sharp tip of the outer tube. For a higher curvature, this demands a thicker heat-shrink polymer that directly increases the external diameter of the pre-curved tube, which makes it challenging to slide into another during deployment. It is possible to have more than two glass CTR tubes, as demonstrated in Figure 3.1C. However, one needs to take into account the permissible clearance that will guarantee smooth sliding between each concentric tube. For this purpose, we are limited to the commercially available dimensions ([Polymicro Technologies](#)). This study was also conducted under the constraint of using tubes  $< 500\mu\text{m}$  in diameter. The tube diameter depends on the commercially available dimensions, but the smallest tube size in this experiment is the **tube-1= 90 : 20  $\mu\text{m}$** , with an achievable radius of curvature of  $\sim 5\text{mm}$  (Figure 3.3B). Therefore, the actualization of an effectively working CTR with more than two tubes will require a customized set of glass tubes, with the specified dimensions to permit free sliding or turning.



---

# Chapter 4

## Miniaturized PCR made of glass

---

<b>4.1</b>	<b>Objective</b>	110
<b>4.2</b>	<b>Robot architecture and modeling</b>	110
4.2.1	Design concept and architecture	110
4.2.2	Modeling	112
<b>4.3</b>	<b>The PCR design analysis</b>	115
4.3.1	Workspace	116
4.3.2	End-Effector Orientation	117
4.3.3	Manipulability	118
4.3.4	Stiffness	120
<b>4.4</b>	<b>Geometrical design parameter analysis</b>	122
4.4.1	Actuation length	122
4.4.2	End-effector dimension	124
<b>4.5</b>	<b>Model validation and experimental results</b>	127
4.5.1	Prototype design and fabrication	127
4.5.2	Experimental demonstrations and validations	129
<b>4.6</b>	<b>Conclusion</b>	132

## 4.1 OBJECTIVE

To tackle the limitation and challenge of large workspace/rotation associated with miniaturized parallel manipulators in the literature and discussed in Chapter 1, we present the smallest PCR capable of generating rotations over 90° of the end-effector in a tiny volume. In addition, while the vast majority of PCRs use beams and rods of metal due to their flexibility and availability, the proposed prototype uses optical glass fibers, which have the benefits of high elasticity, small diameter, and the possibility of using them to transmit energy to an active end-effector. Thus, the proposed miniaturized PCR has 3-DoFs (orientation in tip/tilt angles and the end-effector contraction/extension), which were actualized using 3 glass optical fibers arranged in 120° apart. The robot was used to demonstrate various path movements e.g. circular and square in vertical and horizontal planes using the inverse kinematic model (IKM). Its miniaturized design could permit integration onto an endoscope or multi-backbone robot tip for enhanced dexterity in micro-manipulation operation. One key possible application of the proposed PCR is the sample handling under SEM which will benefit from the large tip and tilt angles of the end-effector in a tiny volume. In fact, in this Chapter, we also investigated in detail the effect of the geometrical parameters of the robot in terms of the achievable workspace, stiffness, and manipulability, followed by assessing experimentally the workspace and the model validation on different path followings.

## 4.2 ROBOT ARCHITECTURE AND MODELING

The architectural design of the miniaturized glass PCR is characterized by high workspace volume due to its structural design and kinematics. The robot architecture is focused on using three legs with the specific configuration presented in Figure 4.1, to obtain 3-DoFs with a large workspace in a confined space, though there are other configuration possibilities as discussed in Chapter-1. The details of the robot design concept, modeling, and prototype are discussed below as follows.

### 4.2.1 Design concept and architecture

The schematic of the 3-leg miniaturized glass PCR is shown in Figure 4.1. Basically, the components of the robot's mechanical structural design include 1) an end-effector, 2) legs 3) a fixed base, and 4) an actuation unit.

#### 4.2.1.a End-effector

This is located at the distal end of the robot, which can also be called the mobile platform. It is usually used to hold the robot link in position at the top and could be functionalized for a target application. The design shape of the end-

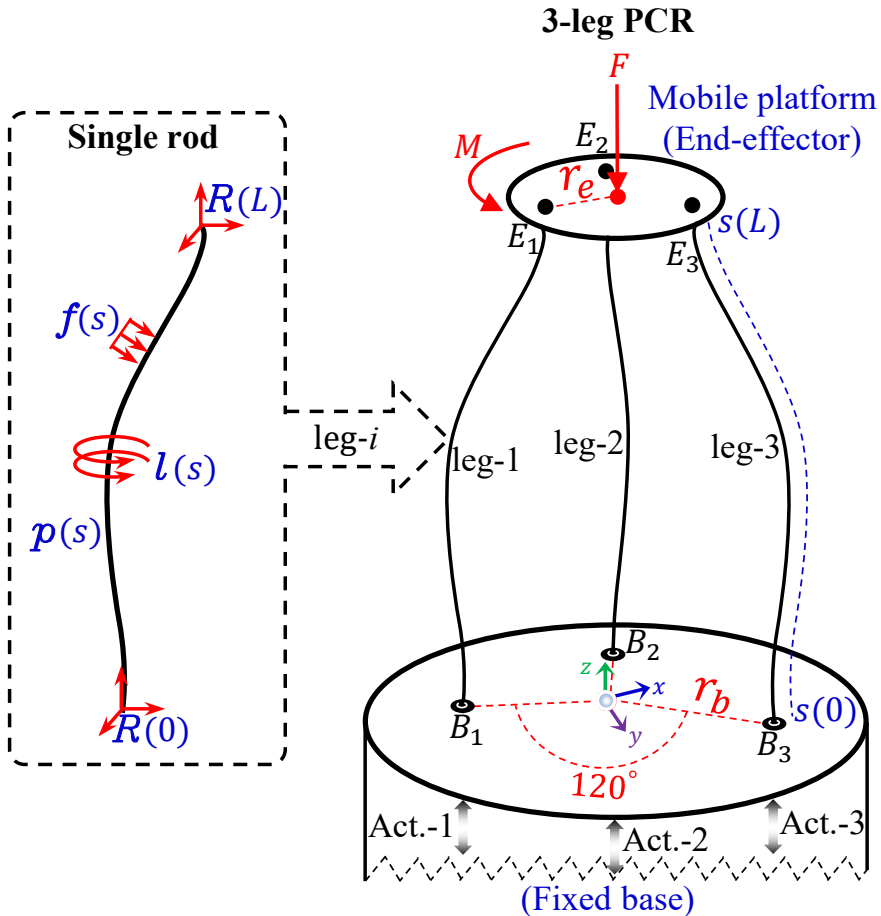


**Figure 4.1:** The schematics of the 3-leg Glass PCR and considering a flexible single rod for the Cosserat rod formulation

effector is circular with a circumradius  $r_e$ . The effect of variation of end-effector dimension as a function of the robot geometrical parameter was analyzed in detail in the subsequent Section.

#### 4.2.1.b legs

These consist of three straight and flexible standard glass optical fibers  $i \in [1, 3]$  considered as rod. While one end is fixed to the end-effector, the other is connected to the actuator unit. In this thesis, we have considered the use of linear actuation, which is located below the fixed base (Figure 4.1). The region above the fixed base is called the robot's flexible part because the robot configuration depends on the link deformation upon actuation. The different rod lengths are used to actualize different robot configurations. The movement from one neutral configuration to another is used to actualize linear robot translation/displacement in the  $z$ -axis. Uneven leg configuration results in tilting/bending of the robot end-effector about  $x$ - and  $y$ -axis.

### 4.2.1.c Fixed base

This comprises the base structure that gives fixed stable frame to the robot and provides the path through which each optical fiber passes when actuated. The hole design pattern is given in Cartesian coordinate at points  $B_1, B_2$  and  $B_3$ , which are arranged  $120^\circ$  apart on a circumradius of  $r_b$  (Figure 4.1).

### 4.2.1.d Actuation unit

This provides the linear translation of each link with an actuation range  $L^* \leq q_i \leq L$ , for  $i \in [1, 3]$ . In addition, this also provides the support upon which the rods are attached. The different robot configurations and end-effector poses are achieved by varying the different linear joint variables  $q_i$ .

## 4.2.2 Modeling

### 4.2.2.a BVP of 3leg PCR

For predicting the pose/configuration of a PCR, a geometrical exact model is important. To model the proposed miniaturized 3-leg glass PCR, we applied the modeling framework proposed in [Black 18a, Till 15], which treats a PCR as a boundary value problem (BVP) by neglecting the dynamics of the rod. With the Cosserat rod framework [Antman 05], a rod can be described by a  $12 \times 1$  vector of twist and wrench along its arc length. Additional constitutive laws relating to the kinematics variables and material strain (bending, torsion, shear, and extension)

**Table 4.1:** Notation and definitions

Symbol	Definition	Symbol	Definition
$*$	In a stress free state	$\mathbf{K}_{se,i} \in \mathbb{R}^{3 \times 3}$	Shear & extension stiffness matrix diag([GA, GA, EA])
$'$	Derivative with respect to arc-length	$\mathbf{K}_{bt,i} \in \mathbb{R}^{3 \times 3}$	Bending and torsion stiffness matrix diag([EI, EI, GJ])
$\hat{\cdot}$	Convert $\mathbb{R}^3$ to $\mathfrak{so}(3)$	$A \in \mathbb{R}$	Area of link cross-section ( $\pi r^2$ )
$\check{\cdot}$	Inverse of $\hat{\cdot}$ operation e.g. $(\hat{a})\check{=} = a$	$\rho \in \mathbb{R}$	Link material density
$s \in \mathbb{R}$	Reference arc length	$\mathbf{g} \in \mathbb{R}^3$	Gravitational acceleration vector
$i \in [1, 3]$	link indexing	$\mathbf{f} \in \mathbb{R}^3$	Distributed force/weight ( $\rho A g$ )
$L_i \in \mathbb{R}$	Rod length from base to the end-effector	$\mathbf{l} \in \mathbb{R}^3$	Distributed moment but neglected
$r_e \in \mathbb{R}$	Radius of the end-effector from its centroid	$\mathbf{F} \in \mathbb{R}^3$	External applied force at end-effector centroid in global frame (& gravity acting on the end-effector)
$r_b \in \mathbb{R}$	Radius of the base-plate from its centroid	$\mathbf{M} \in \mathbb{R}^3$	External applied moment at end-effector centroid in global frame
$\theta_i^b \in \mathbb{R}$	Angle between two links at the base-plate	$\mathbf{p}_e \in \mathbb{R}^3$	Position of end-effector centroid in global frame
$\theta_i^e \in \mathbb{R}$	Angle between two links at the end-effector	$\mathbf{R}_e \in \text{SO}(3)$	Orientation of end-effector centroid in global frame
$\mathbf{p}_i(s) \in \mathbb{R}^3$	Position of $i$ th link as a function of $s$	$\alpha \in \mathbb{R}$	End-effector roll angle in global frame
$\mathbf{R}_i(s) \in \text{SO}(3)$	Orientation of $i$ th link as a function of $s$	$\beta \in \mathbb{R}$	End-effector pitch angle in global frame
$\mathbf{v}_i(s) \in \mathbb{R}^3$	Link linear rate of change in the local frame and its stress-free state is $\mathbf{v}^* = [0 \ 0 \ 1]^T$	$\mathbf{q}_i \in \mathbb{R}^3$	Actuation/Motor displacement in $z$ -axis position
$\mathbf{u}_i(s) \in \mathbb{R}^3$	Link curvature in the local frame and its stress-free state is $\mathbf{u}^* = [0 \ 0 \ 0]^T$	$L_i^* \in \mathbb{R}$	Link length at minimum actuation stroke length ( $\mathbf{q}_i = 0$ )
$\mathbf{m}_i(s) \in \mathbb{R}^3$	Internal moment in the link in global coordinate	$\mathbf{J} \in \mathbb{R}^{3 \times 3}$	Jacobian matrix mapping changes in end-effector position ( $\mathbf{p}_e$ ) to change in actuation variable ( $\mathbf{q}_i$ )
$\mathbf{n}_i(s) \in \mathbb{R}^3$	Internal force in the link in global coordinate	$\mathbf{K} \in \mathbb{R}^{3 \times 3}$	Stiffness matrix mapping changes in end-effector position ( $\mathbf{p}_e$ ) to change in external force ( $\mathbf{F}$ )
$G \in \mathbb{R}$	Shear modulus of link material	$J \in \mathbb{R}$	Polar moment of area about $z$ -axis ( $2I$ )
$E \in \mathbb{R}$	Young's modulus of link material	$I \in \mathbb{R}$	Second moment of area about $x$ - and $y$ -axis ( $\frac{\pi r^4}{4}$ )

are also considered. Using the Cosserat rod framework and considering a rod as a function of arc length ( $s$ ) (see Figure 4.1), the following differential equations were derived using static Cosserat rod model approach detailed in Table 4.2. For simplicity and brevity, the meaning of all the variables and symbols used in this chapter are summarized in Table 4.1.

Rod equations	Remarks on their physical meaning
$\dot{\mathbf{p}} = \mathbf{R}\mathbf{v}$	the rod's Cartesian centerline position $\mathbf{p}(s) \in \mathbb{R}^3$ evolves along the arc length according to this differential kinematic relation.
$\dot{\mathbf{R}} = \mathbf{R}\hat{\mathbf{u}}$	also, the rotation matrix $\mathbf{R}_i(s) \in SO(3)$ evolves along the rod arc length according to this differential kinematic relationship.
$\dot{\mathbf{v}} = \mathbf{v}^* + \mathbf{K}_{se}^{-1} \mathbf{R}^T \mathbf{n}$	using some material constitutive law (stress-strain) involving the stiffness homogeneous transformation matrix of shear and extension $\mathbf{K}_{se}^{-1}$ to relate the rod internal forces $\mathbf{n}(s)$ to the rod linear rate of change $\mathbf{v}(s) \in \mathbb{R}^3$ , analogous to velocity vector.
$\dot{\mathbf{u}} = \mathbf{u}^* + \mathbf{K}_{bt}^{-1} \mathbf{R}^T \mathbf{m}$	applying material constitutive law/equation involving the stiffness homogeneous transformation matrix of bending and torsion $\mathbf{K}_{bt}^{-1}$ to relate the rod internal moments $\mathbf{m}(s)$ to the angular rate of change $\mathbf{u}(s) \in \mathbb{R}^3$ , analogous to curvature vector. The curvature vector is similar to the angular velocity vector of a rigid body expressed in body-frame coordinates, except the derivative is with respect to arc length instead of time.
$\dot{\mathbf{n}} = -\mathbf{f}$	the differential equation for internal force $\mathbf{n}(s)$ considering the force balance on some infinitesimal slice of the rod for static equilibrium case.
$\dot{\mathbf{m}} = -\dot{\mathbf{p}} \times \mathbf{n} - \mathbf{l}$	the differential equation for the internal moment $\mathbf{m}(s)$ derived from considering the moment balance of an infinitesimal rod section.

**Table 4.2:** Static Cosserat rod equations expressed as a set of nonlinear ODEs in the arc length dimension.

Although the Cosserat rod model merely describes the shape evolution of each individual link. The overall robot modeling has to take into account the inherent boundary conditions (proximal and distal), due to the PCR structural design e.g. the geometrical constraints, and rigid body static equilibrium (Refer Figure 4.1). These are provided as a set of boundary equations given below Table 4.3.

Boundary conditions/equations	Remarks on their physical meaning
$\mathbf{p}_i(0) = r_b[\cos\theta_i^b, \sin\theta_i^b, 0]^T$	the pose boundary condition imposed by baseplate due to the chosen hole attachment pattern in Cartesian coordinates.
$\mathbf{r}_i = r_e[\cos\theta_i^e, \sin\theta_i^e, 0]^T$	pose boundary conditions imposed due to the hole pattern at the mobile platform or end-effector. It gives a constant vector in the local end-effector frame from the platform centroid to a rod attachment point.
$\mathbf{p}_i(L_i) = \mathbf{p}_e + \mathbf{R}_e \mathbf{r}_i$	the end-effector joins the three rods, resulting in attachment constraints which gives this position constraint equation considering the end-effector centroid in global coordinates $\mathbf{p}_e$ and the rotation $\mathbf{p}_e$ .
$[\log(\mathbf{R}_i(L_i)^T \mathbf{R}_e)]^\vee = \mathbf{0}$	whereas this give the geometrical attachment constrain as regards to the orientation constrain equation, considering that the rods ends are glued to fixed position.
$\mathbf{F} = \sum_{i=1}^3 [\mathbf{n}_i(L_i)]$	rigid body static equilibrium equation due to external force vectors $\mathbf{F}$ , acting or applied at the mobile platform or end-effector centroid. The weight of the platform can be accounted for by $\mathbf{F} = mg$ .
$\mathbf{M} = \sum_{i=1}^3 [\mathbf{m}_i(L_i) + \mathbf{R}_e^T \mathbf{r}_i \times \mathbf{n}_i(L_i)]$	rigid body static equilibrium equation considering the case of external moment vectors $\mathbf{M}$ , acting or applied at the mobile platform or end-effector centroid.

**Table 4.3:** The boundary conditions for the entire robot modeling which consist of the hole attachment pattern leading to the geometric constrain equations and the rigid body equilibrium equation due to external wrench (force and moment) acting on the end-effector.

The overall robot derivation is composed of each rod modeled by the Cosserat rod equations with a linear elastic constitutive equation (Table 4.2) and the boundary conditions presented in Table 4.3. From the computation, the actuator link displacement for the particular robot configuration is derived as  $q_i = L_i - L_i^*$ .

#### 4.2.2.b Numerical solution with shooting method

The shooting method was used for solving the BVP model. Although this numerical approach comes with the price of convergence problems and computational burden for its accuracy. One benefit is that the same model formulation can be used for both the forward kinematic model (FKM) and the inverse kinematic model (IKM) by using the respective input guess comprising the unknown and input variables (Table 4.4).

Kinematic model	Unknowns variables	Input variables	Output variables
FKM	$\mathbf{p}_e, \mathbf{R}_e, \mathbf{n}_i, m_i$	$\mathbf{q}_i$	$\mathbf{p}_e, \mathbf{R}_e$
IKM	$\mathbf{q}_i, \mathbf{n}_i, \mathbf{m}_i$	$\mathbf{p}_e, \mathbf{R}_e$	$\mathbf{q}_i$

**Table 4.4:** The FKM and IKM with their respective different unknowns, inputs, and output variables for the numerical computation using the shooting method.

The shooting method iteratively updates the guess values of the unknowns and output variables until the boundary conditions are satisfied within the solver tolerance (Figure 4.2). The non-linear optimization solver applies the Levenberg-Marquardt/Trust-Region-Dogleg algorithm while using the “ode45” MATLAB function to integrate the rod, for each nested loop numerically.

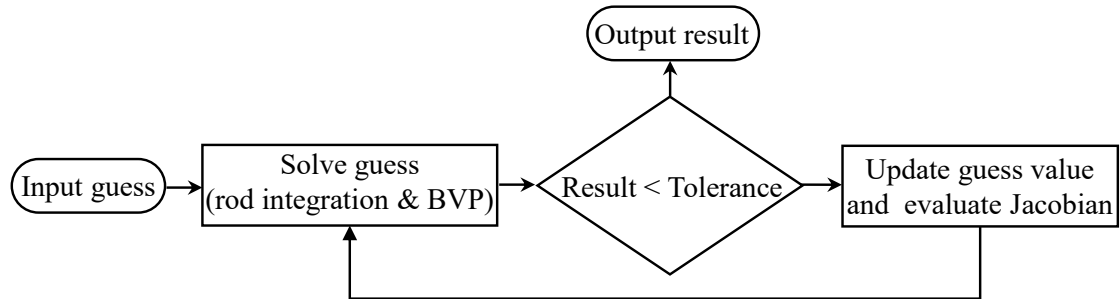


**Figure 4.2:** The miniature glass 3-leg PCR shooting method solver flowchart for the FKM and IKM. The variables to be evaluated for either the FKM or the IKM are given in Table 4.6.

## 4.3 THE PCR DESIGN ANALYSIS

We consider the end-effector and base link arrangement pattern to be an equilateral triangle on a circumradius  $r_e$  and  $r_b$  respectively (Figure 4.1). While the end-effector translates in the  $z$ -axis and bends about the  $x$ -axis (roll) and  $y$ -axis (pitch), the base is fixed in position. In addition, equal tube length is considered for each link of the PCR design, and all the dimensions are defined in the global base frame. The initial configuration of the end-effector platform is given

as  $p_e = [0, 0, L^*]^T$ . The links are coupled to the end-effector by a fixed joint, such that  $\mathbf{R}_e = \mathbf{R}_i$  at the end-effector position. Likewise, the legs have a fixed orientation at the base, since it is set fixed/glued to the linear actuators. The robot design is highly dependent on the geometrical parameters and choice of materials, for the obtainable workspace/pose, manipulability, and stiffness. In the following, we investigated the different design variables, which are analyzed in detail below.

### 4.3.1 Workspace

The workspace is the volume enclosure reachable by the PCR end-effector position  $\mathbf{p}_e$  and orientation  $\mathbf{R}_e$ , for the different obtainable configurations. These are obtained by sampling the actuation variable  $\mathbf{q}_i$ . The workspace is derived as the pose (position and orientation) of the end-effector centroid with respect to each robot's configuration, for different discretized iterations of actuation variable  $\mathbf{q}_i$ . For each iteration of  $\mathbf{q}_i$ , the FKM is computed via the shooting method, which derives the end-effector centroid pose from the boundary conditions defined by the actuator positions. Using the material property of a standard single-mode optical fiber with  $125\mu\text{m}$  diameter and imposing robot geometrical parameters of  $r_e = 0.5\text{mm}$ ,  $r_b = 5r_e$ ,  $l_i = 12r_e$  and  $\mathbf{q}_i = 18r_e$ , just like the experimental pro-

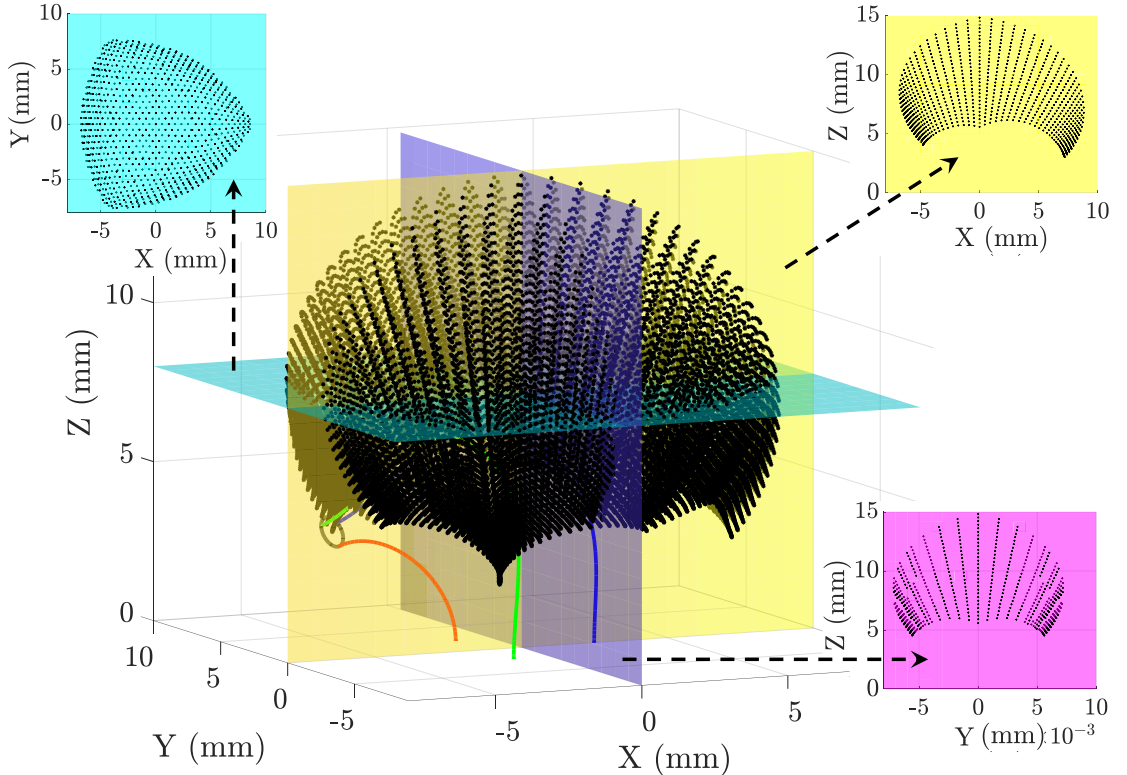


**Figure 4.3:** Workspace of the miniature glass PCR showing the different plane cuts and its boundary shape. This is used to compute the achievable workspace volume of the robot.

totype. We evaluated the workspace of the PCR in the vertical x-axis plane at  $x = 0$ , the vertical y-axis plane at  $y = 0$ , and the horizontal plane cut at  $z = 8\text{mm}$  respectively (see Figure 4.3).

The  $\mathbf{q}_i$  within the vertical and horizontal plane cut of the workspace is then used further to analyze the workspace, the pose of the robot end-effector centroid, manipulability, and robot stiffness for the different configurations in the selected planes. For better visualization and detailed analysis with regard to the evolution of the PCR variables under investigation,  $\mathbf{q}_i$  iterates for 27,000 different combinations of sample points.

Figure 4.3 presents the entire workspace of the miniaturized PCR, which covers a volume space of  $1174\text{mm}^3$ . The result from the top view or the horizontal plane cut of the PCR workspace depicts a boundary shape of a “Reuleaux triangle”. This has a constant width curve property [Wikipedia 22] as all points on the boundary side are said to be equidistant from the opposite vertex. By Blaschke–Lebesgue theorem, the area enclosed by a Reuleaux triangle with width  $w$  is given by  $\approx 0.70447w^2$ . Therefore, the boundary area of Figure 4.3 for the horizontal plane cut at  $z = 8\text{mm}$  (in light green), using Blaschke–Lebesgue theorem gives  $162.8\text{mm}^2$  as  $w = 15.2\text{mm}$ , and then, using MATLAB boundary function (default shrink factor of 0.5) computes the boundary area as  $169.9\text{mm}^2$ . This confirms and validates theoretically, the result shape of the robot workspace model computation for the miniaturized glass PCR.

### 4.3.2 End-Effector Orientation

The end-effector orientation is the rotation angle of the end-effector centroid about the  $x$ - and  $y$ -axis, which is represented as the roll angle and pitch angle respectively. It is computed for the different robot configurations within the various plane cuts in the workspace. The roll angle is taken as the rotation about the x-axis as Figure 4.4A presents the color map of the obtainable roll angle, for the different robot configurations within the workspace. From the color gradient, one will notice that all the roll angles are 0 in the vertical cut plane at  $x = 0$ . Whereas it spreads radially in the other planes, which has a value of  $+117^\circ$  to  $-82^\circ$ . For the pitch angle, Figure 4.4B presents the color gradient for the variation of the end-effector rotation about the  $y$ -axis. Again, one will see that the pitch angle for all points in the  $y$ -axis is 0, whereas, for  $x$ -axis, its value ranges between  $\pm 84^\circ$ . This is due to the PCR leg arrangement pattern, which permits higher bending in the  $x$ -axis plane more than in the  $y$ -axis plane for the different robot configurations (see the different planar cut of Figure 4.3). The result of the design analysis is very important in terms of visualizing the different obtainable orientations in roll and pitch angles within the workspace. It is also a very useful parameter for addressing future application requirements or specifications.

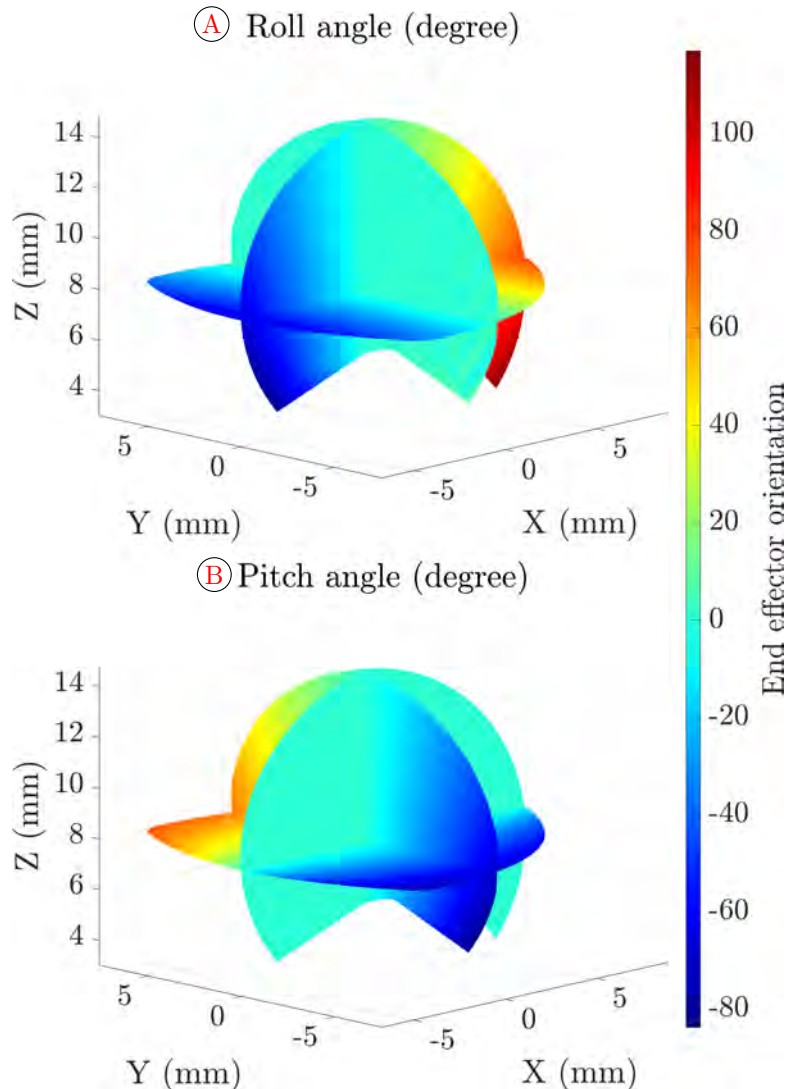


**Figure 4.4:** Variation of end-effector orientations within the workspace, **A)** end-effector rotation about the  $x$ -axis, whereas **B)** end-effector rotation about the  $y$ -axis.

### 4.3.3 Manipulability

Manipulability is the measure of the robot's motion capability at a given configuration. To investigate the manipulability of the miniature glass PCR, we evaluated the condition number at every configuration in the sampled points within the workspace. Here, we used the 2-norm condition number  $\eta$  of the Jacobian matrix  $\mathbf{J}$ , given in Equation 4.1.

$$\eta = \sqrt{\frac{\lambda_{min}(\mathbf{J}^T \mathbf{J})}{\lambda_{max}(\mathbf{J}^T \mathbf{J})}} \quad (4.1)$$

where  $\lambda_{max}$  and  $\lambda_{min}$  are the largest and smallest eigenvalues of  $\mathbf{J}^T \mathbf{J}$  respectively. With this measure, if the condition number approaches 1, this denotes high manipulability. If it approaches 0, it denotes less manipulability and toward singularity configuration which occurs at 0. The Jacobian matrix  $\mathbf{J}$  used for the robot manipulability analysis is computed by observing the change in the end-effector position  $\mathbf{p}_e$  due to a small increment in the joint values  $\mathbf{q}_i$ . The finite difference approach was used (Equation 4.2), where each  $i^{th}$  column of the Jacobian is computed by increasing the joint input  $q_i$  by a small amount.

$$\mathbf{J} \approx \begin{bmatrix} \frac{\mathbf{p}_e - \mathbf{p}_e^*}{\Delta q_1} & \frac{\mathbf{p}_e - \mathbf{p}_e^*}{\Delta q_2} & \frac{\mathbf{p}_e - \mathbf{p}_e^*}{\Delta q_3} \end{bmatrix} \quad (4.2)$$

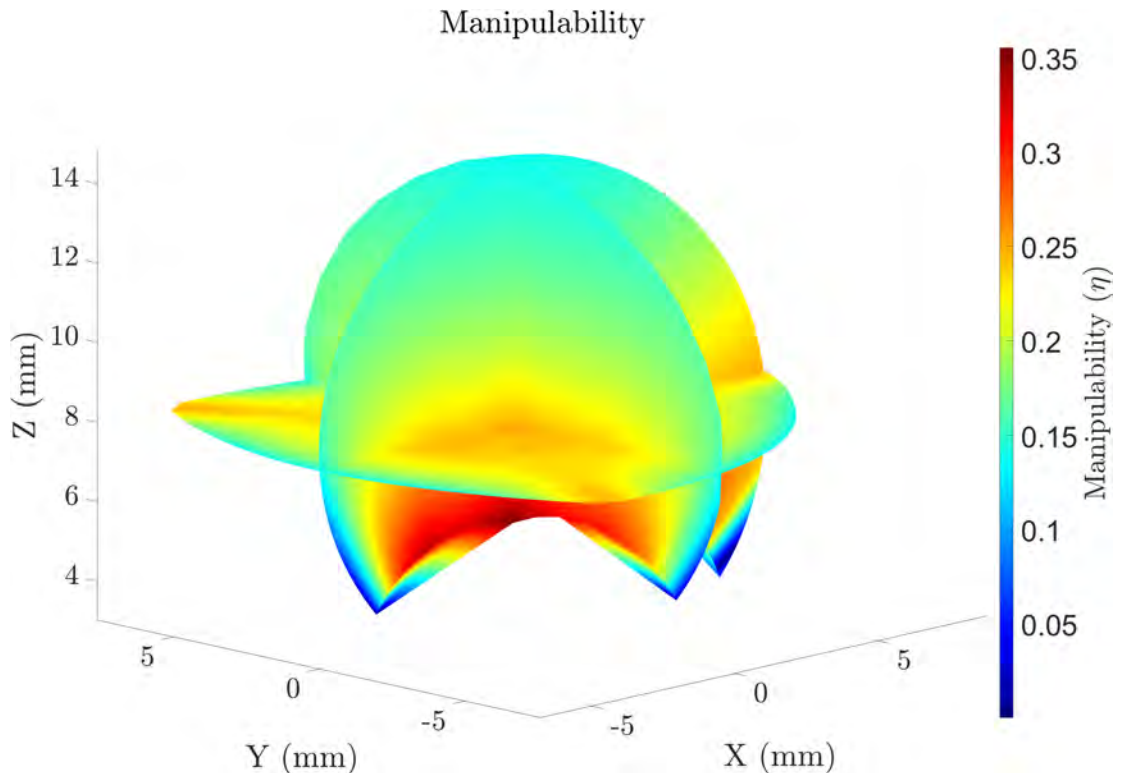


**Figure 4.5:** Robot manipulability in terms of condition number with the workspace which reduces as it spread to the boundary region and maximum at the central part.

The result for the overall computation for the different robot configurations within the workspace, when considering the three-plane cut is presented in Figure 4.5. It shows that the manipulability of the robot is maximum at the central bottom region and decreases radially within the workspace as the robot moves further away towards the boundary. In the Jacobian matrix, we only focused on the use of end-effector position for every configuration, while neglecting the orientation aspect due to the complications of working with their different units. Although we also evaluated  $m = \sqrt{\det(\mathbf{J} \mathbf{J}^T)}$  for the manipulability measure metric, however, that of Equation 4.2 was much more interesting in its representation and

easy to understand as clearly shown in Figure 4.5. Moreover, each manipulability metric approach tends to have its own drawback or issue of representation in a given context e.g. using the ellipsoids approach for a workspace representation will be challenging and hard to intuitively understand. Notwithstanding, we believe that the chosen manipulability measure metric used is sufficient in analyzing and representing the manipulability of the different robot configurations within the workspace.

#### 4.3.4 Stiffness

The stiffness represents the robot's resistance to an externally applied wrench, which comprises a force  $\mathbf{F}$  and a moment  $\mathbf{M}$  (refer to Figure 4.1). This analysis is useful to understand the load-carrying capacity of the PCR for the robot configuration within its workspace. However, the focus of this paper is basically on the robot stiffness due to an applied force. In that regard, we investigated the stiffness of the various plane cuts of the workspace. The comparative result for the different stiffness when a small force is applied in  $x$ -,  $y$ -, and  $z$ -axis is presented in Figure 4.6A, 4.6B, & 4.6C respectively.

Generally, each of the results obtained shows that the stiffness significantly varies with respect to the configuration of the robot within the workspace and also on the direction of the applied force  $F$  e.g in  $x$ -direction (Figure 4.6A),  $y$ -direction (Figure 4.6B) or in  $z$ -direction (Figure 4.6C). The stiffness matrix  $\mathbf{K}$  for each robot configuration within the workspace is computed by the finite difference approach, by observing the change in end-effector position  $\mathbf{p}_e$  due to the small incremental change in the applied force  $\Delta F_i$ , as given in Equation 4.3.

$$\mathbf{K} \approx \begin{bmatrix} \frac{\mathbf{p}_e - \mathbf{p}_e^*}{\Delta F_x} & \frac{\mathbf{p}_e - \mathbf{p}_e^*}{\Delta F_y} & \frac{\mathbf{p}_e - \mathbf{p}_e^*}{\Delta F_z} \end{bmatrix} \quad (4.3)$$

Figure 4.6A–C shows the result of the output stiffness evaluated for the various selected plane within the workspace. Analyzing the stiffness when the force is applied in the  $x$ -,  $y$ -, and  $z$ -axis shows that the stiffness in the  $z$ -axis is the maximum and almost 15 times those in the  $x$ - and  $y$ -axis. Generally for each case, the stiffness is maximum around the central bottom and then spread radially to the boundary of the workspace, where they are minimum. Considering Figure 4.6A where the applied force is in the  $z$ -axis, one would observe that the stiffness is always maximum at the central axis for the neutral configurations (all links equal) and then decreases as the robot tilt or bend away from this axis towards the boundary of the workspace. The stiffness value for each point in the workspace when the force is applied in  $x$ - and  $y$ -axis are not the same, this is due to the robot leg arrangement, where leg-1 is aligned on the  $x$ -axis while leg-2 and leg-3 are aligned at  $120^\circ$  apart. Therefore, the arrangement of the leg pattern

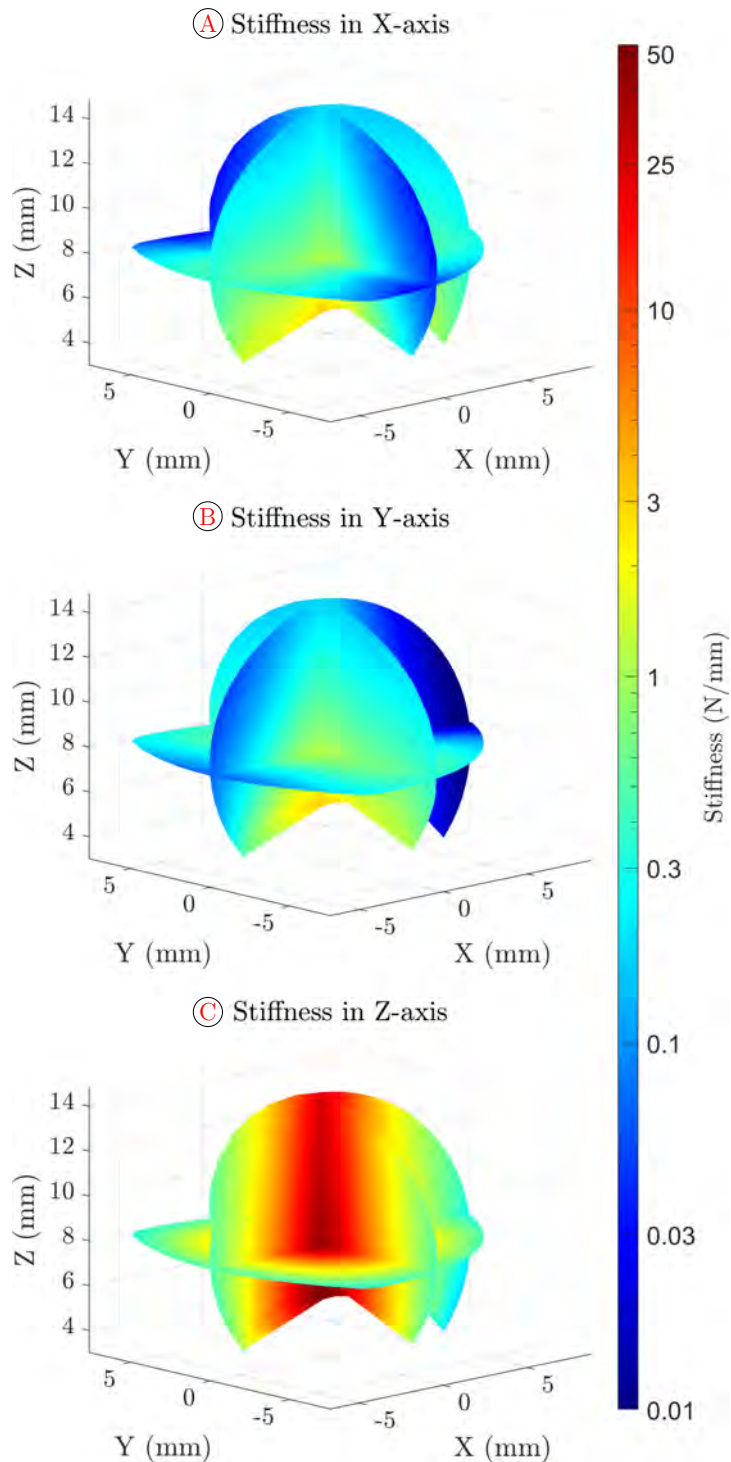


**Figure 4.6:** Variation of stiffness at different configurations of the robot within the workspace, while considering different of the applied load, **A)** along the  $x$ -axis, **B)** along the  $y$ -axis, and **C** along the  $z$ -axis which is the maximum.

influences the stiffness for the different configurations with respect to the applied force direction, as this is seen as the color gradient in Figure 4.6B and Figure 4.6C for  $x$ - and  $y$ -direction respectively.

The end-effector mass is 5.8mg and using a simple mass-spring system, its natural frequencies are about 2kHz in  $x$  and  $y$  directions (taking the stiffness from Figure 4.6 at the center of the horizontal cut  $z = 8$ ). This is considerably higher than the bandwidth of the micro servomotor which is given to travel 9.1mm in 0.14s. This is one of the key reasons why we used the quasi-static modeling approach because it gives a computationally efficient framework for analysis and has been widely used for planning and control [Halm 18]. It is also important when considering a system under equilibrium, which can be related to the modeling involving the rigid body equilibrium and boundary conditions that have to be met.

## 4.4 GEOMETRICAL DESIGN PARAMETER ANALYSIS

The two main considerations for designing a PCR are the material properties and then, the geometrical parameters of the robot. The material properties relate to the inherent properties of the material, for the active part of the PCR e.g. Young's modulus and Poisson ratio which depends on the type of material. Whereas, the geometrical parameter relates to the material dimension, geometric shape, and sizes, along with coupling or structural design. Since we are focused on the use of one material (glass optical fiber), therefore the major analysis is on the effect of the PCR geometrical parameters. The arc length is one of the geometrical key parameters for the PCR design. This variable invariably relates to the actuation length  $\mathbf{q}_i$  of the robot for any given configuration. Another geometrical key parameter of consideration is the effect of the end-effector dimension since this represents the output section of the robot ( $\mathbf{p}_e$  and  $\mathbf{R}_e$ ). Therefore, we investigated the effect of the actuation length and the end-effector dimension, which are detailed below.

### 4.4.1 Actuation length

The variation in the actuation length (linear translation), changes the arc length of the robot. It is very important to analyze the effect of the actuation length, which relates to the variation of arc length that results in the corresponding change of the robot backbone configuration. This is very crucial to PCR design because this parameter helps to determine or easily infer 1) the area of reachable workspace e.g  $L_1, L_2, L_3, L_4, L_5$  and  $L_6$ , 2) the stable or maximum safe region of operation e.g see Figure 4.7 and lastly, 3) the region of desired stiffness/manipulability that best suit the given task. Therefore keeping all the parameters of the robot the same, while varying only the actuation length gives the plot in Figure 4.7. For this analysis, the specification of the robot is given as  $r_e = 0.5\text{mm}$ ,  $r_b = 10r_e$ ,  $L_i^* = 14r_e$ , and  $\mathbf{q}_i = 66r_e$ , which are all specified with respect to the end-effector radius.

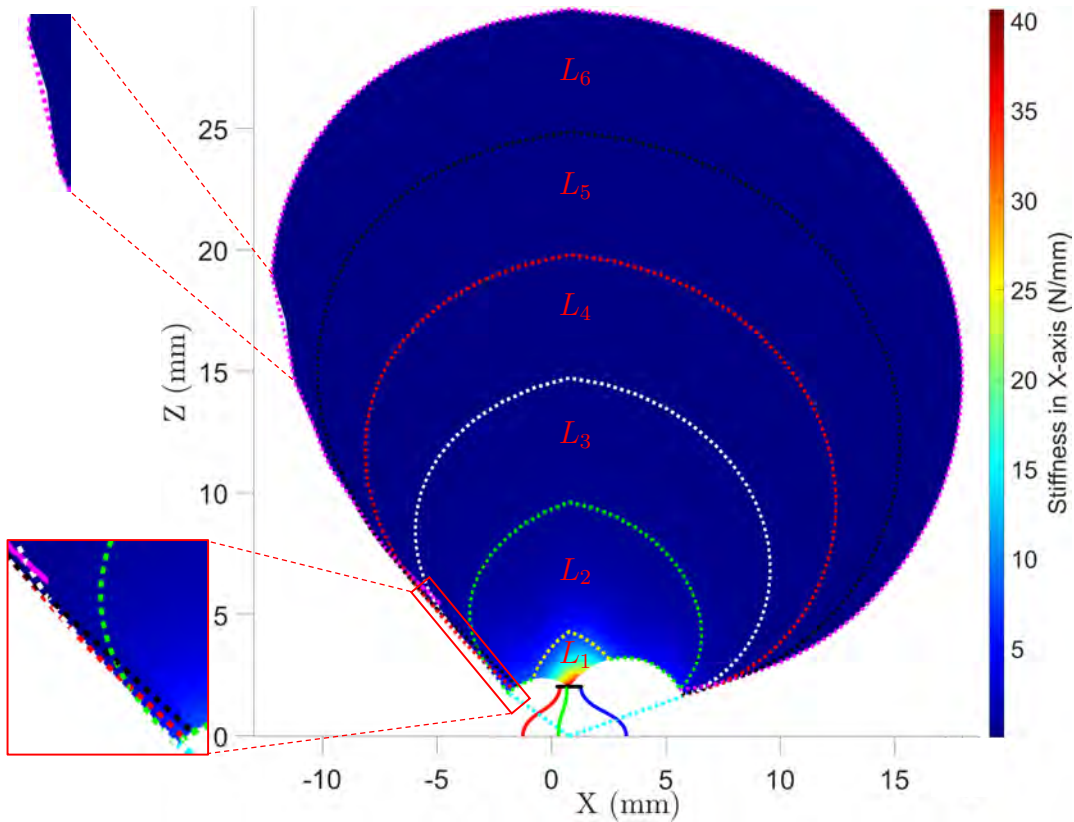


**Figure 4.7:** Vertical plane cut workspace of the miniature glass PCR considering the effect of the actuation length which relates to the robot arc length. Projected areas are unstable regions due to negligible stiffness in long actuation length (see Table 4.5 for corresponding values).

Figure 4.7, shows the vertical  $y$ -axis plane cut of the robot workspace for a maximum arc length of  $L = 30\text{mm}$ . In addition, Table 4.5 presents in detail the variation of reachable workspace area as a function of each corresponding actuation length. The reachable workspace area is very small when the actuation length is 5mm (shown by the region below the yellow dotted line  $L_1$ ) and this is because the robot cannot sustain any strain below  $L_i^* = 3\text{mm}$ . Therefore the non-reachable areas of the PCR within the given specifications are represented by the white-bounded region of the dotted cyan-colored line in Figure 4.7. Another key issue is the instability of the robot configurations at the boundary regions, most especially for  $L_5$  and  $L_6$  due to low robot stiffness at these configurations, which causes an undesirable offset deviation (refer to Figure 4.7). Therefore, care should

**Table 4.5:** The different actuation length with its obtainable workspace area

Reachable region	$L_1$	$L_2$	$L_3$	$L_4$	$L_5$	$L_6$
Actuation length (mm)	5	10	15	20	25	30
Workspace area ( $\text{mm}^2$ )	4	50	89	122	161	275

be taken when designing and controlling a PCR, to ensure that output stiffness is sufficient for the desired tasks, as further design analysis and prototyping are mainly restricted to the fourth boundary region ( $L_4$ ).

#### 4.4.2 End-effector dimension

One of the key geometrical parameters of consideration, in designing a PCR is the dimension of the end-effector. The end-effector couples the rods at the distal mobile end of the robot. Although this part can be functionalized with actuators/sensors or manipulation tools, it is essential to understand the effect of change in the end-effector dimension as regards the manipulability, stiffness, reachable workspace, and obtainable end-effector orientation. To that effect, model analyses were carried out to investigate the effect of different end-effector dimensions. For this particular analysis, only the end-effector dimension  $r_e$  is varied, whereas all other parameters of the robot are held constant. The robot specifications are  $r_b = 2.5\text{mm}$ ,  $l_i = 2r_b$ ,  $q_i = 2r_b$ , while the  $\mathbf{r}_e = [1.5, 1, 0.5, 0.1]r_b$  (refer to Fig. 4.8A). The comparative detail discussion for the four different robot configurations due to changes in the end-effector dimension is analyzed below

##### 4.4.2.a Workspace

The results of Figure 4.8 show clearly the reachable workspace  $\mathbf{p}_e$  of the robot in vertical  $x$ -axis plane when considering the variation of the end-effector dimension. The reachable workspace area is presented in Table 4.6 for different end-effector dimensions, which have a compound ratio of 1 : 1.67 : 2.37 : 2.86. The variation of the end-effector dimension on the obtainable workspace shows that a smaller end-effector dimension results in a larger reachable workspace.

**Table 4.6:** Obtainable workspace area, maximum stiffness, manipulability, and orientation angle due to change of the PCR end-effector dimension

$r_e$ (mm)	W-S (mm <sup>2</sup> )	$K_{z,mx}$ (N/mm)	$K_{y,mx}$ (N/mm)	$K_{x,mx}$ (N/mm)	$\kappa$ max/min	Roll angle (degree)
$1.5r_b$	14.10	140	0.16	1.05	1.00/0.35	+57.5/-57.7
$r_b$	23.62	510	0.24	2.51	0.71/0.35	+72.7/-67.6
$0.5r_b$	33.41	150	0.79	2.84	0.45/0.19	+86.0/-75.7
$0.1r_b$	40.35	45	9.19	8.91	0.45/0.10	+89.8/-76.7

$r_e$ : end-effector radius

$r_e$ : Base radius

W-S: Workspace area

$K_{z,mx}$ : Maximum z-axis stiffness

$K_{z,mx}$ : Maximum y-axis stiffness

$K_{x,mx}$ : Maximum x-axis stiffness

$\kappa$ : Condition number (manipulability)

Roll angle: Maximum orientation angle about x-axis in the right and left part

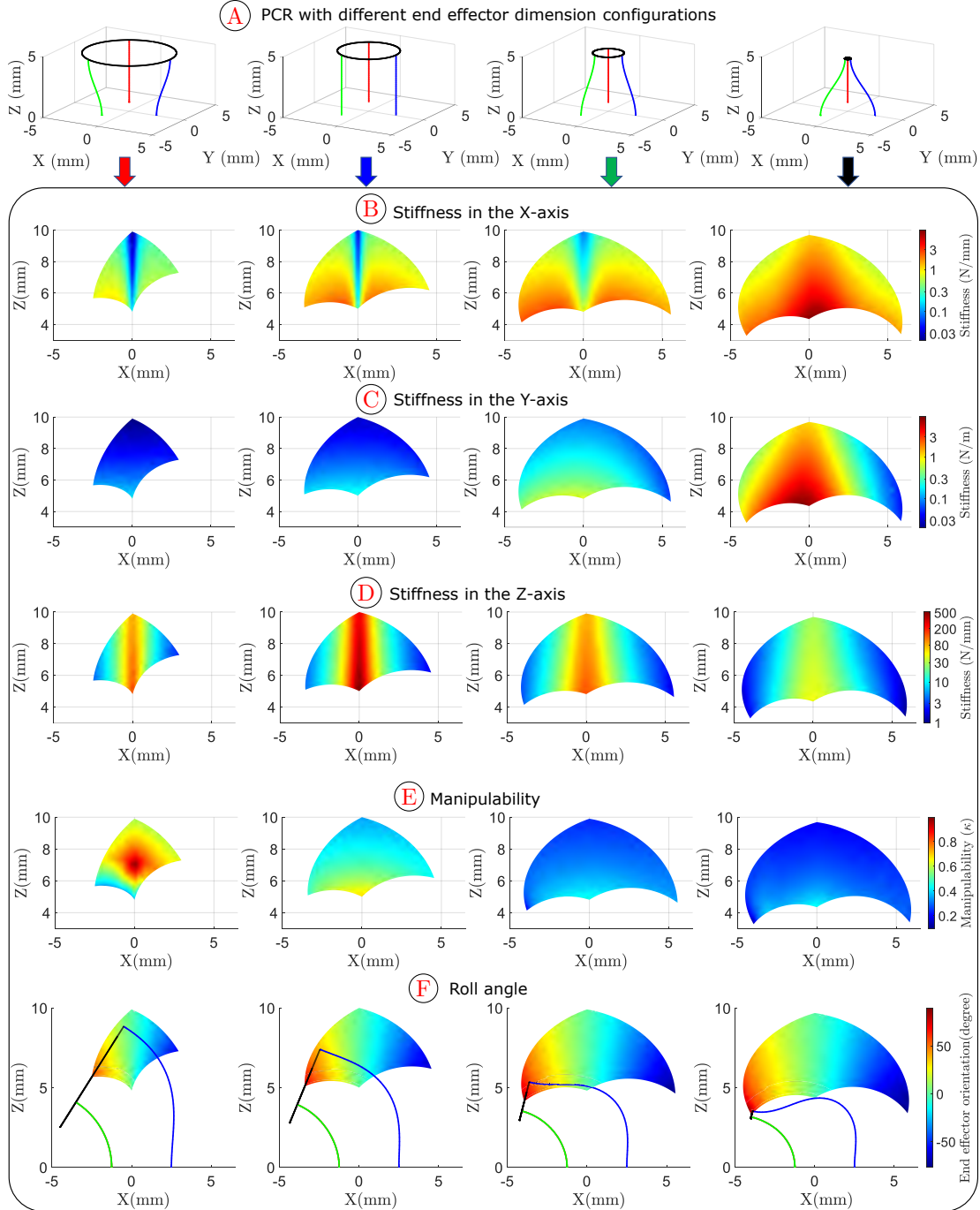


**Figure 4.8:** Workspace vertical plane cut showing the effect of end-effector geometrical parameters on the overall performance of the PCR in terms of stiffness, manipulability, and end-effector position and orientation. **A)** Robot shape for the different end-effectors which are  $r_e = [1.5, 1, 0.5, 0.1]r_b$ , **B)** and **C**) are that of stiffness when the force is applied in the  $x$ - and  $y$ -axis respectively, **D**) Stiffness variation when the force is applied in the  $z$ -axis, **E**) Manipulability variation considering each end-effector dimension, **F**) Obtainable end-effector orientation for each robot configuration.

#### 4.4.2.b Stiffness

Figure 4.8B, C, and D, represent the stiffness variation due to applied force in  $x$ -,  $y$ -, and  $z$ -direction respectively for the vertical  $x$ -axis plane. The stiffness values are computed as discussed in section 4.3.4 above. Figure 4.8D, shows the result of the output stiffness for an applied force in the global  $z$ -axis direction. Considering the different robot configurations with various end-effector dimensions as presented in Table 4.6, the maximum stiffness in the  $z$ -axis occurs when  $r_e = r_b$ . This agrees with the fact, that the lesser the stress on the robot links due to the end-effector constraint, the higher the stiffness or resistance to the applied force in the  $z$ -axis. The maximum stiffness for the  $y$ - and  $x$ -axis for each of the end-effector dimensions are presented in Table 4.6. The stiffness in  $y$ - and  $x$ -axis increases as the end-effector dimension decreases (Figure 4.8B and C). This can be related to the fact that the bigger the end-effector, the higher the chances of perturbation with applied force in  $x$ - and  $y$ - directions. Whereas the smaller the end-effector, the higher the stress resistance because the links are tightly constrained to a smaller area. Therefore, the influence of external forces is important to the resultant PCR design in terms of the robot's load-carrying capacity.

#### 4.4.2.c Manipulability

Figure 4.8E relates to the manipulability of the robot configuration within the workspace as detailed under section 4.3.3. Though a smaller end-effector PCR design, has the advantage of a large reachable workspace, the drawback becomes lower manipulability as shown in Figure 4.8E. In essence, the bigger the end-effector dimension, the higher the robot's dexterity for a given configuration (see Table 4.6). Therefore, there is a compromise between the reachable workspace and the manipulability to ensure the efficient operation of the robot.

#### 4.4.2.d End-Effector orientation

Figure 4.8F represents the end-effectors rotation about the  $x$ -axis. Comparing the obtainable roll angle due to change in the end-effector dimension shows that, the smaller the end-effector, the higher the reachable roll angle just like that of the workspace. The maximum obtainable roll angle for each of the different end-effector dimensions is given in Table 4.6. The higher roll angle associated with having a smaller end-effector is linked to its ability to reach the higher boundary regions and having a larger workspace unlike in the case of a larger end-effector dimension. In general, having a smaller end-effector help to reach a tighter bending angle, which is desirable for most manipulators.

## 4.5 MODEL VALIDATION AND EXPERIMENTAL RESULTS

### 4.5.1 Prototype design and fabrication

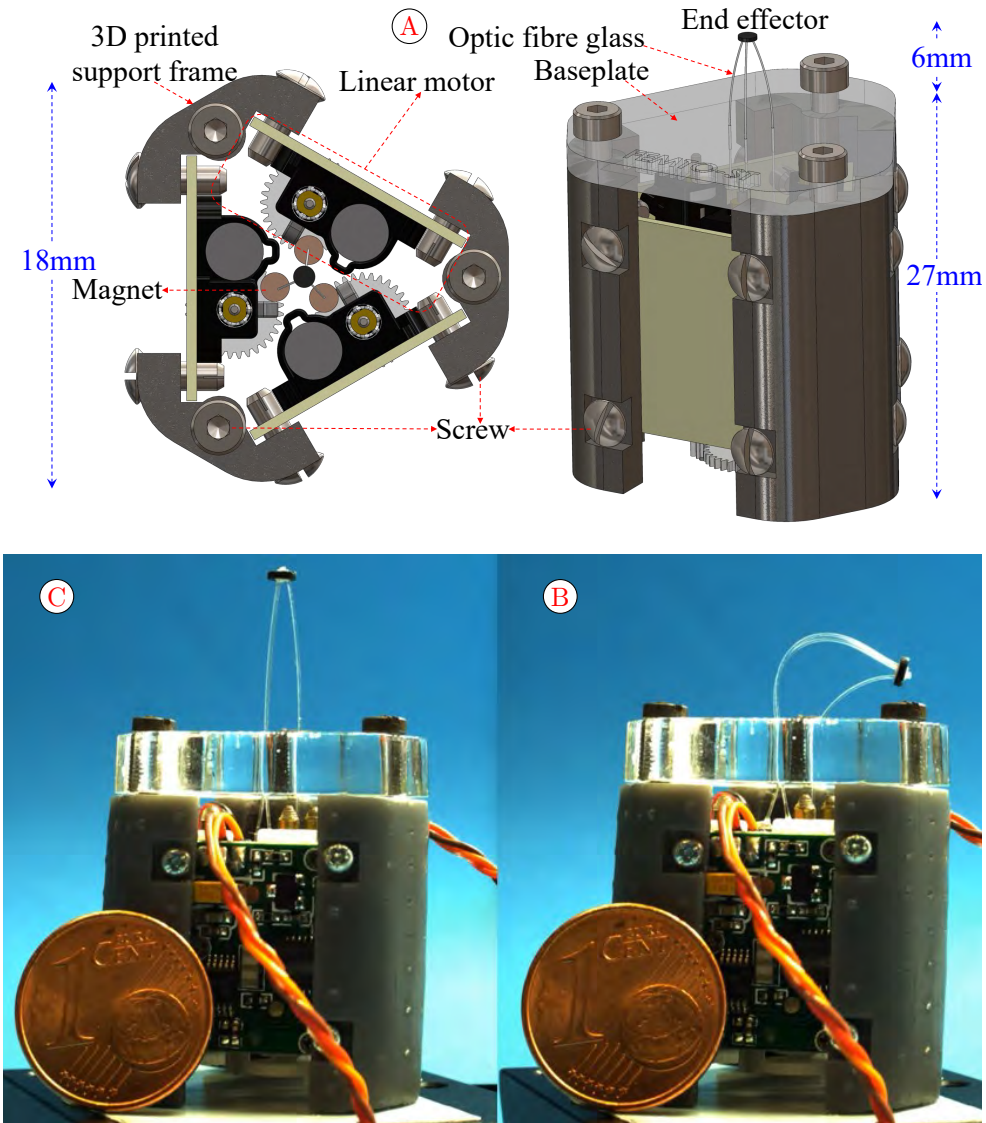


**Figure 4.9:** The miniaturized PCR made of glass, **A)** Computer-aided design (CAD) of the entire robot and its different components **B)** Prototype of the robot in maximal extension configuration **C)** Prototype of the robot in maximal bending configuration.

The prototype of the proposed 3-leg miniaturized glass PCR is presented in Figure 4.9. It can be divided into 3 major aspects, which include: 1) the actuation unit 2) the parallel flexible structure, and 3) the controllers. The flexible part of the PCR is made of glass optical fibers, the vertical frame body support was fabricated by 3D print, while the actuation unit top and baseplate were done by laser cut.

In general, the miniaturized glass PCR prototype has a compact structure with a simple design for rapid, miniaturized, and inexpensive fabrication. These are all detailed below.

#### 4.5.1.a Actuation unit

The actuation unit has a height of 27mm and a circumradius of 14mm. The servomotors were placed in an equilateral triangular arrangement, so as to optimize space. Moreover, the prototype design support is made of three vertical 3D printed frame support parts, for easy assembly and optimized fast prototyping. The high precision of the laser cut permits obtaining three holes through a plexiglass baseplate on a 2.5mm circumradius (Figure 4.9). Three holes of 300 $\mu$ m provide the guide support through which the optical glass fibers are deployed and also help to constrain the link below the baseplate top in a straight configuration. Detailed measurements and arrangement of the various components of the miniaturized glass PCR are all shown in Figure 4.9.

The miniature linear servomotors used for this experiment are “*Spektrum RC 1.8 Gram Linear Ultra Micro Servo*”, which have a maximal speed of 65mm/s, a stroke of 9.1mm and position repeatability of  $\pm 0.14$ mm. Their size dimension is 8.2mm x 15mm x 16mm. The horizontal top plate provides rigid support for the standing 3D printed parts as well as the needed small aperture hole through which the optic fiberglass passes during the robot’s manipulation.

#### 4.5.1.b Flexible structure

The flexible part of the robot consists of a set of three optical fibers. This part also includes the distal rigid plate end-effector that couples together the optical fibers. For the robot prototype design, a standard glass optical fiber of diameter 125 $\mu$ m was used with a length  $L_i^*$  of 6mm from the fixed base platform to the mobile end-effector. The small end-effector is a 500 $\mu$ m lightweight thickness carbon fiber plate.

#### 4.5.1.c Controller

The discrete pose of the robot is computed via the model on the computer using MATLAB which is connected to the Arduino board. In order to smoothen the motor acceleration and deceleration, an S-curve velocity profile for the generation of input control signal was implemented in the Arduino. Considering the glass material used and the miniaturized size of the robot, the S-curve velocity profile help to avoid the robot’s abrupt movement or jiggling stoppage and also ensure simultaneous acceleration/deceleration of the three links at the same time (see Figure 4.10). The theoretical detail for the S-curve velocity profile adopted for the micromotor control is provided in [Arevalo 01].

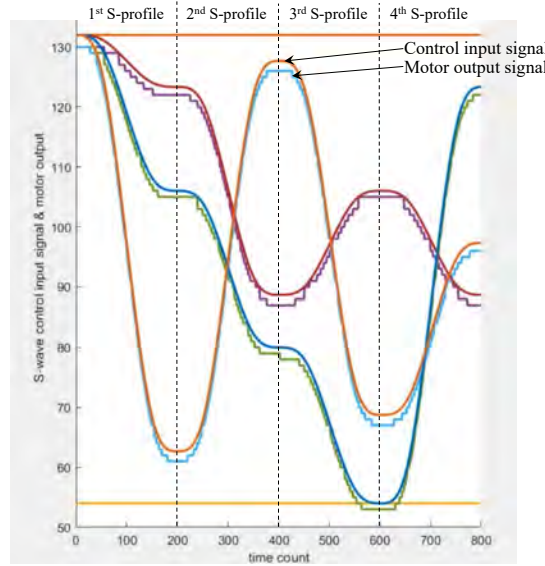


**Figure 4.10:** S-velocity profile plot for the robot control input (3 smooth curves for the 3 motors) and their corresponding output servo motor signals (3 step signal curves).

## 4.5.2 Experimental demonstrations and validations

### 4.5.2.a Workspace validation

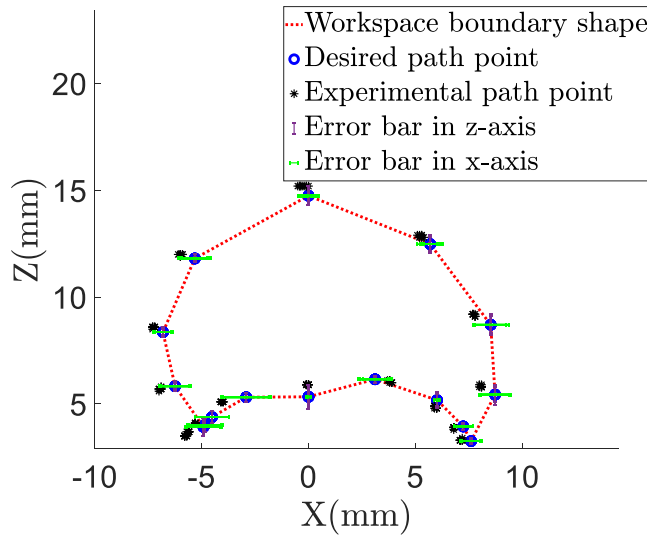


**Figure 4.11:** Experimental validation for the boundary workspace based on FKM.

The vertical  $x-z$  plane for the workspace boundary validation of the miniature glass PCR is shown in Figure 4.11, for five repetitive movements (see video [here](#)). The FKM was used for the computation of the workspace boundary path. The validation of the boundary workspace is shown in Figure 4.11, which has a mean error in  $x$ - and  $z$ -axis as 0.58mm and 0.28mm respectively. In addition, the stan-

dard deviation in the  $x$ - and  $z$ -axis is given as 0.29mm and 0.15mm respectively. The realized result shows the capability and flexibility of the robot to reach these extreme points within its boundary, without suffering fracture. This validates the FKM of the robot while considering extreme positions and one can see how close the results match.

#### 4.5.2.b IKM Validation

For the validation of the IKM, we carried out different path following that involved 1) a circumradius path movement in the vertical plane, 2) a circular path in the horizontal plane, and 3) two different types of square path movement. These are discussed in detail below.

##### 4.5.2.b.1 Circumradius path

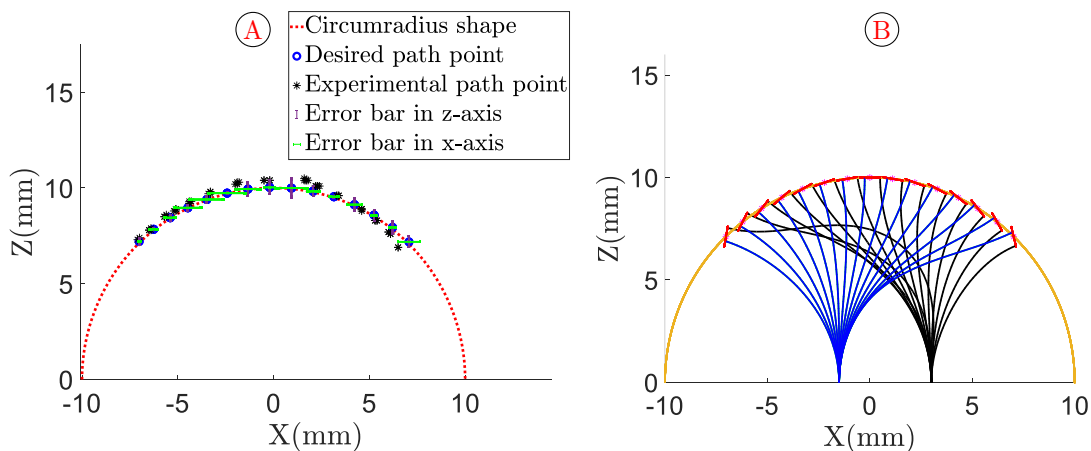


**Figure 4.12:** Circumradius validation on a vertical plane along the 10 mm circular path using IKM in  $XZ$  plane. **A)** the experimental validation result and **B)** simulation plotting showing the various configuration of the robot for the desired circumradius path following. Each path was evaluated at least four times, and the error was computed for each point along the path.

The IKM was used here to compute the circumradius path points on a radius of 10mm. Figure 4.13B, shows the side view of the simulation model for the different robot configurations. The validation result of this path shape is shown in Figure 4.13A and the demonstration video [here](#). It has a mean error in  $x$ - and  $z$ -axis as 0.25mm and 0.39mm respectively, while the standard deviation in  $x$ - and  $z$ -axis is gotten as 0.15mm and 0.23mm respectively. The result obtained shows how the robot follows the desired circular red line with a 10mm radius. It validates the modeling with a satisfactory result when considering also the use of cheap servo motors for the implementation.

##### 4.5.2.b.2 Circular path

To further validate the robot IKM in a horizontal  $z$ -axis plane, a circular path tracing was demonstrated. To actualize this, a set of path points for the desired

path within the robot workspace were computed using the IKM. The result of the circular shape path is shown in Figure 4.13A, which has a circular diameter of 8mm in  $x$ - and  $y$ -axis at a height of 5mm in  $z$ -axis (video demonstration [here](#)). The error in  $x$ - and  $y$ -axis was computed as 0.20mm and 0.31mm respectively, whereas the standard deviations in  $x = 0.13\text{mm}$  and in  $y = 0.19\text{mm}$ . The shape of the output result considering the end-effector centroid position follows to some extent, the desired circular red line as shown in Figure 4.13A. This validation result shows the accuracy of the IKM (shown by the error bar) and how close the experimental points follow the desired path.

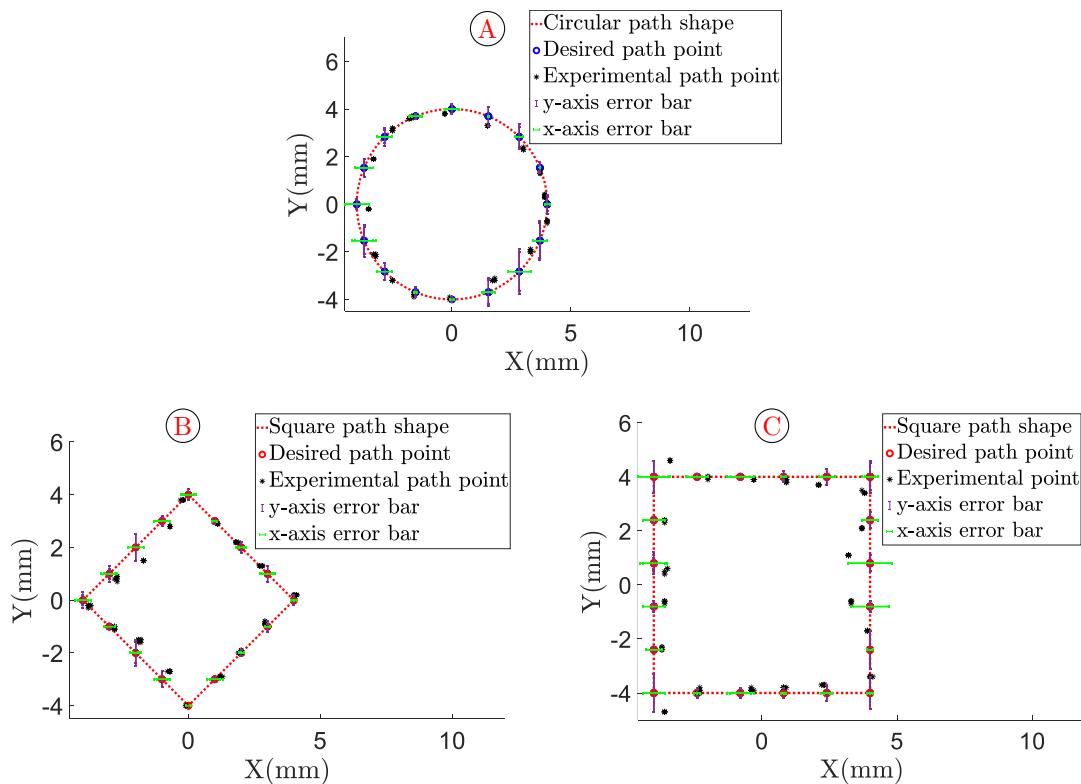


**Figure 4.13:** Experimental validation for horizontal plane path tracing by the miniaturized glass PCR A) 8mm circular path, B) and C) square paths. Each path was evaluated at least four times and the error was computed for each point along the path.

#### 4.5.2.b.3 Square path

Finally, two different square paths were executed as shown in Figure 4.13B & C. The first square path (Figure 4.13B), is a diagonal square within a circular diameter of 8mm (see video [here](#)). The diagonal vertices of the square are 8mm in both the  $x$ - and  $y$ -axis. The experimental validation gave a mean error in  $x$  and  $y$  as 0.18 and 0.20 respectively, while the standard deviation error is estimated as  $x = 0.09\text{mm}$  and  $y = 0.13\text{mm}$ . Next is the square path tracing with horizontal and vertical sides of 8mm in  $x$ - and  $y$ -axis (refer Figure 4.13C and demonstration video [here](#)). The realized experimental validation has a mean error in  $x$  and

$y$  as 0.36mm and 0.29mm respectively and the standard deviation is gotten as  $x = 0.22\text{mm}$  and  $y = 0.22\text{mm}$ . For both cases, the experimental points which are the end-effector centroid, tend to follow the desired square path with a considerable level of deviation/error given above. The various PCR validation results obtained are satisfactory and conclusive but limited by the use of cheap servomotors which have fairly low precision.

## 4.6 CONCLUSION

Parallel continuum robots (PCRs) are flexible manipulators, whose configuration is determined by the controlled deformation of their parallel-arranged elastic links. They are of great interest for micro-manipulation applications due to their intrinsic compliance, their extrinsic actuation, and their miniaturization potential. However, one key challenge in micromanipulators with parallel architectures involves miniaturizing the robot size and having a large workspace. To overcome this huddle, we proposed a miniaturized glass PCR, particularly using a standard optics fiber of diameter  $125\mu\text{m}$ . The design of the miniaturized glass PCR is characterized by high workspace volume, due to its structural design and kinematics. The miniaturized glass PCR has great potential for high scalability since the active parts are made of flexible glass rods and it also has an outstanding large workspace when compared to other miniaturized parallel manipulators.

To the best of our knowledge, this is the smallest PCR in the literature, also to consider is that, it is made of glass and possesses the capability of reaching large tip-tilt angles in a tiny volume. Investigation of different geometrical parameters of the robot design was carried out. It was realized that smaller end-effector PCR has a larger workspace in position and in orientation but consequently a lesser manipulability and vice versa. The robot stiffness varies according to the robot's configuration and the direction of the applied force. The stiffness is larger when the force is applied  $z$ -axis compared to the  $x$ - and  $y$ -axis and it is always maximum at the central bottom region while decreasing radially to the boundary end. We validated the robot FKM and IKM which was based on the Cosserat rod formulation and the shooting method that was used to demonstrate the workspace boundary, path deployment, vertical plane circumradius path tracing, and horizontal plane circular and square path tracing operation. The experimental validation result shows that the platform is able to reach tip-tilt angles from  $-84^\circ$  to  $117^\circ$  in a space of 15 mm wide and 10 mm high and to follow conveniently desired paths within its workspace.

Although, the footprint of the entire robot can be further scaled-down if a smaller actuation unit can be integrated or using a different microscale actuation technique at the microscale e.g. capillary forces, or thermal expansion. More importantly, we have made the link on how the key model parameters influence

the performance of the robot which was suggested as future work in [Mauze 20]. In addition, the realized smallest spatial PCR in the literature has an unprecedented tube dimension of  $125\mu m$ , that is made of standard glass optical fiber. The future prospects of this new generation of miniaturized robots made of glass (CTR and PCR) are really boundless, which is going to pave the way for a different domain of research exploring the use of glass for diverse applications.



# Conclusions and Perspectives

In this Ph.D., we have studied and investigated two glass continuum robots of interest. A glass continuum robot is a flexible robotic structure composed primarily of links made of glass. The first one is the concentric tube robot (CTR) and the second one is the parallel continuum robot (PCR), which are both analogous to the traditional serial and parallel robot respectively. These two continuum robots have been the key subject of our research investigation and this dissertation. For brevity, this section discussion is focused on areas of our key contribution and challenges.

In Chapter-1, we discussed the state-of-the-art of continuum robots, particularly CTRs and PCRs. Starting with CTR, we first address the literature gap by studying in detail the design and fabrication aspect of CTRs and then proposed to the research community our different findings as presented in a journal paper [Nwafor 23b]. First, we addressed the different methods for the design and fabrication of the tubes, actuation unit, and end-effector, which are the three main compositions of a CTR. Secondly, a unified scheme for CTRs classification is proposed to the research community, which is based on their actuation unit architecture. Last but not least, a set of specification information for assessing upcoming CTR prototypes is presented and we suggested to the community the essence and need towards having a common platform for faster development and advancement in this field, other than the usual fabrication of new CTR each year by each group, which is majorly focused towards increasing the chances of publication acceptance. To that effect, we have also created a site [CTR Prototyping Resources](#), that contains the specifications of all the physical CTR prototypes in the literature as a way of establishing a common platform. As regards PCRs, we gave a concise detail on the review of existing prototypes and conceptualize a general way of classifying them, which is either planar or spatial. A review of the different classical modeling of continuum robots was also studied, with major emphasis on the classical approaches in the literature we adopted for the different validation (FKM and IKM), demonstrations (different path following and applications), and investigation analysis (stability and stiffness)

In Chapter-2, the focus was our major research contribution in regard to CTR. In this aspect, we were able to actualize a new generation of CTR prototype with a sub-millimeter design made of glass, which was used for various experimental demonstrations after its model validation. A novel approach to obtaining a pre-curved tube in glass using thin heat shrink on glass capillary was presented, which was characterized and used to pre-curved planar or 3D complex tube shapes like a helix. This was even extended to the pre-curving of standard optical glass and in

fact, the external tube diameter can be as low as  $90\mu\text{m}$  with a  $5\text{mm}$  obtainable radius of curvature, which permit to actualize the smallest CTR ever. The approach is simple, fast, inexpensive, and with a possibility for patient-procedural or specific customization, thanks to the use of a 3D printed mold. These made it possible to the realization of different pre-curved tubes for various target applications ranging from vitreoretinal deployment using a fish eye under OCT visualization to laser transmission capability of a pre-curved optical fiber for possible light-driven end-effector actuation or laser surgery operation. Overall, for kinematic modeling, the obtained results show that the general model framework in the literature can as well be applied to miniaturized sub-millimeter CTR that is made of glass material. Finally, this robot was called “Caturo”, which stands for capillary tube robot as presented in a journal paper [Nwafor 22].

In Chapter-3, on the other hand as regards PCR, to the best of our knowledge, we were also able to achieve the smallest PCR compared to those in the literature. The novel design of the 3-DOF non-planar configuration makes use of the inexpensive standard glass optical fiber, for the continuum deformable robot links. This has the benefits of high elasticity, small diameter, and the possibility of using them to transmit energy to an active end-effector. Using the general Cosserat rod formulation along with the variable curvature kinematic approach, we were able to model, simulate and investigate the effect of various geometrical parameters of the robot (actuation length and end-effector dimension) on the obtainable/variation of robot stiffness, manipulability, and end-effector orientation within the entire workspace. We went further to demonstrate different shape path tracing consisting of a horizontal plane circular and square and then, vertical plane circumradius, and workspace boundary path, which presents the robot capability and model validation. This work has been published in [Nwafor 23a].

One major challenge is related to microfabrication and assembly of the designed end-effector for the CTR and the PCR, considering specific task applications or micro-manipulation. In fact, for the PCR, most of the attachments were done using glue which limits parts decoupling or modular parts. With necessary micro-fabrication and the right micro-assembly, various coupling parts can be developed and possibly, interchangeable end-effectors. Moreover, one may wish to obtain an all-in-one design in glass, using the 3D fabrication capability of the FEMTO-print machining but the present technology does not guarantee such. Finally, to actualize microscale continuum robots, then MEMS actuators are to be used but currently, their fabrication is challenging and their output stroke is often very small.

Lastly, most CTRs in the literature including ours is just single-arm design. This is due to the challenge of designing a handheld and compact actuation unit with the available miniaturized motors/actuators for the high number of DOFs required. Moreover, long tubes are prone to instability. Although, a hybrid Nitinol-glass tube can be integrated into the redesign.

## PERSPECTIVES

### Short-term

The short-term perspective project can span from 6-months to one year of active research. Some of the features and projects to advance upon within a short-term framework or possible master projects are detailed below

#### 4.6.0.a Hybrid and multi-arm CTR design

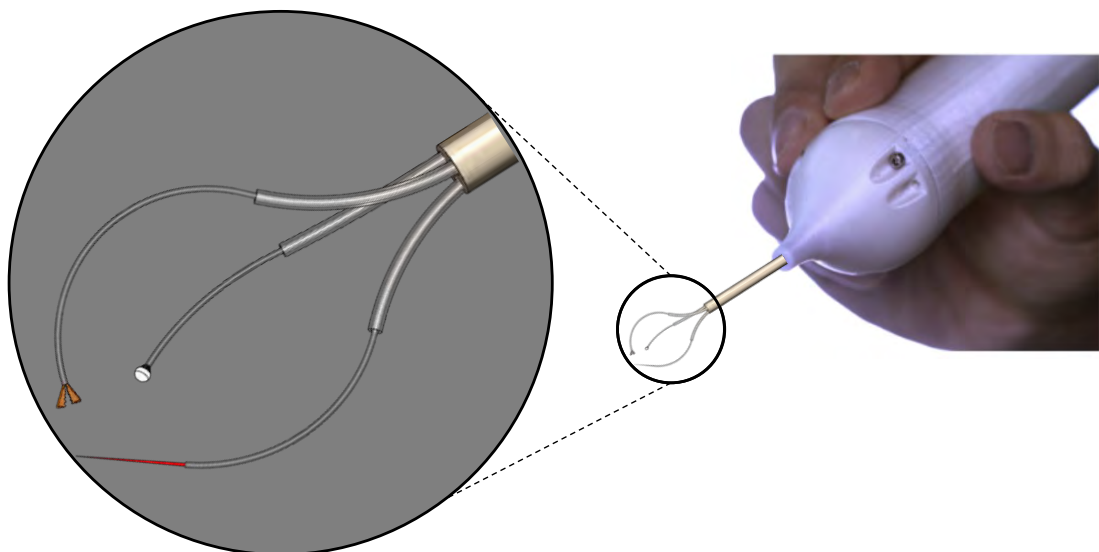


**Figure 4.14:** Future proposition for compact handheld multi-arm CTR design

Currently, Nitinol is the predominant material used for CTR design and prototyping, but there are some drawbacks regarding the level of miniaturization. This challenge can be alleviated by using micro-glass tubes as an alternative or to complement the existing design. Using the micro-glass tubes, it was possible to obtain the lowest radius of curvature down to 5 mm, three times smaller compared to that of Nitinol in the literature having 15 mm [Sears 06]. Moreover, the sub-millimeter pre-curved glass tubes have the smallest possible external diameter (glass has a diameter of 0.09mm, while the CTR Nitinol tube in the literature has a diameter of 0.41mm [Lin 15]). However, one can obtain a straight Nitinol tube with an external diameter of 0.25mm online ([Johnson Matthey](#)). With the current results obtained by the use of sub-millimeter glass capillaries, it is possible to propose a hybrid CTR design, composed of both the predominant Nitinol and glass. In this design, the glass pre-curved tubes with the smallest diameters and radius of curvatures can be integrated into a miniaturized Nitinol at the distal region. In this scenario, instead of the usual insertion of straight fiber optics for laser-associated application, with our novel approach, a pre-curved optical fiber will be part of the robot backbone. This gives higher precision, control, and increased dexterity

permitting it to reach inaccessible regions. In this regard, the benefits of the two materials can be harnessed and effectively used towards advancing in applications such as robot-assisted microsurgery.

Possible single-port multi-arm deployment of glass CTR is another aspect of research exploration. From the state of the art, most CTRs in the literature are single-arm prototypes with few exceptions of multi-arm design as presented in Figure 4.14. Moreover, with the current push for more invasiveness, this comes with the demand for possible single-port multi-arm deployment in MIS, which leads to less incision/blood loss and faster recovery. To that effect, Figure 4.14 presents a possible handheld compact design with three-arm CTR conceptualization. Among the multi-arm, we have the gripper for holding while the laser for cutting and then, the camera for visualization/lighting at the surgical site. Considering we are working with a sub-millimeter range CTRs, therefore obtaining a miniaturized design integrated on a single endoscopic arm as presented in Figure 4.14 could be possible. This will pave the way towards meeting the present demand for single port deployment and further miniaturization, which comes with huge benefits.

### Pre-curved 3-leg PCR and a hybrid continuum robot architecture

Almost all the PCRs in the family considered in this thesis uses straight flexible legs for the robot design and fabrication. Just as we categorized PCR as a multi-backbone continuum robot, here, we propose a hybrid design comprising of CTRs in parallel to fabricate a PCR (see Figure 4.15). Particularly, each robot's leg consists of a CTR kinematics, which is composed of a nested pre-curved tube(s), that deforms upon actuation. Figure 4.15A shows a configuration where the external tube can be assumed to be a straight rigid path through which the pre-curved internal tubes are deployed from. This design concept is used to actualize a pure translation to pure rotation movement of the end-effector. Figure 4.15B presents the case of a PCR with a composition of two-tube 3 CTRs arranged in parallel, which is an extension of that presented in Figure 4.15A but with a more possible DoFs. Figure 4.15C presents the model simulation of the first case study of a PCR with pre-curved legs. The design architecture basically consists of three pre-curved CTR links connected to a common end-effector with the assumption that the fixed base act as a dominant external straight tube. This robot configuration permits to convert pure translation at the base to pure rotation of the mobile platform when actuated by translation. Each flexible link of the PCR is made of a pre-curved capillary, which will be deployed from the base. As the inner capillary link is deployed via linear actuation at the base, the robot end-effector or distal plate rotates, resulting in what we call pure translation to pure rotation mechanics. The upper plots of Figure 4.15C, display the initial robot configuration before actuation. Whereas the plots below depict its corresponding configuration after actuation with the end-effector rotating a 90° about the  $z$ -axis. This concept permits the actualization of torsion motion at the end-effector by using pre-curved continuum tube/rod links instead of conventional straight links. The model frame-

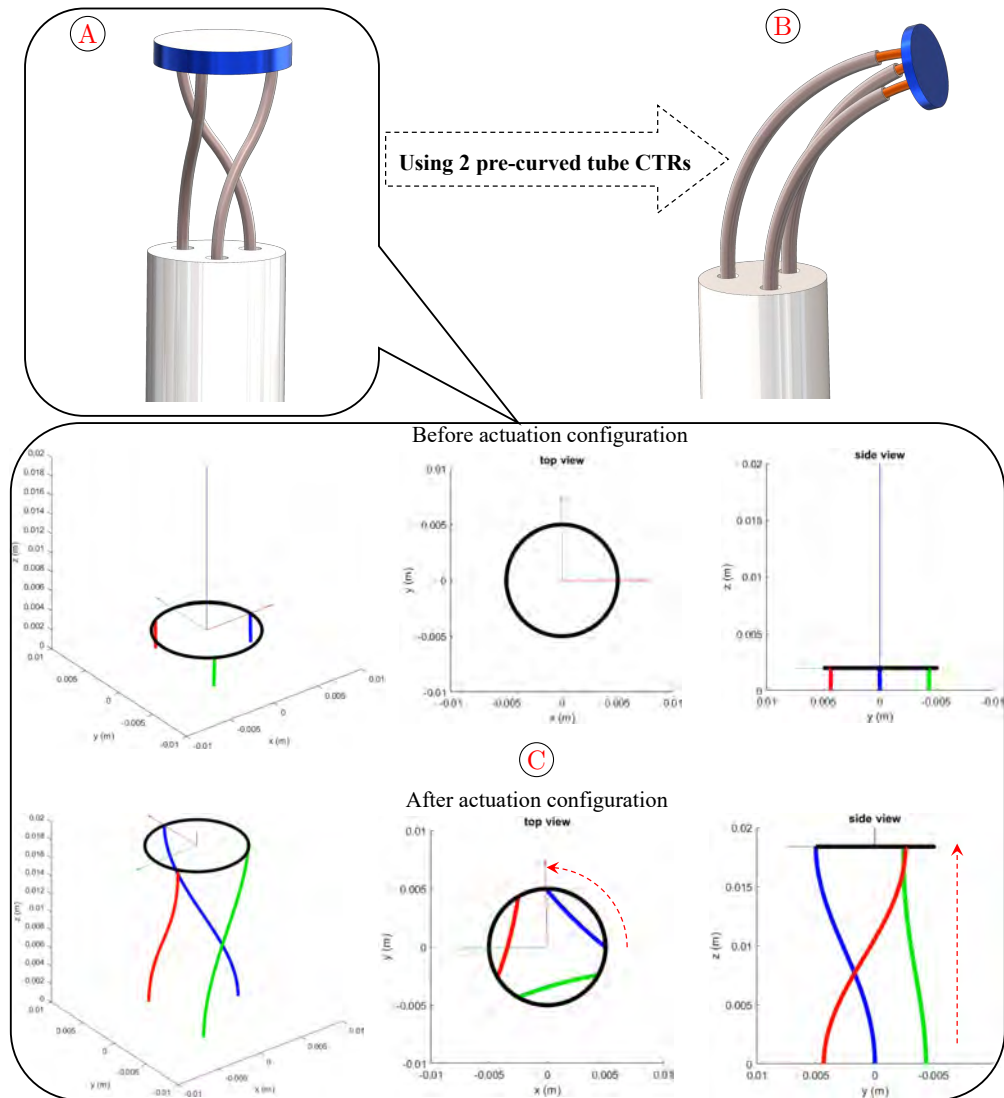


**Figure 4.15:** Design of PCR with pre-curved legs. **A)** CAD of a PCR with pre-curved legs for pure translation to pure rotation upon actuation as shown by the simulations below, **B)** CAD of a PCR composed of two-tube CTRs which is a further extension of that presented in **A** with an introduction of a second pre-curved tube, **C)** model simulation of the PCR design in **A** for which the **up**) shows the initial robot configuration while **below**) presents the configuration upon linear actuation resulting in a 90° end-effector rotation.

work is the same as that used for the miniaturized PCR in Chapter 4 above, just that this takes into account the rod pre-curvature vector values. The next phase is the prototype fabrication design and then, the experimental validation, which is followed by a proposed application.

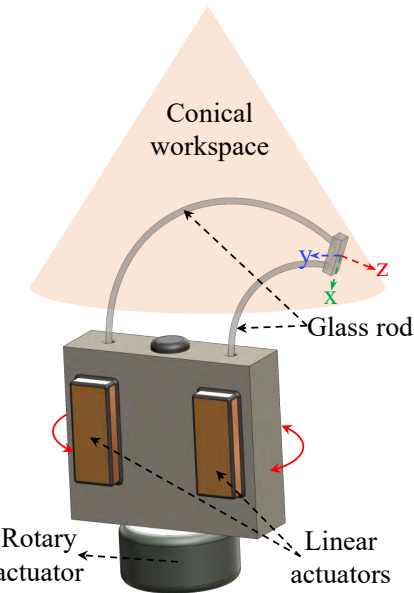


**Figure 4.16:** 3-DoF miniature PCR redesign using piezo-driven actuators for possible use in the scanning electron microscope (SEM), while the miniature planar version without the rotary actuator can suit transmission electron microscopes (TEM) micromanipulation application.

#### MEMS actuated planar PCR

A new concept of a 3-DoF design for a miniaturized PCR is presented in Figure 4.16. This design is basically composed of two slender rods possibly optical fiber, which was previously used for PCR design in Chapter 4. It will be deformed upon actuation of the two miniature linear actuators that are coupled to each link. The benefit of this novel redesign is in regards to the possible integration of MEMS actuators rather than DC motors and this will further miniaturize the overall design. This has a huge prospect for micromanipulation requiring a large workspace with a small robot footprint. The architectural design permits obtaining a planar bending about  $x$  and  $y$ -axis, which is achieved using linear actuators. With this concept, it could be possible to deploy it to transmission electron microscopes (TEM) for sample micromanipulation. Optionally, one can integrate a rotary actuator, which can produce out-of-plane rotation about  $z$ -axis. With this design concept, the workspace volume gives a conical shape whose size is dependent on the linear actuation stroke and the linked material. This design will have a faster computational time as only two-rod integration is required to determine the actuation length.

#### Automatic/self-calibration

Calibrating at the joint level is a crucial aspect of robotics, as it directly impacts the attainable precision/accuracy and unlike serial robotic arms, which have rigid links and joints, continuum robots are made of flexible materials that bend and twist [Vincent Modes 20]. Due to their jointless design, specific cal-

ibration methods are necessary that involve an automatic method for aligning pre-curved elastic tubes for effective robot calibration. Two possible approaches are the integration of a sensor at the distal tip to calibrate its pose and the other is by investigating with a non-contact sensing technology like electromagnetic induction, cameras. CTRs are the smallest family in continuum robots and working with a sub-millimeter CTR design, the main challenge is identifying the possible nano-scale detectable sensor or methodology like electromagnetic approach for actualizing automatic identification of the sub-millimeter CTR tip pose or body configuration. Although, calibration procedures for CTRs in literature have been investigated sparsely, but they are important in improving the accuracy of a robot. In the literature, it has been used for a tendon-actuated robot in [Zheng 18, Chikhaoui 19, Wang 19a], also for CTR under constant curvature assumption in [Webster 08b, Webster 09b, Vincent Modes 20], a generalized case in [Rucker 10d] and in fact, for a PCR in [Wu 19].

#### 4.6.0.b Control and dynamic analysis

Robot control involves determining the appropriate actuation to achieve a desired state, which is essential for performing a specific task. The state of a continuum robot encompasses several aspects, including the end-effector pose, the robot's shape, isolated/distributed forces, and stiffness, as well as its kinematic performance [Chikhaoui 18a]. The robotic community has reached a consensus in traditional serial and parallel robotics regarding various aspects. This includes the use of rigid links in the design, specific actuation types such as prismatic, revolute, and cylindrical joints, and the application of modeling techniques like Denavit-Hartenberg parameters. These have resulted in a well-developed and shared foundation for devising control strategies. On the other hand, the use of different actuation methods, kinematic structures, modeling approaches, and sensors for continuum robots has led to increased diversity and made it more challenging to find a universal control approach [Trivedi 08b, Rus 15]. This issue comes with the question of "what type of continuum robot are you working upon?", so as to identify the best control method that best fits and can guarantee optimum results.

Contemporary methods for controlling continuum robots are categorized into three main types: open-loop control, closed-loop control, or a hybrid approach that combines elements of both. In open-loop control, the primary reliance is on model inversion (IKM) to determine appropriate actuation values for achieving the desired state. This method proves advantageous when sensor integration is either unavailable or not preferred for the control process. To achieve higher accuracy with this method, the 3D FEM approach is encouraged which considers a lot of different non-linearities such as friction, and boundary contacts. On the other hand, the closed-loop control takes it further by incorporating feedback of the robot's actuator/state. Therefore, the desired state is achieved by using both the measured error and the model, which gives a better result accuracy. For higher accuracy, a configuration state-based feedback control is encouraged either by us-

ing visual servoing or an electromagnetic sensor approach. Though this increases the complexity of the system for medical applications, they are a necessary requirement. Moreover, the derivation of the dynamics of continuum robots is still ongoing research, which can lead to more effective automatic control. These are areas of key focus in modeling, though some stride has been made in this aspect in [Zheng 12, Godage 11a, Godage 16, Chirikjian 94, Audoly 13, Yu 05, Renda 14, Lang 11, Rucker 11a, Janabi-Sharifi 21b, Till 19b], but the actualization is still far fetched as to implementing the physical robot design/control.

### Long-term

The impact of long-term goals in a continuum robot project for the future is significant. Various areas of advancement such as modeling, control, and navigation strategies are needed as well as the target application development for public usage, patents, and possible commercialization. The long-term perspective projects are in the range of more than one year and possibly Ph.D. projects.

#### End-effectors for CTR

Functionalizing CTR with an end-effector is vital for task-specific applications. CTR end-effectors are often wire-driven. In the literature and see in Appendix-C, the smallest CTR end-effector has a diameter size of 1 mm [Dupont 09b], which would be unsuitable for the sub-millimeter glass CTR. Integrating an end-effector into the sub-millimeter glass CTR tip will be challenging due to the difficulties associated with micro-fabrication and micro-assembly. Although, the possibility of actualizing this will be beneficial for the use of small-scale and application-specific tasks in clinical interventions. The two major considerations for micron-size end-effector integration are typically the use of light-driven and pressurized fluid through the innermost tube aperture. Glass capillaries could guide light to actuate a thermal micro-gripper [Benouhiba 21] or an optical fiber tip self-regulated photo-mechanical actuator system with a contactless sensing probe [Wani 17]. Several microfluidic principles, such as micro-pistons, can be exploited for tip actuation as well [Volder 10]. Some of the possible pneumatic or hydraulic end-effectors that could be integrated into the glass CTR tip include a 3D 100 $\mu\text{m}$  compliant end-effector with an integrated force sensor [Power 18], a 150 $\mu\text{m}$  capillary tip microgripper [Barbot 20], and a 0.15mm<sup>2</sup> micro piston actuator [De Volder 09]. Finally, actualizing these will definitely add more value to the application capabilities of the miniaturized CTR.

#### Towards medical applications

For every medical device under development, the goal is to push toward clinical trial and its possible commercialization. As regards the sub-millimeter glass CTR, the long-term target is to advance its development and bring it into practical use in healthcare settings. Basically, clinical trials are an essential step in

evaluating the safety and efficacy of new medical technologies before they can be widely adopted. By conducting clinical trials, one can gather data on the performance of the CTR in real-world scenarios and assess its benefits and potential risks. This process helps to establish the robot's reliability, validate its capabilities, and refine its functionality based on clinical feedback. Particularly, to advance the CTR toward clinical trials and possible commercialization, several key steps are to be considered. These include: 1) further research and development, 2) preclinical studies 3) regulatory approval 4) clinical trials proper 5) commercialization strategy, and then, 6) market entry. The commercialization of the CTR involves making it available for widespread use in healthcare settings. This typically involves manufacturing, regulatory approvals, marketing, and distribution. Successful commercialization requires addressing various challenges, such as regulatory compliance, cost-effectiveness, market acceptance, and integration into existing healthcare systems. It is important to note that the specific progress, requirements, and challenges associated with pushing the CTR toward clinical trial and commercialization may vary depending on the particular research and development efforts and the regulatory landscape in different countries or regions. In France for example, basically, the demand and requirements are beyond the annual project feasibility. Though, through rigorous research, clinical validation, regulatory compliance, and strategic commercialization efforts, the CTR can move closer to clinical trials and eventual commercialization, potentially revolutionizing minimally invasive procedures and benefiting patients and healthcare providers alike.

### End-effectors for PCR

This involves the design, micro-fabrication, and functionalization of a PCR with a small-scale or miniaturized tip device for a task-specific application. The integration of micro end-effectors in PCRs enables precise manipulation and control at a smaller scale, making them suitable for applications such as microsurgery, micromanipulation, and micro-assembly. By combining the advantages of PCR, such as flexibility and those of parallel robot configuration, the system can effectively perform delicate tasks in confined spaces with the help of miniature end-effectors. This integration process requires careful design, compatibility analysis, and optimization to achieve effective performance. To actualize successful integration, several factors need to be considered, such as the mechanical compatibility between the end-effector and the robot's flexible elements, the actuation and control mechanisms, and the overall system dynamics. These aspects must be carefully analyzed and optimized to ensure efficient and reliable performance. Research and development in the field of micro end-effector fabrication and integration for PCRs is not pronounced with only a hand few recorded in the literature. The key focus in this area is on the design and fabrication approach, which involves the micro-fabrication technique, actuation/control, and integration/functionalization strategy. The goal is to improve PCR capabilities by making them application-

oriented and enabling them likewise to perform complex tasks at the microscale. Since the design of our miniaturized PCR makes use of standard optical fiber, this means we can employ light-driven actuated end-effectors. Moreover, PCRs are stiffer thanks to their parallel architectural configuration, which means they can effectively carry more loads than CTRs. One can choose to implement any of the suitable examples listed above for the case of CTR.

### PCR as SEM manipulators

One key application of the miniaturized PCR made of glass is focused on integrating it into the SEM for robotized arm sample micromanipulation. Notably, the SEM provides high-resolution imaging capabilities. By integrating the miniaturized PCR into the SEM, one can leverage the advantages of both systems. While SEM provides visual feedback, allowing for monitoring and analysis of the micromanipulation tasks, on the other hand, the PCR will be used for precise and dexterous manipulation within the SEM's confined space. Additionally, the miniaturized PCR will be equipped with specialized end-effectors or tools suitable for micromanipulation tasks within the SEM. These end-effectors can vary depending on the specific application and may include microgrippers, microtools, or microsensors.

The integration process typically involves designing and fabricating the miniaturized PCR to be compatible with the SEM environment. This includes considering the size, weight, and mechanical constraints of the robot to ensure it can operate within the SEM's chamber, and by ensuring the robot's actuation mechanism does not generate electromagnetic interference that could affect the SEM's imaging quality and capability/functionality. Furthermore, the control system of the robot should be designed to enable precise and coordinated motion while taking into account the limitations imposed by the SEM environment. The aim is to enhance micromanipulation capabilities within the SEM by enabling tasks such as sample manipulation, assembly, or cell manipulation at the microscale. One good possibility is the use of piezoelectric drives having a nanometer resolution and tiny size e.g. squiggle which has a dimension of 1.8 x 1.8 x 6mm. The piezo-based drive concepts do not generate magnetic fields and are not influenced by them, thereby making piezo stepping drives particularly suitable for SEM/TEM application [PI 23, Guan 11]. In this scenario, the sample can be placed on the miniature PCR robot for in-depth visualization or manipulation with the help of the micro-scale end-effector during image scanning.

---

---

## Appendix A

### Tube design approaches

---

<b>A.1</b>	<b>Tube design approaches . . . . .</b>	147
A.1.1	Optimization of a Tube Set: . . . . .	147
A.1.2	Modification of the Mechanical Properties of Tubes via material removal: . . . . .	149
<b>A.2</b>	<b>Tube Design: Perspectives . . . . .</b>	150

## Appendix A. Tube design approaches

**Table A.1:** Overview of the synthesis approach proposed in the literature for CTRs, classified by objective.

Objective	Year	Research team	Optimization approach	Optimized parameters: Tube length	Optimized parameters: Tube curv.	Kinematic model	Application
Collision avoidance, tip position and orientation	2022	Lin et al. [Lin ]	SNOPT for tube design + motion planner (gradient-based)	✓	✓	TC	Laryngoscopy, Heart biopsy
	2019	Baykal et al. [Baykal 19]	ASA for tube design + motion planner (gradient-free)	✓	✓	TC	Lung biopsy
	2017	Baykal et al. [Baykal 17]	(gradient-free)				
	2015	Baykal et al. [Baykal 15b]					
Maximize reachability, collision avoidance	2012	Torres et al. [Torres 12]	RRT for tube design + RRT for motion planner (gradient-free)	✓	✓	TC	Lung biopsy
	2015	Bergeles et al. [Bergeles 15]	Nelder-Mead (gradient-free)	✓	✓	TR and TC	Hydrocephalus treatment, cardiac surgery
Maximize elastic stability, minimize tube lengths and curv., collision avoidance, stability	2018	Girerd et al. [Girerd 18a]	Brute force (gradient-free)	✓	✓	TC	Olfactory cleft biopsy
	2017	Boushaki et al. [Boushaki 16a]	Pareto grid search (gradient-free)	✓	✓	TC	Deep anterior brain tumor surgery
Maximize field of view	2015	Hendrick et al. [Hendrick 15c]	Brute force (gradient-free)	✓	✓	DS	Prostate surgery
Maximize elastic stability	2017	Ha et al. [Ha 17]	Steepest descent (gradient-based)	✓	✓	TC	-
	2014	Ha et al. [Ha 14b]					
Maximization of collaborative configurations between two CTRs	2018	Chikhaoui et al. [Chikhaoui 18b]	Particle swarm (gradient-free)	✓	✓	TC	-
Maximize workspace, robot structural stiffness	2019	Granna et al. [Granna 19] †	Particle swarm (gradient-free)	✓	✓	TC with external loads	-
Maximize surface coverage	2016	Noh et al. [Noh 16]	Nelder-Mead (gradient-free)	✓	✓	TR	
	2017	Granna et al. [Granna 17b], Granna 19]	Particle swarm (gradient-free)	✓	✓	TR	Malignant brain tumors ablation
Maximize volume coverage	2017	Granna et al. [Granna 17a]	Brute force, Greedy optimization (gradient-free)	✓	✓	TR	Intracerebral hemorrhage evacuation
	2013	Burgner-Kahrs et al. [Burgner 13b]	Brute force (gradient-free)	✓	✓	TR	
Minimize robot distance to path	2013	Burgner-Kahrs et al. [Burgner 13a]	Nelder-Mead (gradient-free)	✓	✓	TC	Pituitary gland surgery
	2011	Burgner-Kahrs et al. [Burgner 11]	Nelder-Mead (gradient-free)	✓	✓	TR	Skull base surgery
Minimize robot distance to path	2019	Farooq et al. [Farooq 19b]	Nelder-Mead (gradient-free)	✓	✓	-	Vitroretinal surgery
	2016	Farooq et.al [Farooq 16]					Ligation
Minimize robot distance to path	2018	Morimoto et al. [Morimoto 18]	Analytical formulation	✓	✓	TR	Kidney stone removal
	2017	Morimoto et al. [Morimoto 17a]					
	2016	Morimoto et al. [Morimoto 16a]					
	2011	Bedell et al. [Bedell 11]	Generalized pattern search (gradient-free)	✓	✓	TR	Cardiac surgery
Minimize tube lengths and curvature, collision avoidance	2011	Anor et al. [Anor 11a]	Generalized pattern search (gradient-free)	✓	✓	DS	Hydrocephalus treatment
	2011						

\*: Method applied to a dual-arm robot

DS: Dominant stiffness

ASA: Adaptive simulated annealing (gradient-free)

RRT: Rapidly-exploring random trees (gradient-free)

‡: Also includes optimization of tube inner and outer diameters

†: Also includes optimization of tube inner and outer diameters and Young's modulus

TR: Torsionally-rigid

TC: Torsionally-compliant

## A.1 TUBE DESIGN APPROACHES

The synthesis of tubes is divided into two distinct categories: (1) the synthesis of a tube set to get the appropriate robot shape for certain tasks, and (2) the synthesis of tubes to achieve the desired mechanical properties through structural alterations.

### A.1.1 Optimization of a Tube Set:

Table A.1 presents the tube set design approaches for CTRs, organized by the objective function. Despite a high number of design variables included in the kinematic models, as detailed in the previous section, it is visible in Table A.1 that the methods developed so far only lead to the synthesis of a subset of design parameters, with the others being pre-selected. In all methods, the tube number, for example, is defined beforehand. Designers frequently use 3 tubes, which enables tip pose control with 6 DOF for fully actuated tubes. However, we see that the use of 2 tubes is also a popular option and that only a few researchers have looked at the use of 4 tubes [Sears 06, Gosline 12, Dupont 12] or even 5 tubes [Dupont 12]. In addition, the tube materials, inner diameters, and outer diameters are usually predefined, except in [Granna 19] where they are optimized, and in [Lin ] where the tube diameters are optimized. As a result of this decision, the bending and torsion stiffnesses of the tubes, which are significant factors influencing the robot shape, are predefined, which restricts the design space of CTRs. This choice is typically made to reduce the computational time and complexity of the synthesis. Additionally, the tube curvatures in synthesis approaches are typically restricted to constant curvature sections [Bergeles 15], with the exception of a few approaches that investigate the advantages of tubes with continuously varying curvature along their lengths [Ha 14b, Ha 17]. In fact, CTR tubes are normally considered to have a straight section followed by a section with constant curvature. This choice may be justified by the simpler kinematic models that can be used with the constant curvature assumption, as well as the simplicity of fabricating the tubes and determining their curvature after their shape setting. Additionally, despite the fact that every method in Table A.1 except for [Ha 14b, Ha 17] uses constant-curvature tubes with two sections, this limitation nonetheless allowed researchers to work on a variety of applications and areas in human anatomy, as seen in Table A.1. In addition to limiting the number of design variables and tube shapes considered, CTR designers have also introduced various design guidelines in order to further simplify the synthesis problem. Bedell et al. proposed a decoupling of the robot in navigation and a manipulation section [Bedell 11], which was later integrated into the work of Bergeles et al. [Bergeles 15]. This decoupling has been reused in [Girerd 18b] for the search of feasible CTR shapes with navigation and an exploration section. Bergeles et al. [Bergeles 15] further proposed that the stiffness of each link of the robot should dominate the stiffness of the previous ones, derived rules for approximate follow-the-leader deployment, and proposed the use of

either fixed or varying curvature links for the robot, with the goal of simplifying the synthesis problem.

Diverse objective functions have been implemented for the synthesis of CTRs and can be classified into two main categories. The first category corresponds to objective functions related to the task to be performed, including mostly obstacle avoidance and reachability. The goal in these scenarios is to design a set of tubes to enable the robot tip to reach a desired pose in Cartesian space or to sweep a given volume, as illustrated particularly in [Bedell 11, Burgner 11, Burgner 13a, Burgner 13b, Bergeles 15]. The second category corresponds to objective functions that constrain the design of the CTR or its joint values, in order to guide solvers towards a feasible robot. For instance, tube lengths and curvatures are usually minimized in order to avoid loopings of the robot in the anatomy [Anor 11a] or to increase its stiffness or remain in the admissible stress limit of the material [Bedell 11]. While not being an objective constraints on the material strain have also been implemented in [Lin ] to ensure tube mechanical integrity during usage. Researchers also sought to maximize the robot stability [Girerd 18a, Bergeles 15, Boushaki 16a, Ha 17, Ha 14b] in order to avoid having multiple solutions to the direct kinematic model, which results in a snapping phenomenon occurring due to the accumulated torsional energy releasing when they are actuated. In addition, it should be noted that most work has focused on the synthesis of CTRs by assessing collisions for a fully deployed configuration only. While this ensures that the deployed robot meets the desired performance, it does not guarantee that the robot can deploy to the site of interest without colliding with the anatomy. In order to achieve a collision-free path, the synthesis of the CTR must be coupled to a motion planner in order to take the deployment of the robot into account. This approach has been explored in the work of Torres et al. [Torres 12], with an RRT (Rapidly-exploring Random Tree) to sample the design parameters and another RRT to sample the joint variables, Baykal et al. [Baykal 15b, Baykal 15a, Baykal 17], with methods that enable the obtention of tube geometries as well as a motion plan, and more recently in Lin et al. [Lin ].

Overall, it can be observed from Table A.1 that all design algorithms proposed to date are gradient-free optimization approaches, except the recent work of Lin et al. [Lin ]. Other exceptions are [Ha 14b, Ha 17], however these works did not consider task objectives and constraints. This trend can be attributed to the difficulties of formulating the kinematic model of CTRs in a way that is differentiable with respect to its design variables, since the robot shape is obtained by a boundary value problem followed by two integrations. It can also be explained by the variety of constraints, such as collisions with the anatomy, computed from triangular meshes that represent the areas of interest [Bergeles 15], and optimization objectives, such as volumes swept by the robot tip, computed using ratios of voxels [Granna 17b, Granna 19], that have been easier to integrate in gradient-free frameworks due to their formulations.

---

### A.1.2 Modification of the Mechanical Properties of Tubes via material removal:

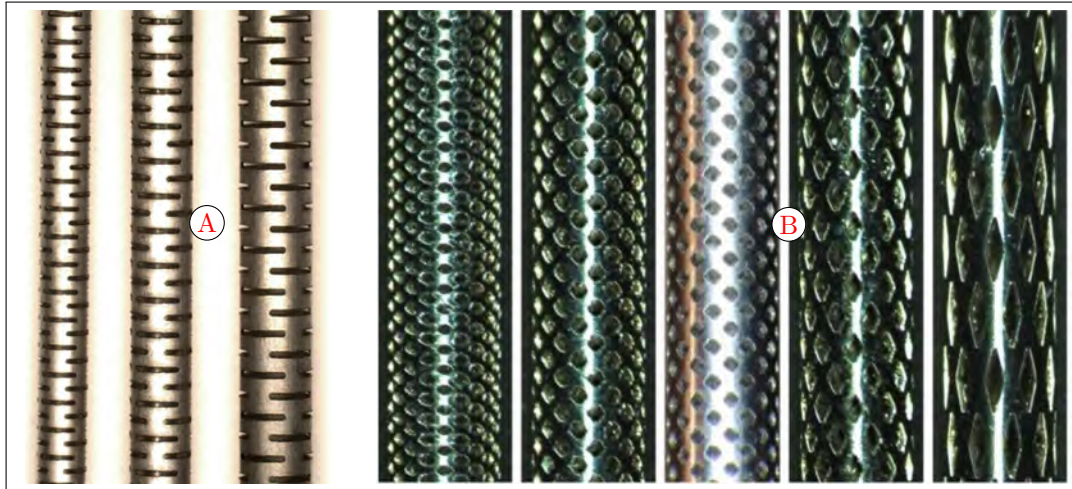


**Figure A.1:** Example of pattern shapes proposed by researchers, with (A) parameterized patterns simulated using FEA [Lee 15] and (B) diamond-shape patterns obtained using topology optimization [Luo 21].

While the approaches presented previously deal with the design of a set of tubes, each of them having an annular cross-section along their entire length, more recent research has investigated ways to modify the mechanical properties of the tubes, via structural modifications. These structural modifications take the form of patterns where tube material is removed, as illustrated in Figure A.1. The geometry of the patterns enables independent modifications of the bending and torsional stiffnesses of the tubes, which are normally related by Poisson's ratio in the case of a uniform material along the radius and length of the tubes. The goal of using such patterns is to lower the bending to torsional stiffness ratio of CTR tubes in order to obtain stability for the robot and avoid any snapping phenomena during usage [Gilbert 16a, Hendrick 15a, Peyron 19]. In particular, tube patterning has been investigated for use in follow-the-leader deployment [Girerd 18c, Girerd 20c], for which unstable robots must have their tubes patterned to obtain stability while keeping a desired robot shape. In general, tube patterning approaches to date have included the use of helical tubes composed of multiple layers [Azimian 14a], patterned or cellular tubes [Azimian 14a, Kim 14, Lee 15], and patterns defined using topology optimization [Xin 18, Luo 21], more particularly with rhombus patterns identified in [Luo 21]. Cases of helically-patterned Nitinol tubes for use as steerable needles have also been reported in the literature [Rox 20a]. While the above approaches have focused on the structural modification of tubes that affects their bending stiffness as uniformly as possible around their circumference, recent research has shown the advantages of patterning tubes to obtain direction-dependent flexural rigidity [Rucker 22]. Indeed, it was shown that patterning planar, piecewise-constant curvature tubes in their curvature plane enable stability

to be obtained more efficiently, while preserving most of the structural stiffness of the tubes, which is highly beneficial for tasks that require interactions between the robot and tissue, for instance.

Despite the advantages of tube patterning on CTR stability, it has been observed that translating and rotating patterned tubes relative to one another can be difficult, due to physical interference between their notches [Kim 14]. One solution adopted was to insert thin PTFE tubes between patterned tubes in order to isolate their notches. However, such tubes tend to wear after repetitive motions of the tubes and do not constitute a permanent solution [Kim 14]. In order to improve the CTR stability, another approach has been to decrease the tube wind-up along the transmission lengths by using a more torsionally rigid material compared to the material of the deployed portion of the tubes. For this purpose, researchers have combined stainless steel transmission lengths with deployed Nitinol tube lengths [Lin 15, Bruns 21].

## A.2 TUBE DESIGN: PERSPECTIVES

With regard to the tube design, there are a number of improvements that can be made. First, the current synthesis approaches fail to take advantage of all design variables, as most of them are being preselected. Indeed, the tube inner and outer diameters, the tube materials, and a number of constant-curvature sections are usually pre-defined and thus not optimized. Yet, these parameters play an important role in the variety of shapes that a CTR can adopt. In addition, current tube geometries considered, usually composed of a straight section followed by a curved one, could be generalized to tubes with more than two sections or with continuously varying curvature along their lengths. However, such an increase in the number of design variables might not lead to tractable problems for the gradient-free algorithms used in the literature to date, and the community could benefit from the investigation of gradient-based approaches, such as in Lin et al. [Lin ]. Although, optimizing variables such as tube materials and the number of tube sections is difficult in gradient-based approaches since these variables take non-continuous values. Thus, there is a need for optimization approaches that can handle a large number of continuous and discontinuous design variables in order to push the boundaries of CTR tube design forward. Furthermore, more accurate kinematic models, that include the effects of tube clearance and friction between them [Lock 11a, Ha 19] could be included in the tube design algorithms in order to increase the shape fidelity representation of these robots. Including tube anisotropy in design approaches would also be of interest to extend the capabilities of CTRs. However, locally patterning tubes along their circumferences and lengths usually lead to non-uniform bending and torsional stiffnesses along these directions. As a result, translating and rotating such tubes could lead to tip pose oscillations, which have not been quantified in current research. The research community does not seem to have converged to a specific pattern, which means that additional

work could be required in order to identify the most efficient pattern geometries. Tube design should also incorporate path planning, as in most recent approaches, in order to ensure a collision-free deployment of the robot to the target. Current planning is limited by the accuracy of the kinematic models, which neglect tube clearance and friction, leading to a 3-D shape of the robot which is, in practice, different from the predicted one. The use of more advanced kinematic models could lead to improved path planning and tube designs. In addition, CTR stability should also be included in the planning of these robots for tube synthesis purposes. Although current design approaches have led to tube sets capable of accessing hard-to-reach areas of the human body, these approaches significantly reduce the overall design space, which could lead to sub-optimal results or failure to succeed in given scenarios.



---

---

## Appendix B

### CTR actuation units

---

<b>B.1</b>	<b>CTR actuation units . . . . .</b>	154
B.1.1	Actuation Unit Elements . . . . .	155
B.1.2	Parallel Actuation Units . . . . .	155
B.1.3	Hybrid Actuation Units . . . . .	157
B.1.4	Serial Actuation Units . . . . .	158
<b>B.2</b>	<b>Actuation Units: Perspectives . . . . .</b>	159

## B.1 CTR ACTUATION UNITS

Actuation units enable the conversion of energy into mechanical movement. For CTRs, the actuation is achieved by translating and rotating the tubes relative to one another [Webster 06b, Sears 06]. Their actuation unit is simply composed of a set of actuation block(s), where each block is individually connected to the proximal end of a tube and generates the desired translation and rotation to drive that tube, as shown in Figure B.1. Generally, the number of tubes to be deployed and the required DOF per tube determine the number of actuation blocks in an actuation unit. The total number of DOF of a CTR is usually given as  $2n$ , where  $n$  is the number of tubes and 2 corresponds to one DOF in rotation and 1 DOF in translation. Despite their importance, actuation units are often described in less detail in the literature compared to the tubes themselves, and often they appear in figures without technical specifications regarding their design and kinematic architecture.

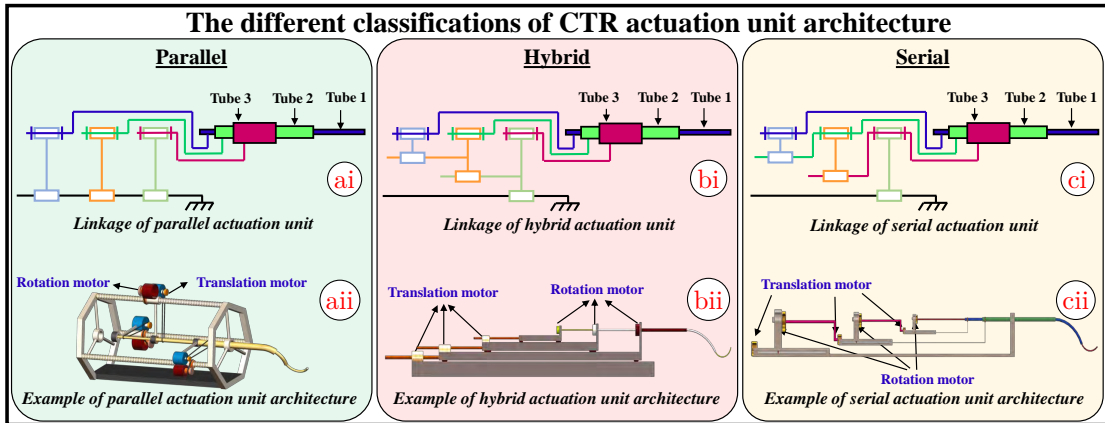


**Figure B.1:** The different classifications of CTR actuation units ai) The kinematic graph of parallel actuation unit, aii) The structural example of parallel actuation unit, bi) The kinematic graph of hybrid actuation unit, bii) The structural example of hybrid actuation unit, ci) The kinematic graphs of serial actuation unit, cii) The structural example of serial actuation unit.

Although the physical appearances of some actuation units have similarities, their internal architectures may differ. Rather than using the various nomenclatures in the literature e.g. multi-arm, MRI-compatible, bimanual, autoclavable, reusable etc., we propose a more general but distinct classification approach based on the actuation unit architecture as presented in Figure B.1. The actuation kinematics of a CTR deals with the actuation block arrangement and the mechanism of deployment. There are two types of block arrangements — parallel and serial — and their combination can result in fully parallel, fully serial, or hybrid architectures (or actuation units). For fully parallel architectures, the translations and rotations of each block are decoupled, as each one is independent and specific to one particular tube. For fully serial types, the translation or rotation in each block

is mechanically coupled to the preceding actuation blocks, thereby influencing the resultant movement of the preceding tubes with respect to the actuation unit base. For hybrid architectures, the translations are coupled, but the rotations remain independent or vice-versa. The actuation unit prototypes presented to date in the literature fall into either the parallel or the hybrid category, with no examples of prototypes based on the serial architecture. In this section, we discuss the general components of all actuation units, followed by key aspects of each distinct actuation unit architecture.

### B.1.1 Actuation Unit Elements

Irrespective of the choice of the actuation unit architecture or design requirements, the actuation unit of a CTR is always located at the proximal end of the tubes and contains the following essential elements.

1. **Translation Stage:** this section of the actuation block controls the translation of the tube, and its design determines the overall range of motion for the associated tube. Common components include: a rail-guide, a gear/belt/screw drive, an actuator (brushed DC motor, stepper motor, brushless DC motor, pneumatic or piezoelectric drive), and position sensor.
2. **Rotation Stage:** this section of the actuation block houses the mechanism/components for the rotational motion about the tube axis. The components that are associated with this section include gears, pulleys, bearings, actuators, and sensors.
3. **Tube Holders:** these elements are used to grasp the CTR tubes during deployment. While they can deform and potentially block inner tubes, screws radially pressing on the tubes have been used. Custom chucks as well as compressed rubber rings have also been used [Florea 22] and enable detachable designs, which can make sterilization easier. Glue has been used as well but results in permanent attachment.
4. **Support Frame:** this part serves as the main platform, upon which the other parts of the actuation unit are attached, and provides the necessary support during actuation.

### B.1.2 Parallel Actuation Units

This category of actuation units operates based on a parallel actuation architecture, as shown in Figure B.1ai and B.1a(ii) for the kinematic graph and the structural design, respectively. Although their structural design, which depends on the type of actuation components and coupling mechanism used, might differ in construction or appearance, as shown in Figure B.2, their

kinematics remain the same. The parallel architecture is the most commonly used actuation unit in the literature, as can be seen in our online CTR Prototyping Resources [CTR actuation unit repository](#).

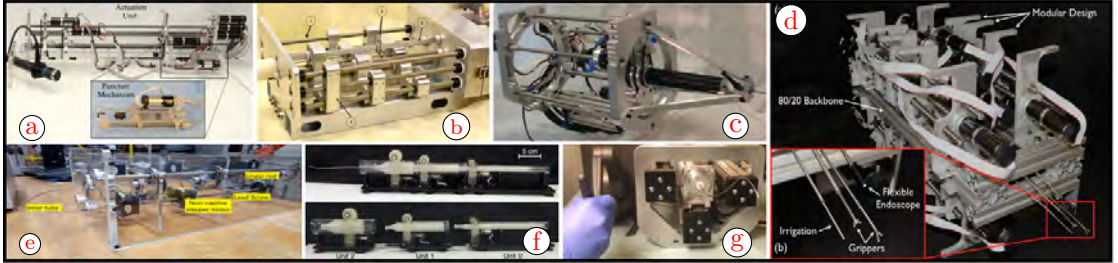


**Figure B.2:** Different parallel actuation unit prototypes a) An actuation unit with a puncturing mechanism by Swaney et al [Swaney 15c], b) A multi-arm CTR actuation unit composing of 1) Lead screws connect translational motors in the motor pack to each carrier. 2) Square shafts connect rotational motors to tube bases through gear trains. 3) Tubes of the concentric tube manipulators can be seen here. 4) Tube carrier, by Hendrick et al [Hendrick 14a] c) A parallel actuation unit with a nose-like design structure by Gosline et al. in [Gosline 12], d) A 4-arm 24 DOF CTR parallel actuation unit with 3 fully-actuated tubes per arm by Swaney et al. in [Swaney 12], e) A transparent casing 3 DOF actuated unit by Esakkiappan et al. in [Esakkiappan 19], f) A novel parallel actuation unit with a roller gear mechanism fabricated using additive manufacturing by Morimoto et al. in [Morimoto 17b], and g) A teleoperated CTR with parallel actuation unit by Xu in [Xu 17].

One example of a parallel actuation unit was presented by Swaney et al. in [Swaney 15c], where the actuation unit also incorporates a puncturing mechanism (Fig. B.2a). Another example of a system with a parallel architecture was presented by Hendrick et al. in [Hendrick 14a] and illustrated in Fig. B.2b. This system was designed to actuate two CTRs and has the benefit of being hand-held, with passive attachments to compensate for the weight of the device. Another parallel actuation unit prototype presented by Gosline et al. in [Gosline 12], has a protruded front design that helps to reduce the interference caused by having the bulk actuation unit close to the patient and thereby, provides more free space in case other medical devices are to be introduced as well (Fig. B.2c). Esakkiappan et al. proposed a 50 cm long CTR prototype composed of two tubes with 3 DOF in total and actuated via a parallel actuation unit [Esakkiappan 19]. The actuation unit uses stepper motors with rotary pulley mechanisms (Fig. B.2e). Morimoto et al. in [Morimoto 17b, Girerd 20d], presented a compact, lightweight, hand-held, and parallel actuation unit, where all the mechanical parts except the motors were fabricated using additive manufacturing. The design uses roller gears to enable rotation and translation in a compact form factor, along with a decoupled actuating structure, where each tube is controlled by an independent detachable actuation block (Fig. B.2f). Another parallel CTR actuation unit prototype was presented by Xu in [Xu 17]. It was designed for teleoperated surgical tasks (Fig. B.2g). The

6 DOF CTR can be controlled by a haptic device. Finally, Swaney et al. designed a multi-arm 24 DOF CTR for single-nostril skull base surgery [Swaney 12]. This parallel CTR actuation unit contains four independent sub-actuation units for simultaneous deployment of 4 arms, each of them being composed of 3 tubes, all actuated in rotation and translation (Fig. B.2d).

The popularity of parallel actuation units can be explained by several factors. First, compared to hybrid or serial systems, it is easier to make parallel actuation units with modular components and actuation blocks. Indeed, the independence between each block enables the removal of some of the integration constraints that are inherent to serial and hybrid actuation units due to mechanical couplings between the blocks. Such modularity could have also lead to more cost-effective designs. In addition, the positioning accuracy in translation and rotation relative to the actuation unit base is better in parallel actuation units, since there is no error accumulation due to the stacking of the actuation blocks.

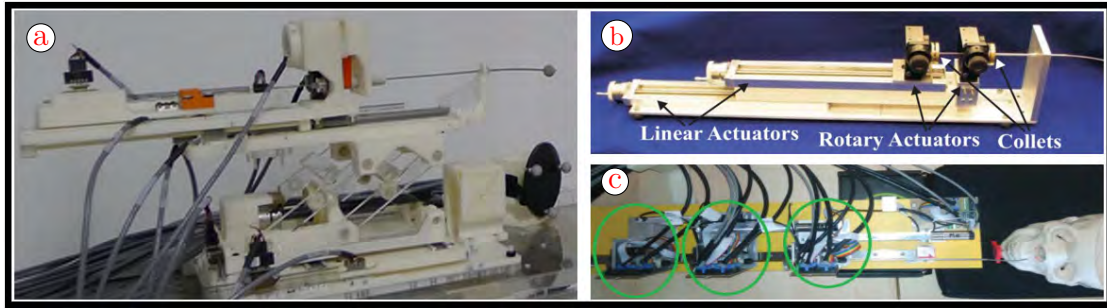


**Figure B.3:** The hybrid actuation unit prototypes, with a) MRI compatible 6-DOF piezoelectric actuation unit by Su et al. in [Su 16], b) Manually-actuated unit with precise tube positioning by Rucker et al. in [Rucker 10b], c) Structurally linked hybrid actuation unit by Boushaki in [Boushaki 16c, Boushaki 16b].

### B.1.3 Hybrid Actuation Units

The hybrid actuation architecture combines the serial and parallel block arrangements, resulting in interconnected blocks. Figure B.1bi and Figure B.1bii show a case study of hybrid kinematics and structural design, respectively, with translation blocks placed in series and rotation blocks placed in parallel. This structure is common in the literature for hybrid architectures, as shown in Figure B.3 considering existing prototypes.

Several hybrid actuation units have been developed to date. For example, an MRI-compatible, hybrid actuation unit was proposed by Su et al. in [Su 16]. They created a 6 DOF, piezo-electrically actuated prototype to enable MRI-guided deployment of a pre-curved and steerable CTR. As shown in Figure B.3a, this design consists of different translation stages assembled on top of each other, which results in a simultaneous movement of all modules placed on top of the actuated one, while each tube rotates independently. Another hybrid, but manually actuated design, was developed by Rucker et al. in [Rucker 10b]. As shown in Figure B.3b,

it was used to actuate two tubes with the outer tube held at a fixed location, while the inner tube was translated to five different positions and rotated to eight evenly spaced angular positions for each translation step. Finally, Boushaki et al. in [Boushaki 16c], presented a hybrid actuation unit with all three translations arranged in series and rotations arranged in parallel, as shown in Figure B.3c.

Compared to some parallel actuation unit prototypes that have their translation stages attached at fixed locations with limited stroke, a benefit of the hybrid architecture is the increased stroke length achieved via the translation of the translation stages relative to the actuation unit base. However, this benefit comes at the cost of lower absolute positioning accuracy in translation relative to the actuation unit base, since the translation stages are stacked in series.

#### B.1.4 Serial Actuation Units

Noteworthy to mention is the serial actuation architecture, which is characterized by a purely serial arrangement, as shown in Figure B.1ci and B.1cii, for the kinematics and structural design respectively. Here, each individual actuation is mechanically coupled to one another, thereby resulting in simultaneous transmission of actuation to all the preceding blocks. The idea of this particular actuation unit architecture has already been presented in the literature (see [Boushaki 16c, Alfalahi 20]), but to date, there have not been any prototypes with this type of architecture, as visible in our online CTR Prototyping Resources [CTR actuation unit repository](#).

The lack of developed prototypes could be explained by several reasons. First, the actuated degrees of freedom of such serial architectures are coupled. This feature is only useful in special cases, such as FTL deployment, where tubes need to follow a sequential deployment sequence that requires groups of tubes to move at the same velocity [Gilbert 15b, Garriga 18]. However, because tubes must move at different velocities for general CTR deployment, the serial actuation architecture does not typically simplify the actuation strategy. Second, since the actuation stages of serial architectures are stacked on each other, the absolute position accuracy of the tubes relative to the base of the actuation unit is lower in translation and rotation compared to parallel architectures, and lower in rotation compared to the hybrid architectures proposed to date, since positioning errors add up. Third, stacking the actuation stages on top of each other also results in the center of mass of the actuation unit moving more than for parallel or hybrid architectures, since the bases of the motor supports are also required to move. To conclude, the serial architecture seems to have some downsides, but could potentially be used advantageously for CTR with FTL deployment, where their architecture is well-suited to the required actuation sequence.

## B.2 ACTUATION UNITS: PERSPECTIVES

CTR development has mainly been focused on the tubes, while actuation units were simply viewed as means for moving them. However, with the maturation of the field, researchers have come to realize the importance of actuation units for general CTR performance. In addition, design features, such as sterilizability, required for commercial use, are becoming of interest and will place more focus on the actuation unit design. In fact, when designing a CTR actuation unit, there are several critical parameters that must be considered. First, the application itself dictates several constraints on the robot deployment and workflow. These constraints will inform, for example, whether the design must be MRI compatible, sufficiently compact or even hand-held, and which portions must be sterilizable. The application will also affect the number of tubes required and the types of actuation sequences needed. Second, one must select an actuation unit architecture that is most suitable based on the given design constraints. This selection will involve weighing the relative benefits and complexities of the architectures. To date, parallel architecture has been the most widely used, thanks to its simplicity, modular design, and high accuracy. Hybrid architectures with translation actuators in series have also been proposed and can expand the translation stroke of some parallel architecture designs. While the serial architecture could be of interest for FTL deployment, its downsides have limited its development so far. Third, one must determine the structural design and elementary components for the actuation unit. Irrespective of having the same actuation unit architecture, the structural design and components differ based on application and available material, as shown in Fig. B.2. Finally, the actuation unit must be physically built, assembled, and calibrated. Appropriate design and fabrication techniques must be selected for its structure, while other components such as motors, gears, nuts and screw rods, must typically be purchased.

There are numerous additional challenges associated with CTR actuation unit design. In particular, there are several requirements that must be met to ensure compatibility in a clinical setting, including sterilizability, safety, compatibility with associated medical imaging, and ease of integration in the clinical workflow. While several of these requirements were often overlooked in much of the older literature, researchers have recently started to design actuation systems with the goal of meeting these needs. For example, Graves et al. [Graves 12] proposed a compact and inexpensive CTR design, which has the potential for one-time use and is disposable after surgery. Burgner et al. in [Burgner 12] proposed a manually actuated, reusable approach, consisting of an actuation unit that is autoclavable and requires no oil lubrication. Burgner et al. in [Burgner 13b], then extended the reusable approach by creating a sterilizable and biocompatible design that uses a sterile bag/drape to isolate the detachable motor pack from the other autoclave sterilized parts of the robot, and this concept has since been adopted for multiple designs [Hendrick 15c, Hendrick 19, Gilbert 16e]. In order to address the issue of MRI compatibility and integration with existing clinical workflows, researchers

have proposed the use of either pneumatic or piezoelectric actuators. However, there are only a handful of such designs in the literature (refer to our online CTR Prototyping Resources [CTR actuation unit repository](#)), likely due to their control complexity and size. Since CTRs are mostly used for medical interventions, sterilization considerations become very important. Yet this aspect is not significantly discussed in the literature, with little detail on the use/design of a sterile boundary or isolation drape. Finally, our proposed classification system based on the actuation unit architecture in Figure B.1, could be used to uniquely identify and categorize new CTR prototypes (as used in [CTR actuation unit repository](#)), and to ease the selection/development of an architecture.

---

---

## Appendix C

### CTR end-effectors

---

<b>C.1</b>	<b>CTR end-effectors</b>	162
C.1.1	Manipulation	162
C.1.2	Inspection	163
C.1.3	Excision/Resection	163
C.1.4	Hybridized Architectures	164
<b>C.2</b>	<b>End Effectors: Perspectives</b>	164

## C.1 CTR END-EFFECTORS

The last component of a CTR is the end effector, which is deployed at the tip. There are many innovative designs, and they can be classified based on the task to be performed. We focus here on designs for manipulation, inspection, excision and resection, and navigation.

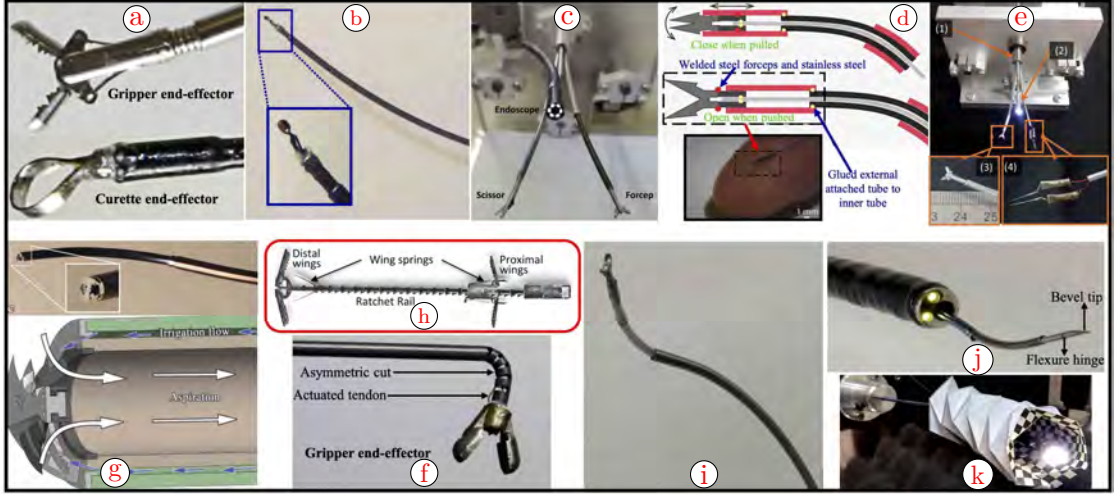


**Figure C.1:** Different CTR end effector prototypes: a) Gripper and curette end effectors [Burgner 14a], b) Tip mounted forceps end effector [Dupont 09a], c) Multi-arm CTR with scissors and forceps [Wang 20a], d) The design description and prototype of forceps gripper end effector [Lin 15], e) A multi-channel CTR with forceps pair for tissue grasping and electric coagulator for tissue ablation [Yu 16], f) Tissue removing end effector design prototype [Vasilyev 15a], h) Metal MEMS tissue approximation detachable end effector [Gosline 12], g) Needle-sized wrist gripper [Swaney 16], i) Cable-driven CTR disposable micro end effector [Prasai 16], j) Beveled tip end effector [Swaney 15c], k) RGB camera end effector navigating through an origami tunnel [Girerd 20b].

### C.1.1 Manipulation

Many end effectors are designed for manipulating objects or tissues at the surgical site. The types of manipulations to be performed include grasping, retracting, stabilizing, holding, gripping, turning, tilting, picking, placing, adjusting, pushing or pulling. Burgner et al. in [Burgner 14a], proposed a prototype with two different end effectors, shown in Figure C.1a. The first consists of a 4 mm long gripper with 110° of opening angle when fully opened, that was disassembled from a flexible grasper (Endo-Jaw, FB-211K, Olympus, Japan) and assembled at the tip of the innermost tube of a CTR. The second is an ellipse-like steel ribbon curette (with a major radius of 2 mm, a minor radius of 1.75 mm, and a height of 1.15 mm), which was attached directly to the innermost tube. Dupont et al. in [Dupont 09a] presented a 1 mm diameter tip mounted forceps, shown in Figure C.1b, which is

connected to a wire deployed inside the CTR and linearly actuated to open or close the forceps tip. A multi-arm CTR proposed by Wang et al. in [Wang 20a] consists of a remotely-controlled 1.8 mm diameter medical forceps end effector connected to a 6 DOF CTR for manipulation purposes, as shown in Figure C.1c. Lin et al. in [Lin 15], presented a gripper design consisting of a 300  $\mu\text{m}$  diameter steel forceps, which are welded to a 27G stainless steel tubing and glued to the CTR distal tip as shown in Figure C.1d. The forceps is used for gripping by pushing out or pulling-in of the attached Nitinol wire, in order to open or close the gripper respectively. Yu et al. in [Yu 16], presented a multi-arm CTR prototype with two flexible, sterilized end effectors which are deployed through the inner tube. One of these end effectors consisted of a 1.8 mm diameter mini forceps pair for tissue grasping, as shown in Fig. C.1e. Dupont et al. in [Dupont 16], demonstrated a CTR with a gripper for tissue manipulation during laser dissection operation.

### C.1.2 Inspection

This category of end effectors includes the use of lighting sources and cameras (e.g. for endoscopic usage) for in vivo visualization of the area of interest during navigation or at the surgical site. One example is the three-arm CTR system proposed by Wang et al. in [Wang 20a], in which one of the CTR outlet channels contains a 4 DOF active vision arm. This arm is attached to an endoscope, which is used for visual feedback as shown in Figure C.1c. Another example was presented by Yu et al. [Yu 16], where a multi-arm CTR prototype was equipped with a 4 mm diameter vision channel, having a 110° lens view angle endoscope attached at the tip for visual feedback (Figure C.1e). Girerd et al. [Girerd 20b], demonstrated the use of an RGB camera at the tip of a CTR, for visualizing and detecting areas during a simultaneous localization and mapping deployment strategy with approximate FTL behavior, through an origami tunnel (Figure C.1k).

### C.1.3 Excision/Resection

This category of end effectors includes mechanisms that enable cutting, puncturing, stitching, excision, ablation or dissection. These tasks are common across many procedures and a number of different prototypes have been developed for such purposes. For example, Wang et al. in [Wang 20a], proposed a multi-arm CTR with one arm equipped with a remotely controlled 2 mm diameter scissor end effector (Figure C.1c) for dissection inside the skull. Vasilyev et al. [Vasilyev 15a] proposed a surgical device with tissue removal capabilities for a beating heart surgery. The prototype is fabricated using a special metal manufacturing MEMS process (eFAB by Microfabrica), which enables the incorporation of micron-scale features into a single device that is deployed through a steerable CTR to the surgical site. The prototype incorporates both aspiration and irrigation features for tissue removal and is shown in Figure C.1f. Yu et al. in [Yu 16] presented a multi-arm CTR prototype with two end effectors, including a customized electric coagulator for tissue ablation, as shown in Figure C.1e. In addition, Gosline et al. proposed a

detachable end effector, shown in Figure C.1h, which was prototyped using metal additive manufacturing [Gosline 12]. It was designed to close or seal abnormal openings, such as the heart atria, by puncturing, pulling, and stitching two tissue layers together. Another aspect is the suction operation, which was achieved by connecting an aspirator at the end of the innermost cannula, for intracerebral hemorrhage evacuation as presented in [Burgner 13b, Godage 15b]. Finally, there are areas where CTRs are used for tissue cutting, by passing an optical fiber with a laser through the innermost tube to the surgical site, as demonstrated in the same video by Dupont et al. in [Dupont 16]. This technique of using fiber optics was further extended to laser ablation of real cholesteatoma cells in [Nguyen 22] and also, for laser-induced thermotherapy in the brain [Granna 18].

#### C.1.4 Hybridized Architectures

In order to improve the dexterity at the distal end of the CTR end effector and achieve stringent pose requirements in confined spaces, hybridized robot architectures have been proposed. These mechanisms involve the integration of another form of actuation, such as tendons or flexure hinges, at the distal end. Prasai et al. in [Prasai 16] demonstrated a 2 mm diameter, cable-driven end effector using a polyolefin tube and acrylic and steel strings. It can be mounted on a CTR as shown in Figure C.1i and has the ability to bend in all directions using the three control cables spaced 120° apart. Another example is a needle-sized wrist design that can be used to maneuver around tight corners [Swaney 16]. This end effector, which was presented by Swaney et al., is tendon actuated and composed of an asymmetrically patterned nitinol tube designed to reach tighter curvatures with lower tendon actuation forces. It also contains an attachable ring curette or gripper, as shown in Figure C.1g. One drawback of the asymmetric cutouts is that it is limited to one-directional bending, compared to the design of Prasai et al. in [Prasai 16], which can bend in all directions. Other asymmetrically cut nitinol tube designs were investigated by Eastwood et al. in [Eastwood 17]. Swaney et al. in [Swaney 15c], presented a functionalized needle with a spring-loaded puncturing mechanism for tissue opening. The steerable needle consists of a flexure joint, as shown in Figure C.1j, and helps to follow higher curvature paths through tissue.

### C.2 END EFFECTORS: PERSPECTIVES

The end effectors have traditionally been the least discussed topic in the CTR literature, due to the focus on tube geometries first, then followed by the actuation units. Typically, the size of a CTR decreases from the proximal to the distal end (i.e. from the actuation unit to the tubes themselves and finally to the end effector). Moreover, the end effector has to be deployed or integrated at the tip of the smallest (innermost) tube of the robot, which means that the end effector must be small (millimeter scale or less). Due to the desire to further decrease sur-

gical invasiveness and to enable multi-arm deployment via a single port, further miniaturization of the tube dimensions will likely be needed. These requirements pose a great challenge for the realization of submillimeter-scale end effectors. Difficulties in fabricating, integrating, and actuating such small-scale end effectors likely explain why there are very few end effectors reported in the literature to date. In fact, researchers often use end effectors taken directly from off-the-shelf medical tools, rather than designing their own. These remaining challenges call for significant dedicated research with regard to the design and fabrication of customized/miniatuerized end effectors, capable of fitting and taking advantage of the small hollow passage of the internal tube. Concerning the drawbacks on the microfabrication of end effectors, the focus on developing systems for commercial use could potentially boost its development in the future. One notable missing aspect in the literature is the implementation of interchangeable end-effector designs. This capability would enable robots to easily perform multiple functions without the need to change the entire tube set or actuation system.



---

---

## Appendix D

### Applications of CTRs in MIS

---

**Table D.1:** Applications of CTRs in MIS

MIS	TARGETED DISEASES	SURGICAL CONCEPT OF CLINICALLY AVAILABLE INSTRUMENTS	CLINICAL NEED	CLINICAL MERIT OF CTR	REFERENCES
Brain Surgery	Hydrocephalus - Intracerebral hemorrhage - epilepsy - pituitary gland tumors	Image-guided endoscopic navigation using one of the two approaches: 1) Transcranial Approach 2) Transnasal Approach. Insertion and pivoting of rigid, straight tools within the brain. Bone drilling is required in the 2nd Approach.	Reaching deep and complex surgical sites within the brain is ergonomically difficult. Risk of healthy brain tissue injury. Simultaneous deployment of multiple tools within the same nostril within a single nostril.	Enhanced workspace reachability. Reduced trauma to healthy brain tissue. Reduced volume of bone drilled in the case of EEA. Feasibility of multiple tool insertions within a single nostril.	[Anor 11a, Butler 12, Burgner 11, Granna 18, Swaney 12]
Lung Surgery	Lung cancer - CAO	Image-guided bronchoscope navigation from the patient's mouth to the bronchi. Complex instrument angulation to reach target points	high intraoperative trauma that results from bronchoscope manipulation. 32.3% of patients suffer broken teeth, hyperextension, or hyper-flexion of the neck	Design optimization and preoperative planning decreased limited device angulation. the force on the patient's head and neck is reduced by 95%	[Swaney 15b, Baykal 19, Gafford 20, Torres 12]
Cardiac Surgery	PFO	Fluoroscopy/3DUS guided catheters are inserted, retracted, and twisted at their knob.	Insufficient mechanical interaction with tissue. Control uncertainty and loss of haptic feedback.	Effective interaction with the heart tissue, with the integration of MEMS. Enhanced tip controllability (force and stiffness)	[Bedell 11, Vasilyev 15b, Gosline 12, Butler 11]
Gastric Surgery	Obesity	Orally introduced gastroscope. Folding of the stomach wall to reduce its size by stitching and knot tying.	Repetitive attachment and detachment of stitching needle are difficult by NOTES.	Replication of the conventional stitching mechanism (by the extension/retraction of a curved needle from an outer cannula)	[Xu 11]
Prostate Surgery	Benign Hyperplasia	An endoscope inserted through the urethra allows laser resection of excess prostate tissue to restore urine flow.	Manipulation of the whole endoscope for accurate laser targeting. Narrow urethra paths.	no more than 30° device deflection is required to cover the workspace.	[Hendrick 15c, Hendrick 14b]

**Table D.2:** Applications of CTRs in MIS

MIS	TARGETED DISEASES	SURGICAL CONCEPT OF CLINICALLY AVAILABLE INSTRUMENTS	CLINICAL NEED	CLINICAL MERIT OF CTR	REFERENCES
Kidney Surgery	Pediatric Stones	Kidney Subcostal approach: Opening is made under the 12th rib, followed by tool navigation through the renal pelvis to the kidney.	Compact anatomy of pediatrics. Diversity in patients' anatomy.	Patient-specific CTRs designs are produced based on safe path planning. Reduced injury risk.	[Morimoto 17a, Morimoto 18]
Larynx Surgery	Larynx/Thyroid Tumors	Orally introduced endoscopes. Forceps are used for tissue resection	Lack of maneuverability for following the curvilinear path of the larynx	Highly dexterous and flexible surgical manipulators. Accurate biopsy collection is achieved by incorporating forceps at the tip of the CTR.	[Friedrich 18]
Eye Surgery	Retinal Detachment - Epiretinal Membranes - Uveitis	A straight tool is inserted from the sclera. Manipulation is achieved by pivoting. Repetitive insertion of tools is required. The eye needs to be moved outward to allow reaching the posterior retinal arteries leading to excessive trauma	Enlarged incisions and wound bleeding/infection risk. Eye lens damage is possible due to tool manipulation. Need for Submillimeter tools. Difficult tool exchange during the surgery.	Successful workspace reachability. Minimal proximal motion. Decreased risk of lens damage. Fast and easy tube exchange, with different tools at their tips. Sufficient tip force for artery puncturing. Stylet can achieve up to 128.5° turns	[Lin 15, Farooq 19b, Nwafor 22]
Fetal Surgery	OSB	Insertion of US guided fetoscope into the uterus to remove the defect. The lesion formed is sutured, and sealed.	Possibility of preterm birth and maternal/fetal complications. Loss of maneuverability and depth perception.	Multi-scale, surgical manipulators with robust triangulation, and high bandwidth end-effectors. Simultaneous deployment of multiple working arms (smaller than 12 mm in diameter). Optimal field of view.	[Vandebroek 19]
Liver Surgery	Liver Tumors	An ablation probe is targeted to the tumor either using RF energy or chemical ablation. The procedure is performed under real-time CT imaging	Difficult coverage of the entire diseased region. Significant healthy tissue is exposed to the ablative agent.	tip position errors are less than 2mm. Maximum exposure of diseased tissue and Minimum injury to healthy tissue.	[Graves 12]



---

---

## Appendix E

### Precurved Optical Fibre Join by Fusion and RealSense D405 stereo depth camera of precurved tube

---

Figure E.1 below shows the pre-curved glass optical fiber, that is fabricated via our approach and after which the fusion joining of the two separate parts to allow the transmission of the Laser. Here, the pre-curved optical fiber can be integrated as part of the robot's backbone.

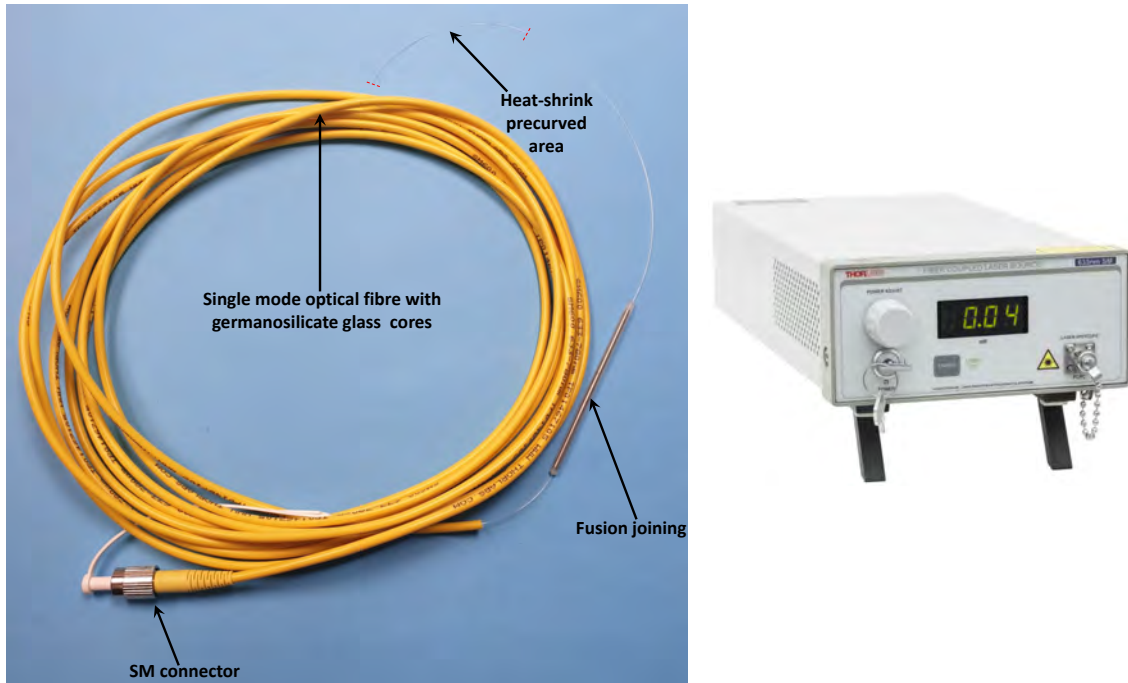


**Figure E.1:** Precurved optical fibre join by fusion

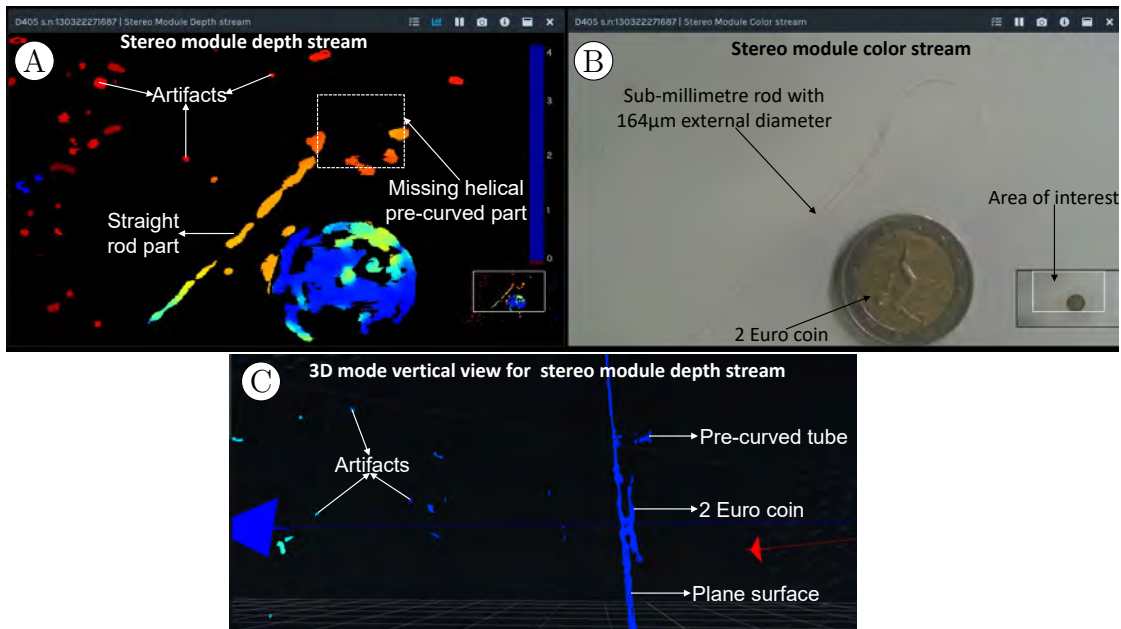


**Figure E.2:** RealSense D405 stereo depth camera with two lenses for submillimeter accuracy range 3D image capturing feature. We used the helical pre-curved tube to mimic out-of-plane tube deformation configuration **A)** using the stereo module **depth stream** for image capturing of two different samples comprising of the helical pre-curved tube and a 2 Euro coin, one could see on the image labeling the missing helical part of the sub-millimeter pre-curved tube, **B)** the same image with the two samples but in normal camera color streaming **C)** using the 3D pattern projection depth stream mode in vertical view configuration, one could see that the 2 Euro coin shape was much closer to the coin shape compared to the case of the micro-scale helical tube and moreover, there were lots of artifacts, which was very difficult to filter out.



# Bibliography

- [Abdel-Nasser 21] M. Abdel-Nasser & O. Salah. *New continuum surgical robot based on hybrid concentric tube-tendon driven mechanism.* Proceedings of the Institution of Mechanical Engineers, Part C: Journal of Mechanical Engineering Science, vol. 235, no. 24, pages 7550–7568, 2021.
- [AbuZaiter 15] A. AbuZaiter, E. L. Ng, M. S. M. Ali & S. Kazi. *Minature parallel manipulator using TiNiCu shape-memory-alloy microactuators.* In 2015 10th Asian Control Conference (ASCC), pages 1–4, 2015.
- [Ahronovich 21] E. Z. Ahronovich, N. Simaan & K. M. Joos. *A Review of Robotic and OCT-Aided Systems for Vitreoretinal Surgery.* Advances in Therapy, vol. 38, pages 2114 – 2129, 2021.
- [Al-Mangour 15] B. Al-Mangour. Powder metallurgy of stainless steel: State-of-the art, challenges, and development, pages 37–80. Nova Science, 01 2015.
- [Alfalahi 20] H. Alfalahi, F. Renda & C. Stefanini. *Concentric Tube Robots for Minimally Invasive Surgery: Current Applications and Future Opportunities.* IEEE Transactions on Medical Robotics and Bionics, vol. 2, no. 3, pages 410–424, 2020.
- [Alfalahi 21] H. Alfalahi, F. Renda, C. Messer & C. Stefanini. *Exploiting the instability of eccentric tube robots for distal force control in minimally invasive cardiac ablation.* Proceedings of the Institution of Mechanical Engineers, Part C: Journal of Mechanical Engineering Science, vol. 235, no. 23, pages 7212–7232, 2021.
- [Aloi 18a] V. Aloi, C. Black & C. Rucker. *Stiffness control of parallel continuum robots.* In Dynamic Systems and Control Conference, volume 51890, page V001T04A012. American Society of Mechanical Engineers, 2018.
- [Aloi 18b] V. Aloi, C. Black & C. Rucker. *Stiffness Control of Parallel Continuum Robots.* In ASME 2018 Dynamic Systems and Control Conference, volume 1 of *Dynamic Systems and Control Conference*, 09 2018. V001T04A012.

- [Aloi 22] V. A. Aloi. *Model Based Force Estimation and Stiffness Control for Continuum Robots*. Doctoral dissertation, University of Tennessee, 2022.
- [Altuzarra 19a] O. Altuzarra, D. Caballero, F. Campa & C. Pinto. Forward and inverse kinematics in 2-dof planar parallel continuum manipulators: Proceedings of the 7th european conference on mechanism science, pages 231–238. Springer, Cham, 01 2019.
- [Altuzarra 19b] O. Altuzarra, D. Caballero, F. J. Campa & C. Pinto. *Position analysis in planar parallel continuum mechanisms*. Mechanism and Machine Theory, vol. 132, pages 13–29, February 2019.
- [Altuzarra 19c] O. Altuzarra, D. Caballero, Q. Zhang & F. Campa. Kinematic characteristics of parallel continuum mechanisms, pages 293–301. Springer, Cham, 01 2019.
- [Amanov 15] E. Amanov, T.-D. Nguyen & J. Burgner-Kahrs. *Additive manufacturing of patient-specific tubular continuum manipulators*. In Medical Imaging, volume 9415, page 94151, 2015.
- [Amanov 21] E. Amanov, T.-D. Nguyen & J. Burgner-Kahrs. *Tendon-driven continuum robots with extensible sections—A model-based evaluation of path-following motions*. The International Journal of Robotics Research, vol. 40, no. 1, pages 7–23, 2021.
- [Andrius 01] M. Andrius, S. Juodkazis, V. Mizeikis, M. Watanabe, S. Matsuo, J. Nishii & H. Misawa. *Fabrication of 3D interconnected network of microchannels inside silica by femtosecond irradiation and etching*. In M. C. Gower, H. Helvajian, K. Sugioka & J. J. Dubowski, éditeurs, Laser Applications in Microelectronic and Optoelectronic Manufacturing VI, volume 4274, pages 469 – 477. International Society for Optics and Photonics, SPIE, 2001.
- [Anor 11a] T. Anor, J. Madsen & P. Dupont. *Algorithms for Design of Continuum Robots Using the Concentric Tubes Approach: A Neurosurgical Example*. In IEEE International Conference on Robotics and Automation, ICRA, pages 667–673, 05 2011.
- [Anor 11b] T. Anor, J. R. Madsen & P. Dupont. *Algorithms for design of continuum robots using the concentric tubes approach: A neurosurgical example*. In 2011 IEEE International Conference on Robotics and Automation, pages 667–673, 2011.

- [Antman 05] S. Antman. *Nonlinear Problems of Elasticity*; 2nd ed. Springer, Dordrecht, 2005.
- [Arevalo 01] V. M. Arevalo. *Sinusoidal Velocity Profiles for Motion Control*. In 2001 ASPE Control of Precision Systems, Philadelphia, PA, USA, 2001.
- [Armanini 23] C. Armanini, F. Boyer, A. T. Mathew, C. Duriez & F. Renda. *Soft Robots Modeling: A Structured Overview*. IEEE Transactions on Robotics, vol. 39, no. 3, pages 1728–1748, 2023.
- [Ashkenasi 12] D. Ashkenasi, T. Kaszemeikat, N. Mueller, A. Lemke & H. J. Eichler. *Machining of glass and quartz using nanosecond and picosecond laser pulses*. In G. Hennig, X. Xu, B. Gu & Y. Nakata, éditeurs, Laser Applications in Microelectronic and Optoelectronic Manufacturing (LAMOM) XVII, volume 8243, page 82430M. International Society for Optics and Photonics, SPIE, 2012.
- [Atzeni 10] E. Atzeni, L. Iuliano, P. Minetola & A. Salmi. *Redesign and cost estimation of rapid manufactured plastic parts*. Rapid Prototyping Journal, vol. 16, pages 308–317, 08 2010.
- [Atzeni 12] E. Atzeni & A. Salmi. *Economics of additive manufacturing for end-useable metal parts*. The International Journal of Advanced Manufacturing Technology, vol. 62, 10 2012.
- [Audoly 13] B. Audoly, N. Clauvelin, P.-T. Brun, M. Bergou, E. Grinspun & M. Wardetzky. *A discrete geometric approach for simulating the dynamics of thin viscous threads*. Journal of Computational Physics, vol. 253, pages 18–49, 2013.
- [Ayvali 12] E. Ayvali, C.-P. Liang, M. Ho, Y. Chen & J. P. Desai. *Towards a discretely actuated steerable cannula for diagnostic and therapeutic procedures*. The International Journal of Robotics Research, vol. 31, no. 5, pages 588–603, 2012. PMID: 22639482.
- [Azamat 18] Y. Azamat, K. Koganezawa & Y. Yamamoto. *Design and Kinematics of Cable-Driven Continuum Robot Arm with Universal Joint Backbone*. In 2018 IEEE International Conference on Robotics and Biomimetics (ROBIO), pages 2444–2449, 2018.
- [Azimian 14a] H. Azimian, P. Francis, T. Looi & J. Drake. *Structurally-redesigned concentric-tube manipulators with improved stability*. In IEEE/RSJ International Conference on Intelligent Robots and Systems, pages 2030–2035, 2014.

- [Azimian 14b] H. Azimian, P. Francis, T. Looi & J. Drake. *Structurally-redesigned concentric-tube manipulators with improved stability*. In 2014 IEEE/RSJ International Conference on Intelligent Robots and Systems, pages 2030–2035, 2014.
- [Badani 07] K. Badani, S. Kaul & M. Menon. *Evolution of robotic radical prostatectomy - Assessment after 2766 procedures*. Cancer, vol. 110, pages 1951–8, 11 2007.
- [Baek 16] C. Baek, K. Yoon & D.-N. Kim. *Finite element modeling of concentric-tube continuum robots*. Structural Engineering and Mechanics, vol. 57, pages 809–821, 2016.
- [Bai 12a] S. Bai & C. Xing. *Shape modeling of a concentric-tube continuum robot*. In IEEE International Conference on Robotics and Biomimetics (ROBIO), pages 116–121, 2012.
- [Bai 12b] S. Bai & C. Xing. *Shape modeling of a concentric-tube continuum robot*. In 2012 IEEE International Conference on Robotics and Biomimetics (ROBIO), pages 116–121, 2012.
- [Baran 17a] Y. Baran, K. Rabenorosoa, G. J. Laurent, P. Rougeot, N. Andreff & B. Tamadazte. *Preliminary results on OCT-based position control of a concentric tube robot*. In IEEE/RSJ International Conference on Intelligent Robots and Systems (IROS), pages 3000–3005, 2017.
- [Baran 17b] Y. Baran, K. Rabenorosoa, G. J. Laurent, P. Rougeot, N. Andreff & B. Tamadazte. *Preliminary results on OCT-based position control of a concentric tube robot*. In 2017 IEEE/RSJ International Conference on Intelligent Robots and Systems (IROS), pages 3000–3005, 2017.
- [Barbot 20] A. Barbot, M. Power, F. Seichepine & G.-Z. Yang. *Liquid seal for compact micropiston actuation at the capillary tip*. Science Advances, vol. 6, no. 22, page 5660, 2020.
- [Baudet 19] E. Baudet, Y. Ledemi, P. Larochelle, S. Morency & Y. Messaddeq. *3D-printing of arsenic sulfide chalcogenide glasses*. Opt. Mater. Express, vol. 9, no. 5, pages 2307–2317, May 2019.
- [Baykal 15a] C. Baykal. Design optimization algorithms for concentric tube robots. Master’s thesis, *University of North Carolina at Chapel Hill*, 2015.

- [Baykal 15b] C. Baykal, L. G. Torres & R. Alterovitz. *Optimizing design parameters for sets of concentric tube robots using sampling-based motion planning*. In IEEE/RSJ International Conference on Intelligent Robots and Systems, pages 4381–4387, 2015.
- [Baykal 17] C. Baykal & R. Alterovitz. *Asymptotically Optimal Design of Piecewise Cylindrical Robots using Motion Planning*. In Robotics: Science and Systems, 2017.
- [Baykal 19] C. Baykal, C. Bowen & R. Alterovitz. *Asymptotically optimal kinematic design of robots using motion planning*. Autonomous robots, vol. 43, no. 2, pages 345–357, 2019.
- [Bedell 11] C. Bedell, J. Lock, A. Gosline & P. E. Dupont. *Design optimization of concentric tube robots based on task and anatomical constraints*. In IEEE International Conference on Robotics and Automation, pages 398–403, 2011.
- [Bellouard 05] Y. Bellouard, A. A. Said & P. Bado. *Integrating optics and micro-mechanics in a single substrate: a step toward monolithic integration in fused silica*. Opt. Express, vol. 13, no. 17, pages 6635–6644, Aug 2005.
- [Bellouard 11] Y. Bellouard. *On the bending strength of fused silica flexures fabricated by ultrafast lasers (Invited)*. Opt. Mater. Express, vol. 1, no. 5, pages 816–831, Sep 2011.
- [Benouhiba 21] A. Benouhiba, L. Wurtz, J.-Y. Rauch, J. Agnus, K. Rabenorosoa & c. clévy. *NanoRobotic Structures with Embedded Actuation via Ion Induced Folding*. Advanced Materials, vol. 33, 11 2021.
- [Beresna 11] M. Beresna, M. Gecevičius & P. G. Kazansky. *Polarization sensitive elements fabricated by femtosecond laser nanostructuring of glass*  
*Invited*  
. Opt. Mater. Express, vol. 1, no. 4, pages 783–795, Aug 2011.
- [Bergeles 15] C. Bergeles, A. H. Gosline, N. V. Vasilyev, P. J. Codd, P. J. del Nido & P. E. Dupont. *Concentric Tube Robot Design and Optimization Based on Task and Anatomical Constraints*. in IEEE Transactions on Robotics, vol. 31, no. 1, pages 67–84, 2015.

- [Black 17] C. B. Black. *Modeling, Analysis, Force Sensing and Control of Continuum Robots for Minimally Invasive Surgery*. Doctoral dissertation, University of Tennessee, 2017.
- [Black 18a] C. B. Black, J. Till & D. C. Rucker. *Parallel Continuum Robots: Modeling, Analysis, and Actuation-Based Force Sensing*. IEEE Transactions on Robotics, vol. 34, no. 1, pages 29–47, 2018.
- [Black 18b] C. B. Black, J. Till & D. C. Rucker. *Parallel Continuum Robots: Modeling, Analysis, and Actuation-Based Force Sensing*. IEEE Transactions on Robotics, vol. 34, no. 1, pages 29–47, February 2018.
- [Boettcher 21] G. Boettcher, S. Lilge & J. Burgner-Kahrs. *Design of a Reconfigurable Parallel Continuum Robot With Tendon-Actuated Kinematic Chains*. IEEE Robotics and Automation Letters, vol. 6, no. 2, pages 1272–1279, April 2021.
- [Boushaki 16a] M. Boushaki, C. Liu, B. Herman, V. Trevillot, M. Akkari & P. Poignet. *Optimization of concentric-tube robot design for deep anterior brain tumor surgery*. In 14th International Conference on Control, Automation, Robotics and Vision (ICARCV), pages 1–6, 2016.
- [Boushaki 16b] M. Boushaki, C. Liu, B. Herman, V. Trevillot, M. Akkari & P. Poignet. *Optimization of concentric-tube robot design for deep anterior brain tumor surgery*. In 2016 14th International Conference on Control, Automation, Robotics and Vision (ICARCV), pages 1–6, 2016.
- [Boushaki 16c] M. N. Boushaki. *Design Optimization and Control for Concentric Tube Robot in Assisted Single-Access Laparoscopic Surgery*. Doctoral dissertation, Université Montpellier, October 2016.
- [Boylan 11] J. F. Boylan & Z. C. Lin. *Heat Treatment for Cold Worked Nitinol to Impart Shape Setting Capability Without Eventually Developing Stress-Induced Martensite*, July 2011.
- [Bressan 08] J. Bressan, D. Daros, A. Sokolowski, R. Mesquita & C. Barbosa. *Influence of hardness on the wear resistance of 17-4 PH stainless steel evaluated by the pin-on-disc testing*. Journal of Materials Processing Technology, vol. 205, no. 1, pages 353–359, 2008.

- [Briot 22a] S. Briot & A. Goldsztejn. *Singularity Conditions for Continuum Parallel Robots*. IEEE Transactions on Robotics, vol. 38, no. 1, pages 507–525, February 2022.
- [Briot 22b] S. Briot & A. Goldsztejn. *Singularity Conditions for Continuum Parallel Robots*. IEEE Transactions on Robotics, vol. 38, no. 1, pages 507–525, 2022.
- [Bruns 21] T. L. Bruns, A. A. Remirez, M. A. Emerson, R. A. Lathrop, A. W. Mahoney, H. B. Gilbert, C. L. Liu, P. T. Russell, R. F. Labadie, K. D. Weaver & I. Robert J. Webster. *A modular, multi-arm concentric tube robot system with application to transnasal surgery for orbital tumors*. The International Journal of Robotics Research, vol. 40, no. 2-3, pages 521–533, 2021.
- [Bryson 14] C. E. Bryson & D. C. Rucker. *Toward parallel continuum manipulators*. In 2014 IEEE International Conference on Robotics and Automation (ICRA), pages 778–785, Hong Kong, China, May 2014. IEEE.
- [Burgner 11] J. Burgner, P. J. Swaney, D. C. Rucker, H. B. Gilbert, S. T. Nill, P. T. Russell, K. D. Weaver & R. J. Webster III. *A bi-manual teleoperated system for endonasal skull base surgery*. In IEEE/RSJ International Conference on Intelligent Robots and Systems, pages 2517–2523, 2011.
- [Burgner 12] J. Burgner, P. J. Swaney, T. L. Bruns, M. S. Clark, D. C. Rucker, E. C. Burdette & R. J. Webster. *An Autoclavable Steerable Cannula Manual Deployment Device: Design and Accuracy Analysis*. Journal of Medical Devices, Transactions of the ASME, vol. 6, no. 4, pages 1–7, 2012.
- [Burgner 13a] J. Burgner, H. B. Gilbert & R. J. Webster. *On the computational design of concentric tube robots: Incorporating volume-based objectives*. In IEEE International Conference on Robotics and Automation, pages 1193–1198, 2013.
- [Burgner 13b] J. Burgner, P. J. Swaney, R. A. Lathrop, K. D. Weaver & R. J. Webster. *Debulking from within: A robotic steerable cannula for intracerebral hemorrhage evacuation*. in IEEE Transactions on Biomedical Engineering, vol. 60, no. 9, pages 2567–2575, 2013.
- [Burgner 14a] J. Burgner, D. C. Rucker, H. B. Gilbert, P. J. Swaney, P. T. Russell, K. D. Weaver & R. J. Webster. *A telerobotic system for transnasal surgery*. IEEE/ASME Transactions on Mechatronics, vol. 19, no. 3, pages 996–1006, 2014.

- [Burgner 14b] J. Burgner Kahrs, H. B. Gilbert, J. Granna, P. J. Swaney & R. J. Webster. *Workspace characterization for concentric tube continuum robots*. In IEEE/RSJ International Conference on Intelligent Robots and Systems, pages 1269–1275, 2014.
- [Burgner 15a] J. Burgner Kahrs, D. C. Rucker & H. Choset. *Continuum Robots for Medical Applications: A Survey*. IEEE Transactions on Robotics, vol. 31, no. 6, pages 1261–1280, 2015.
- [Burgner 15b] J. Burgner Kahrs, D. C. Rucker & H. Choset. *Continuum Robots for Medical Applications: A Survey*. in IEEE Transactions on Robotics, vol. 31, no. 6, pages 1261–1280, 2015.
- [Burgner 15c] J. Burgner Kahrs, D. C. Rucker & H. Choset. *Continuum robots for medical applications: A survey*. IEEE Transactions on Robotics, vol. 31, no. 6, pages 1261–1280, 2015.
- [Butler 11] E. J. Butler, C. Folk, A. Cohen, N. V. Vasilyev, R. Chen, P. J. del Nido & P. E. Dupont. *Metal MEMS tools for beating-heart tissue approximation*. In 2011 IEEE International Conference on Robotics and Automation, pages 411–416, 2011.
- [Butler 12] E. J. Butler, R. Hammond-Oakley, S. Chawarski, A. H. Gosline, P. Codd, T. Anor, J. R. Madsen, P. E. Dupont & J. Lock. *Robotic neuro-endoscope with concentric tube augmentation*. In IEEE/RSJ International Conference on Intelligent Robots and Systems, pages 2941–2946, 2012.
- [Butt 22] M. A. Butt, G. S. Voronkov, E. P. Grakhova, R. V. Kultuyarov, N. L. Kazanskiy & S. N. Khonina. *Environmental Monitoring: A Comprehensive Review on Optical Waveguide and Fiber-Based Sensors*. Biosensors, vol. 12, no. 11, 2022.
- [Camarillo 08] D. B. Camarillo, C. F. Milne, C. R. Carlson, M. R. Zinn & J. K. Salisbury. *Mechanics Modeling of Tendon-Driven Continuum Manipulators*. IEEE Transactions on Robotics, vol. 24, no. 6, pages 1262–1273, 2008.
- [Campa 19] F. Campa, M. Diez, D. Diaz-Caneja & O. Altuzarra. *A 2 dof continuum parallel robot for pick & place collaborative tasks*. In IFToMM World Congress on Mechanism and Machine Science, pages 1979–1988. Springer, 2019.
- [Campbell 05] S. Campbell, F. Dear, D. Hand & D. Reid. *Single-pulse femtosecond laser machining of glass*. Journal of Optics A: Pure and Applied Optics, vol. 7, page 162, 02 2005.

- [Cangan 22] B. G. Cangan, S. E. Navarro, B. Yang, Y. Zhang, C. Duriez & R. K. Katzschmann. *Model-Based Disturbance Estimation for a Fiber-Reinforced Soft Manipulator using Orientation Sensing*. In 2022 IEEE/RSJ International Conference on Intelligent Robots and Systems (IROS), pages 9424–9430, 2022.
- [Chang 08] S.-H. Chang, S. chin Lee & T.-P. Tang. *Effect of Shot Peening Treatment on Forging Die Life*. Materials Transactions, vol. 49, pages 619–623, 2008.
- [Chen 19] G. Chen, Z. Zhang, Z. Chen & H. Wang. A general discretization-based approach for the kinetostatic analysis of closed-loop rigid/flexible hybrid mechanisms, pages 269–276. Springer, Cham, 01 2019.
- [Chen 21a] G. Chen, Y. Kang, Z. Liang, Z. Zhang & H. Wang. *Kinetostatics modeling and analysis of parallel continuum manipulators*. Mechanism and Machine Theory, vol. 163, page 104380, 2021.
- [Chen 21b] G. Chen, Y. Kang, Z. Liang, Z. Zhang & H. Wang. *Kinetostatics modeling and analysis of parallel continuum manipulators*. Mechanism and Machine Theory, vol. 163, page 104380, September 2021.
- [Cheng 03a] Y. Cheng, K. Sugioka, K. Midorikawa, M. Masuda, K. Toyoda, M. Kawachi & K. Shihoyama. *Control of the cross-sectional shape of a hollow microchannel embedded in photostructurable glass by use of a femtosecond laser*. Opt. Lett., vol. 28, no. 1, pages 55–57, Jan 2003.
- [Cheng 03b] Y. Cheng, K. Sugioka, K. Midorikawa, M. Masuda, K. Toyoda, M. Kawachi & K. Shihoyama. *Three-dimensional micro-optical components embedded in photosensitive glass by a femtosecond laser*. Opt. Lett., vol. 28, no. 13, pages 1144–1146, Jul 2003.
- [Chikhaoui 16] M. T. Chikhaoui, K. Rabenorosoa & N. Andreff. *Kinematics and performance analysis of a novel concentric tube robotic structure with embedded soft micro-actuation*. Mechanism and Machine Theory, vol. 104, pages 234–254, 2016.
- [Chikhaoui 18a] M. T. Chikhaoui & J. Burgner-Kahrs. *Control of Continuum Robots for Medical Applications: State of the Art*. In ACTUATOR 2018; 16th International Conference on New Actuators, pages 1–11, 2018.

- [Chikhaoui 18b] M. T. Chikhaoui, J. Granna, J. Starke & J. Burgner-Kahrs. *Toward Motion Coordination Control and Design Optimization for Dual-Arm Concentric Tube Continuum Robots*. IEEE Robotics and Automation Letters, vol. 3, no. 3, pages 1793–1800, 2018.
- [Chikhaoui 19] M. T. Chikhaoui, S. Lilge, S. Kleinschmidt & J. Burgner-Kahrs. *Comparison of Modeling Approaches for a Tendon Actuated Continuum Robot With Three Extensible Segments*. IEEE Robotics and Automation Letters, vol. 4, no. 2, pages 989–996, 2019.
- [Chirikjian 94] G. S. Chirikjian. *Hyper-redundant manipulator dynamics: a continuum approximation*. Advanced Robotics, vol. 9, no. 3, pages 217–243, 1994.
- [Chitalia 18] Y. Chitalia, X. Wang & J. P. Desai. *Design, Modeling and Control of a 2-DoF Robotic Guidewire*. In 2018 IEEE International Conference on Robotics and Automation (ICRA), pages 32–37, 2018.
- [Choi 07] J. Choi, B. Jeon & B. Kim. *Chemical-assisted ultrasonic machining of glass*. Journal of Materials Processing Technology, vol. 191, no. 1, pages 153–156, 2007. Advances in Materials and Processing Technologies, July 30th - August 3rd 2006, Las Vegas, Nevada.
- [Comber 13] D. B. Comber, E. J. Barth, R. J. Webster III & J. S. Neimat. *Open-Loop Tip Accuracy of an MRI-Compatible Active Cannula Robot*. In Conference: The Hamlyn Symposium on Medical Robotics, pages 112–113, 2013.
- [Comber 17] D. B. Comber, E. B. Pitt, H. B. Gilbert, M. W. Powellson, E. S. Matijevich, J. S. Neimat, R. J. Webster & E. J. Barth. *Optimization of Curvilinear Needle Trajectories for Transforaminal Hippocampotomy*. Operative Neurosurgery, vol. 13, pages 15 – 22, 2017.
- [Company 23] B. Company. *Borosilicate Glass*, 2023.
- [Comte 02] C. Comte & J. von Stebut. *Microprobe-type measurement of Young's modulus and Poisson coefficient by means of depth sensing indentation and acoustic microscopy*. Surface and Coatings Technology, vol. 154, no. 1, pages 42–48, 2002.
- [Cooperstein 18] I. Cooperstein, E. Shukrun, O. Press, A. Kamyshny & S. Magdassi. *Additive Manufacturing of Transparent Silica Glass from Solutions*. ACS Applied Materials & Interfaces, vol. 10, no. 22, pages 18879–18885, 2018. PMID: 29741081.

- [corporation 22a] M. corporation. *Nitinol Tube*, 2022.
- [Corporation 22b] N. M. Corporation. *FEP Heat Shrink Tubing Technical Information*, 2022.
- [Cuellar 87] E. Cuellar, D. Roberts & L. Middleman. *Static fatigue lifetime of optical fibers in bending*. Fiber and Integrated Optics, vol. 6, no. 3, pages 203–213, 1987.
- [Datsiou 19] K. C. Datsiou, E. Saleh, F. Spirrett, R. Goodridge, I. Ashcroft & D. Eustice. *Additive manufacturing of glass with laser powder bed fusion*. Journal of the American Ceramic Society, vol. 102, no. 8, pages 4410–4414, 2019.
- [Davis 96] K. M. Davis, K. Miura, N. Sugimoto & K. Hirao. *Writing waveguides in glass with a femtosecond laser*. Opt. Lett., vol. 21, no. 21, pages 1729–1731, Nov 1996.
- [De Volder 09] M. De Volder, F. Ceyssens, D. Reynaerts & R. Puers. *Microsized Piston-Cylinder Pneumatic and Hydraulic Actuators Fabricated by Lithography*. Journal of Microelectromechanical Systems, vol. 18, no. 5, pages 1100–1104, 2009.
- [Destino 18] J. F. Destino, N. A. Dudukovic, M. A. Johnson, D. T. Nguyen, T. D. Yee, G. C. Egan, A. M. Sawvel, W. A. Steele, T. F. Baumann, E. B. Duoss, T. Suratwala & R. Dylla-Spears. *3D Printed Optical Quality Silica and Silica-Titania Glasses from Sol-Gel Feedstocks*. Advanced Materials Technologies, vol. 3, no. 6, page 1700323, 2018.
- [Devreker 15] A. Devreker, B. Rosa, A. Desjardins, E. J. Alles, L. C. Garcia-Peraza, E. Maneas, D. Stoyanov, A. L. David, T. Vercauteren, J. Deprest, S. Ourselin, D. Reynaerts & E. V. Poorten. *Fluidic actuation for intra-operative in situ imaging*. In 2015 IEEE/RSJ International Conference on Intelligent Robots and Systems (IROS), pages 1415–1421, September 2015.
- [Donat 23] H. Donat, P. Mohammadi & J. Steil. *Data-Driven Estimation of Forces Along the Backbone of Concentric Tube Continuum Robots*. In 2023 IEEE International Conference on Robotics and Automation (ICRA), pages 2662–2668, 2023.
- [Duerig 99] T. Duerig, A. Pelton & D. Stöckel. *An overview of NiTiNol medical applications*. Materials Science and Engineering: A, vol. 273, pages 149–160, 12 1999.

- [Dupont 09a] P. E. Dupont, J. Lock & E. Butler. *Torsional kinematic model for concentric tube robots*. In IEEE International Conference on Robotics and Automation, pages 3851–3858, 2009.
- [Dupont 09b] P. E. Dupont, J. Lock & E. Butler. *Torsional kinematic model for concentric tube robots*. In 2009 IEEE International Conference on Robotics and Automation, pages 3851–3858, 2009.
- [Dupont 10a] P. E. Dupont, J. Lock & B. Itkowitz. *Real-time position control of concentric tube robots*. In IEEE International Conference on Robotics and Automation, pages 562–568, 2010.
- [Dupont 10b] P. E. Dupont, J. Lock, B. Itkowitz & E. Butler. *Design and Control of Concentric-Tube Robots*. IEEE Transactions on Robotics, vol. 26, no. 2, pages 209–225, 2010.
- [Dupont 10c] P. E. Dupont, J. Lock, B. Itkowitz & E. Butler. *Design and control of concentric-tube robots*. in IEEE Transactions on Robotics, vol. 26, no. 2, pages 209–225, 2010.
- [Dupont 12] P. Dupont, A. Gosline, N. Vasilyev, J. Lock, E. Butler, C. Folk, A. Cohen, R. Chen, G. Schmitz & P. del Nido. *Concentric Tube Robots for Minimally Invasive Surgery*. Hamlyn Symposium on Medical Robotics, 01 2012.
- [Dupont 16] P. Dupont. *Concentric Tube Robot Chicken Leg Dissection*, Sep 23, 2016.
- [Dupont 21] P. E. Dupont, B. J. Nelson, M. Goldfarb, B. Hannaford, A. Menciassi, M. K. O’Malley, N. Simaan, P. Valdastri & G.-Z. Yang. *A decade retrospective of medical robotics research from 2010 to 2020*. Science Robotics, vol. 6, no. 60, page eabi8017, 2021.
- [Duriez 13] C. Duriez. *Control of elastic soft robots based on real-time finite element method*. In 2013 IEEE International Conference on Robotics and Automation, pages 3982–3987, 2013.
- [Dwyer 17] G. Dwyer, F. Chadebecq, M. T. Amo, C. Bergeles, E. Maneas, V. Pawar, E. V. Poorten, J. Deprest, S. Ourselin, P. De Coppi, T. Vercauteren & D. Stoyanov. *A Continuum Robot and Control Interface for Surgical Assist in Fetsoscopic Interventions*. IEEE Robotics and Automation Letters, vol. 2, no. 3, pages 1656–1663, 2017.
- [Dwyer 20] G. Dwyer. *Robotic Actuation for Fetsoscopic Interventions*. Doctoral dissertation, University College London, August 2020.

- [Dylla-Spears 20] R. Dylla-Spears, T. D. Yee, K. Sasan, D. T. Nguyen, N. A. Dudukovic, J. M. Ortega, M. A. Johnson, O. D. Herrera, F. J. Ryerson & L. L. Wong. *3D printed gradient index glass optics*. Science Advances, vol. 6, no. 47, page eabc7429, 2020.
- [D'Ettorre 21] C. D'Ettorre, A. Mariani, A. Stilli, F. Rodriguez y Baena, P. Valdastri, A. Deguet, P. Kazanzides, R. H. Taylor, G. S. Fischer, S. P. DiMaio, A. Menciassi & D. Stoyanov. *Accelerating Surgical Robotics Research: A Review of 10 Years With the da Vinci Research Kit*. IEEE Robotics Automation Magazine, vol. 28, no. 4, pages 56–78, 2021.
- [Eastwood 17] K. Eastwood, P. Francis, H. Azimian, A. Swarup, T. Looi, J. Drake & H. Naguib. *Design of a Contact-Aided Compliant Notched-Tube Joint for Surgical Manipulation in Confined Workspaces*. Journal of Mechanisms and Robotics, vol. 10, 10 2017.
- [EHRAT 17] B. EHRAT. Real-time control of industrial robots for shape setting nitinol rods. Master's thesis, *University of Illinois*, 2017.
- [Eklund 08] E. J. Eklund, A. M. Shkel, S. Knappe, E. Donley & J. Kitching. *Glass-blown spherical microcells for chip-scale atomic devices*. Sensors and Actuators A: Physical, vol. 143, no. 1, pages 175–180, 2008. Micromechanics Section of Sensors and Actuators (SAMM), based on contributions revised from the Technical Digest of the IEEE 20th International Conference on Micro Electro Mechanical Systems (MEMS 2007).
- [Erol-Taygun 13] M. Erol-Taygun, K. Zheng & A. R. Boccaccini. *Nanoscale Bioactive Glasses in Medical Applications*. International Journal of Applied Glass Science, vol. 4, no. 2, pages 136–148, 2013.
- [Esakkiappan 19] S. Esakkiappan, B. Shirinzadeh & W. Wei. *Development of a cost-effective actuation unit for three DOF concentric tube robot in minimally invasive surgery*. IEEE/ASME International Conference on Advanced Intelligent Mechatronics, AIM, vol. 2019-July, pages 1013–1018, 2019.
- [Falkenhahn 15] V. Falkenhahn, A. Hildebrandt, R. Neumann & O. Sawodny. *Model-based feedforward position control of constant curvature continuum robots using feedback linearization*. In 2015 IEEE International Conference on Robotics and Automation (ICRA), pages 762–767, 2015.

- [Farooq 16] M. Farooq, S. Park, J. Park & S. Ko. *Shape optimization of a novel ligation tool using a concentric tube mechanism*. In 16th International Conference on Control, Automation and Systems, pages 413–418, 2016.
- [Farooq 18] M. Farooq, W. Kim & S. Y. Ko. *A robotic suture-passing device for possible use in SILS and NOTES*. The International Journal of Medical Robotics and Computer Assisted Surgery, vol. 14, page e1916, 05 2018.
- [Farooq 19a] M. Farooq & S. Y. Ko. *An Automated Extracorporeal Knot-tying System Using Two Concentric Tube Robotic Arms for Deployment through a 3-mm Port*. International Journal of Control, Automation and Systems, vol. 18, 08 2019.
- [Farooq 19b] M. Farooq, B. Xu & S. Y. Ko. *A concentric tube-based 4-DOF puncturing needle with a novel miniaturized actuation system for vitrectomy*. BioMedical Engineering OnLine, vol. 18, 04 2019.
- [Fascio 99] V. Fascio, R. Wuthrich, D. Viquerat & H. Langen. *3D microstructuring of glass using electrochemical discharge machining (ECDM)*. In MHS'99. Proceedings of 1999 International Symposium on Micromechatronics and Human Science (Cat. No.99TH8478), pages 179–183, 1999.
- [Fateri 14a] M. Fateri & A. Gebhardt. *Jewelry Fabrication via Selective Laser Melting of Glass*. In Engineering Systems Design and Analysis, volume Volume 1: Applied Mechanics; Automotive Systems; Biomedical Biotechnology Engineering; Computational Mechanics; Design; Digital Manufacturing; Education; Marine and Aerospace Applications, page V001T06A005, 07 2014.
- [Fateri 14b] M. Fateri & A. Gebhardt. *Selective Laser Melting of Soda-Lime Glass Powder*. International Journal of Applied Ceramic Technology, vol. 12, 10 2014.
- [FEMTOprint 17] FEMTOprint. *Standardisation of microfluidics. Opportunity for innovative technologies*, 2017. [Online; accessed 15-July-2023].
- [FEMTOprint 18a] FEMTOprint. *How three-dimensional thinking is turning a piece of material into smart medical devices*, 2018. [Online; accessed 16-July-2023].
- [FEMTOprint 18b] FEMTOprint. *Transparent Suspended Microchannel Resonator*, 2018. [Online; accessed 16-July-2023].

- [FEMTOprint 23] FEMTOprint. *FEMTOprint TESTIMONIALS*, 2023. [Online; accessed 16-July-2023].
- [Fernando 17] P. Fernando, M. Zhang, Z. Pei & W. Cong. *Intermittent and Continuous Rotary Ultrasonic Machining of K9 Glass: An Experimental Investigation*. Journal of Manufacturing and Materials Processing, vol. 1, no. 2, 2017.
- [Fichera 21] L. Fichera. *Bringing the light inside the body to perform better surgery*. Science Robotics, vol. 6, no. 50, page eabf1523, 2021.
- [Fischbach 10] K. D. Fischbach, K. Georgiadis, F. Wang, O. Dambon, F. Klocke, Y. Chen & A. Y. Yi. *Investigation of the effects of process parameters on the glass-to-mold sticking force during precision glass molding*. Surface and Coatings Technology, vol. 205, no. 2, pages 312–319, 2010.
- [Florea 22] A. N. Florea, D. S. Ropella, E. Amanov, S. D. H. III & R. J. W. III. *Design of a modular, multi-arm concentric tube robot featuring roller gears*. In C. A. Linte & J. H. Siewerdsen, éditeurs, Medical Imaging 2022: Image-Guided Procedures, Robotic Interventions, and Modeling, volume 12034, pages 37 – 42. International Society for Optics and Photonics, SPIE, 2022.
- [Friedrich 18] D. Friedrich, V. Modes, T. Hoffmann, J. Greve, P. Schuler & J. Burgner-Kahrs. *Teleoperated tubular continuum robots for transoral surgery - feasibility in a porcine larynx model*. The International Journal of Medical Robotics and Computer Assisted Surgery, vol. 14, page e1928, 06 2018.
- [Furusho 05] J. Furusho, T. Ono, R. Murai, T. Fujimoto, Y. Chiba & H. Horio. *Development of a curved multi-tube (CMT) catheter for percutaneous umbilical blood sampling and control methods of CMT catheters for solid organs*. In IEEE International Conference Mechatronics and Automation, 2005, volume 1, pages 410–415 Vol. 1, 2005.
- [Füzesi 07] F. Füzesi, A. Jornod, P. Thomann, M. D. Plimmer, G. Duddle, R. Moser, L. Sache & H. Bleuler. *An electrostatic glass actuator for ultrahigh vacuum: A rotating light trap for continuous beams of laser-cooled atoms*. Review of Scientific Instruments, vol. 78, no. 10, 10 2007. 103109.
- [Gafford 20] J. B. Gafford, S. Webster, N. Dillon, E. Blum, R. Hendrick, F. Maldonado, E. A. Gillaspie, O. B. Rickman, S. D. Herrell & R. J. Webster. *A Concentric Tube Robot System for*

- Rigid Bronchoscopy: A Feasibility Study on Central Airway Obstruction Removal.* Annals of Biomedical Engineering, vol. 48, no. 1, pages 181–191, 2020.
- [Gallardo 21] O. F. Gallardo, B. Mauze, R. Dahmouche, C. Duriez & G. J. Laurent. *Turning an Articulated 3-PPSR Manipulator into a Parallel Continuum Robot.* In 2021 IEEE/RSJ International Conference on Intelligent Robots and Systems (IROS), pages 4955–4960, Prague, Czech Republic, September 2021. IEEE.
- [Ganji 09] Y. Ganji & F. Janabi-Sharifi. *Catheter Kinematics for Intracardiac Navigation.* IEEE Transactions on Biomedical Engineering, vol. 56, no. 3, pages 621–632, 2009.
- [Gao 10] S.-l. Gao, R.-C. Zhuang, J. Zhang, J.-W. Liu & E. Mäder. *Glass Fibers with Carbon Nanotube Networks as Multifunctional Sensors.* Advanced Functional Materials, vol. 20, no. 12, pages 1885–1893, 2010.
- [Gao 16] A. Gao, J. P. Carey, R. J. Murphy, I. Iordachita, R. H. Taylor & M. Armand. *Progress toward robotic surgery of the lateral skull base: Integration of a dexterous continuum manipulator and flexible ring curette.* In 2016 IEEE International Conference on Robotics and Automation (ICRA), pages 4429–4435, 2016.
- [Garner 17] S. M. Garner, X. Li & m.-H. Huang. Introduction to flexible glass substrates, chapitre 1, pages 1–33. John Wiley & Sons, Ltd, 2017.
- [Garriga 18] A. Garriga Casanovas & F. Rodriguez y Baena. *Complete follow-the-leader kinematics using concentric tube robots.* International Journal of Robotics Research, vol. 37, no. 1, pages 197–222, 2018.
- [Gharbi 23] A. Gharbi, A. Y. Kallel, O. Kanoun, W. Cheikhrouhou-Koubaa, C. H. Contag, I. Antoniac, N. Derbel & N. Ashammakhi. *A Biodegradable Bioactive Glass-Based Hydration Sensor for Biomedical Applications.* Micromachines, vol. 14, no. 1, 2023.
- [Gilbert 13] H. B. Gilbert & R. J. Webster. *Can concentric tube robots follow the leader?* In IEEE International Conference on Robotics and Automation, pages 4881–4887, 2013.
- [Gilbert 15a] H. B. Gilbert, R. J. Hendrick & R. J. Webster III. *Elastic stability of concentric tube robots: A stability measure and design test.* IEEE Transactions on Robotics, vol. 32, no. 1, pages 20–35, 2015.

- [Gilbert 15b] H. B. Gilbert, J. Neimat & R. J. Webster. *Concentric Tube Robots as Steerable Needles: Achieving Follow-the-Leader Deployment*. IEEE Transactions on Robotics, vol. 31, no. 2, pages 246–258, 2015.
- [Gilbert 16a] H. B. Gilbert, R. J. Hendrick & R. J. Webster. *Elastic Stability of Concentric Tube Robots: A Stability Measure and Design Test*. IEEE Transactions on Robotics, vol. 32, no. 1, pages 20–35, 2016.
- [Gilbert 16b] H. B. Gilbert, D. C. Rucker & R. J. Webster III. Concentric tube robots: The state of the art and future directions, pages 253–269. Robotics Research. Springer Tracts in Advanced Robotics, 2016.
- [Gilbert 16c] H. B. Gilbert & R. J. Webster. *Rapid, Reliable Shape Setting of Superelastic Nitinol for Prototyping Robots*. IEEE Robotics and Automation Letters, vol. 1, no. 1, pages 98–105, 2016.
- [Gilbert 16d] H. B. Gilbert & R. J. Webster. *Rapid, Reliable Shape Setting of Superelastic Nitinol for Prototyping Robots*. IEEE Robotics and Automation Letters, vol. 1, no. 1, pages 98–105, 2016.
- [Gilbert 16e] H. B. Gilbert, W. R. J, G. Michael, S. Nilanjan, S. Nabil & M. M. I. *Concentric Tube Robots: Design, Deployment, and Stability*. Doctoral dissertation, Vanderbilt University, 2016.
- [Girerd 17a] C. Girerd, K. Rabenorosoa, P. Rougeot & P. Renaud. *Towards optical biopsy of olfactory cells using concentric tube robots with follow-the-leader deployment*. In IEEE/RSJ International Conference on Intelligent Robots and Systems (IROS), pages 5661–5887, 2017.
- [Girerd 17b] C. Girerd, K. Rabenorosoa, P. Rougeot & P. Renaud. *Towards optical biopsy of olfactory cells using concentric tube robots with follow-the-leader deployment*. In 2017 IEEE/RSJ International Conference on Intelligent Robots and Systems (IROS), pages 5661–5887, 2017.
- [Girerd 18a] C. Girerd. *Conception de robots à tubes concentriques et application à l'inspection des cellules olfactives*. Doctoral dissertation, Université de Strasbourg, January 2018.
- [Girerd 18b] C. Girerd, T. Lihoreau, K. Rabenorosoa, B. Tamadazte, M. Benassarou, L. Tavernier, L. Pazart, E. Haffen, N. Andreff & P. Renaud. *In Vivo Inspection of the Olfactory Ep-*

- ithelium: Feasibility of Robotized Optical Biopsy.* Annals of Biomedical Engineering (ABME), vol. 46, pages 1951–1961, June 2018.
- [Girerd 18c] C. Girerd, K. Rabenorosoa & P. Renaud. Combining tube design and simple kinematic strategy for follow-the-leader deployment of concentric tube robots, pages 23–31. Springer International Publishing, Springer Cham, 2018.
- [Girerd 20a] C. Girerd, A. V. Kudryavtsev, P. Rougeot, P. Renaud, K. Rabenorosoa & B. Tamadazte. *SLAM-Based Follow-the-Leader Deployment of Concentric Tube Robots.* IEEE Robotics and Automation Letters, vol. 5, no. 2, pages 548–555, 2020.
- [Girerd 20b] C. Girerd, A. V. Kudryavtsev, P. Rougeot, P. Renaud, K. Rabenorosoa & B. Tamadazte. *SLAM-Based Follow-the-Leader Deployment of Concentric Tube Robots.* IEEE Robotics and Automation Letters, vol. 5, no. 2, pages 548–555, 2020.
- [Girerd 20c] C. Girerd, T. Schlinquer, N. Andreff, P. Renaud & K. Rabenorosoa. *Design of Concentric Tube Robots using Tube Patterning for Follow-the-Leader Deployment.* Journal of Mechanisms and Robotics, vol. 13, no. 1, pages 1–10, aug 2020.
- [Girerd 20d] C. Girerd & T. K. Morimoto. *Design and Control of a Hand-Held Concentric Tube Robot for Minimally Invasive Surgery.* IEEE Transactions on Robotics, pages 1–17, 2020.
- [Godage 11a] I. S. Godage, D. T. Branson, E. Guglielmino, G. A. Medrano-Cerda & D. G. Caldwell. *Dynamics for biomimetic continuum arms: A modal approach.* In 2011 IEEE International Conference on Robotics and Biomimetics, pages 104–109, 2011.
- [Godage 11b] I. S. Godage, D. T. Branson, E. Guglielmino, G. A. Medrano-Cerda & D. G. Caldwell. *Shape function-based kinematics and dynamics for variable length continuum robotic arms.* In 2011 IEEE International Conference on Robotics and Automation, pages 452–457, 2011.
- [Godage 11c] I. S. Godage, E. Guglielmino, D. T. Branson, G. A. Medrano-Cerda & D. G. Caldwell. *Novel modal approach for kinematics of multisection continuum arms.* In 2011 IEEE/RSJ International Conference on Intelligent Robots and Systems, pages 1093–1098, 2011.

- [Godage 15a] I. S. Godage, G. A. Medrano-Cerda, D. T. Branson, E. Guglielmino & D. G. Caldwell. *Modal kinematics for multisegment continuum arms*. Bioinspiration Biomimetics, vol. 10, no. 3, page 035002, may 2015.
- [Godage 15b] I. S. Godage, A. A. Remirez, R. Wirz, K. D. Weaver, J. Burgner-Kahrs & R. J. Webster. *Robotic intracerebral hemorrhage evacuation: An in-scanner approach with concentric tube robots*. In 2015 IEEE/RSJ International Conference on Intelligent Robots and Systems (IROS), pages 1447–1452, 2015.
- [Godage 16] I. S. Godage, G. A. Medrano-Cerda, D. T. Branson, E. Guglielmino & D. G. Caldwell. *Dynamics for variable length multisegment continuum arms*. The International Journal of Robotics Research, vol. 35, no. 6, pages 695–722, 2016.
- [Goldman 14] R. E. Goldman, A. Bajo & N. Simaan. *Compliant Motion Control for Multisegment Continuum Robots With Actuation Force Sensing*. IEEE Transactions on Robotics, vol. 30, no. 4, pages 890–902, 2014.
- [GoodFellow 21] GoodFellow. *Nitinol Tube - Standard Products*, 2021.
- [Gosline 12] A. H. Gosline, N. V. Vasilyev, E. J. Butler, C. Folk, A. Cohen, R. Chen, N. Lang, P. J. Del Nido & P. E. Dupont. *Percutaneous intracardiac beating-heart surgery using metal MEMS tissue approximation tools*. International Journal of Robotics Research, vol. 31, no. 9, pages 1081–1093, 2012.
- [Gottmann 17] J. Gottmann, M. Hermans, N. Repiev & J. Ortmann. *Selective Laser-Induced Etching of 3D Precision Quartz Glass Components for Microfluidic Applications—Up-Scaling of Complexity and Speed*. Micromachines, vol. 8, no. 4, 2017.
- [Grace 22] D. Grace, J. Lee-Ortiz, M. Garcia, A. Contreras-Esquin, A. Tekes & A. A. Amiri Moghadam. *Development of a Novel Six DOF Soft Parallel Robot*. In SoutheastCon 2022, pages 81–86, 2022.
- [Granna 17a] J. Granna, Y. Guo, K. D. Weaver & J. Burgner-Kahrs. *Comparison of Optimization Algorithms for a Tubular Aspiration Robot for Maximum Coverage in Intracerebral Hemorrhage Evacuation*. Journal of Medical Robotics Research, vol. 02, no. 01, page 1750004, 2017.

- [Granna 17b] J. Granna, A. Nabavi & J. Burgner-Kahrs. *Toward Computer-Assisted Planning for Interstitial Laser Ablation of Malignant Brain Tumors Using a Tubular Continuum Robot*. In M. Descoteaux, L. Maier-Hein, A. Franz, P. Janin, D. L. Collins & S. Duchesne, éditeurs, Medical Image Computing and Computer-Assisted Intervention (MICCAI 2017), pages 557–565, Cham, 2017. Springer International Publishing.
- [Granna 18] J. Granna, A. Nabavi & J. Burgner-Kahrs. *Computer-assisted planning for a concentric tube robotic system in neurosurgery*. International Journal of Computer Assisted Radiology and Surgery, vol. 14, 11 2018.
- [Granna 19] J. Granna. *Multi-objective particle swarm optimization for the structural design of concentric tube continuum robots for medical applications*. Doctoral dissertation, Hannover : Gottfried Wilhelm Leibniz Universität, 2019.
- [Grassmann 18] R. Grassmann, V. Modes & J. Burgner-Kahrs. *Learning the Forward and Inverse Kinematics of a 6-DOF Concentric Tube Continuum Robot in SE(3)*. In 2018 IEEE/RSJ International Conference on Intelligent Robots and Systems (IROS), pages 5125–5132, 2018.
- [Grassmann 22] R. M. Grassmann, R. Z. Chen, N. Liang & J. Burgner-Kahrs. *A Dataset and Benchmark for Learning the Kinematics of Concentric Tube Continuum Robots*. In 2022 IEEE/RSJ International Conference on Intelligent Robots and Systems (IROS), pages 9550–9557, 2022.
- [Graves 12] C. M. Graves, A. Slocum, R. Gupta & C. J. Walsh. *Towards a compact robotically steerable thermal ablation probe*. In IEEE International Conference on Robotics and Automation, pages 709–714, 2012.
- [Guan 11] W. Guan, A. Lockwood, B. J. Inkson & G. Möbus. *A Piezoelectric Goniometer Inside a Transmission Electron Microscope Goniometer*. Microscopy and Microanalysis, vol. 17, no. 5, page 827–833, 2011.
- [Ha 14a] J. Ha, F. C. Park & P. E. Dupont. *Achieving elastic stability of concentric tube robots through optimization of tube precurvature*. In 2014 IEEE/RSJ International Conference on Intelligent Robots and Systems, pages 864–870, 2014.

- [Ha 14b] J. Ha, F. C. Park & P. E. Dupont. *Achieving elastic stability of concentric tube robots through optimization of tube precurvature*. In IEEE/RSJ International Conference on Intelligent Robots and Systems, pages 864–870, 2014.
- [Ha 17] J. Ha, F. C. Park & P. E. Dupont. *Optimizing Tube Precurvature to Enhance the Elastic Stability of Concentric Tube Robots*. IEEE Transactions on Robotics, vol. 33, no. 1, pages 22–37, 2017.
- [Ha 19] J. Ha, G. Fagogenis & P. E. Dupont. *Modeling Tube Clearance and Bounding the Effect of Friction in Concentric Tube Robot Kinematics*. IEEE Transactions on Robotics, vol. 35, no. 2, pages 353–370, 2019.
- [Habibi 18] H. Habibi, C. Yang, R. Kang, I. D. Walker, I. S. Godage, X. Dong & D. T. Branson. *Modelling an Actuated Large Deformation Soft Continuum Robot Surface Undergoing External Forces Using a Lumped-Mass Approach*. In 2018 IEEE/RSJ International Conference on Intelligent Robots and Systems (IROS), pages 5958–5963, 2018.
- [Habibi 19] H. Habibi, C. Yang, I. S. Godage, R. Kang, I. D. Walker & I. Branson David T. *A Lumped-Mass Model for Large Deformation Continuum Surfaces Actuated by Continuum Robotic Arms*. Journal of Mechanisms and Robotics, vol. 12, no. 1, page 011014, 10 2019.
- [Hahn 72] T. A. Hahn & R. K. Kirby. *Thermal Expansion of Fused Silica from 80 to 1000 K - Standard Reference Material 739*. AIP Conference Proceedings, vol. 3, no. 1, pages 13–24, 1972.
- [Haldimann 06] M. Haldimann. *Fracture strength of structural glass elements: analytical and numerical modelling, testing and design*. 01 2006.
- [Halm 18] M. Halm & M. Posa. *A Quasi-static Model and Simulation Approach for Pushing, Grasping, and Jamming*. In Workshop on the Algorithmic Foundations of Robotics, 2018.
- [Hata 99] S. Hata, K. Sato & A. Shimokohbe. *Fabrication of thin film metallic glass and its application to microactuators*. In K. H. Chau & S. Dimitrijev, éditeurs, Device and Process Technologies for MEMS and Microelectronics, volume 3892, pages 97 – 108. International Society for Optics and Photonics, SPIE, 1999.

- [He 10] F. He, Y. Cheng, L. Qiao, C. Wang, Z. Xu, K. Sugioka, K. Midorikawa & J. Wu. *Two-photon fluorescence excitation with a microlens fabricated on the fused silica chip by femtosecond laser micromachining*. Applied Physics Letters, vol. 96, no. 4, 01 2010. 041108.
- [He 14] F. He, Y. Liao, J. Lin, J. Song, L. Qiao, Y. Cheng & K. Sugioka. *Femtosecond Laser Fabrication of Monolithically Integrated Microfluidic Sensors in Glass*. Sensors, vol. 14, no. 10, pages 19402–19440, 2014.
- [He 18] B. He, S. Xu & Z. Wang. *Research on Stiffness of Multibackbone Continuum Robot Based on Screw Theory and Euler-Bernoulli Beam*. Mathematical Problems in Engineering, vol. 2018, pages 1–16, 05 2018.
- [Hench 91] L. L. Hench. *Bioceramics: From Concept to Clinic*. Journal of the American Ceramic Society, vol. 74, no. 7, pages 1487–1510, 1991.
- [Hendrick 14a] R. J. Hendrick, S. D. Herrell & R. J. Webster. *A multi-arm hand-held robotic system for transurethral laser Prostate surgery*. In IEEE International Conference on Robotics and Automation (ICRA), pages 2850–2855, 2014.
- [Hendrick 14b] R. J. Hendrick, S. D. Herrell & R. J. Webster. *A multi-arm hand-held robotic system for transurethral laser Prostate surgery*. In IEEE International Conference on Robotics and Automation (ICRA), pages 2850–2855, 2014.
- [Hendrick 15a] R. J. Hendrick, H. B. Gilbert & R. J. Webster. *Designing snap-free concentric tube robots: A local bifurcation approach*. In IEEE International Conference on Robotics and Automation (ICRA), pages 2256–2263, 2015.
- [Hendrick 15b] R. J. Hendrick, H. B. Gilbert & R. J. Webster. *Designing snap-free concentric tube robots: A local bifurcation approach*. In 2015 IEEE International Conference on Robotics and Automation (ICRA), pages 2256–2263, 2015.
- [Hendrick 15c] R. J. Hendrick, C. R. Mitchell, S. D. Herrell & R. J. Webster. *Hand-held transendoscopic robotic manipulators: A transurethral laser prostate surgery case study*. International Journal of Robotics Research, vol. 34, no. 13, pages 1559–1572, 2015.

- [Hendrick 19] R. J. Hendrick, I. Robert J. Webster, S. D. Herrell, P. J. Swaney & R. Lathrop. *CONCENTRIC TUBE ROBOT*, October 2019.
- [Hnatovsky 06] C. Hnatovsky, R. Taylor, E. Simova, R. Pattathil, D. Rayner, V. Bhardwaj & P. Corkum. *Fabrication of Microchannels in Glass Using Focused Femtosecond Laser Radiation and Selective Chemical Etching*. Applied Physics A, vol. 84, pages 47–61, 07 2006.
- [Hof 17] L. A. Hof & J. Abou Ziki. *Micro-Hole Drilling on Glass Substrates—A Review*. Micromachines, vol. 8, no. 2, 2017.
- [Hopkins 15] J. B. Hopkins, J. Rivera, C. Kim & G. Krishnan. *Synthesis and Analysis of Soft Parallel Robots Comprised of Active Constraints*. Journal of Mechanisms and Robotics, vol. 7, no. 1, 02 2015. 011002.
- [Hoppe 11] A. Hoppe, N. Güldal & A. Boccaccini. *A Review of The Biological Response to Ionic Dissolution Products From Bioactive Glasses and Glass-Ceramics*. Biomaterials, vol. 32, pages 2757–74, 04 2011.
- [Hrma 12] P. Hrma & S. Han. *Effect of Glass Composition on Activation Energy of Viscosity in Glass-Melting-Temperature Range*. Journal of Non-Crystalline Solids, vol. 358, 08 2012.
- [Huang 22] X. Huang, X. Zhu & G. Gu. *Kinematic Modeling and Characterization of Soft Parallel Robots*. IEEE Transactions on Robotics, vol. 38, no. 6, pages 3792–3806, 2022.
- [in China 22] M. in China. *Nitinol Tube Manufacturers & Suppliers*, 2022.
- [Intuitive 21] Intuitive, 2021.
- [Iyengar 20] K. Iyengar, G. Dwyer & D. Stoyanov. *Investigating exploration for deep reinforcement learning of concentric tube robot control*. International Journal of Computer Assisted Radiology and Surgery, vol. 15, 06 2020.
- [Iyengar 21] K. Iyengar & D. Stoyanov. *Deep Reinforcement Learning for Concentric Tube Robot Control with a Goal-Based Curriculum*. In 2021 IEEE International Conference on Robotics and Automation (ICRA), pages 1459–1465, 2021.
- [Janabi-Sharifi 21a] F. Janabi-Sharifi, A. Jalali & I. D. Walker. *Cosserat Rod-Based Dynamic Modeling of Tendon-Driven Continuum Robots: A Tutorial*. IEEE Access, vol. 9, pages 68703–68719, 2021.

- [Janabi-Sharifi 21b] F. Janabi-Sharifi, A. Jalali & I. D. Walker. *Cosserat Rod-Based Dynamic Modeling of Tendon-Driven Continuum Robots: A Tutorial*. IEEE Access, vol. 9, pages 68703–68719, 2021.
- [Jelle 15] B. P. Jelle, S. E. Kalnæs & T. Gao. *Low-emissivity materials for building applications: A state-of-the-art review and future research perspectives*. Energy and Buildings, vol. 96, pages 329–356, 2015.
- [Jiang 15] L. Jiang, B. Gao & J. Zhao. *Kinematic and static analysis of a cable-driven parallel robot with a flexible link spine*. In 2015 IEEE International Conference on Robotics and Biomimetics (ROBIO), pages 31–36, 2015.
- [Jin 15] Y. Jin, H. Chanal & F. Paccot. Parallel robots, pages 2091–2127. Springer London, London, 2015.
- [Johnson 11] A. D. Johnson. *Hyperelastic shape Setting Devices and Fabrication Methods*, April 2011.
- [Jones 05] B. Jones & I. Walker. *A New Approach to Jacobian Formulation for a Class of Multi-Section Continuum Robots*. In Proceedings of the 2005 IEEE International Conference on Robotics and Automation, pages 3268–3273, 2005.
- [Jones 18] F. R. Jones & N. T. Huff. *19 - The structure and properties of glass fibers*. In A. R. Bunsell, éditeur, Handbook of Properties of Textile and Technical Fibres (Second Edition), The Textile Institute Book Series, pages 757–803. Woodhead Publishing, second edition edition, 2018.
- [Kalogeropoulos 22] A. S. Kalogeropoulos, S. R. Redwood, C. J. Allen, H. Hurrell, O. Chehab, R. Rajani, B. Prendergast & T. Patterson. *A 20-year journey in transcatheter aortic valve implantation: Evolution to current eminence*. Frontiers in Cardiovascular Medicine, vol. 9, 2022.
- [Kapoor 17] D. Kapoor. *Nitinol for Medical Applications: A Brief Introduction to the Properties and Processing of Nickel Titanium Shape Memory Alloys and their Use in Stents*. Johnson Matthey Technology Review, vol. 61, pages 66–76, 01 2017.
- [Karnaushkin 21] P. Karnaushkin & Y. Konstantinov. *An Experimental Technique for Aligning a Channel Optical Waveguide with an Optical Fiber Based on Reflections from the Far End of the Waveguide*. Instruments and Experimental Techniques, vol. 64, pages 709–714, 09 2021.

- [Kathrin 20] N. Kathrin, S. Tim, L. Sven, X. Dhezu, B.-K. Jessica & O. Tobias. *Modeling, Calibration, and Evaluation of a Planar Parallel Continuum Robot based on Tendon Actuation*. IEEE Robotics and Automation Letter, vol. 5, no. 4, pages 5811 – 5818, 2020.
- [Khaled 21] K. Khaled & U. Berardi. *Current and future coating technologies for architectural glazing applications*. Energy and Buildings, vol. 244, page 111022, 2021.
- [Khmyrov 14] R. Khmyrov, S. Grigoriev, A. Okunkova & A. Gusarov. *On the Possibility of Selective Laser Melting of Quartz Glass*. Physics Procedia, vol. 56, page 345–356, 12 2014.
- [Khmyrov 16] R. Khmyrov, C. Protasov, S. Grigoriev & A. Gusarov. *Crack-free selective laser melting of silica glass: single beads and monolayers on the substrate of the same material*. The International Journal of Advanced Manufacturing Technology, vol. 85, 07 2016.
- [Khoshnam 13] M. Khoshnam & R. V. Patel. *A pseudo-rigid-body 3R model for a steerable ablation catheter*. In 2013 IEEE International Conference on Robotics and Automation, pages 4427–4432, 2013.
- [Kikutani 02] Y. Kikutani, T. Horiuchi, K. Uchiyama, H. Hisamoto, M. Tokeshi & T. Kitamori. *Glass microchip with three-dimensional microchannel network for 2 × 2 parallel synthesis*. Lab on a chip, vol. 2, pages 188–92, 12 2002.
- [Kim 08] J. H. Kim, T. J. Kang & W. Yu. *Mechanical modeling of self-expandable stent fabricated using braiding technology*. Journal of biomechanics, vol. 41 15, pages 3202–12, 2008.
- [Kim 12] M. J. Kim, J. K. Lee, Y. Hwang, D. H. Cha, H. J. Kim & J. H. Kim. *Experimental study of the diamond turning characteristics of tungsten carbide (Co 0.5%) when using a chamfered diamond biten*. Journal of the Korean Ceramic Society, vol. 61, 11 2012.
- [Kim 14] J.-S. Kim, D.-Y. Lee, K. Kim, S. Kang & K.-J. Cho. *Toward a solution to the snapping problem in a concentric-tube continuum robot: Grooved tubes with anisotropy*. In IEEE International Conference on Robotics and Automation (ICRA), pages 5871–5876, 2014.

- [Kim 19a] J. Kim, W.-Y. Choi, S. Kang, C. Kim & K.-J. Cho. *Continuously Variable Stiffness Mechanism Using Nonuniform Patterns on Coaxial Tubes for Continuum Microsurgical Robot*. IEEE Transactions on Robotics, vol. 35, no. 6, pages 1475–1487, 2019.
- [Kim 19b] K.-H. Kim, K.-J. Hwang, H. Lee, S.-M. Jeong, D. Lee & S.-Y. Bae. *Improvement of adhesion properties of glass prepared using SiC-deposited graphite mold via low-temperature chemical vapor deposition*. Journal of the Korean Ceramic Society, vol. 57, 12 2019.
- [Kim 20a] B. C. Kim, J. Y. Cho, M.-H. Lee, J. T. Han & J. S. Woo. *Graphite block derived from natural graphite with bimodal particle size distribution*. SN Applied Sciences, vol. 2, 2020.
- [Kim 20b] J. Kim, W. Lee, S. Kang, K.-J. Cho & C. Kim. *A Needlescopic Wrist Mechanism With Articulated Motion and Kinematic Tractability for Micro Laparoscopic Surgery*. IEEE/ASME Transactions on Mechatronics, vol. 25, no. 1, pages 229–238, 2020.
- [Kim 20c] J. Kim, T. Looi, A. Newman & J. Drake. *Development of Deployable Bending Wrist for Minimally Invasive Laparoscopic Endoscope*. In 2020 IEEE/RSJ International Conference on Intelligent Robots and Systems (IROS), pages 3048–3054, 2020.
- [Kim 20d] S. Kim, J. Kim, Y.-H. Joung, S. Ahn, C. Park, J. Choi & C. Koo. *Monolithic 3D micromixer with an impeller for glass microfluidic systems*. Lab on a Chip, vol. 20, 11 2020.
- [Kim 21] D. Kim, S.-H. Kim, T. Kim, B. B. Kang, M. Lee, W. Park, S. Ku, D. Kim, J. Kwon, H. Lee, J. Bae, Y. Park, K.-J. Cho & S. Jo. *Review of machine learning methods in soft robotics*. PLoS ONE, vol. 16, 2021.
- [Klein 15a] J. Klein. Additive manufacturing of optically transparent glass. Master's thesis, *Massachusetts Institute of Technology (MIT)*, 2015.
- [Klein 15b] J. Klein, M. Stern, G. Franchin, M. Kayser, C. Inamura, S. Dave, J. Weaver, P. Houk, P. Colombo, M. Yang & N. Oxman. *Additive Manufacturing of Optically Transparent Glass*. 3D Printing and Additive Manufacturing, vol. 2, 04 2015.

- [Klein 15c] J. Klein, M. Stern, G. Franchin, M. Kayser, C. Inamura, S. Dave, J. C. Weaver, P. Houk, P. Colombo, M. Yang & N. Oxman. *Additive Manufacturing of Optically Transparent Glass*. 3D Printing and Additive Manufacturing, vol. 2, no. 3, pages 92–105, 2015.
- [Klocke 04] F. Klocke, A. J. W. McClung & C. Ader. *Direct Laser Sintering of Borosilicate Glass*. International Solid Freeform Fabrication Symposium, 2004.
- [Koehler 19] M. Koehler, A. M. Okamura & C. Duriez. *Stiffness Control of Deformable Robots Using Finite Element Modeling*. IEEE Robotics and Automation Letters, vol. 4, no. 2, pages 469–476, 2019.
- [Kometani 04] R. Kometani, T. Morita, K. Watanabe, T. Hoshino, K. Kondo, K. Kanda, Y. Haruyama, T. Kaito, J.-i. Fujita, M. Ishida, Y. Ochiai & S. Matsui. *Nanomanipulator and actuator fabrication on glass capillary by focused-ion-beam-chemical vapor deposition*. Journal of Vacuum Science Technology B: Microelectronics and Nanometer Structures Processing, Measurement, and Phenomena, vol. 22, no. 1, pages 257–263, 01 2004.
- [Kotz-Helmer 17a] F. Kotz-Helmer, K. Arnold, W. Bauer, D. Schild, N. Keller, K. Sachsenheimer, T. Nargang, C. Richter, D. Helmer & B. Rapp. *Three-dimensional printing of transparent fused silica glass*. Nature, vol. 544, pages 337–339, 04 2017.
- [Kotz Helmer 17b] F. Kotz Helmer, K. Arnold, W. Bauer, D. Schild, N. Keller, K. Sachsenheimer, T. Nargang, C. Richter, D. Helmer & B. Rapp. *Three-dimensional printing of transparent fused silica glass*. Nature, vol. 544, pages 337–339, 04 2017.
- [Kotz 17] F. Kotz Helmer, K. Arnold, W. Bauer, D. Schild, N. Keller, K. Sachsenheimer, T. Nargang, C. Richter, D. Helmer & B. Rapp. *Three-dimensional printing of transparent fused silica glass*. Nature, vol. 544, pages 337–339, 04 2017.
- [Kotz 18a] F. Kotz, P. Risch, K. Arnold, S. Sevim, J. Puigmartí-Luis, A. Quick, M. Thiel, A. Hrynevich, P. D. Dalton, D. Helmer & B. E. Rapp. *Fabrication of arbitrary three-dimensional suspended hollow microstructures in transparent fused silica glass*. Nature Communications, vol. 10, 2018.

- [Kotz 18b] F. Kotz, N. Schneider, A. Striegel, A. Wolfschläger, N. Keller, M. Worgull, W. Bauer, D. Schild, M. Milich, C. Greiner, D. Helmer & B. E. Rapp. *Glassomer—Processing Fused Silica Glass Like a Polymer.* Advanced Materials, vol. 30, no. 22, page 1707100, 2018.
- [Kotz 19] F. Kotz Helmer, P. Risch, K. Arnold, S. Sevim, J. Puigmarti-Luis, A. Quick, M. Thiel, A. Hrynevich, P. Dalton, D. Helmer & B. Rapp. *Fabrication of arbitrary three-dimensional suspended hollow microstructures in transparent fused silica glass.* Nature Communications, vol. 10, 03 2019.
- [Kotz 21] F. Kotz, A. S. Quick, P. Risch, T. Martin, T. Hoose, M. Thiel, D. Helmer & B. E. Rapp. *Two-Photon Polymerization of Nanocomposites for the Fabrication of Transparent Fused Silica Glass Microstructures.* Advanced Materials, vol. 33, no. 9, page 2006341, 2021.
- [KotzHelmer 17] F. KotzHelmer, K. Arnold, W. Bauer, D. Schild, N. Keller, K. Sachsenheimer, T. Nargang, C. Richter, D. Helmer & B. Rapp. *Three-dimensional printing of transparent fused silica glass.* Nature, vol. 544, pages 337–339, 04 2017.
- [KREISS 74] H.-O. KREISS & G. SCHERER. *Finite Element and Finite Difference Methods for Hyperbolic Partial Differential Equations.* In C. de Boor, éditeur, Mathematical Aspects of Finite Elements in Partial Differential Equations, pages 195–212. Academic Press, 1974.
- [Kronig 18] L. Kronig, P. Hörler, J.-P. Kneib & M. Bouri. *Design and performances of an optical metrology system to test position and tilt accuracy of fiber positioners .* In R. Navarro & R. Geyl, éditeurs, Advances in Optical and Mechanical Technologies for Telescopes and Instrumentation III, volume 10706, page 107066B. International Society for Optics and Photonics, SPIE, 2018.
- [Kuang 11] J. Kuang, X. H. Wang, A. M. Liu & H. Zhu. *Study on the Complex Strengthening Processes of 5Cr2NiMoVS<sub>i</sub> Steel Large Hot Forging Dies.* Advanced Materials Research, vol. 189-193, pages 1056 – 1061, 2011.
- [Kudryavtsev 18] A. V. Kudryavtsev, M. T. Chikhaoui, A. Liadov, P. Rougeot, F. Spindler, K. Rabenorosoa, J. Burgner-Kahrs, B. Tamadazte & N. Andreff. *Eye-in-Hand Visual Servoing of Concentric Tube Robots.* IEEE Robotics and Automation Letters, vol. 3, no. 3, pages 2315–2321, 2018.

- [Kuntz 20] A. Kuntz, A. Sethi, R. J. Webster & R. Alterovitz. *Learning the Complete Shape of Concentric Tube Robots*. IEEE Transactions on Medical Robotics and Bionics, vol. 2, no. 2, pages 140–147, 2020.
- [Kuo 17] C.-H. Kuo, Y.-C. Chen & T.-Y. Pan. *Continuum Kinematics of a Planar Dual-Backbone Robot Based on Pseudo-Rigid-Body Model: Formulation, Accuracy, and Efficiency*. In International Design Engineering Technical Conferences and Computers and Information in Engineering Conference, volume Volume 5A 41st Mechanisms and Robotics Conference, 08 2017.
- [Kutzer 11] M. D. Kutzer, S. M. Segreti, C. Y. Brown, M. Armand, R. H. Taylor & S. C. Mears. *Design of a new cable-driven manipulator with a large open lumen: Preliminary applications in the minimally-invasive removal of osteolysis*. In 2011 IEEE International Conference on Robotics and Automation, pages 2913–2920, 2011.
- [Lakhal 16] O. Lakhal, A. Melingui & R. Merzouki. *Hybrid Approach for Modeling and Solving of Kinematics of a Compact Bionic Handling Assistant Manipulator*. IEEE/ASME Transactions on Mechatronics, vol. 21, no. 3, pages 1326–1335, 2016.
- [Lang 11] H. Lang, J. Linn & M. Arnold. *Multi-body dynamics simulation of geometrically exact Cosserat rods*. Multibody System Dynamics, vol. 25, pages 285–312, 03 2011.
- [Lathrop 10] R. A. Lathrop, D. C. Rucker & R. J. Webster. *Guidance of a steerable cannula robot in soft tissue using preoperative imaging and conoscopic surface contour sensing*. In IEEE International Conference on Robotics and Automation, pages 5601–5606, 2010.
- [Lee 15] D. Y. Lee, J. Kim, J. S. Kim, C. Baek, G. Noh, D. N. Kim, K. Kim, S. Kang & K. J. Cho. *Anisotropic Patterning to Reduce Instability of Concentric-Tube Robots*. IEEE Transactions on Robotics, vol. 31, no. 6, pages 1311–1323, 2015.
- [Lenssen 12a] B. Lenssen & Y. Bellouard. *Optically transparent glass micro-actuator fabricated by femtosecond laser exposure and chemical etching*. Applied Physics Letters, vol. 101, no. 10, 09 2012. 103503.

- [Lenssen 12b] B. Lenssen & Y. Bellouard. *Optically transparent glass micro-actuator fabricated by femtosecond laser exposure and chemical etching*. Applied Physics Letters, vol. 101, no. 10, pages 1–5, 2012.
- [Leveziel 22] M. Leveziel, W. Haouas, G. J. Laurent, M. Gauthier & R. Dahmouche. *MiGriBot: A miniature parallel robot with integrated gripping for high-throughput micromanipulation*. Science Robotics, vol. 7, no. 69, page eabn4292, 2022.
- [Li 17] Z. Li, L. Wu, H. Ren & H. Yu. *Kinematic comparison of surgical tendon-driven manipulators and concentric tube manipulators*. Mechanism and Machine Theory, vol. 107, pages 148–165, 2017.
- [Li 20] C. Li, X. Gu, X. Xiao & C. Lim. *Cadaveric feasibility study of a teleoperated parallel continuum robot with variable stiffness for transoral surgery*. Medical Biological Engineering Computing, vol. 58, 07 2020.
- [Liang 09] C. Liang, L. Ding, A. Wang, Z. Ma, J. Qiu & T. Zhang. *Microwave-Assisted Preparation and Hydrazine Decomposition Properties of Nanostructured Tungsten Carbides on Carbon Nanotubes*. Industrial Engineering Chemistry Research - IND ENG CHEM RES, vol. 48, 03 2009.
- [Liang 21] N. Liang, R. M. Grassmann, S. Lilge & J. Burgner-Kahrs. *Learning-based Inverse Kinematics from Shape as Input for Concentric Tube Continuum Robots*. In 2021 IEEE International Conference on Robotics and Automation (ICRA), pages 1387–1393, 2021.
- [Lilge 20] S. Lilge, K. Nuelle, G. Boettcher, S. Spindeldreier & J. Burgner-Kahrs. *Tendon Actuated Continuous Structures in Planar Parallel Robots: A Kinematic Analysis*. Journal of Mechanisms and Robotics, vol. 13, no. 1, 12 2020. 011025.
- [Lilge 21] S. Lilge, K. Nuelle, G. Boettcher, S. Spindeldreier & J. Burgner-Kahrs. *Tendon Actuated Continuous Structures in Planar Parallel Robots: A Kinematic Analysis*. Journal of Mechanisms and Robotics, vol. 13, no. 1, page 011025, February 2021.
- [Lilge 23] S. Lilge & J. Burgner-Kahrs. *Kinetostatic Modeling of Tendon-Driven Parallel Continuum Robots*. IEEE Transactions on Robotics, vol. 39, no. 2, pages 1563–1579, 2023.

- [Lima 15] R. Lima, P. Leao, M. Piazzetta, A. Monteiro, L. Shiroma, A. Gobbi & E. Carrilho. *Sacrificial adhesive bonding: A powerful method for fabrication of glass microchips*. Scientific Reports, vol. 5:13276, 08 2015.
- [Lin 97] J. Lin & C. W. Brown. *Sol-gel glass as a matrix for chemical and biochemical sensing*. TrAC Trends in Analytical Chemistry, vol. 16, no. 4, pages 200–211, 1997.
- [Lin 15] F. Lin, C. Bergeles & G. Yang. *Biometry-based concentric tubes robot for vitreoretinal surgery*. In 37th Annual International Conference of the IEEE Engineering in Medicine and Biology Society (EMBC), pages 5280–5284, 2015.
- [Lin ] J. Lin, C. Girerd, J. Yan, J. Hwang & T. K. Morimoto. *A Generalized Framework for Concentric Tube Robot Design Using Gradient-Based Optimization*. IEEE Transactions on Robotics (T-RO), 2022 (Accepted, to appear).
- [Liu 18a] C. Liu, B. Qian, X. Liu, L. Tong & J. Qiu. *Additive manufacturing of silica glass using laser stereolithography with a top-down approach and fast debinding*. RSC Adv., vol. 8, pages 16344–16348, 2018.
- [Liu 18b] C. Liu, B. Qian, R. Ni, X. Liu & J. Qiu. *3D printing of multicolor luminescent glass*. RSC Adv., vol. 8, pages 31564–31567, 2018.
- [Liu 21] H. Liu, W. Lin & M. Hong. *Hybrid laser precision engineering of transparent hard materials: challenges, solutions and applications*. Light: Science Applications, vol. 10, 12 2021.
- [Liu 22] X. Liu, Y. Yang & J. Qiu. *Emerging techniques for customized fabrication of glass*. Journal of Non-Crystalline Solids: X, vol. 15, page 100114, 2022.
- [Lock 10a] J. Lock, G. Laing, M. Mahvash & P. Dupont. *Quasistatic Modeling of Concentric Tube Robots with External Loads*. in IEEE/RSJ International Conference on Intelligent Robots and Systems., vol. 2010, pages 2325–2332, 12 2010.
- [Lock 10b] J. Lock, G. Laing, M. Mahvash & P. E. Dupont. *Quasistatic modeling of concentric tube robots with external loads*. In 2010 IEEE/RSJ International Conference on Intelligent Robots and Systems, pages 2325–2332, 2010.
- [Lock 11a] J. Lock & P. E. Dupont. *Friction modeling in concentric tube robots*. IEEE International Conference on Robotics and Automation, pages 1139–1146, 2011.

- [Lock 11b] J. Lock & P. E. Dupont. *Friction modeling in concentric tube robots*. In 2011 IEEE International Conference on Robotics and Automation, pages 1139–1146, 2011.
- [Lu 17] Y. Lu, C. Zhang, S. Song & M. Q.-H. Meng. *Precise motion control of concentric-tube robot based on visual servoing*. In IEEE International Conference on Information and Automation (ICIA), pages 299–304, 2017.
- [Luethi 98] B. Luethi, R. Reber, J. Mayer, E. Wintermantel, J. Janczak-Rusch & L. Rohr. *An energy-based analytical push-out model applied to characterise the interfacial properties of knitted glass fibre reinforced PET*. Composites Part A: Applied Science and Manufacturing, vol. 29, no. 12, pages 1553–1562, 1998.
- [Luo 14] J. Luo, H. Pan & E. C. Kinzel. *Additive Manufacturing of Glass*. Journal of Manufacturing Science and Engineering, vol. 136, no. 6, 10 2014. 061024.
- [Luo 16a] J. Luo, L. Gilbert, D. Peters, D. Bristow, R. Landers, J. Goldstein, A. Urbas & E. Kinzel. *Bubble formation in additive manufacturing of glass*. In SPIE Defense and Security, page 982214, 05 2016.
- [Luo 16b] J. Luo, L. J. Gilbert, D. A. Bristow, R. G. Landers, J. T. Goldstein, A. M. Urbas & E. C. Kinzel. *Additive manufacturing of glass for optical applications*. In B. Gu, H. Helvajian & A. Piqué, éditeurs, Laser 3D Manufacturing III, volume 9738, page 97380Y. International Society for Optics and Photonics, SPIE, 2016.
- [Luo 17] J. Luo, L. J. Gilbert, C. Qu, R. G. Landers, D. A. Bristow & E. C. Kinzel. *Additive Manufacturing of Transparent Soda-Lime Glass Using a Filament-Fed Process*. Journal of Manufacturing Science and Engineering, vol. 139, no. 01 2017. 061006.
- [Luo 18a] J. Luo, J. M. Hostetler, L. Gilbert, J. T. Goldstein, A. M. Urbas, D. A. Bristow, R. G. Landers & E. C. Kinzel. *Additive manufacturing of transparent fused quartz*. Optical Engineering, vol. 57, no. 4, page 041408, 2018.
- [Luo 18b] J. Luo, J. M. Hostetler, L. Gilbert, J. T. Goldstein, A. M. Urbas, D. A. Bristow, R. G. Landers & E. C. Kinzel. *Additive manufacturing of transparent fused quartz*. Optical Engineering, vol. 57, no. 4, page 041408, 2018.

- [Luo 21] K. A. X. J. Luo, J. Kim, T. Looi & J. Drake. *Design Optimization for the Stability of Concentric Tube Robots*. IEEE Robotics and Automation Letters, vol. 6, no. 4, pages 8309–8316, 2021.
- [Lv 13] D. Lv, H. Wang, Y. Tang, Y. Huang & Z. Li. *Influences of vibration on surface formation in rotary ultrasonic machining of glass BK7*. Precision Engineering, vol. 37, no. 4, pages 839–848, 2013.
- [Mader 21a] M. Mader, L. Hambitzer, P. Schlautmann, S. Jenne, C. Greiner, F. Hirth, D. Helmer, F. Kotz-Helmer & B. E. Rapp. *Melt-Extrusion-Based Additive Manufacturing of Transparent Fused Silica Glass*. Advanced Science, vol. 8, no. 23, page 2103180, 2021.
- [Mader 21b] M. Mader, O. Schlatter, B. Heck, A. Warmbold, A. Dorn, H. Zappe, P. Risch, D. Helmer, F. Kotz & B. E. Rapp. *High-throughput injection molding of transparent fused silica glass*. Science, vol. 372, no. 6538, pages 182–186, 2021.
- [Magee 06] J. Magee, K. G. Watkins, W. M. Steen, J. Magee, K. G. Watkins & W. M. Steen. *Advances in laser forming Advances in laser forming*. Laser Applications, vol. 235, no. 1998, 2006.
- [Mahoney 16a] A. Mahoney, H. Gilbert & R. Webster. A Review of Concentric Tube Robots: Modeling, Control, Design, Planning, and Sensing, pages 181–202. Encyclopedia of Medical Robotics, Minimally Invasive Surgical Robotics, 2016.
- [Mahoney 16b] A. W. Mahoney, P. L. Anderson, P. J. Swaney, F. Maldonado & R. J. Webster. *Reconfigurable parallel continuum robots for incisionless surgery*. In 2016 IEEE/RSJ International Conference on Intelligent Robots and Systems (IROS), pages 4330–4336, 2016.
- [Makarets 14] D. Makarets, G. Noh, K. Kim & D. Lee. *Preliminary study of utilizing plastic tubes as a component of continuum robots*. In 2014 14th International Conference on Control, Automation and Systems (ICCAS 2014), pages 217–220, 2014.
- [Makwana 21] M. Makwana & H. Patolia. *Forward Kinematics of Delta Manipulator by Novel Hybrid Neural Network*. International Journal of Mathematical, Engineering and Management Sciences, vol. 6, pages 1694–1708, 12 2021.

- [Manakov 21] R. A. Manakov, D. Y. Kolpashchikov, V. V. Danilov, N. V. Laptev, I. P. Skirnevskiy & O. M. Gerget. *Visual shape and position sensing algorithm for a continuum robot*. IOP Conference Series: Materials Science and Engineering, vol. 1019, no. 1, page 012066, jan 2021.
- [Mantzaris 01] N. V. Mantzaris, P. Daoutidis & F. Srienc. *Numerical solution of multi-variable cell population balance models: I. Finite difference methods*. Computers Chemical Engineering, vol. 25, no. 11, pages 1411–1440, 2001.
- [Marcus 14] H. J. Marcus, A. Hughes-Hallett, T. P. Cundy, G.-Z. Yang, A. Darzi & D. Nandi. *Da vinci robot-assisted Keyhole Neurosurgery: A cadaver study on feasibility and safety*. Neurosurgical Review, vol. 38, no. 2, page 367–371, 2014.
- [Matthewson 93] M. J. Matthewson. *Optical fiber mechanical testing techniques*. In D. K. Paul, éditeur, Fiber Optics Reliability and Testing: A Critical Review, volume 10272, pages 34 – 61. International Society for Optics and Photonics, SPIE, 1993.
- [Matthey 0] J. Matthey. *Nitinol technical properties*, (2020).
- [Mattos 11] L. S. Mattos, G. Dagnino, G. Becattini, M. Dellepiane & D. G. Caldwell. *A virtual scalpel system for computer-assisted laser microsurgery*. In 2011 IEEE/RSJ International Conference on Intelligent Robots and Systems, pages 1359–1365, 2011.
- [Mattos 21] L. S. Mattos, A. Acemoglu, A. Geraldes, A. Laborai, A. Schoob, B. Tamadazte, B. Davies, B. Wacogne, C. Pieralli, C. Barbalata, D. G. Caldwell, D. Kundrat, D. Pardo, E. Grant, F. Mora, G. Barresi, G. Peretti, J. Ortiz, K. Rabenorosoa, L. Tavernier, L. Pazart, L. Fichera, L. Guastini, L. A. Kahrs, M. Rakotondrabe, N. Andreff, N. Deshpande, O. Gaiffe, R. Renevier, S. Moccia, S. Lescano, T. Ortmaier & V. Penza.  *$\mu$ RALP and Beyond: Micro-Technologies and Systems for Robot-Assisted Endoscopic Laser Microsurgery*. Frontiers in Robotics and AI, vol. 8, 2021.
- [Mauze 20] B. Mauze, R. Dahmouche, G. J. Laurent, A. N. Andre, P. Rougeot, P. Sandoz & C. Clevy. *Nanometer Precision With a Planar Parallel Continuum Robot*. IEEE Robotics and Automation Letters, vol. 5, no. 3, pages 3806–3813, July 2020.

- [Mauzé 20] B. Mauzé, R. Dahmouche, G. J. Laurent, A. N. André, P. Rougeot, P. Sandoz & C. Clévy. *Nanometer Precision With a Planar Parallel Continuum Robot*. IEEE Robotics and Automation Letters, vol. 5, no. 3, pages 3806–3813, 2020.
- [Mauzé 21a] B. Mauzé, G. J. Laurent, R. Dahmouche & C. Clévy. *Micrometer Positioning Accuracy With a Planar Parallel Continuum Robot*. Frontiers in Robotics and AI, vol. 8, 2021.
- [Mauzé 21b] B. Mauzé, G. J. Laurent, R. Dahmouche & C. Clévy. *Micrometer Positioning Accuracy With a Planar Parallel Continuum Robot*. Frontiers in Robotics and AI, vol. 8, 2021.
- [Mačković 17] M. Mačković, T. Przybilla, C. Dieker, P. Herre, S. Romeis, H. Stara, N. Schrenker, W. Peukert & E. Spiecker. *A Novel Approach for Preparation and In Situ Tensile Testing of Silica Glass Membranes in the Transmission Electron Microscope*. Frontiers in Materials, vol. 4, 2017.
- [McCann 15] S. R. McCann, Y. Sato, V. Sundaram, R. R. Tummala & S. K. Sitaraman. *Study of cracking of thin glass interposers intended for microelectronic packaging substrates*. In 2015 IEEE 65th Electronic Components and Technology Conference (ECTC), pages 1938–1944, 2015.
- [McClintock 18] H. McClintock, F. Z. Temel, N. Doshi, J.-s. Koh & R. J. Wood. *The milliDelta: A high-bandwidth, high-precision, millimeter-scale Delta robot*. Science Robotics, vol. 3, no. 14, 2018.
- [Meng 15] X. Meng, Q. Yang, F. Chen, C. Shan, K. Liu & X. Hou. *Fabrication of three-dimensional micro-Rogowski coil based on femtosecond laser micromachining*. Applied Physics A: Materials Science and Processing, vol. 120, no. 2, pages 669–674, 2015.
- [Minami 93] K. Minami, S. Kawamura & M. Esashi. *Fabrication of distributed electrostatic micro actuator (DEMA)*. Journal of Microelectromechanical Systems, vol. 2, no. 3, pages 121–127, 1993.
- [Minitube 22] Minitube. *Leading custom manufacturing of high precision miniature metallic tubing, tubular parts, and assemblies.*, 2022.
- [Minko 13] N. Minko & V. Nartsev. *Factors affecting the strength of the glass (review)*. vol. 18, pages 1616–1624, 01 2013.

- [Minoshima 01] K. Minoshima, A. M. Kowalevicz, I. Hartl, E. P. Ippen & J. G. Fujimoto. *Photonic device fabrication in glass by use of nonlinear materials processing with a femtosecond laser oscillator*. Opt. Lett., vol. 26, no. 19, pages 1516–1518, Oct 2001.
- [Mirrors 21] T. W. Mirrors. *Different Properties of Glass*, 2021.
- [Mishra 18] A. K. Mishra, A. Mondini, E. Del Dottore, A. Sadeghi, F. Tramacere & B. Mazzolai. *Modular Continuum Manipulator: Analysis and Characterization of Its Basic Module*. Biomimetics, vol. 3, no. 1, 2018.
- [Mishuk 19] E. Mishuk, J. Shklovsky, Y. Berg, N. Vengerovsky, T. Paul, Z. Kotler, Y. Tsur, Y. Shacham-Diamond, S. Krylov & I. Lubomirsky. *Femtosecond laser processing of ceria-based micro actuators*. Microelectronic Engineering, vol. 217, page 111126, 2019.
- [Mitros 20] Z. Mitros, S. Sadati, C. Seneci, E. Bloch, K. Leibrandt, M. Khadem, L. d. Cruz & C. Bergeles. *Optic Nerve Sheath Fenestration With a Multi-Arm Continuum Robot*. IEEE Robotics and Automation Letters, vol. 5, no. 3, pages 4874–4881, 2020.
- [Mitros 21] Z. Mitros, S. Sadati, R. Henry, L. Cruz & C. Bergeles. *From Theoretical Work to Clinical Translation: Progress in Concentric Tube Robots*. Annual Review of Control Robotics and Autonomous Systems, vol. 5, 01 2021.
- [Mitros 22] Z. Mitros. *Design and Modeling of Multi-Arm Continuum Robots*. Doctoral dissertation, Université catholique de Louvain, January 2022.
- [Mittholiya 16] K. Mittholiya, P. Anshad, A. Mallik, S. Bhardwaj, A. Hegde, A. Bhatnagar, R. Bernard, J. Dharmadhikari, D. Mathur & A. Dharmadhikari. *Inscription of waveguides and power splitters in borosilicate glass using ultrashort laser pulses*. Journal of Optics, 09 2016.
- [Moghadam 15] A. A. A. Moghadam, A. Kouzani, K. Torabi, A. Kaynak & M. Shahinpoor. *Development of a novel soft parallel robot equipped with polymeric artificial muscles*. Smart Materials and Structures, vol. 24, no. 3, page 035017, feb 2015.
- [Mohelnikova 09] J. Mohelnikova & H. Altan. *Evaluation of Optical and Thermal Properties of Window Glazing*. WSEAS Transactions on Environment and Development, vol. 5, 01 2009.

- [Montanero 10] J. Montanero, A. Gañán-Calvo, A. Acero & E. Vega. *Micrometer glass nozzles for flow focusing*. Journal of Micromechanics and Microengineering, vol. 20, page 075035, 06 2010.
- [Moore 20] D. Moore, L. Barbera, K. Masania & A. Studart. *Three-dimensional printing of multicomponent glasses using phase-separating resins*. Nature Materials, vol. 19, pages 1–6, 02 2020.
- [Morimoto 16a] T. K. Morimoto, J. D. Greer, M. H. Hsieh & A. M. Okamura. *Surgeon design interface for patient-specific concentric tube robots*. In IEEE/RAS-EMBS International Conference on Biomedical Robotics and Biomechatronics, pages 41–48, 2016.
- [Morimoto 16b] T. K. Morimoto & A. M. Okamura. *Design of 3-D printed concentric tube robots*. IEEE Transactions on Robotics, vol. 32, no. 6, pages 1419–1430, 2016.
- [Morimoto 16c] T. K. Morimoto & A. M. Okamura. *Design of 3-D printed concentric tube robots*. IEEE Transactions on Robotics, vol. 32, no. 6, pages 1419–1430, 2016.
- [Morimoto 17a] T. Morimoto, J. Cerrolaza, M. Hsieh, K. Cleary, A. Okamura & M. G. Linguraru. *Design of patient-specific concentric tube robots using path planning from 3-D ultrasound*. In Annual International Conference of the IEEE Engineering in Medicine and Biology Society, volume 2017, pages 165–168, 07 2017.
- [Morimoto 17b] T. K. Morimoto, E. W. Hawkes & A. M. Okamura. *Design of a Compact Actuation and Control System for Flexible Medical Robots*. in IEEE Robotics and Automation Letters, vol. 2, no. 3, pages 1579–1585, 2017.
- [Morimoto 18] T. K. Morimoto, J. D. Greer, E. W. Hawkes, M. H. Hsieh & A. M. Okamura. *Toward the design of personalized continuum surgical robots*. Annals of Biomedical Engineering, vol. 46, no. 10, pages 1522–1533, 2018.
- [Nazir 19] S. I. Nazir & Y. Bellouard. *A Monolithic gimbal micro-mirror fabricated and remotely tuned with a femtosecond laser*. Micromachines, vol. 10, no. 9, pages 1–17, 2019.
- [Neppalli 07] S. Neppalli & B. A. Jones. *Design, construction, and analysis of a continuum robot*. In 2007 IEEE/RSJ International Conference on Intelligent Robots and Systems, pages 1503–1507, 2007.

- [Neppalli 09] S. Neppalli, M. A. Csencsits, B. A. Jones & I. D. Walker. *Closed-Form Inverse Kinematics for Continuum Manipulators*. Advanced Robotics, vol. 23, no. 15, pages 2077–2091, 2009.
- [Nguyen 17] D. T. Nguyen, C. Meyers, T. D. Yee, N. A. Dudukovic, J. F. Destino, C. Zhu, E. B. Duoss, T. F. Baumann, T. Suratwala, J. E. Smay & R. Dylla-Spears. *3D-Printed Transparent Glass*. Advanced Materials, vol. 29, no. 26, page 1701181, 2017.
- [Nguyen 22] D. V. A. Nguyen, C. Girerd, Q. Boyer, P. Rougeot, O. Lehmann, L. Tavernier, J. Szewczyk & K. Rabenorosoa. *A Hybrid Concentric Tube Robot for Cholesteatoma Laser Surgery*. IEEE Robotics and Automation Letters, vol. 7, no. 1, pages 462–469, 2022.
- [Nimesis 21] Nimesis. *NIMESIS TECHNOLOGY*, 2021.
- [Niza 10] M. Niza, M. Komori, T. Nomura, I. Yamaji, N. Nishiyama, M. Ishida & Y. Shimizu. *Test rig for micro gear and experimental analysis on the meshing condition and failure characteristics of steel micro involute gear and metallic glass one*. Mechanism and Machine Theory, vol. 45, no. 12, pages 1797–1812, 2010.
- [Noh 16] G. Noh, S. Y. Yoon, S. Yoon, K. Kim, W. Lee, S. Kang & D. Lee. *Expeditious design optimization of a concentric tube robot with a heat-shrink plastic tube*. In 2016 IEEE/RSJ International Conference on Intelligent Robots and Systems (IROS), pages 3671–3676, 2016.
- [Nuelle 20] K. Nuelle, T. Sterneck, S. Lilge, D. Xiong, J. Burgner-Kahrs & T. Ortmaier. *Modeling, Calibration, and Evaluation of a Tendon-Actuated Planar Parallel Continuum Robot*. IEEE Robotics and Automation Letters, vol. 5, no. 4, pages 5811–5818, October 2020.
- [Nwafor 22] C. Nwafor, G. Laurent, P. Rougeot & K. Rabenorosoa. *The Caturo: A Submillimeter Diameter Glass Concentric Tube Robot with High Curvature*. Advanced Intelligent Systems, vol. 5, page 2200308, 12 2022.
- [Nwafor 23a] C. Nwafor, G. J. Laurent & K. Rabenorosoa. *Miniature Parallel Continuum Robot Made of Glass: Analysis, Design, and Proof-of-Concept*. IEEE/ASME Transactions on Mechatronics, pages 1–9, 2023.

- [Nwafor 23b] C. J. Nwafor, C. Girerd, G. J. Laurent, T. K. Morimoto & K. Rabenorosoa. *Design and Fabrication of Concentric Tube Robots: A Survey*. IEEE Transactions on Robotics, pages 1–19, 2023.
- [Okada 08] A. Okada, Y. Uno, J. McGeough, K. Fujiwara, K. Doi, K. Uemura & S. Sano. *Surface finishing of stainless steels for orthopedic surgical tools by large-area electron beam irradiation*. CIRP Annals, vol. 57, no. 1, pages 223–226, 2008.
- [Omnexus 21] Omnexus. *Linear Coefficient of Thermal Expansion Values of Several Plastics*, 2021.
- [Onan 20] B. Onan. *Minimal access in cardiac surgery*. The Turkish Journal of Thoracic and Cardiovascular Surgery, vol. 28, pages 708–724, 10 2020.
- [Orehkov 15] A. L. Orekhov, C. E. Bryson, J. Till, S. Chung & D. C. Rucker. *A surgical parallel continuum manipulator with a cable-driven grasper*. In 2015 37th Annual International Conference of the IEEE Engineering in Medicine and Biology Society (EMBC), pages 5264–5267, 2015.
- [Orehkov 16a] A. L. Orekhov, C. B. Black, J. Till, S. Chung & D. C. Rucker. *Analysis and Validation of a Teleoperated Surgical Parallel Continuum Manipulator*. IEEE Robotics and Automation Letters, vol. 1, no. 2, pages 828–835, July 2016.
- [Orehkov 16b] A. L. Orekhov, C. B. Black, J. Till, S. Chung & D. C. Rucker. *Analysis and Validation of a Teleoperated Surgical Parallel Continuum Manipulator*. IEEE Robotics and Automation Letters, vol. 1, no. 2, pages 828–835, 2016.
- [Orehkov 17] A. L. Orekhov, V. A. Alo & D. C. Rucker. *Modeling parallel continuum robots with general intermediate constraints*. In 2017 IEEE International Conference on Robotics and Automation (ICRA), pages 6142–6149, Singapore, Singapore, May 2017. IEEE.
- [Osellame 03] R. Osellame, S. Taccheo, M. Marangoni, R. Ramponi, P. Laporta, D. Polli, S. D. Silvestri & G. Cerullo. *Femtosecond writing of active optical waveguides with astigmatically shaped beams*. J. Opt. Soc. Am. B, vol. 20, no. 7, pages 1559–1567, Jul 2003.
- [Pai 02] D. K. Pai. *STRANDS: Interactive Simulation of Thin Solids using Cosserat Models*. Computer Graphics Forum, vol. 21, no. 3, pages 347–352, 2002.

- [Peiyi 21] W. Peiyi, F. Zhao, X. Wang & M. Song. *Follow-the-Leader Deployment of the Interlaced Continuum Robot Based on the Unpowered Lock Mechanism.* In International Conference on Intelligent Robotics and Applications, pages 448–459, 10 2021.
- [Pelton 99] A. Pelton & T. Duerig. *Shape memory alloy treatment*, November 1999.
- [Pelton 04] A. Pelton, D. T & S. D. *A guide to shape memory and superelasticity in Nitinol medical devices.* Minimally invasive therapy & allied technologies : MITAT : official journal of the Society for Minimally Invasive Therapy, vol. 13, pages 218–21, 09 2004.
- [Perrone 75] N. Perrone & R. Kao. *A general finite difference method for arbitrary meshes.* Computers Structures, vol. 5, no. 1, pages 45–57, 1975.
- [Peyron 18] Q. Peyron, Q. Boehler, K. Rabenorosoa, B. J. Nelson, P. Renaud & N. Andreff. *Kinematic Analysis of Magnetic Continuum Robots Using Continuation Method and Bifurcation Analysis.* IEEE Robotics and Automation Letters, vol. 3, no. 4, pages 3646–3653, 2018.
- [Peyron 19] Q. Peyron, K. Rabenorosoa, N. Andreff & P. Renaud. *A numerical framework for the stability and cardinality analysis of concentric tube robots: Introduction and application to the follow-the-leader deployment.* Mechanism and Machine Theory, vol. 132, pages 176–192, 2019.
- [Peyron 22] Q. Peyron, Q. Boehler, P. Rougeot, P. Roux, B. J. Nelson, N. Andreff, K. Rabenorosoa & P. Renaud. *Magnetic concentric tube robots: Introduction and analysis.* The International Journal of Robotics Research, vol. 41, pages 418 – 440, 2022.
- [PHILLIPS 65] C. J. PHILLIPS. *THE STRENGTH AND WEAKNESS OF BRITTLE MATERIALS.* American Scientist, vol. 53, no. 1, pages 20–51, 1965.
- [Physics 03] A. Physics & F.-s.-u. Jena. *Femtosecond waveguide writing : a new avenue to three-dimensional integrated.* Applied Physics, vol. 111, pages 109–111, 2003.
- [PI 23] PI. *Electron Microscopy: Nonmagnetic Drives and Stages for Vacuum*, 2023.

- [Picho 22] K. Picho, B. Persons, J. F. d'Almeida, N. E. Pacheco, C. Reynolds & L. Fichera. *Multi Jet Fusion of Nylon-12: A Viable Method to 3D-print Concentric Tube Robots?* Hamlyn Symposium 2022, 2022.
- [Pitt 16] E. B. Pitt, P. J. Swaney, H. B. Gilbert, Y. Chen, R. J. Webster & E. J. Barth. *Enabling Helical Needle Trajectories with Minimal Actuation : A Screw-Based Approach to Concentric Tube Needle Deployment.* Vanderbilt, 2016.
- [Pourafzal 21] M. Pourafzal, A. Talebi & K. Rabenorosoa. *Piecewise constant strain kinematic model of externally loaded concentric tube robots.* Mechatronics, vol. 74, page 102502, 04 2021.
- [Power 18] M. Power, A. Thompson, S. Anastasova & G.-Z. Yang. *A Monolithic Force-Sensitive 3D Microgripper Fabricated on the Tip of an Optical Fiber Using 2-Photon Polymerization.* Small, vol. 14, page 1703964, 02 2018.
- [Prakash 17] S. Prakash & S. Kumar. Microchannel fabrication via direct laser writing, pages 163–188. Elsevier Ltd, 2017.
- [Prasai 16] A. B. Prasai, A. Jaiprakash, A. K. Pandey, R. Crawford, J. Roberts & L. Wu. *Design and fabrication of a disposable micro end effector for concentric tube robots.* In 14th International Conference on Control, Automation, Robotics and Vision (ICARCV), pages 1–6, 2016.
- [Proctor 67] B. A. Proctor, I. Whitney & J. W. Johnson. *The strength of fused silica.* Proceedings of the Royal Society of London. Series A. Mathematical and Physical Sciences, vol. 297, pages 534 – 557, 1967.
- [Qi 21] B. Qi, Z. Yu, Z. K. Varnamkhasti, Y. Zhou & J. Sheng. *Toward a Telescopic Steerable Robotic Needle for Minimally Invasive Tissue Biopsy.* IEEE Robotics and Automation Letters, vol. 6, no. 2, pages 1989–1996, 2021.
- [Queste 10] S. Queste, R. Salut, S. Clatot, J.-Y. Rauch & C. Malek. *Manufacture of Microfluidic Glass Chips by Deep Plasma Etching, Femtosecond Laser Ablation, and Anodic Bonding.* Microsystem Technologies, vol. 16, pages 1485–1493, 01 2010.
- [Rafael 16] S. Rafael Ribeiro, C. Louter & T. Klein. *Flexible transparency: A study on thin glass adaptive façade panels.* In Challenging Glass 6 - Conference on Architectural and Structural Applications of Glass, TU Delft, Netherlands, pages 135–148, 2016.

- [Rao 22] P. Rao, Q. Peyron & J. Burgner-Kahrs. *Shape Representation and Modeling of Tendon-Driven Continuum Robots Using Euler Arc Splines*. IEEE Robotics and Automation Letters, vol. 7, no. 3, pages 8114–8121, 2022.
- [Remirez 16] A. A. Remirez & R. J. W. III. *Endoscopes and robots for tight surgical spaces: use of precurved elastic elements to enhance curvature*. In R. J. W. III & Z. R. Yaniv, éditeurs, Medical Imaging 2016: Image-Guided Procedures, Robotic Interventions, and Modeling, volume 9786, page 97860R. International Society for Optics and Photonics, SPIE, 2016.
- [Renda 14] F. Renda, M. Giorelli, M. Calisti, M. Cianchetti & C. Laschi. *Dynamic Model of a Multibending Soft Robot Arm Driven by Cables*. IEEE Transactions on Robotics, vol. 30, no. 5, pages 1109–1122, 2014.
- [Riojas 18] K. E. Riojas, R. J. Hendrick & R. J. Webster. *Can Elastic Instability Be Beneficial in Concentric Tube Robots?* IEEE Robotics and Automation Letters, vol. 3, no. 3, pages 1624–1630, 2018.
- [Rivera 14] J. A. Rivera & C. J. Kim. *Spatial parallel soft robotic architectures*. In 2014 IEEE/RSJ International Conference on Intelligent Robots and Systems, pages 548–553, 2014.
- [Robert 10] I. Robert J. Webster & B. A. Jones. *Design and Kinematic Modeling of Constant Curvature Continuum Robots: A Review*. The International Journal of Robotics Research, vol. 29, no. 13, pages 1661–1683, 2010.
- [Rogers 95] T. Rogers & J. Kowal. *Selection of glass, anodic bonding conditions and material compatibility for silicon-glass capacitive sensors*. Sensors and Actuators A: Physical, vol. 46, no. 1, pages 113–120, 1995.
- [Römer 15] G.-w. Römer & B. Huis. *In-plane laser forming for high precision alignment Ger Folkersma*. Optical Engineering, 2015.
- [Rone 14] W. S. Rone & P. Ben-Tzvi. *Continuum Robot Dynamics Utilizing the Principle of Virtual Power*. IEEE Transactions on Robotics, vol. 30, no. 1, pages 275–287, 2014.
- [Rosa 15] H. G. Rosa, J. C. V. Gomes & E. A. T. de Souza. *Transfer of an exfoliated monolayer graphene flake onto an optical fiber end face for erbium-doped fiber laser mode-locking*. 2D Materials, vol. 2, no. 3, page 031001, jul 2015.

- [Rox 20a] M. Rox, M. Emerson, T. E. Ertop, I. Fried, M. Fu, J. Hoelscher, A. Kuntz, J. Granna, J. E. Mitchell, M. Lester, F. Maldonado, E. A. Gillaspie, J. A. Akulian, R. Alterovitz & R. J. Webster. *Decoupling Steerability From Diameter: Helical Dovetail Laser Patterning for Steerable Needles*. IEEE Access, vol. 8, pages 181411–181419, 2020.
- [Rox 20b] M. F. Rox, D. S. Ropella, R. Hendrick, E. Blum, R. P. Naftel, H. C. Bow, S. D. Herrell, K. D. Weaver, L. B. Chambliss & R. J. Webster III. *Mechatronic Design of a Two-Arm Concentric Tube Robot System for Rigid Neuroendoscopy*. IEEE/ASME Transactions on Mechatronics, 2020.
- [Rox 20c] M. F. Rox, D. S. Ropella, R. J. Hendrick, E. Blum, R. P. Naftel, H. C. Bow, S. D. Herrell, K. D. Weaver, L. B. Chambliss & R. J. Webster III. *Mechatronic Design of a Two-Arm Concentric Tube Robot System for Rigid Neuroendoscopy*. IEEE/ASME Transactions on Mechatronics, vol. 25, no. 3, pages 1432–1443, 2020.
- [Rucker 08] D. C. Rucker & R. J. Webster. *Mechanics-based modeling of bending and torsion in active cannulas*. In 2nd IEEE RAS EMBS International Conference on Biomedical Robotics and Biomechatronics, pages 704–709, 2008.
- [Rucker 09] D. C. Rucker & R. J. Webster. *Parsimonious evaluation of concentric-tube continuum robot equilibrium conformation*. IEEE Transactions on Biomedical Engineering, vol. 56, no. 9, pages 2308–2311, 2009.
- [Rucker 10a] D. C. Rucker, B. A. Jones & R. J. Webster. *A model for concentric tube continuum robots under applied wrenches*. In 2010 IEEE International Conference on Robotics and Automation, pages 1047–1052, 2010.
- [Rucker 10b] D. C. Rucker, B. A. Jones & R. J. Webster III. *A Geometrically Exact Model for Externally Loaded Concentric-Tube Continuum Robots*. IEEE Transactions on Robotics, vol. 26, no. 5, pages 769–780, 2010.
- [Rucker 10c] D. C. Rucker, B. A. Jones & R. J. Webster III. *A geometrically exact model for externally loaded concentric-tube continuum robots*. IEEE transactions on robotics, vol. 26, no. 5, pages 769–780, 2010.

- [Rucker 10d] D. C. Rucker, I. Robert J. Webster, G. S. Chirikjian & N. J. Cowan. *Equilibrium Conformations of Concentric-tube Continuum Robots*. The International Journal of Robotics Research, vol. 29, no. 10, pages 1263–1280, 2010. PMID: 25125773.
- [Rucker 10e] D. C. Rucker, R. J. Webster III, G. S. Chirikjian & N. J. Cowan. *Equilibrium conformations of concentric-tube continuum robots*. The International Journal of Robotics Research, vol. 29, no. 10, pages 1263–1280, 2010.
- [Rucker 11a] D. C. Rucker & R. J. Webster III. *Statics and Dynamics of Continuum Robots With General Tendon Routing and External Loading*. IEEE Transactions on Robotics, vol. 27, no. 6, pages 1033–1044, 2011.
- [Rucker 11b] D. C. Rucker. *The mechanics of continuum robots: Model-based sensing and control*. Doctoral dissertation, Vanderbilt University, 2011.
- [Rucker 22] C. Rucker, J. Childs, P. Molaei & H. B. Gilbert. *Transverse Anisotropy Stabilizes Concentric Tube Robots*. IEEE Robotics and Automation Letters, vol. 7, no. 2, pages 2407–2414, 2022.
- [Rus 15] D. Rus & M. Tolley. *Design, fabrication and control of soft robots*. Nature, vol. 521, pages 467–75, 05 2015.
- [Russell 01] S. Russell. Smst-2000: Proceedings of the international conference on shape memory and superelastic technologies. A S M International, 2001.
- [Russo 23] M. Russo, S. M. H. Sadati, X. Dong, A. Mohammad, I. D. Walker, C. Bergeles, K. Xu & D. A. Axinte. *Continuum Robots: An Overview*. Advanced Intelligent Systems, vol. 5, no. 5, page 2370020, 2023.
- [Sabetian 19] S. Sabetian. Self-collision detection and avoidance for dual-arm concentric tube robots. Master’s thesis, *Institute of Biomaterials and Biomedical Engineering University of Toronto*, 2019.
- [Sakurai 15] J. Sakurai & S. Hata. *Characteristics of Ti-Ni-Zr Thin Film Metallic Glasses / Thin Film Shape Memory Alloys for Micro Actuators with Three-Dimensional Structures*. International Journal of Automation Technology, vol. 9, pages 662–667, 11 2015.

- [Sasan 20] K. Sasan, A. Lange, T. D. Yee, N. Dudukovic, D. T. Nguyen, M. A. Johnson, O. D. Herrera, J. H. Yoo, A. M. Sawvel, M. E. Ellis, C. M. Mah, R. Ryerson, L. L. Wong, T. Suratwala, J. F. Destino & R. Dylla-Spears. *Additive Manufacturing of Optical Quality Germania–Silica Glasses*. ACS Applied Materials & Interfaces, vol. 12, no. 5, pages 6736–6741, 2020. PMID: 31934741.
- [Satava 04] R. Satava. *Robotic surgery: From past to future - A personal journey*. The Surgical clinics of North America, vol. 83, pages 1491–500, xii, 01 2004.
- [Satava 11] R. M. Satava. Future directions in robotic surgery, pages 3–11. Springer US, Boston, MA, 2011.
- [Schegg 23] P. Schegg, E. Ménager, E. Khairallah, D. Marchal, J. Dequidt, P. Preux & C. Duriez. *SofaGym: An Open Platform for Reinforcement Learning Based on Soft Robot Simulations*. Soft Robotics, vol. 10, no. 2, pages 410–430, 2023. PMID: 36476150.
- [Scholze 91] H. Scholze. Properties of glass, pages 156–364. Springer New York, New York, NY, 1991.
- [Scott 17] G. Scott. *optical fiber mechanical reliability*. White paper WP8002, Review of research at corning’s optical fiber strength laboratory, One Riverfront plaza corning, New york, USA, July 2017. Corning Incorporate.
- [Sears 06] P. Sears & P. Dupont. *A Steerable Needle Technology Using Curved Concentric Tubes*. In IEEE/RSJ International Conference on Intelligent Robots and Systems, pages 2850–2856, 2006.
- [Sears 07] P. Sears & P. E. Dupont. *Inverse Kinematics of Concentric Tube Steerable Needles*. In IEEE International Conference on Robotics and Automation, pages 1887–1892, 2007.
- [Sefati 19] S. Sefati, R. Hegeman, F. Alambeigi, I. Iordachita & M. Armand. *FBG-Based Position Estimation of Highly Deformable Continuum Manipulators: Model-Dependent vs. Data-Driven Approaches*. In 2019 International Symposium on Medical Robotics (ISMR), pages 1–6, 2019.
- [Shahabi 19] E. Shahabi & C.-H. Kuo. Solving inverse kinematics of a planar dual-backbone continuum robot using neural network: Proceedings of the 7th european conference on mechanism science, pages 355–361. Springer Cham, 01 2019.

- [Shan 15] C. Shan, F. Chen, Q. Yang, Y. Li, H. Bian, J. Yong & X. Hou. *High-level integration of three-dimensional micro-coils array in fused silica*. Optics Letters, vol. 40, no. 17, page 4050, 2015.
- [Shi 17] C. Shi, X. Luo, P. Qi, T. Li, S. Song, Z. Najdovski, T. Fukuda & H. Ren. *Shape Sensing Techniques for Continuum Robots in Minimally Invasive Surgery: A Survey*. IEEE Transactions on Biomedical Engineering, vol. 64, no. 8, pages 1665–1678, 2017.
- [Shirai 21] K. Shirai. *Interpretation of the apparent activation energy of glass transition*. Journal of Physics Communications, vol. 5, no. 9, page 095013, sep 2021.
- [Shrivastava 04] S. Shrivastava & A. International. Medical device materials: Proceedings from the materials & processes for medical devices conference 2003, 8-10 september 2003, anaheim, califorinia. ASM International, 2004.
- [Singh 17] I. Singh, M. Singh, P. M. Pathak & R. Merzouki. *Optimal work space of parallel continuum manipulator consisting of compact bionic handling arms*. In 2017 IEEE International Conference on Robotics and Biomimetics (ROBIO), pages 258–263, 2017.
- [SMST 21] SMST. *Shape Memory Alloy Links*, 2021.
- [Song 18] H. Song, J. Dan, X. Chen, J. Xiao & J. Xu. *Experimental investigation of machinability in laser-assisted machining of fused silica*. International Journal of Advanced Manufacturing Technology, vol. 97, no. 1-4, pages 267–278, 2018.
- [Song 23] H. Song, E. Park, H. J. Kim, C.-I. Park, T.-S. Kim, Y. Young Kim & S. Ryu. *Free-form optimization of pattern shape for improving mechanical characteristics of a concentric tube*. Materials Design, vol. 230, page 111974, 2023.
- [Streltsov 01] A. M. Streltsov & N. F. Borrelli. *Fabrication and analysis of a directional coupler written in glass by nanojoule femtosecond laser pulses*. Opt. Lett., vol. 26, no. 1, pages 42–43, Jan 2001.
- [Su 16] H. Su, G. Li, D. C. Rucker, R. J. Webster & G. S. Fischer. *A Concentric Tube Continuum Robot with Piezoelectric Actuation for MRI-Guided Closed-Loop Targeting*. Annals of Biomedical Engineering, vol. 44, no. 10, pages 2863–2873, 2016.

- [Sun 18] B. Sun, J. Lin & M. Fu. *Dependence of processing window and microstructural evolution on initial material state in direct electric resistance heat treatment of NiTi alloy.* Materials and Design, vol. 139, pages 549–564, 2018.
- [Sun 20] C. Sun, L. Chen, J. Liu, J. S. Dai & R. Kang. *A hybrid continuum robot based on pneumatic muscles with embedded elastic rods.* Proceedings of the Institution of Mechanical Engineers, Part C: Journal of Mechanical Engineering Science, vol. 234, no. 1, pages 318–328, 2020.
- [surgical 22] V. surgical. *Virtuoso surgical*, 2022.
- [Sven 20] L. Sven, N. Kathrin, B. Georg, S. Svenja & B.-K. Jessica. *Tendon Actuated Continuous Structures in Planar Parallel Robots: A Kinematic Analysis.* ASME Journal of Mechanisms and Robotics, vol. 13, no. 1, page 11, 2020.
- [Sven 21] L. Sven & B.-K. Jessica. *Design, Modeling and Evaluation of Tendon Driven Parallel Continuum Robots.* In Workshop on Parallel Robot or not Parallel Robots? New Frontiers of Parallel Robotics, IEEE International Conference on Robotics and Automation, 2021.
- [Sven 22] L. Sven & B.-K. Jessica. *Kinetostatic Modeling of Tendon-Driven Parallel Continuum Robots.* IEEE Transactions on Robotics, 2022.
- [Swaney 12] P. J. Swaney, J. M. Croom, J. Burgner, H. B. Gilbert, D. C. Rucker, R. J. Webster III, K. D. Weaver & P. T. Russell III. *Design of a quadramanual robot for single-nostril skull base surgery.* In Dynamic Systems and Control Conference, volume 45318, pages 387–393, 2012.
- [Swaney 15a] P. J. Swaney, H. B. Gilbert, R. J. Hendrick, O. Commichau, R. Alterovitz & R. J. {Webster III}. *Transoral steerable needles in the lung: How non-annular concentric tube robots can improve targeting.* Hamlyn Symposium on Medical Robotics, pages 37–38, 2015.
- [Swaney 15b] P. J. Swaney, A. W. Mahoney, A. A. Remirez, E. Lamers, B. I. Hartley, R. H. Feins, R. Alterovitz & R. J. Webster. *Tendons, concentric tubes, and a bevel tip: Three steerable robots in one transoral lung access system.* IEEE International Conference on Robotics and Automation (ICRA), pages 5378–5383, 2015.

- [Swaney 15c] P. J. Swaney, A. W. Mahoney, A. A. Remirez, E. Lamers, B. I. Hartley, R. H. Feins, R. Alterovitz & R. J. Webster. *Tendons, concentric tubes, and a bevel tip: Three steerable robots in one transoral lung access system.* IEEE International Conference on Robotics and Automation (ICRA), pages 5378–5383, 2015.
- [Swaney 16] P. Swaney, P. York, H. Gilbert, J. Burgner-Kahrs & R. Webster. *Design, Fabrication, and Testing of a Needle-Sized Wrist for Surgical Instruments.* Journal of Medical Devices, vol. 11, 09 2016.
- [swiftglass 23] swiftglass. *Properties of Glass Materials*, 2023.
- [Takahashi 05] M. Takahashi, K. Sugimoto & R. Maeda. *Nanoimprint of Glass Materials with Glassy Carbon Molds Fabricated by Focused-Ion-Beam Etching.* Japanese Journal of Applied Physics, vol. 44, no. 7S, page 5600, jul 2005.
- [Takahashi 13] S. Takahashi, K. Horiuchi, K. Tatsukoshi, M. Ono, N. Imajo & T. Mobely. *Development of Through Glass Via (TGV) formation technology using electrical discharging for 2.5/3D integrated packaging.* In 2013 IEEE 63rd Electronic Components and Technology Conference, pages 348–352, 2013.
- [Tang 21] T. Tang, Y. Yuan, Y. Yalikun, Y. Hosokawa, M. Li & Y. Tanaka. *Glass based micro total analysis systems: Materials, fabrication methods, and applications.* Sensors and Actuators B: Chemical, vol. 339, page 129859, 2021.
- [Tay 06] F. Tay, C. Iliescu, J. Jing & J. Miao. *Defect-free wet etching through Pyrex glass using Cr/Au mask.* Microsystem Technologies, vol. 12, pages 935–939, 01 2006.
- [Thamo 21] B. Thamo, F. Alambeigi, K. Dhaliwal & M. Khadem. *A Hybrid Dual Jacobian Approach for Autonomous Control of Concentric Tube Robots in Unknown Constrained Environments.* In 2021 IEEE/RSJ International Conference on Intelligent Robots and Systems (IROS), pages 2809–2815, 2021.
- [Thamo 23] B. Thamo, D. Hanley, K. Dhaliwal & M. Khadem. *Data-Driven Steering of Concentric Tube Robots in Unknown Environments via Dynamic Mode Decomposition.* IEEE Robotics and Automation Letters, vol. 8, no. 2, pages 856–863, 2023.
- [Thomasnet 21] Thomasnet. *Nitinol Tubing Suppliers*, 2021.

- [Tielen 14] V. Tielen & Y. Bellouard. *Three-Dimensional Glass Monolithic Micro-Flexure Fabricated by Femtosecond Laser Exposure and Chemical Etching*. *Micromachines*, vol. 5, no. 3, pages 697–710, 2014.
- [Till 15] J. Till, C. E. Bryson, S. Chung, A. Orekhov & D. C. Rucker. *Efficient computation of multiple coupled Cosserat rod models for real-time simulation and control of parallel continuum manipulators*. In 2015 IEEE International Conference on Robotics and Automation (ICRA), pages 5067–5074, Seattle, WA, USA, May 2015. IEEE.
- [Till 17a] J. Till & D. C. Rucker. *Elastic Stability of Cosserat Rods and Parallel Continuum Robots*. *IEEE Transactions on Robotics*, vol. 33, no. 3, pages 718–733, June 2017.
- [Till 17b] J. Till & D. C. Rucker. *Elastic Stability of Cosserat Rods and Parallel Continuum Robots*. *IEEE Transactions on Robotics*, vol. 33, no. 3, pages 718–733, 2017.
- [Till 19a] J. Till, V. Aloi & C. Rucker. *Real-time dynamics of soft and continuum robots based on Cosserat rod models*. *The International Journal of Robotics Research*, vol. 38, no. 6, pages 723–746, 2019.
- [Till 19b] J. D. Till. *On the Statics, Dynamics, and Stability of Continuum Robots: Model Formulations and Efficient Computational Schemes*. Doctoral dissertation, University of Tennessee, 2019.
- [Toggweiler 13] S. Toggweiler, J. Leipsic, R. K. Binder, M. Freeman, M. Barbanti, R. H. Heijmen, D. A. Wood & J. G. Webb. *Management of Vascular Access in Transcatheter Aortic Valve Replacement: Part 1: Basic Anatomy, Imaging, Sheaths, Wires, and Access Routes*. *JACC: Cardiovascular Interventions*, vol. 6, no. 7, pages 643–653, 2013.
- [Tomozawa 96] M. Tomozawa. *Fracture of Glasses*. Annual Review of Materials Science, vol. 26, no. 1, pages 43–74, 1996.
- [Tong 18] L. Tong. *Micro/Nanofibre Optical Sensors: Challenges and Prospects*. *Sensors*, vol. 18, no. 3, 2018.
- [Toombs 22a] J. T. Toombs, M. Luitz, C. C. Cook, S. Jenne, C. C. Li, B. E. Rapp, F. Kotz-Helmer & H. K. Taylor. *Volumetric additive manufacturing of silica glass with microscale computed axial lithography*. *Science*, vol. 376, no. 6590, pages 308–312, 2022.

- [Toombs 22b] J. T. Toombs, M. Luitz, C. C. Cook, S. Jenne, C. C. Li, B. E. Rapp, F. Kotz-Helmer & H. K. Taylor. *Volumetric additive manufacturing of silica glass with microscale computed axial lithography*. Science, vol. 376, no. 6590, pages 308–312, 2022.
- [Torres 12] L. G. Torres, R. J. Webster & R. Alterovitz. *Task-oriented design of concentric tube robots using mechanics-based models*. In IEEE/RSJ International Conference on Intelligent Robots and Systems, pages 4449–4455, 2012.
- [Trivedi 08a] D. Trivedi, A. Lotfi & C. D. Rahn. *Geometrically Exact Models for Soft Robotic Manipulators*. IEEE Transactions on Robotics, vol. 24, no. 4, pages 773–780, 2008.
- [Trivedi 08b] D. Trivedi, C. Rahn, W. Kier & I. Walker. *Soft Robotics: Biological Inspiration, State of the Art, and Future Research*. Applied Bionics and Biomechanics, vol. 5, pages 99–117, 12 2008.
- [ValletRegí 03] M. ValletRegí, C. V. Ragel & A. J. Salinas. *Glasses with Medical Applications*. European Journal of Inorganic Chemistry, vol. 2003, no. 6, pages 1029–1042, 2003.
- [Vandebroek 19] T. Vandebroek, M. Ourak, C. Gruijthuijsen, A. Javaux, J. Legrand, T. Vercauteren, S. Ourselin, J. Deprest & E. Poorten. *Macro-Micro Multi-Arm Robot for Single-Port Access Surgery*. In 2019 IEEE/RSJ International Conference on Intelligent Robots and Systems (IROS), page 425–432. IEEE Press, 2019.
- [Vanneste 20] F. Vanneste, O. Goury, J. Martinez, S. Lefebvre, H. Delingette & C. Duriez. *Anisotropic Soft Robots Based on 3D Printed Meso-Structured Materials: Design, Modeling by Homogenization and Simulation*. IEEE Robotics and Automation Letters, vol. PP, pages 1–1, 01 2020.
- [Vanneste 21] F. Vanneste, O. Goury & C. Duriez. *Enabling the control of a new degree of freedom by using anisotropic material on a 6-DOF parallel soft robot*. In 2021 IEEE 4th International Conference on Soft Robotics (RoboSoft), pages 636–642, 2021.
- [Vasilyev 15a] N. V. Vasilyev, A. H. Gosline, A. Veeramani, M. T. Wu, G. P. Schmitz, R. T. Chen, V. Arabagi, P. J. del Nido & P. E. Dupont. *Tissue removal inside the beating heart using a robotically delivered metal MEMS tool*. The International Journal of Robotics Research, vol. 34, no. 2, pages 236–247, 2015.

- [Vasilyev 15b] N. V. Vasilyev, A. H. Gosline, A. Veeramani, M. T. Wu, G. P. Schmitz, R. T. Chen, V. Arabagi, P. J. del Nido & P. E. Dupont. *Tissue removal inside the beating heart using a robotically delivered metal MEMS tool*. The International Journal of Robotics Research, vol. 34, no. 2, pages 236–247, 2015.
- [Vincent Modes 20] J. B.-K. Vincent Modes. *Calibration of Concentric Tube Continuum Robots: Automatic Alignment of Precurved Elastic Tubes*. IEEE Robotics and Automation Letters, vol. 5, no. 1, pages 103–110, 2020.
- [Vitiello 13] V. Vitiello, S.-L. Lee, T. P. Cundy & G.-Z. Yang. *Emerging Robotic Platforms for Minimally Invasive Surgery*. IEEE Reviews in Biomedical Engineering, vol. 6, pages 111–126, 2013.
- [Vlasov 94] Y. Vlasov, E. Bychkov & A. Legin. *Chalcogenide glass chemical sensors: Research and analytical applications*. Talanta, vol. 41, no. 6, pages 1059–1063, 1994.
- [Volder 10] M. D. Volder & D. Reynaerts. *Pneumatic and hydraulic microactuators: a review*. Journal of Micromechanics and Microengineering, vol. 20, no. 4, page 043001, mar 2010.
- [von Witzendorff 18] P. von Witzendorff, L. Pohl, O. Suttmann, P. Heinrich, A. Heinrich, J. Zander, H. Bragard & S. Kaierle. *Additive manufacturing of glass: CO<sub>2</sub>-Laser glass deposition printing*. Procedia CIRP, vol. 74, pages 272–275, 2018. 10th CIRP Conference on Photonic Technologies [LANE 2018].
- [Waltermann 15] C. Waltermann, A. L. Baumann, K. Bethmann, A. Doering, J. Koch, M. Angelmahr & W. Schade. *Femtosecond laser processing of evanescence field coupled waveguides in single mode glass fibers for optical 3D shape sensing and navigation*. In G. Pickrell, E. Udd & H. H. Du, éditeurs, Fiber Optic Sensors and Applications XII, volume 9480, page 948011. International Society for Optics and Photonics, SPIE, 2015.
- [Wang 09] S. Wang, D. Sun, S. Hata, J. Sakurai & A. Shimokohbe. *Fabrication of thin film metallic glass (TFMG) pipe for a cylindrical ultrasonic linear micro-actuator*. Sensors and Actuators A: Physical, vol. 153, no. 1, pages 120–126, 2009.

- [Wang 10] D. Wang, T. Shi, J. Pan, G. Liao, Z. Tang & L. Liu. *Finite element simulation and experimental investigation of forming micro-gear with Zr–Cu–Ni–Al bulk metallic glass*. Journal of Materials Processing Technology, vol. 210, no. 4, pages 684–688, 2010.
- [Wang 18] J. Wang, D. Zhang, T. Ma, S. Song, W. Liu & M. Q.-H. Meng. *A New Solution for the Inverse Kinematics of Concentric-Tube Robots*. In 2018 IEEE International Conference on Cyborg and Bionic Systems (CBS), pages 234–239, 2018.
- [Wang 19a] L. Wang & N. Simaan. *Geometric Calibration of Continuum Robots: Joint Space and Equilibrium Shape Deviations*. IEEE Transactions on Robotics, vol. 35, no. 2, pages 387–402, 2019.
- [Wang 19b] X. Wang, D. Zhuang, S. Geng, Y. Liu & R. Kang. *Stability Analysis of Rod-Driven Continuum Robots Based on Finite Element Models to Avoid Buckling*. In 2019 IEEE 9th Annual International Conference on CYBER Technology in Automation, Control, and Intelligent Systems (CYBER), pages 215–220, 2019.
- [Wang 20a] J. Wang, X. Yang, P. Li, S. Song, L. Liu & M. Q. Meng. *Design of a multi-arm concentric-tube robot system for transnasal surgery*. Medical and Biological Engineering and Computing, vol. 58, no. 3, pages 497–508, 2020.
- [Wang 20b] L. Wang. Modeling and simulation of concentric and eccentric tube continuum robots. Master’s thesis, *The University of Western Ontario*, 2020.
- [Wang 21] X. Wang, Y. Li & K.-W. Kwok. *A Survey for Machine Learning-Based Control of Continuum Robots*. Frontiers in Robotics and AI, vol. 8, 2021.
- [Wang 23] W. Wang, X. Yu, Y. Zhao, L. Li, Y. Li, Y. Tian & F. Xi. *A Simplified Method for Inverse Kinematics of a Flexible Panel Continuum Robot for Real-Time Shape Morphing*. Machines, vol. 11, page 104, 01 2023.
- [Wani 17] O. Wani, H. Zeng & A. Priimagi. *A light-driven artificial flytrap*. Nature Communications, vol. 8, page 15546, 05 2017.
- [Watanabe 02] W. Watanabe, D. Kuroda, K. Itoh & J. Nishii. *Fabrication of Fresnel zone plate embedded in silica glass by femtosecond laser pulses*. Opt. Express, vol. 10, no. 19, pages 978–983, Sep 2002.

- [Webster III 07] R. J. Webster III. *Design and Mechanics of Continuum Robots for Surgery*. Doctoral dissertation, Johns Hopkins University, 2007.
- [Webster 06a] R. J. Webster, A. M. Okamura & N. J. Cowan. *Toward Active Cannulas: Miniature Snake-Like Surgical Robots*. In 2006 IEEE/RSJ International Conference on Intelligent Robots and Systems, pages 2857–2863, 2006.
- [Webster 06b] R. J. Webster, A. M. Okamura & N. J. Cowan. *Toward Active Cannulas: Miniature Snake-Like Surgical Robots*. In IEEE/RSJ International Conference on Intelligent Robots and Systems, pages 2857–2863, 2006.
- [Webster 08a] R. J. Webster, J. M. Romano & N. J. Cowan. *Kinematics and calibration of active cannulas*. In IEEE International Conference on Robotics and Automation, pages 3888–3895, 2008.
- [Webster 08b] R. J. Webster, J. M. Romano & N. J. Cowan. *Kinematics and calibration of active cannulas*. In 2008 IEEE International Conference on Robotics and Automation, pages 3888–3895, 2008.
- [Webster 09a] R. J. Webster, J. M. Romano & N. J. Cowan. *Mechanics of precurved-tube continuum robots*. IEEE Transactions on Robotics, vol. 25, no. 1, pages 67–78, 2009.
- [Webster 09b] R. J. Webster, J. M. Romano & N. J. Cowan. *Mechanics of Precurved-Tube Continuum Robots*. IEEE Transactions on Robotics, vol. 25, no. 1, pages 67–78, 2009.
- [Webster 09c] R. J. Webster, J. P. Swensen, J. M. Romano & N. J. Cowan. *Closed-form differential kinematics for concentric-tube continuum robots with application to visual servoing*. In Experimental Robotics: The Eleventh International Symposium, pages 485–494. Springer, 2009.
- [Webster 10] R. J. Webster & B. A. Jones. *Design and kinematic modeling of constant curvature continuum robots: A review*. International Journal of Robotics Research, vol. 29, no. 13, pages 1661–1683, 2010.
- [Wei 09] W. Wei, R. E. Goldman, H. F. Fine, S. Chang & N. Simaan. *Performance Evaluation for Multi-arm Manipulation of Hollow Suspended Organs*. IEEE Transactions on Robotics, vol. 25, no. 1, pages 147–157, 2009.

- [Wei 21] Y. Wei, G. Chen, S. Tang, Z. Zhang, X. Duan & H. Wang. Design of a reconfigurable planar parallel continuum manipulator with variable stiffness, pages 803–813. Springer, Cham, 10 2021.
- [Wen 21] X. Wen, B. Zhang, W. Weipeng, F. Ye, S. Yue, H. Guo, G. Gao, Y. Zhao, Q. Fang, C. Nguyen, X. Zhang, J. Bao, J. Robinson, P. Ajayan & J. Lou. *3D-printed silica with nanoscale resolution*. Nature Materials, vol. 20, pages 1–6, 11 2021.
- [Wen 22] K. Wen & J. Burgner-Kahrs. *Modeling and Analysis of Tendon-Driven Parallel Continuum Robots Under Constant Curvature and Pseudo-Rigid-Body Assumptions*. Journal of Mechanisms and Robotics, vol. 15, no. 4, 11 2022. 041003.
- [Wikipedia 22] Wikipedia. *Reuleaux triangle — Wikipedia, The Free Encyclopedia*. <http://en.wikipedia.org/w/index.php?title=Reuleaux%20triangle&oldid=1104199141>, 2022. [Online; accessed 04-October-2022].
- [Wlodarczyk 19] K. Wlodarczyk, D. Hand & M. Maroto-Valer. *Maskless, rapid manufacturing of glass microfluidic devices using a picosecond pulsed laser*. Scientific Reports, vol. 9, page 20215, 12 2019.
- [Wondraczek 22] L. Wondraczek, E. Bouchbinder, A. Ehrlicher, J. Mauro, R. Sajzew & M. Smedskjaer. *Advancing the Mechanical Performance of Glasses: Perspectives and Challenges*. Advanced Materials, vol. 34, page 2109029, 04 2022.
- [Wu 10] D. Wu, Q. Zhang, G. Ma, Y. Guo & D. Guo. *Laser bending of brittle materials*. Optics and Lasers in Engineering, vol. 48, no. 4, pages 405–410, 2010.
- [Wu 15] L. Wu, B. L.-W. Tan & H. Ren. *Prototype development of a hand-held robotic light pipe for intraocular procedures*. In 2015 IEEE International Conference on Robotics and Biomimetics (ROBIO), pages 368–373, 2015.
- [Wu 17a] G. Wu, G. Shi & Y. Shi. *Modeling and analysis of a parallel continuum robot using artificial neural network*. In 2017 IEEE International Conference on Mechatronics (ICM), pages 153–158, 2017.

- [Wu 17b] L. Wu, R. Crawford & J. Roberts. *Dexterity Analysis of Three 6-DOF Continuum Robots Combining Concentric Tube Mechanisms and Cable-Driven Mechanisms.* IEEE Robotics and Automation Letters, vol. 2, no. 2, pages 514–521, 2017.
- [Wu 19] G. Wu & G. Shi. *Experimental statics calibration of a multi-constraint parallel continuum robot.* Mechanism and Machine Theory, vol. 136, pages 72–85, 2019.
- [Wu 22] G. Wu & G. Shi. *Design, modeling, and workspace analysis of an extensible rod-driven Parallel Continuum Robot.* Mechanism and Machine Theory, vol. 172, page 104798, 2022.
- [Xin Jue Luo 18] K. A. Xin Jue Luo, T. Looi, S. Sabetian & J. Drake. *Designing Concentric Tube Manipulators for Stability Using Topology Optimization.* In 2018 IEEE/RSJ International Conference on Intelligent Robots and Systems (IROS), pages 1764–1769, 2018.
- [Xin 18] K. A. Xin Jue Luo, T. Looi, S. Sabetian & J. Drake. *Designing Concentric Tube Manipulators for Stability Using Topology Optimization.* In IEEE/RSJ International Conference on Intelligent Robots and Systems (IROS), pages 1764–1769, 2018.
- [Xiong 12] W. Xiong, Y. Zhou, X. He, Y. Gao, M. Mahjouri-Samani, L. Jiang, T. Baldacchini & Y. Lu. *Simultaneous additive and subtractive three-dimensional nanofabrication using integrated two-photon polymerization and multiphoton ablation.* Light: Science and Applications, vol. 1, no. APRIL, 2012. Funding Information: This research work was financially supported by National Science Foundation (CMMI 0900419 and 0758199) and National Natural Science Foundation of China (grant no. 90923039).
- [Xu 10a] K. Xu & N. Simaan. *Intrinsic Wrench Estimation and Its Performance Index for Multisegment Continuum Robots.* IEEE Transactions on Robotics, vol. 26, no. 3, pages 555–561, 2010.
- [Xu 10b] W. Xu, F. Zhou, C. Ouyang, W. Ye, M. Yao & B. Xu. *Mechanical properties of small-diameter polyurethane vascular grafts reinforced by weft-knitted tubular fabric.* Journal of biomedical materials research. Part A, vol. 92, 1, pages 1–8, 2010.

- [Xu 11] K. Xu, J. Zhao, J. Geiger, A. J. Shih & M. Zheng. *Design of an endoscopic stitching device for surgical obesity treatment using a N.O.T.E.S approach.* In 2011 IEEE/RSJ International Conference on Intelligent Robots and Systems, pages 961–966, 2011.
- [Xu 14] R. Xu, S. F. Atashzar & R. V. Patel. *Kinematic instability in concentric-tube robots: Modeling and analysis.* In 5th IEEE RAS/EMBS International Conference on Biomedical Robotics and Biomechatronics, pages 163–168, 2014.
- [Xu 16a] R. Xu. *Modeling, Sensorization and Control of Concentric-Tube Robots.* Doctoral dissertation, The University of Western Ontario, January 2016.
- [Xu 16b] W. Xu, J. Chen & H. Lau. *Data-driven methods towards learning the highly nonlinear inverse kinematics of tendon-driven surgical manipulators: XWJ<sub>I</sub>JMRAS<sub>I</sub>K<sub>K</sub>NNR<sub>G</sub>MRELM.* The International Journal of Medical Robotics and Computer Assisted Surgery, vol. 16, no. 1, pages 1–10, 2020.
- [Xu 17] R. Xu. *Modeling , Sensorization and Control of Concentric-Tube Robots.* Doctoral dissertation, The University of Western Ontario, 2017.
- [Xu 20] B. Xu & S. Y. Ko. *Novel force sensing module for a concentric tube-based vitreoretinal surgical robot.* Sensors and Actuators A: Physical, vol. 316, page 112395, 2020.
- [Xu 21] Y. Xu, Y. Li, N. Zheng, Q. Zhao & T. Xie. *Transparent origami glass.* Nature Communications, vol. 12, 07 2021.
- [Yan 22] J. Yan, J. Chen, J. Chen, W. Yan, Q. Ding, K. Yan, J. Du, C. P. Lam, G. K. C. Wong & S. S. Cheng. *A Continuum Robotic Cannula With Tip Following Capability and Distal Dexterity for Intracerebral Hemorrhage Evacuation.* IEEE Transactions on Biomedical Engineering, vol. 69, no. 9, pages 2958–2969, 2022.
- [Yang 01] C. Yang, S.-S. Ho & B. Yan. *Micro Hole Machining of Borosilicate Glass through Electrochemical Discharge Machining (ECDM).* Key Engineering Materials - KEY ENG MAT, vol. 196, pages 149–166, 01 2001.
- [Yang 18a] G.-Z. Yang, J. Bellingham, P. E. Dupont, P. Fischer, L. Floridi, R. Full, N. Jacobstein, V. Kumar, M. McNutt, R. Merrifield *et al.* *The grand challenges of Science Robotics.* Science robotics, vol. 3, no. 14, page eaar7650, 2018.

- [Yang 18b] Z. Yang, X. Zhu & K. Xu. *Continuum Delta Robot: a Novel Translational Parallel Robot with Continuum Joints*. In 2018 IEEE/ASME International Conference on Advanced Intelligent Mechatronics (AIM), pages 748–755, 2018.
- [Yaxi 21] W. Yaxi & Q. Xu. *Design and testing of a soft parallel robot based on pneumatic artificial muscles for wrist rehabilitation*. Scientific Reports, vol. 11, 01 2021.
- [Yazawa 93] T. Yazawa, H. Tanaka, K. Eguchi, S. Yokoyama & T. Arai. *Novel porous glass with chemical resistance and good shaping ability prepared from borosilicate glass containing ZnO*. Journal of Materials Science Letters, vol. 12, pages 263–264, 1993.
- [York 15] P. A. York, P. J. Swaney, H. B. Gilbert & R. J. Webster. *A wrist for needle-sized surgical robots*. In 2015 IEEE International Conference on Robotics and Automation (ICRA), pages 1776–1781. IEEE, 2015.
- [Young 19] E. M. Young & K. J. Kuchenbecker. *Implementation of a 6-DOF Parallel Continuum Manipulator for Delivering Fingertip Tactile Cues*. IEEE Transactions on Haptics, vol. 12, no. 3, pages 295–306, 2019.
- [Yu-Ting 22] L. Yu-Ting, R. Mia, T. Tsu-Chin & H. Jean-Pierre. *The Rise of the Machines in Retina*, 2022.
- [Yu 05] Y.-Q. Yu, L. L. Howell, C. Lusk, Y. Yue & M.-G. He. *Dynamic Modeling of Compliant Mechanisms Based on the Pseudo-Rigid-Body Model*. Journal of Mechanical Design, vol. 127, no. 4, pages 760–765, 02 2005.
- [Yu 16] H. Yu, L. Wu, K. Wu & H. Ren. *Development of a Multi-Channel Concentric Tube Robotic System with Active Vision for Transnasal Nasopharyngeal Carcinoma Procedures*. IEEE Robotics and Automation Letters, vol. 1, no. 2, pages 1172–1178, 2016.
- [Yuan 18] H. Yuan & Z. Li. *Workspace analysis of cable-driven continuum manipulators based on static model*. Robotics and Computer-Integrated Manufacturing, vol. 49, pages 240–252, 2018.
- [Yuan 19] H. Yuan, L. Zhou & W. Xu. *A comprehensive static model of cable-driven multi-section continuum robots considering friction effect*. Mechanism and Machine Theory, vol. 135, pages 130–149, 2019.

- [Yuan 20] J. Yuan, Z. An & J. Zhang. *Effects of hollow microsphere surface property on the mechanical performance of high strength syntactic foams.* Composites Science and Technology, vol. 199, page 108309, 2020.
- [Zaccaria 20] F. Zaccaria, S. Briot, M. T. Chikhaoui, E. Idà & M. Carriato. An analytical formulation for the geometrico-static problem of continuum planar parallel robots, pages 512–520. Springer, Cham, 09 2020.
- [Zaki 20] R. M. Zaki, C. Strutynski, S. Kaser, D. Bernard, G. Hauss, M. Faessel, J. Sabatier, L. Canioni, Y. Messaddeq, S. Danto & T. Cardinal. *Direct 3D-printing of phosphate glass by fused deposition modeling.* Materials Design, vol. 194, page 108957, 2020.
- [Zanini 23] R. Zanini, G. Franceschin, E. Cattaruzza & A. Traviglia. *A review of glass corrosion: the unique contribution of studying ancient glass to validate glass alteration models.* npj Materials Degradation, vol. 7, no. 1, page 38, May 2023.
- [Zhang 98] J. Zhang, K. Sugioka & K. Midorikawa. *High-speed machining of glass materials by laser-induced plasma-assisted ablation using a 532-nm laser.* Applied Physics A: Materials Science & Processing, vol. 67, no. 4, pages 499–501, January 1998.
- [Zhang 20] J. Zhang, H. Wei, Y. Shan, P. Li, Y. Zhao, L. Qi & H. Yu. *Modeling and Experimental Study of a Novel Multi-DOF Parallel Soft Robot.* IEEE Access, vol. 8, pages 62932–62942, 2020.
- [Zhang 22a] J. Zhang, Y. Xiang, C. Wang, Y. Chen, S. C. Tjin & L. Wei. *Recent Advances in Optical Fiber Enabled Radiation Sensors.* Sensors, vol. 22, no. 3, 2022.
- [Zhang 22b] J. Zhang, Q. Fang, P. Xiang, D. Sun, Y. Xue, R. Jin, K. Qiu, R. Xiong, Y. Wang & H. Lu. *A Survey on Design, Actuation, Modeling, and Control of Continuum Robot.* Cyborg and Bionic Systems, vol. 2022, 2022.
- [Zheng 12] T. Zheng, D. T. Branson, R. Kang, M. Cianchetti, E. Guglielmino, M. Follador, G. A. Medrano-Cerda, I. S. Godage & D. G. Caldwell. *Dynamic continuum arm model for use with underwater robotic manipulators inspired by octopus vulgaris.* In 2012 IEEE International Conference on Robotics and Automation, pages 5289–5294, 2012.

- [Zheng 18] T. Zheng, G. Yang, C. Zhang, Y. Wang, W. Shen, Z. Fang & G. Ye. *Self-Calibration of Cable Driven Continuum Robot*. In 2018 IEEE International Conference on Robotics and Biomimetics (ROBIO), pages 2498–2503, 2018.
- [Zheng 20] G. Zheng. *Control of a Silicone Soft Tripod Robot via Uncertainty Compensation*. IEEE Robotics and Automation Letters, vol. 5, no. 2, pages 2801–2807, 2020.
- [Zhou 19] M. Zhou, X. Hao, A. Eslami, K. Huang, C. Cai, C. Lohmann, N. Navab, A. Knoll, M. A. Nasseri & C. Xia. *6DOF Needle Pose Estimation for Robot-Assisted Vitreoretinal Surgery*. IEEE Access, vol. PP, pages 1–1, 04 2019.
- [Zhou 20] M. Zhou, Q. Yu, K. Huang, S. Mahov, A. Eslami, M. Maier, C. P. Lohmann, N. Navab, D. Zapp, A. Knoll & M. A. Nasseri. *Towards Robotic-Assisted Subretinal Injection: A Hybrid Parallel–Serial Robot System Design and Preliminary Evaluation*. IEEE Transactions on Industrial Electronics, vol. 67, no. 8, pages 6617–6628, 2020.
- [Zusman 90] R. Zusman, C. Rottman, M. Ottolenghi & D. Avnir. *Doped sol-gel glasses as chemical sensors*. Journal of Non-Crystalline Solids, vol. 122, no. 1, pages 107–109, 1990.
- [Řiháková 15] L. Řiháková & H. Chmelickova. *Laser Micromachining of Glass, Silicon, and Ceramics*. Advances in Materials Science and Engineering, vol. 2015, pages 1–6, 03 2015.

## Bibliography

---

## List of Figures

- 1 The three classes of MIS intervention instruments A) Flexible needle with a straight shaft having a bevel tip that steers and changes its direction upon application of lateral force at the base. Its drawback is high dependence on solid tissue penetration to produce lateral tip motion and secondly, it cannot maneuver through curved cavity/anatomy, B) Straight and stiff shaft with a tip-mounted articulated tool, which reaches the surgical site through a straight path. It is difficult to steer through complex anatomy and the tool manipulation can often cause tissue deformation e.g. forceps and da Vinci, Intuitive Surgical tools, C) Elongated steerable device with a flexible backbone. They consist of flexible catheters or multistage dexterous devices like continuum robots..... 3
  
- 2 Transition from conventional rigid robot to continuum robot due to its benefits, A) a typical conventional serial robot with discrete links connected by joints B) a hyper-redundant type of rigid robot in order to increase its dexterity and maneuverability, C) continuum robot type with infinite DOFs and deformable link(s) which is safer for human-to-robot interaction. .... 4
  
- 3 Trend in medical robotic devices with a paradigm shift from rigid link/articulated robots to continuum robots on the bases of backbone flexibility and level of miniaturization. .... 7

4	Different 3D miniature devices and monolithic microstructure fabricated in glass <b>A)</b> Volumetric 3D printing of silica glass with microscale computed axial lithography to fabricate a 3D transparent and complex microfluidic structure, having trusses and lattice with minimum feature sizes of $50\mu\text{m}$ , [Toombs 22a], <b>B)</b> Microfluidic device using laser micro-welding process in which the two glass plates are permanently bonded together without using any adhesives nor intermediate layer [Wlodarczyk 19], <b>C)</b> SEM image of a $500\text{nm}$ diameter silica micro/nanofibre (MNF) tied into a ring and placed on a $60\mu\text{m}$ diameter human hair, with the MNF often used for optical sensors [Tong 18], <b>D)</b> Intertwined microfluidic spiral channels in fused silica glass with a channel width of $74\mu\text{m}$ , which is filled with dyes (scale: $140\mu\text{m}$ ) [Kotz 19], <b>E)</b> Quartz glass chip for cell sorting application with a dimension of $34\text{mm} \times 12\text{ mm} \times 2\text{mm}$ , fabricated by selective laser-induced etching [Gottmann 17], <b>F)</b> Top and side view of a nested nozzle in quartz glass for biological application (diameter: $10\text{mm}$ , height: $7\text{mm}$ ), fabricated by selective laser-induced etching [Gottmann 17], <b>G)</b> Quartz glass connector for capillary electrophoresis, diameter $15\text{mm}$ , thickness $2\text{mm}$ , fabricated by selective laser-induced etching [Gottmann 17] <b>H)</b> Transparent suspended microchannel resonator (SMR) in fused silica with fluidic channels with a cross-section around $10\mu\text{m} \times 5\mu\text{m}$ flowing underneath [FEMTOprint 18b], <b>I)</b> Monolithic 3D micromixer with an impeller for glass microfluidic systems using selective laser-induced etching [Kim 20d], <b>J)</b> Microfluidic mixer with 5 inlets and 1 outlet (channels diameter of $100\mu\text{m}$ ) [FEMTOprint 17], <b>K)</b> Passive compliant tool for retinal vein cannulation (RVC) that relies on a buckling mechanical principle [FEMTOprint 18a], <b>L)</b> 3D complex lab-on-a-chip (smallest channel diameter of $3\mu\text{m}$ ) [FEMTOprint 17], <b>M)</b> Optically transparent glass micro-actuator fabricated by femtosecond laser exposure and chemical etching [Lenssen 12a], <b>N)</b> 3D microfluidic channel fabricated by using selective laser-assisted etching [FEMTOprint 23]. . . . .	9
5	Illustration of glass beam bending experiments undergoing several stress deformation for loading and unloading without breaking (see video). The beam is characterized by a $40\mu\text{m}$ thick flexure in its thinnest part, Image © 2011 Optical Society of America [Bellouard 11]. . . . .	10
6	The relationship between the glass capillary bending stress and the obtainable bend radius of curvature for the glass diameters. . . . .	11
1.1	Examples of different types of continuum robots in the literature <b>A)</b> Concentric tube robot (CTR) actuated by axial rotation and translation of pre-curved tubes (image from [Chikhaoui 18a], (online)), <b>B)</b> Hybrid continuum robot with a combination of tendon-driven segments in a concentric assembly manner [Chikhaoui 18a], <b>C)</b> Tendon-driven continuum robot with extensible segments, using self-repelling magnetic spacer disks, (image from [Chikhaoui 18a]), <b>D)</b> Planar tendon actuated parallel continuum robot [Sven 21], <b>E)</b> Stewart type compliant legs parallel continuum robots [Bryson 14]. . . . .	21

---

1.2	Examples of CTR prototypes in the literature <b>A</b> ) Three-tube CTR as Tubes 1 and 2 forms a variable curvature balanced pair that dominate tube 3 [Dupont 10a], <b>B</b> ) Active cannula prototype made of pre-curved superelastic nitinol tubes [Webster 06a], <b>C</b> ) A hand-held CTR prototype with deployed tubes and actuation unit [Girerd 20d], <b>D</b> ) A CTR next to a standard da Vinci laparoscopic tool [Gilbert 16b]. 22
1.3	The various components of a CTR prototyping, along with their respective specifications. The targeted application influences and determines the CTR design and its validation criteria. The CTR tubes are designed based on the geometry of the anatomical area and fabricated with processes that depend on the material selected. The actuation unit is also designed and fabricated using application and tube requirements. End effectors are selected and integrated into the innermost tube. An integration step consists in assembling all of these elements together, along with the implementation of a control system and validation of the CTR performance. .... 23
1.4	Representation of the CTR prototypes in the literature (extracted from our online <b>CTR Prototyping Resources</b> with the necessary parameters) aligned in a single curvature plane for clear presentation. One can observe the number of tubes for each prototype and the considered curvatures. .... 25
1.5	Illustration of a set of CTR tubes, with their design variables represented. .... 26
1.6	A) Joule heating effect by high current flow through the tube [Gilbert 16c], B) Air furnace heat treatment using a metal fixture with brass pins [Gilbert 16c], C) Air furnace annealing process using engraved aluminum mold [Kim 14]. .... 27
1.7	(a) Fabricated heat-shrink plastic tubes and (b) the jig for fabrication of tubes, extracted from [Noh 16]. .... 30
1.8	CTR tube prototypes fabricated with additive manufacturing using different materials and processes. The stereolithography-SLA (for Accura 25). The selective laser sintering-SLS (for Nylon D80, PEBA 2301, and DuraForm). multijet printing-MJP (with different material) by Morimoto et al. [Morimoto 17a]. .... 31
1.9	Applications of CTR for MIS illustrating the different areas of human anatomy for the proposed interventions in literature.... 33
1.10	Schematic representation of rigid link parallel manipulators and parallel continuum robot.... 35

---

1.11 Different PCR prototype design in the literature <b>A</b> ) 6-DoFs Stewart-Gough type of continuum robot [Till 19a], <b>B</b> ) A 6-DOF articulation PCR design prototype with possible intermediate constraints for large deflection [Orekhov 17], <b>C</b> ) & <b>D</b> ) Tendon actuated planar PCRs [Sven 20, Nuelle 20], <b>E</b> ) miniaturized 6-DoFs Stewart-Gough type of continuum robot with gripper [Till 19b], <b>F</b> ) A modular type of PCR consisting of operative and control units [Mishra 18], <b>G</b> ) Delta type pneumatically actuated silicon rubber PCR [Huang 22], <b>H</b> ) An SMA actuated miniature PCR prototype [AbuZaiter 15], <b>I</b> ) A slender flexible link PCR design type [Wei 21], <b>J</b> ) 6-DOF articulated PCR design [Gallardo 21], <b>K</b> ) Three-limb 6-DOF PCR prototype design [Chen 21a]. . . . .	36
1.12 General classification of PCRs based on their structural design configuration or architecture, which is either non-planar that is characterized by out-of-plane motion or planar, which is restricted to in-plane motion when actuated. . . . .	38
1.13 Schematic diagram for the different types of spatial PCRs in the literature <b>A</b> ) vertical linear actuator rod or slender tendon PCR type, <b>B</b> ) horizontal linear actuator rod or slender tendon PCR type, <b>C</b> ) Electric/pneumatic driven PCR type, <b>D</b> ) wire/cable and disk actuated PCR type. . . . .	40
1.14 A state-of-the-art of spatial PCRs in the literature considering their actuation DOFs versus the leg length, so as to compare their individual sizes. <b>A</b> ) Miniature 6-DOF PCR with a cable-driven grasper [Orekhov 15], <b>B</b> ) A design that turns an articulated 3-PPSR Manipulator into a PCR [Gallardo 21], <b>C</b> ) A 6-DOF articulation PCR design with possible intermediate constrained with disk integration for large displacement [Orekhov 17], <b>D</b> ) Three-limb 6-DOF PCR prototype design [Chen 21a], <b>E</b> ) Stewart-Gough configuration PCR which allows for full six degrees of freedom end effector control [Aloi 22], <b>F</b> ) A similar 6-DoF Stewart-Gough type of continuum robot [Bryson 14], <b>G</b> ) An SMA actuated miniature PCR prototype [AbuZaiter 15], <b>H</b> ) Delta type pneumatically actuated silicon rubber PCR [Huang 22], <b>I</b> ) A modular type of PCR consisting of operative and control units [Mishra 18], <b>H</b> ) Three DOF multi-constrain PCR [Wu 19].....	40

1.15	Different approaches of modeling continuum robots in the literature based. This is arranged in terms of the kinematic framework and the mechanical formulation used while considering either the discrete or continuous approach. <b>A)</b> Approximation of continuous shape by series of discretized rigid links connected by spherical or revolute joints, <b>B)</b> Constant curvature with geometrical arc segment representation of continuum shape, <b>C)</b> Variable curvature which involves a continuously evolving reference frame achieved by integrating along the continuum rod, <b>D)</b> representation of the robot kinematics in a 3D shape dimension, <b>E)</b> Lumped parameter mechanics which approximate the response of a continuum robot upon actuation or load by using discrete spring( $k$ ) mass( $m$ ), damper( $c$ ) system, <b>F)</b> Energy-based mechanics formulation to describe the continuum robot shape while using any of the kinematic frameworks, <b>G)</b> Non-energy-based approaches using the classical elasticity theorems that consider the conservation/equilibrium relationship of forces and moment acting on the continuum link/robot. ....	42
1.16	The geometry of a continuum robot provides a means of determining the pose of points along it [Nepalli 07, Webster III 07]. Using arc geometry approach with $\mathbf{p} = [r(1 - \cos\theta) \quad 0 \quad r\sin\theta]^T$ , and then $\mathbf{R}_y(\theta)$ & $\mathbf{R}_z(\phi) \in \text{SO}(3)$ . Left figure, consider $\phi = 0$ then the arc segment lies in $x - z$ plane whereas, the right figure is a case where the arc rotates $\phi$ out of $x - z$ plane.....	44
1.17	Flowchart for shooting method for numerical solver. The input variables are specified, and the unknown and output variables are guessed. ....	51
2.1	FLWE fabrication process. <b>A)</b> FEMTOprint machine, <b>B)</b> automatic ultrasonic wet etching station <b>C)</b> FLWE step-by-step fabrication process: <b>1)</b> the design of the laser-machining process utilizing specialized software, such as ALPHACAM, <b>2)</b> the direct laser writing of the pattern onto the substrate with a zoomed part showing the trenching/grooving pattern of the laser exposure within the substrate, <b>3)</b> the release of the desired structure through wet etching in a KOH or HF etchant, <b>4)</b> the 3D shape structure .....	64
2.2	Circular cantilever tube fixed at one end .....	65
2.3	Sensitivity analysis plot of a microbeam structure, which helps one to easily visualize the combination of internal diameter, external diameter, and tube length for a given/required stiffness value or range. ....	66
2.4	Analysis of the expected results of the microglass fabricated by FLWE, <b>A)</b> The CAD drawing of the different standing tubes with the inscribed specifications on a 1.7mm thick glass sample. <b>B)</b> and <b>C)</b> the different tube dimensions/specifications to be fabricated by the FLWE with their corresponding expected stiffness value using Equ 2.1 .....	67

## List of Figures

---

2.5	The experimental result for the microglass rods fabricated by FLWE which was characterized A) characterization set-up for measuring the bending stiffness of each rod B) sample during characterization C) table of the results, D) - I) show the results of the designed external/internal diameters versus the realized ones along with the measured bending stiffness for each one.....	68
2.6	Pre-curved glass tube shaping by only thermal treatment approach, (A) plot of temperature and time duration for the heat treatment and the molds used, though the capillaries shattered in the furnace, (B) & (C) reduced temperature and time duration with different step ramp for both cases while using a solid steel mold. The outcome result shows straight glass capillaries without a pre-curved part, (D) & (E) maintained the same maximum temperature but with a longer duration of constant 800°C followed by natural cooling in the air. The result shows a high spring-back and no pre-curved shape, (F) only the maximum temperature was increased to 900°C and the result shows a lesser spring-back, (G) to observe the elastic property of the glass, the temperature was reduced to 850°C and lasted 30 minutes duration. The resultant output had little spring back but fragile for robot integration, (H) & (I) the maximum temperature was increased to 900°C under the same conditions as the previous for both cases. The result shows no spring back which was an interesting result but will be extremely difficult to be used for the robot design due to its fragility. ....	71
2.7	The pre-curved tube fabrication process: 1) inserting the glass capillary into the thin heat-shrink polymer tubing; 2) constraining it to the desired 3D printed mold shape; 3) applying thermal treatment in the furnace for a short period; and 4) obtaining the pre-curved microglass tube.....	74
2.8	The characterization and validation of the novel shaping approach, A) Sample of the pre-curved glass tubes to be analyzed, B) Plot of the characterization and validation which were conducted for two different heat durations. The circle points are the various results while the lines are the least square algorithm. The radius of curvature in Y versus the mold radius of curvature in X was validated, as demonstrated by the star points on the plot, C) The 3D printed mold with five different radii of curvature that was used to constrain the glass in shape during the heat treatment, D) Obtaining the radius of curvature of each sample using curve fitting, E) Fabrication results that were used for the validation of the process. ....	75
2.9	The three-point bending stiffness test result and analysis, A) the experimental set-up B) bending stiffness plot for for tube with 100mm external tube diameter and 20mm internal diameter for the case of with (red line) and without heat shrink (black line), C) bending stiffness but with 165mm external tube diameter and 100mm internal diameter, while D) bending stiffness with 356mm external tube diameter and 249mm internal diameter. ....	76
2.10	Three-point bending stiffness test .....	77

3.1	The Caturo: a capillary flexible CTR made of glass, with a high curvature and a sub-millimetric diameter. <b>A)</b> Arrangement of CTR tubes considering the case of dominance stiffness pair, where the inner tube that is characterized by a smaller diameter and less stiffness is inserted and conforms to the shape of the larger and thicker outer tubes, represented as “Before deployment”. During the deployment operation, each individual tube morphs into its original pre-curved shape as the robot takes its final configuration, represented as “After deployment”. <b>B)</b> A robotized two-tube Caturo, with sub-millimeter diameters (0.16mm & 0.35mm) and a very low radius of curvature (11.5mm), during a deployment. <b>C)</b> A comparison of three tube CTR configurations between the conventional Nitinol material and that of the sub-millimeter glass (diameter of each tube is displayed). <b>D)</b> The actuation unit is characterized by two DoF; the outer tube is fixed to the robot base while the inner tube is attached to the linear and rotary actuation for the demonstrations in this paper.....	83
3.2	Sub-millimetre pre-curved glass tube samples with obtainable shapes and curvatures, such as the simple planar to complex helical curvatures, for various demonstrations of sub-millimeter glass tube flexibility and ability to slide into each other for possible CTR configurations or deployment. ....	84
3.3	The Caturo CTR actuation unit design, showing the description of the CTR tube arrangement procedure and its deployment principle, <b>(A)</b> The design of the robot consisting of the schematic and <b>(B)</b> the CAD and <b>(C)</b> the realized prototype with the vital parts identified. The robot has two sections: the tube and the actuation unit.....	85
3.4	The FKM (red arrow) and IKM (blue arrow) model flow .....	88
3.5	Two tube configuration with two sections for the Caturo FKM.....	89
3.6	Sub-millimetre glass CTR FKM validation and comparison for two different cases. <b>(A)</b> aligned configuration where the two tubes are in the same direction, and <b>(B)</b> anti-aligned configuration in which the tubes are in the opposite direction. ....	89
3.7	The inverse kinematic modeling of a single segment continuum robot using a closed-form analytic approach .....	90
3.8	Sub-millimetre glass CTR path following based on IKM <b>(A)</b> Simulation results of the path tracing using the closed-form geometric approach to the IKM <b>(B)</b> Experimental result for a square path following which is achieved using a two DoF Caturo, <b>(C)</b> Open loop control block scheme using the IKM for square path, <b>(D)</b> The positioning accuracy of the Caturo with overall root mean square error of 0.201mm, for the open loop control based using the IKM. ....	92
3.9	Stability analysis of micro-glass CTR under torsion, which is used to validate the effect of change in transmission length for two different cases, as displayed in <i>Experiment-A</i> and <i>Experiment-B</i> with a change in the curvature and active curve length of the tubes.....	94

---

3.10	A 3D conical-spiral trajectory free space deployment strategy; which has a 4 x 4 mm tip attachment for better visualization during the navigation. . . . .	97
3.11	Demonstration of a complex helical pre-curved glass tube free space deployment, showing the flexibility of the glass tube in forward and reverse movement. . . . .	98
3.12	The robot's small scale size and its flexibility for a constraint path deployment maneuvering through a less than 1 mm orifice of three needles, using only one pre-curved tube with a 54.4mm radius of curvature. . . . .	99
3.13	The possibility of emitting laser through a pre-curved optical glass fiber to the end-effector tip, where the proximal end is connected to a laser source. . . . .	101
3.14	A two-in-one demonstration of the capability of the robot for either transferring a liquid sample or specimen from one point to another and its ability for drug delivery or sample collection. . . . .	102
3.15	Vitreoretinal deployment through an eye of a fish with an OCT viewing capability. . . . .	103
3.16	Sub-millimetre pre-curved glass tubes and the unprecedented region of interest we operate when comparing all the inner smallest CTR pre-curved tubes for the prototypes in the literature. It involves the conventional Nitinol (in red marker) and 3D printed technology (in green marker) and that of the sub-millimeter glass tubes (in blue marker). The external radius and radius of curvature of the innermost tube prototypes in literature were considered. The percentage lines are the recoverable maximum strain below permanent deformation or fracture for different tubes with an average of 8% for Nitinol [Webster 06a] (solid red line) and around 1% for glass [Cuellar 87] (solid blue line). . . . .	105
4.1	The schematics of the 3-leg Glass PCR and considering a flexible single rod for the Cosserat rod formulation . . . . .	111
4.2	The miniature glass 3-leg PCR shooting method solver flowchart for the FKM and IKM. The variables to be evaluated for either the FKM or the IKM are given in Table 4.6. . . . .	115
4.3	Workspace of the miniature glass PCR showing the different plane cuts and its boundary shape. This is used to compute the achievable workspace volume of the robot. . . . .	116
4.4	Variation of end-effector orientations within the workspace, <b>A</b> ) end-effector rotation about the $x$ -axis, whereas <b>B</b> ) end-effector rotation about the $y$ -axis. . . . .	118
4.5	Robot manipulability in terms of condition number with the workspace which reduces as it spread to the boundary region and maximum at the central part. . . . .	119

---

4.6	Variation of stiffness at different configurations of the robot within the workspace, while considering different of the applied load, <b>A</b> ) along the $x$ -axis, <b>B</b> ) along the $y$ -axis, and <b>C</b> ) along the $z$ -axis which is the maximum. . . . .	121
4.7	Vertical plane cut workspace of the miniature glass PCR considering the effect of the actuation length which relates to the robot arc length. Projected areas are unstable regions due to negligible stiffness in long actuation length (see Table 4.5 for corresponding values). . . . .	123
4.8	Workspace vertical plane cut showing the effect of end-effector geometrical parameters on the overall performance of the PCR in terms of stiffness, manipulability, and end-effector position and orientation. <b>A</b> ) Robot shape for the different end-effectors which are $r_e = [1.5, 1, 0.5, 0.1]r_b$ , <b>B</b> ) and <b>C</b> ) are that of stiffness when the force is applied in the $x$ - and $y$ - axis respectively, <b>D</b> ) Stiffness variation when the force is applied in the $z$ -axis, <b>E</b> ) Manipulability variation considering each end-effector dimension, <b>F</b> ) Obtainable end-effector orientation for each robot configuration. . . . .	125
4.9	The miniaturized PCR made of glass, <b>A</b> ) Computer-aided design (CAD) of the entire robot and its different components <b>B</b> ) Prototype of the robot in maximal extension configuration <b>C</b> ) Prototype of the robot in maximal bending configuration. . . . .	127
4.10	S-velocity profile plot for the robot control input (3 smooth curves for the 3 motors) and their corresponding output servo motor signals (3 step signal curves). . . . .	129
4.11	Experimental validation for the boundary workspace based on FKM. . . . .	129
4.12	Circumradius validation on a vertical plane along the 10 mm circular path using IKM in $XZ$ plane. <b>A</b> ) the experimental validation result and <b>B</b> ) simulation plotting showing the various configuration of the robot for the desired circumradius path following. Each path was evaluated at least four times, and the error was computed for each point along the path. . . . .	130
4.13	Experimental validation for horizontal plane path tracing by the miniaturized glass PCR A) 8mm circular path, B) and C) square paths. Each path was evaluated at least four times and the error was computed for each point along the path. . . . .	131
4.14	Future proposition for compact handheld multi-arm CTR design . . . . .	137
4.15	Design of PCR with pre-curved legs. <b>A</b> ) CAD of a PCR with pre-curved legs for pure translation to pure rotation upon actuation as shown by the simulations below, <b>B</b> ) CAD of a PCR composed of two-tube CTRs which is a further extension of that presented in <b>A</b> with an introduction of a second pre-curved tube, <b>C</b> ) model simulation of the PCR design in <b>A</b> for which the <b>up</b> ) shows the initial robot configuration while <b>below</b> ) presents the configuration upon linear actuation resulting in a $90^\circ$ end-effector rotation. . . . .	139

4.16 3-DoF miniature PCR redesign using piezo-driven actuators for possible use in the scanning electron microscope (SEM), while the miniature planar version without the rotary actuator can suit transmission electron microscopes (TEM) micromanipulation application. ....	140
A.1 Example of pattern shapes proposed by researchers, with (A) parameterized patterns simulated using FEA [Lee 15] and (B) diamond-shape patterns obtained using topology optimization [Luo 21]. ....	149
B.1 The different classifications of CTR actuation units ai) The kinematic graph of parallel actuation unit, aii) The structural example of parallel actuation unit, bi) The kinematic graph of hybrid actuation unit, bii) The structural example of hybrid actuation unit, ci) The kinematic graphs of serial actuation unit, cii) The structural example of serial actuation unit. ....	154
B.2 Different parallel actuation unit prototypes a) An actuation unit with a puncturing mechanism by Swaney et al [Swaney 15c], b) A multi-arm CTR actuation unit composing of 1) Lead screws connect translational motors in the motor pack to each carrier. 2) Square shafts connect rotational motors to tube bases through gear trains. 3) Tubes of the concentric tube manipulators can be seen here. 4) Tube carrier, by Hendrick et al [Hendrick 14a] c) A parallel actuation unit with a nose-like design structure by Gosline et al. in [Gosline 12], d) A 4-arm 24 DOF CTR parallel actuation unit with 3 fully-actuated tubes per arm by Swaney et al. in [Swaney 12], e) A transparent casing 3 DOF actuated unit by Esakkiappan et al. in [Esakkiappan 19], f) A novel parallel actuation unit with a roller gear mechanism fabricated using additive manufacturing by Morimoto et al. in [Morimoto 17b], and g) A teleoperated CTR with parallel actuation unit by Xu in [Xu 17]....	156
B.3 The hybrid actuation unit prototypes, with a) MRI compatible 6-DOF piezoelectric actuation unit by Su et al. in [Su 16], b) Manually-actuated unit with precise tube positioning by Rucker et al. in [Rucker 10b], c) Structurally linked hybrid actuation unit by Boushaki in [Boushaki 16c, Boushaki 16b]. ....	157

C.1	Different CTR end effector prototypes: a) Gripper and curette end effectors [Burgner 14a], b) Tip mounted forceps end effector [Dupont 09a], c) Multi-arm CTR with scissors and forceps [Wang 20a], d) The design description and prototype of forceps gripper end effector [Lin 15], e) A multi-channel CTR with forceps pair for tissue grasping and electric coagulator for tissue ablation [Yu 16], f) Tissue removing end effector design prototype [Vasilyev 15a], h) Metal MEMS tissue approximation detachable end effector [Gosline 12], g) Needle-sized wrist gripper [Swaney 16], i) Cable-driven CTR disposable micro end effector [Prasai 16], j) Beveled tip end effector [Swaney 15c], k) RGB camera end effector navigating through an origami tunnel [Girerd 20b].....	162
E.1	Precurved optical fibre join by fusion .....	172
E.2	RealSense D405 stereo depth camera with two lenses for submillimeter accuracy range 3D image capturing feature. We used the helical pre-curved tube to mimic out-of-plane tube deformation configuration <b>A</b> ) using the stereo module <b>depth stream</b> for image capturing of two different samples comprising of the helical pre-curved tube and a 2 Euro coin, one could see on the image labeling the missing helical part of the sub-millimeter pre-curved tube, <b>B</b> ) the same image with the two samples but in normal camera color streaming <b>C</b> ) using the 3D pattern projection depth stream mode in vertical view configuration, one could see that the 2 Euro coin shape was much closer to the coin shape compared to the case of the micro-scale helical tube and moreover, there were lots of artifacts, which was very difficult to filter out. ....	173

## List of Figures

---

## List of Tables

1.1	Mechanical comparison of the different tube materials. ....	28
2.1	Different glass 3D printing techniques/technology.....	60
2.2	3-point bending stiffness analysis for comparing the effect of thin heat shrink polymer on capillary glass .....	77
3.1	The different demonstrations and their respective Caturo tube specifications .....	87
3.2	Prototype tube specifications for the forward kinematic model.....	88
3.3	Prototype tube specifications for path tracing using the IKM.....	93
3.4	Prototype tube specifications for the stability analysis/investigation .	94
3.5	Prototype tube specifications for the 3D conical-spiral free space deployment .....	97
3.6	Prototype tube specifications for helical pre-curved CTR glass deployment .....	98
3.7	Prototype tube specifications for constraint deployment through 3-needles .....	100
3.8	Prototype tube specifications for the deployment of pre-curved optical fiber with laser transmission .....	101
3.9	Prototype tube specifications for fluid suction and delivery .....	102
3.10	Prototype tube specifications for vitreoretinal deployment under the OCT .....	104
4.1	Notation and definitions .....	112
4.2	Static Cosserat rod equations expressed as a set of nonlinear ODEs in the arc length dimension. ....	113
4.3	The boundary conditions for the entire robot modeling which consist of the hole attachment pattern leading to the geometric constrain equations and the rigid body equilibrium equation due to external wrench (force and moment) acting on the end-effector. ....	114

4.4	The FKM and IKM with their respective different unknowns, inputs, and output variables for the numerical computation using the shooting method.....	115
4.5	The different actuation length with its obtainable workspace area .....	123
4.6	Obtainable workspace area, maximum stiffness, manipulability, and orientation angle due to change of the PCR end-effector dimension .....	124
A.1	Overview of the synthesis approach proposed in the literature for CTRs, classified by objective.....	146
D.1	Applications of CTRs in MIS.....	168
D.2	Applications of CTRs in MIS.....	169

**Titre :** Contribution à la Miniaturisation des Robots Continus par l'utilisation du Verre

**Mots clefs:** Contribution, Miniaturisation, Continuum, Robots, Verre

**Résumé :** Les robots continus suscitent un intérêt croissant dans les applications médicales, en raison de leur forme élancée et de leur souplesse, qui les rendent plus sûrs pour l'interaction homme-robot. En outre, ils sont capables de suivre une trajectoire complexe en 3D, grâce à leurs degrés de liberté infinis. L'objectif de cette thèse est de tirer parti de la flexibilité du verre à l'échelle microscopique pour réaliser de nouveaux robots de continuum plus miniatures par rapport à ceux de la littérature. La première contribution est une étude conceptuelle, portant sur la conception et la fabrication de différents prototypes de CTR et dérivant une approche de classification générale tout en proposant à la communauté des chercheurs une méthodologie concise pour l'évaluation des CTR à l'avenir. Deuxièmement, nous avons proposé une nouvelle génération de CTR submillimétrique miniaturisé en verre, dont le tube a un diamètre externe de  $90\mu\text{m}$  et un rayon de courbure de 5mm. En outre, nous avons présenté une approche nouvelle, facile et rapide, spécifique au patient et personnalisable, pour obtenir un tube pré-courbé en verre, qui a été caractérisé, suivi par la validation du modèle de robot (cinématique avant, cinématique inverse et analyse de stabilité). Diverses démonstrations de preuves de concept pour les différentes capacités d'application,

par exemple le déploiement vitréo-rétinien dans un œil de poisson, le déploiement de contraintes au moyen d'aiguilles à trois positions (orifice de 1 mm environ), le déploiement CTR hélicoïdal pré-courbé et à fibre optique avec capacité de transmission laser, et enfin l'aspiration et l'administration de fluides. La troisième contribution a été l'étude et la démonstration d'une PCR 3-DoF miniaturisée utilisant une fibre optique en verre. La conception du robot a une dimension de  $2,5 \times 2,5 \times 6$  mm et peut atteindre un angle de pointe et d'inclinaison de +90 à -80 degrés. Les performances du robot, telles que l'espace de travail, la manipulabilité et la rigidité, ont été évaluées en fonction des variations des différents paramètres géométriques du robot. Pour la validation du modèle, différents mouvements de trajectoire ont été présentés, tels que la circonference du plan vertical et l'espace de travail, suivis par des formes circulaires et carrées dans le plan horizontal, ce qui montre les grandes perspectives du robot pour augmenter la dextérité dans un espace confiné. Enfin, dans les deux cas, l'analyse de la conception du robot était très importante pour étudier la stabilité du robot, pour la CTR en raison de la torsion, et pour la PCR, en raison de la longueur d'actionnement.

**Title :** Contribution to the Miniaturization of Continuum Robots by Using Glass

**Keywords :** Contribution, Miniaturization, Continuum, Robots, Glass

**Abstract :** Continuum robots are gaining increasing interest in medical applications, due to their slender shape and compliant nature which makes them safer for human-to-robot interaction. In addition, they are able to follow a 3D complex path, thanks to their infinite degrees of freedom. The goal of this thesis is to take advantage of glass flexibility at the microscale to actualize novel and more miniature continuum robots when compared to those in the literature. The first contribution is a conceptual study, addressing the design and fabrication of different CTR prototypes and deriving a general classification approach while proposing to the research community a concise methodology for the evaluation of CTR in the future. Secondly, we proposed a new generation of a miniaturized sub-millimeter CTR that is made of glass, which has a tube with an external diameter down to  $90\mu\text{m}$  and a 5mm radius of curvature. Furthermore, we presented a novel, easy, and rapid patient-specific/customizable approach to obtaining a pre-curved tube using glass, which was characterized, followed by the robot model validation (forward kinematic, inverse kinematics, and stability analysis).

Various demonstrations of proofs-of-concept for the different application capabilities e.g. vitreoretinal deployment in a fish eye, constraint deployment through 3-stationed needles ( $\sim 1\text{mm}$  orifice), pre-curved helical and fiber optics CTR deployment with laser transmission capability, and then, fluid suction and delivery. The third contribution was the investigation and demonstration of a miniaturized 3-DoF PCR using glass optical fiber. The robot design has a dimension of  $2.5 \times 2.5 \times 6\text{mm}$  and can reach +90 to -80 degrees in the tip and tilt angle. The robot's performance such as the workspace, manipulability, and stiffness was evaluated as a function of variations of different geometrical parameters of the robot. For the model validation, different path movements were presented such as vertical plane circumradius and workspace followed by the circular and square shapes in the horizontal plane, which shows the great prospect of the robot for increasing dexterity in confined space. Finally, for both cases, the robot design analysis was very important for investigating the robot stability, for CTR due to torsion, and for PCR, due to the actuation length.